

**Solid-State Nuclear Magnetic Resonance of Copper-Amyloid Beta, Amylospheroids,
Fast Magic Angle Spinning**

BY

SUDHAKAR PARTHASARATHY
B.S., University of Madras, 2000
M.S., University of Madras, 2002

THESIS

Submitted as partial fulfillment of the requirements
for the degree of Doctor of Philosophy in Chemistry
in the Graduate college of the
University of Illinois at Chicago, 2013

Chicago, Illinois

Defense committee:

Prof. Yoshitaka Ishii, Chair and Advisor
Prof. Leslie Fung
Prof. Timothy Keiderling
Prof. Justin Lorieau
Dr. Benjamin Ramirez, Center of Structural Biology

I would like to dedicate this thesis
to my mother Yasodha Parthasarathy and father Parthasarathy Gopal
to my grandparents Jayalakshmi Perumal and Perumal Gopal
to my sister Shanmugapriya Suresh
and to my loving wife Srivani Sudhakar

ACKNOWLEDGEMENTS

First, I would like to extend my sincere gratitude and appreciation to my research advisor Dr. Yoshitaka Ishii who continuously supported me throughout the program. I greatly admire him for his guidance and the advice he gave me in becoming a successful researcher. I sincerely thank him for everything, which I learnt from him during the last few years. Next, I would like to thank the members of my thesis committee, Dr. Leslie Fung, Dr. Tim Keiderling, Dr. Justin Lorieau and Dr. Benjamin Ramirez for spending their time in reviewing this thesis and providing their guidance and insight.

Next, I wish to especially thank our collaborators Dr. Ruth Nussinov at NCI, Frederick, MD, USA for the Molecular Dynamics (MD) simulations, Dr. Minako Hoshi at Kyoto University, Kyoto, Japan for providing the ASPD samples, Dr. Masatsune Kainosho at Tokyo Metropolitan University, Tokyo, Japan for providing us the stereo array isotope labeled samples and Dr. Yusuke Nishiyama at JEOL resonance, Tokyo, Japan for providing the 1mm MAS probe and valuable suggestions in trouble shooting the problems in the probe. I would like to thank my fellow senior group members Dr. Nalinda Wickramasinghe, Dr. Medhat Shaibat, Dr. Christopher Jones from whom I have learnt the experimental skills. I also thank Dr. Sandra Chimon, Dr. Fei Long, Dr. Leah Casabianca, Dr. William Tay, Dr. Mirgnayani Kotecha, Brian K. Yoo, Songlin Wang, Yiling Xiao, Yichen Hu, Zhi Yang and Bibek Shestra for their assistance, support, encouragement and friendship. I appreciate the help rendered by Dr. Dan McElheny in the MD simulations and other valuable suggestions for one of the project and I am very grateful to Mr. Don Rippon, Mr. Clint Briscoe, Dr. Randy Puchalski, and Mr. Frank Tobias from the UIC chemistry department for their support in my experiments and research.

ACKNOWLEDGEMENTS (continued)

I am very grateful to my parents, grandparents, uncles Dr. Balakrishnan Perumal, Mr. Chandrasekar Perumal and Mr. Govindaraj Perumal for their extended emotional, financial support, love and kindness throughout my life. I am very thankful to my sister and brother-in-law Mr. M.S.S. Suresh and nephew Hareesh Madana for giving care to my parents in my extended absence. Last but not the least, I would like to thank and appreciate my wife Srivani Sudhakar for her support, encouragement and motivation when things were tough. I could not have done this without your love and affection.

SP

TABLE OF CONTENTS

<u>CONTENTS</u>	<u>PAGE</u>
I) INTRODUCTION.....	1
A) High resolution Solid-State Nuclear Magnetic Resonance of biomolecules.....	1
1) General introduction to Nuclear Magnetic Resonance spectroscopy	1
2) Solid-State Nuclear Magnetic Resonance spectroscopy	1
3) High-resolution Solid-State Nuclear Magnetic Resonance Spectroscopy	2
4) Recent applications of biomolecular Solid-State Nuclear Magnetic Resonance	3
B) Amyloid β protein and Alzheimer's Disease.....	4
1) Neurodegenerative disorders associated with amyloidosis.....	4
2) Alzheimer's disease	4
3) Neuropathology of AD.....	5
4) Diffusible amyloid intermediate assemblies of A β	7
5) Amylospheroid (ASPD) intermediate	8
6) Accumulation of metal ions in amyloid plaques in AD.....	9
7) Redox reactivity of Cu-A β complex and its role in the oxidative stress.....	9
II) GENERAL METHODS	11
A) Nuclear Magnetic Resonance (NMR)	11
1) Nuclear Spin and Boltzmann Distribution.....	11
2) Radiofrequency Pulse.....	14
3) Chemical Shift.....	15
4) Magic Angle Spinning	16
B) Fast and Ultra-fast magic angle spinning for sensitivity enhancement in Solid-State NMR	19
C) Solid-State NMR of paramagnetic proteins.....	20
D) The NMR spectrometer	21
E) Stereo array isotope labeling method in ^1H resolution enhancement in Solid-State NMR	22
III) MOLECULAR-LEVEL EXAMINATION OF Cu^{2+} BINDING STRUCTURE FOR AMYLOID FIBRILS OF 40-RESIDUE ALZHEIMER'S β BY SOLID-STATE NMR SPECTROSCOPY	25
A) Introduction.....	25
B) Results and Discussion	28
C) Conclusion	49
D) Materials and methods.....	51
1) Synthesis and Purification of A β (1-40) Peptide.	51
2) Preparation of A β (1-40) Fibrils for Cu^{2+} -Binding Assay and Solid-State NMR Experiments	52
3) Solid-State NMR Experiments.....	54

TABLE OF CONTENTS (continued)

<u>CONTENTS</u>	<u>PAGE</u>
4) Determination of Cu ²⁺ binding to Aβ(1-40) fibrils using UV-VIS spectroscopy	56
5) Analysis of ¹ H T ₁ values for Cu ²⁺ -bound Aβ(1-40) fibrils	57
6) Chemical shift analysis of Cu ²⁺ -bound and Cu ²⁺ -unbound Aβ(1-40) fibrils	57
IV) NMR BASED CHARACTERIZATION OF STRUCTURES, REDOX REACTIONS, AND REACTIVE OXYGEN SPECIES (ROS) PRODUCTION MECHANISM IN Cu-ION BOUND 40-RESIDUE ALZHEIMER'S β AMYLOID FIBRILS	64
A) Introduction	64
B) Results	66
1) ROS production by Cu-Aβ	66
2) In-situ NMR Detection of Redox Cycling for Cu-bound Aβ fibrils	70
3) Redox reaction and structural information of Cu ⁺ binding to Aβ(1-40) fibrils probed by ¹³ C SSNMR	75
4) Histidine-coordination to Cu ⁺ in Aβ(1-40) fibrils probed by ¹³ C and ¹⁵ N SSNMR	79
5) TEM analysis of the Cu-Aβ(1-40) fibrils with ascorbate	87
6) Solution state NMR studies of Cu-Aβ(1-40) monomer	88
C) Discussion	90
D) Materials and Methods	97
1) Chemicals and reagents	97
2) Synthesis and purification of Aβ(1-40) peptide	97
3) Photometric hydrogen peroxide (H ₂ O ₂) quantification	97
4) Hydroxyl radical detection by fluorescence	98
5) Solution-state NMR	98
6) Transmission electron microscopy (TEM)	99
7) Solid-state NMR	99
8) Sample preparation for SSNMR	100
V) MOLECULAR-LEVEL STRUCTURAL INSIGHT INTO A PATHOLOGICALLY RELEVANT AMYLOID INTERMEDIATE OF ALZHEIMER'S β BY SOLID-STATE NMR SPECTROSCOPY	103
A) Introduction	103
B) Results	105
1) Aβ(1-42) misfolds into a highly ordered conformer in ASPD	107
2) Conformational analysis of ASPD	109
3) ASPD has a parallel β-sheet arrangement	113
4) ASPD Misfolds Differently from Fibril	115
C) Discussion	118
1) Structural Features of ASPD and Significance	118
2) Difference from other Amyloid aggregates for Aβ	119

TABLE OF CONTENTS (continued)

<u>CONTENTS</u>	<u>PAGE</u>
3) Transition to a Toxic Amyloid Intermediate.....	120
D) Materials and Methods	121
VI) CHOICE OF DOPANTS FOR PARAMAGNETIC RELAXATION-ASSISTED CONDENSED DATA COLLECTION METHOD AND ITS APPLICATION AT HIGH MAGNETIC FIELD.....	122
A) Introduction.....	122
B) Results and Discussion	124
1) Choice of paramagnetic dopants	124
2) ¹³ C SSNMR by PACC for α-spectrin II (SpaII 1-147) microcrystals.....	132
3) Spinning speed dependence of ¹ H T ₁	134
4) Low power decoupling at Ultra-fast MAS.....	136
5) PACC at Ultra-fast MAS	138
C) Materials and Methods	142
1) Lysozyme crystallization	142
2) Incubation with paramagnetic reagents.....	142
3) Synthesis of Ni(II)-DO2A.....	143
4) SSNMR experiments.....	144
VII) ¹H INDIRECT DETECTION FOR ¹³C BIOMOLECULAR SOLID-STATE NMR: ENHANCED SENSITIVITY AND RESOLUTION BY A COMBINED USE OF ULTRA-FAST MAGIC ANGLE SPINNING, HIGH FIELD AND STEREO ARRAY ISOTOPE LABELING	146
A) Introduction.....	146
B) Results and Discussion	147
1) Resolution enhancement in ¹ H SSNMR by UFMAS and SAIL.....	147
2) Sensitivity enhancement in ¹³ C SSNMR by ¹ H detection experiments using UFMAS and SAIL	150
C) Experimental section	157
CITED LITERATURE	162
APPENDICES.....	184
A) Permission/Licence for copyrighted images used in this thesis	184
1) Figure 1	184
2) Figure 2	185
3) Figure 5	186
4) Chapter III.....	187
CURRICULUM VITAE.....	188

LIST OF TABLES

<u>TABLE</u>	<u>PAGE</u>
TABLE I. ^{13}C CHEMICAL SHIFTS FOR THE $\text{A}\beta(1-40)$ FIBRILS IN THE PRESENCE AND ABSENCE OF Cu^{2+} . THE SHIFTS WERE REFERENCED WITH TMS.	59
TABLE II. ^{13}C CHEMICAL SHIFTS OF THE $\text{A}\beta(1-40)$ FIBRILS, Cu^{2+} - $\text{A}\beta(1-40)$ FIBRILS, AND Cu^{2+} - $\text{A}\beta(1-40)$ FIBRILS INCUBATED WITH ASCORBATE (Cu^{+} - $\text{A}\beta(1-40)$ FIBRILS). THE CHEMICAL SHIFTS WERE REFERENCED TO TETRAMETHYLSILANE (TMS).	93
TABLE III. SURVEY OF THE ^{13}C , ^{15}N CHEMICAL SHIFTS OF Cu^{+} AND Zn^{2+} BOUND TO HISTIDINE RESIDUES ALONG WITH THE ^{13}C , ^{15}N CHEMICAL SHIFTS OF HISTIDINE TAUTOMERS.....	96
TABLE IV. A LIST OF THE ASPD SAMPLES USED FOR THIS STUDY.....	108
TABLE V. ^{13}C CHEMICAL SHIFTS ASSIGNED FOR THE ASPD SAMPLES WITH PREDICTED TORSION ANGLES.....	112
TABLE VI. COMPARISON OF THE EFFECT OF DIFFERENT PARAMAGNETIC RELAXATION DOPANTS AND THEIR CONCENTRATION DEPENDENCE ON ^1H T_1 AND ^{13}C LINE BROADENING. THE LINE WIDTHS WERE MEASURED ONLY FOR THE SPECTRA WHICH SHOWED CONSIDERABLY SHORT ^1H T_1 'S WHICH WERE USED FOR THE PACC METHOD.....	131

LIST OF FIGURES

<u>FIGURE</u>	<u>PAGE</u>
Figure 1. Cartoon showing the comparison of the healthier neurons in normal human brains and the AD affected human brains.....	6
Figure 2. Size overlap of the natural and synthetic A β oligomers.....	8
Figure 3. Energy level diagram for $I = \frac{1}{2}$ and $I = 1$ nuclei in presence of a magnetic field.	13
Figure 4. Schematic diagram of the orientation of the sample rotor with respect to the applied magnetic field in a MAS experiment.....	19
Figure 5. Design concepts embodied in the SAIL amino acid	24
Figure 6. TEM images of A β (1-40) fibrils (a) without and (b) with Cu $^{2+}$, which is 0.4 mol. eq. to A β	29
Figure 7. Fractions of Cu $^{2+}$ ions that were not bound to A β (1-40) fibrils in a mixture of 500 μ M A β (1-40) fibril solution with CuGly or CuCl $_2$ (0.25-1.0 mM) at three molar ratios of Cu $^{2+}$ to A β ($f_{Cu/A\beta}$) of 0.5, 1.0, and 2.0.....	30
Figure 8. Comparison of 1D ^{13}C CPMAS spectra of A β (1-40) fibrils without (black) and with (red) 0.4 mol. eq. of Cu $^{2+}$, together with signal assignments.....	31
Figure 9. Comparison of 2D $^{13}C/^{13}C$ correlation spectra for the same fibril samples as in Figure 8 without (black) and with (red) Cu $^{2+}$	33
Figure 10. Aromatic regions of ^{13}C CPMAS spectra for (a) His-13, (b) His-14, and (c) Phe-20 sidechains for A β (1-40) fibrils in the hydrated state (black) without and (red) with Cu $^{2+}$	34
Figure 11. Relative signal intensity of ^{13}C resonances in A β (1-40) fibril after Cu $^{2+}$ binding. The error bars indicate the uncertainty due to the noise level.....	35
Figure 12. Amino acid sequence of A β (1-40) and the extent of signal quenching by Cu $^{2+}$ binding (green $\leq 15\%$; orange 15-25%; red $\geq 25\%$).....	36
Figure 13. 2D $^{13}C/^{13}C$ SSNMR spectra between aliphatic and ^{13}CO regions for uniformly ^{13}C - and ^{15}N -labeled A β (1-40) fibrils (black) without and (red) with Cu $^{2+}$, with 1D slices at $\omega_1 =$ (a) 34.6, (b) 43.9, and (c) 59.8 ppm.	38
Figure 14. TEM images of (a) A β (1-40) fibrils (b) A β (1-40) H14A fibrils	39
Figure 15. Comparison of 1D ^{13}C CPMAS spectra of A β (1-40) H14A mutation fibrils without (black) and with (red) 0.4 mol. eq. of Cu $^{2+}$, together with signal assignments.....	40
Figure 16. Final MD structure of Cu $^{2+}$ bound A β (1-40) fibril viewed from (a) one of the N-terminal sides and (b) the fibril axis after three thermal annealing cycles.....	42
Figure 17. Final MD structure of Cu $^{2+}$ bound A β (1-40) fibril viewed from (a) one of the N-terminal sides and (b) the fibril axis after three thermal annealing cycles.....	43
Figure 18. Structural parameters for selected Cu $^{2+}$ coordination geometries in the MD simulation in Figure 16.....	44

LIST OF FIGURES (continued)

<u>FIGURE</u>	<u>PAGE</u>
Figure 19. (a) A schematic of 4-coordination Cu^{2+} (yellow sphere) sphere involving 1/2 N and 2/3 O. (b) Cu^{2+} coordination modes involving coordination in both the axial and equatorial positions.....	45
Figure 20. Cu^{2+} coordination geometries to (a) His-6, His-13, His-14, (b) Asp-1, His-6, His-14, (c) Asp-1, His-14, Val-40 (d) Asp-1, His-13, Val-40	46
Figure 21. Comparison of 1D ^{13}C CPMAS spectra of $\text{A}\beta(1-42)$ fibrils (a) without (black) and (b) with (red) 0.4 mol. eq. of Cu^{2+} , together with signal assignments.....	48
Figure 22. Comparison of 2D $^{13}\text{C}/^{13}\text{C}$ correlation spectra for the same fibrils samples as in Figure 21 (a) without (black) and (b) with (red) Cu^{2+}	49
Figure 23. Time-dependent production of ROS H_2O_2 by $\text{A}\beta(1-40)$ fibrils alone (blue), with 40 μM Cu^{2+} (red), and in the presence of 1 mM ascorbate (green).....	68
Figure 24. Time-dependent production of hydroxyl radical (OH^\bullet) by 40 μM Cu^{2+} alone (orange) and 100 μM Cu^{2+} - $\text{A}\beta(1-40)$ fibrils (green) in the presence of 1 mM ascorbate.....	69
Figure 25. Time-dependent generation of H_2O_2 by 40 μM Cu^{2+} (orange) and 100 μM Cu^{2+} - $\text{A}\beta(1-40)$ fibrils (green) after the addition of 1 mM ascorbate.	70
Figure 26. (a) ^1H T_1 of the Cu^{2+} - $\text{A}\beta(1-40)$ in presence of 1 mol. eq. of ascorbate for 8 h. (b) ^1H T_1 of the Cu^{2+} - $\text{A}\beta(1-40)$ in presence of 1 mol. eq. of ascorbate for 100 h.....	72
Figure 27. ^1H T_1 of the Cu^{2+} - $\text{A}\beta(1-40)$ in presence of 5 mol. eq. of ascorbate. Orange arrows show the period during the rotor was exposed to the air.....	73
Figure 28. Quantification of Cu^+ - $\text{A}\beta(1-40)$ fibrils resulting from reduction of Cu^{2+} by ascorbate.	74
Figure 29. 1D ^{13}C CPMAS SSNMR spectra of (a) $\text{A}\beta(1-40)$ fibrils uniformly ^{13}C - and ^{15}N -labeled at residues Val-12, Ala-21, Gly-33 and selectively ^{13}C labeled Met-35 at ($\epsilon^{13}\text{CH}_3$) (b) with 0.4 mol. eq. of Cu^{2+} , and (c) with both 0.4 and 1 mol. eq. of Cu^{2+} and ascorbate respectively.....	76
Figure 30. ^{13}C DEPT-45 solution state NMR spectra of (a) 2 mM methionine, (b) 2 mM methionine with 0.8 mM CuCl_2 , (c) 2 mM methionine with 0.8 mM CuCl_2 and 2 mM ascorbate, and (d) 2 mM methionine with 2 mM ascorbate.....	77
Figure 31. 2D $^{13}\text{C}/^{13}\text{C}$ fpRFDR spectra of (a) 100 μM $\text{A}\beta(1-40)$ fibrils alone, (b) with 0.4 mol. eq. of Cu^{2+} , and (c) with both Cu^{2+} and 1 mol. eq. ascorbate.....	78
Figure 32. 1D ^{13}C CPMAS (a and b) and 2D $^{13}\text{C}/^{13}\text{C}$ correlation (c and d) spectra of two $\text{A}\beta(1-40)$ fibrils uniformly ^{13}C - and ^{15}N -enriched at residues His-13 (a and c) and His-14 (b and d), respectively, without Cu (black), with Cu^{2+} (green), and with Cu^+ (i.e. after incubation with ascorbate) (purple).....	81

LIST OF FIGURES (continued)

<u>FIGURE</u>	<u>PAGE</u>
Figure 33. 1D ¹⁵ N CPMAS spectra of Aβ(1–40) fibrils (¹⁵ N-labeled at His-13 (a–c) and His-14 (d–f)) alone (a and d), with Cu ²⁺ (b and e), and with Cu ⁺ (Cu ²⁺ and ascorbate, c and f). Addition of Cu ²⁺ to Aβ(1–40) fibrils results in attenuation of the Nε signal at ~ 170 and ~ 169 ppm in both histidine residues (b and e).....	84
Figure 34. 2D ¹³ C/ ¹⁵ N correlation spectra of Aβ(1-40) fibrils ¹³ C- and ¹⁵ N- labeled at His-13 (a-c) and His-14 (d-f) alone (a and d), with Cu ²⁺ (b and d), and with Cu ⁺ (Cu ²⁺ and ascorbate, c and f).....	87
Figure 35. TEM (~10 nm diameter, length > 1 μM) images of the (a) Aβ(1-40) fibrils (100 μM monomer concentration), (b) Aβ(1-40) fibrils incubated with 40 μM Cu ²⁺ for 24 h at 4 °C, and (c) Cu ²⁺ -Aβ(1-40) fibrils incubated with 1 mM ascorbate for 24 h at room temperature.....	88
Figure 36. Solution state ¹ H NMR spectra (aromatic region) of (a) 92 μM Aβ(1–40) monomer, (b) with 37 μM Cu ²⁺ , and (c) with both Cu ²⁺ and 1 mol. eq. of ascorbate.	90
Figure 37. (a) Schematic representation of the double-layered antiparallel cross-β motif (Left), showing β-strands in yellow, the intervening loop in red, and groups of hydrophobic side chains as light green and dark green blocks. (b) Schematic representation of the double-layered parallel cross-β motif identified in WT-Aβ1–40 fibrils by Tycko and co-workers. ^{15, 19, 20}	104
Figure 38. Transmission electron micrograph for the entire ASPD sample used for the NMR analysis in Figure 40.	106
Figure 39. Amino acid sequence of Aβ(1-42), where the residue names are color coded by type of amino acids as follows: negatively charged (red), positively charged (blue), hydrophilic (cyan), and hydrophobic (green) residues.	107
Figure 40. 2D ¹³ C/ ¹³ C SSNMR spectra of ASPD for Aβ(1-42) with a short-range mixing (DARR mixing time of 50 ms) ²⁴⁷ at a spinning speed of 20 kHz.	109
Figure 41. Secondary chemical shift analysis for the 18 residues from four different ASPD samples.....	111
Figure 42. Torsion angle prediction using TALOS software. The predicted torsion angles suggest that (ϕ, ψ) ~ (-120°, 130°), which is consistent with β-sheet structure.	113
Figure 43. ¹³ CO- ¹³ CO interstrand distance measurement (solid circle) for Ala-30 by CT-fpRFDR measurement with simulated dephasing curves for 5.6 Å (purple), 5.8 Å (cyan), and 6.0 Å (blue).....	115
Figure 44. A possible structural model based on the present data. The residues inspected by SSNMR are in bold. The β-sheet regions indicated in Figure 41 and 42 are represented by blue arrows.	116

LIST OF FIGURES (continued)

<u>FIGURE</u>	<u>PAGE</u>
Figure 45. Overlay of the β -sheet region (magenta) on amyloid fibril structure of A β (1-42) obtained by H/D exchange NMR, where the side chains are color coded following that in Figure 41.....	117
Figure 46. Comparison of the 2D $^{13}\text{C}/^{13}\text{C}$ SSNMR spectra of (a) ASPD and (b) Fibrils for A β (1-42) with a short-range mixing (DARR mixing time of 50 ms). The A β (1-42) was uniformly ^{13}C - ^{15}N - labeled at Phe-4, Val-12, Leu-17, Ala-21 and Gly-29.....	118
Figure 47. The comparison of ^{13}C CPMAS spectra of unlabeled lysozyme (a) without dopants (b) with 3 mM Ni(II)-EDTA, and (c) with 10 mM Cu(II)-EDTA.....	126
Figure 48. The comparison of ^{13}C CPMAS spectra of unlabeled lysozyme (a) without dopants (b) with 1mM Gd(III)-DEPTA, and (c) with 20 mM Ni(II)-DO2A.....	128
Figure 49. Comparison of ^{13}C CPMAS spectra of lysozyme (a) with 10 mM Cu(II)-EDTA (b) with 6 mM Ni(II)-EDTA, and (c) with 20 mM Cu(II)-EDTA.....	130
Figure 50. Comparison of ^{13}C CPMAS spectra of 147-residue recombinant protein of the cytoskeletal protein α -spectrin II (Sp α II(1-147)) (a) with 50 mM Cu(II)-EDTA and (b) without doping, together with (c) a difference spectrum..	133
Figure 51. Comparison of $^{13}\text{C}/^{13}\text{C}$ fpRFDR 2D spectra of 147-residue recombinant protein of the cytoskeletal protein α -spectrin II (Sp α II(1-147)) without and with 50 mM Cu(II)-EDTA doping.....	134
Figure 52. Spinning-speed dependence of ^1H T_1 values for Cu(II)-EDTA doped (a) and undoped (b) uniformly ^{13}C - and ^{15}N -labeled ubiquitin samples.....	135
Figure 53. Comparison of the performance of the (a) high power 100 kHz TPPM decoupling at 19 kHz MAS with (b) 8 kHz lpTPPM at 78 kHz ultra-fast MAS in ^{13}C - and ^{15}N - uniformly labeled Alanine sample.....	137
Figure 54. ^1H decoupling field dependence of ^{13}C CPMAS signal intensities under TPPM decoupling for $^{13}\text{C}\alpha$, $^{13}\text{C}\beta$, $^{13}\text{C}\gamma_1$, $^{13}\text{C}\gamma_2$ groups of uniformly ^{13}C - and ^{15}N -labeled L-Isoleuine.....	138
Figure 55. Two dimensional $^{13}\text{C}/^{13}\text{C}$ fpRFDR SSNMR spectrum of uniformly ^{13}C - and ^{15}N -labeled Alanine sample at MAS 78 kHz.....	139
Figure 56. Comparison of the 1D ^{13}C CPMAS of Cu $^{2+}$ -A β (1-40) fibrils uniformly ^{13}C - and ^{15}N -labeled at sites Phe-4, Gly-9, Val-12, Leu-17 and Ala-21 collected at (a) 9.4 T magnet with 3 mg fibrils at MAS 20 kHz with 90 kHz TPPM ^1H decoupling and 1.8 s pulse delay (b) 18.8 T magnet with 1 mg fibrils at MAS 50 kHz with 10 kHz low power TPPM ^1H decoupling and 0.3 s pulse delay.....	140

LIST OF FIGURES (continued)

<u>FIGURE</u>	<u>PAGE</u>
Figure 57. Comparison of the 2D $^{13}\text{C}/^{13}\text{C}$ fpRFDR spectra of Cu^{2+} -A β (1-40) fibrils uniformly ^{13}C - and ^{15}N - labeled at sites Phe-4(Blue), Gly-9(Orange), Val-12(Red), Leu-17(Cyan) and Ala-21(Green) collected at (a) 9.4 T magnet with 3 mg fibrils at MAS 20 kHz with 90 kHz TPPM ^1H decoupling and 1.8 s pulse delay (b) 18.8 T magnet with 1mg fibrils at MAS 50 kHz with 10 kHz lpTPPM ^1H decoupling and 0.28 s pulse delay.	141
Figure 58. Comparison showing the microscope images of lysozyme microcrystals (a) without dopants and (b) with 3 mM Ni(II)-EDTA.....	143
Figure 59. (a, b) The chemical structures of (a) UL-Ile and (b) SAIL-Ile. (c, d) Spinning dependence of ^1H MAS SSNMR spectra of (c) the UL-Ile and (d) SAIL-Ile.....	149
Figure 60. ^1H SSNMR of SAIL-Thr (Chemical structure at the top) at various spinning speeds. The ^1H NMR spectra were obtained with 10 kHz WALTZ-16 ^{13}C decoupling..	150
Figure 61. (a) ^1H detected and (b) ^{13}C detected $^{13}\text{C}/^1\text{H}$ 2D experiment (c) 1D CPMAS of SAIL-Ile at MAS 78kHz d,e) 1D slice along the ^1H chemical shift of 4.1 ppm from (d) the ^1H detected and (e) ^{13}C detected 2D $^{13}\text{C}/^1\text{H}$ correlation SSNMR..	152
Figure 62.(a) ^1H detected (b) ^{13}C detected $^{13}\text{C}/^1\text{H}$ 2D experiment (c) 1D CPMAS of SAIL-Thr at MAS 78kHz. (d,e) 1D slice along the ^1H chemical shift of 4.1 ppm from (d) the ^1H detected and (e) ^{13}C detected 2D $^{13}\text{C}/^1\text{H}$ correlation SSNMR..	153
Figure 63.(a) ^1H detected and (b) ^{13}C detected $^{13}\text{C}/^1\text{H}$ 2D experiment (c) 1D CPMAS of SAIL-Ubq at MAS 78kHz (d-g) 1D slices from ^1H shifts of (d, f) 0.27 ppm and (e, g) 0.58 ppm from (d, f) ^1H detected and (e, g) ^{13}C detected experiments..	154
Figure 64. (a) $^{13}\text{C}/^1\text{H}$ 2D projection from the 3D $^{13}\text{C}/^{13}\text{C}/^1\text{H}$ experiment (b) the secondary structure of Ubq showing the Ile residues which are SAIL labeled (See experimental section for the aminoacid sequence) (c-e) are the representative 2D $^{13}\text{C}/^{13}\text{C}$ slices corresponding to ^1H chemical shifts of (c) 0.16 ppm and (d) 0.35 ppm and (e) 0.48 ppm from the 3D experiment.....	156
Figure 65. Pulse sequence for ^1H -detected 2D $^1\text{H}/^{13}\text{C}$ correlation spectroscopy..	158
Figure 66. Pulse sequence for ^{13}C -detected 2D $^1\text{H}/^{13}\text{C}$ correlation spectroscopy..	159
Figure 67. Pulse sequence for ^1H -detected 3D $^{13}\text{C}/^{13}\text{C}/^1\text{H}$ correlation spectroscopy.....	160

LIST OF ABBREVIATIONS

ΔT	Temperature difference
${}^1\text{H } T_1$	Proton longitudinal relaxation time
A β	Amyloid beta
AD	Alzheimer's Disease
AFM	Atomic-Force Microscopy
APP	Amyloid Precursor Protein
ASPD	Amylospheroids
B ₀	External Magnetic Field
B ₁	Magnetic field due to RF pulse
BCS	Bathocuproine disulfonic acid disodium salt
CCA	Coumarin-3-Carboxylic Acid
CD	Circular Dichroism
Co(II)-EDTA	Ethylenediaminetetraacetic acid cobalt(II) disodium salt
CP	Cross Polarization
CPMAS	Cross Polarization Magic Angle Spinning
CuCl ₂	Copper (II) Chloride
CuGly	Copper (II) Glycinate
Cu(II)-EDTA	Ethylenediaminetetraacetic acid copper(II) disodium salt
cw	Continuous Wave
DSS	4,4-dimethyl-4-silapentane-1-sulfonic acid
EPR	Electron Paramagnetic Resonance
FAD	Familial Alzheimer's Disease
Fmoc	9-Fluorenylmethyloxycarbonyl
fpRFDR	finite pulse Radio Frequency Driven Dipolar Recoupling

LIST OF ABBREVIATIONS (continued)

H ₂ O ₂	Hydrogen Peroxide
HCl	Hydrochloric acid
HD	Huntington's Disease
HPLC	High Performance Liquid Chromatography
HRP	Horse Radish Peroxidase
kHz	Kilo Hertz
lpTPPM	Low Power Two Pulse Phase Modulation
MALDI-TOF	Matrix Assisted Laser Desorption Ionisation-Time of Flight
MD	Molecular Dynamics
MHz	Mega Hertz
Ni(II)-DO2A	1, 4, 7, 10-tetra-azacyclododecane-1,4,7,10-1,7-bis(acetic acid) Nickel(II)
Ni(II)-EDTA	Ethylenediaminetetraacetic acid nickel(II) disodium salt
NMR	Nuclear Magnetic Resonance
OH [·]	Hydroxyl Radical
PACC	Paramagnetic Relaxation Assisted Condensed Data Collection
PD	Parkinson's Disease
PRE	Paramagnetic Relaxation Enhancement
ppm	Parts Per Million
RF	Radio Frequency
ROS	Reactive Oxygen Species
RRC	Research Resource Center
SSNMR	Solid-State Nuclear Magnetic Resonance
<i>t</i> ₁	Signal detection in indirect dimension

LIST OF ABBREVIATIONS (continued)

t_2	Signal detection in direct dimension
TETD	N,N,N',N'-Tetraethylthiuram disulfide
TEM	Transmission Electron Microscopy
ThT	Thioflavin T
TMS	Tetra Methyl Silane
TPPM	Two Pulse Phase Modulation
UIC	University of Illinois at Chicago

SUMMARY

This thesis is comprised of five connected research projects on Cu^{2+} -bound amyloid proteins inspected by solid-state nuclear magnetic resonance (SSNMR) spectroscopy and development of novel methodologies for biomolecular SSNMR. After a brief introduction of the research background in Chapter I, the SSNMR methods used in this thesis are outlined in Chapter II. In Chapter III, we examine the structures of Cu^{2+} -bound amyloid fibrils of Alzheimer's β ($\text{A}\beta$) peptides. Cu^{2+} binding to $\text{A}\beta$ in amyloid fibrils has attracted broad attention, as it was shown that Cu ion concentration elevates in Alzheimer's senile plaque and such association of $\text{A}\beta$ with Cu^{2+} triggers the production of neurotoxic reactive oxygen species (ROS) such as H_2O_2 . However, detailed binding sites and binding structures of Cu^{2+} to $\text{A}\beta$ are still largely unknown for $\text{A}\beta$ fibrils or other aggregates of $\text{A}\beta$. In this work, we examined molecular details of Cu^{2+} binding to amyloid fibrils by detecting paramagnetic signal quenching in 1D and 2D high-resolution ^{13}C Solid-State NMR for full length 40-residue $\text{A}\beta(1-40)$. Selective quenching observed in ^{13}C SSNMR of Cu^{2+} -bound $\text{A}\beta(1-40)$ suggested that primary Cu^{2+} binding sites in $\text{A}\beta(1-40)$ fibrils include $\text{N}\epsilon$ in His-13 and His-14 and carboxyl groups in Val-40 as well as Glu sidechains (Glu-3, Glu-11, and/or Glu-22). ^{13}C chemical shift analysis demonstrated no major structural changes upon Cu^{2+} binding in the hydrophobic core regions (residues 18-25 and 30-36). Although the ROS production via oxidization of Met-35 in the presence of Cu^{2+} has been long suspected, our SSNMR analysis of $^{13}\text{C}\epsilon\text{H}_3\text{-S}$ in Met-35 showed little changes after Cu^{2+} binding, excluding the possibility of Met-35 oxidization by Cu^{2+} alone. Preliminary MD simulations on Cu^{2+} - $\text{A}\beta$ complex in amyloid fibrils confirmed binding sites suggested by the SSNMR results. The MD simulations also indicate the coexistence of a variety of Cu^{2+} -binding modes unique in $\text{A}\beta$ fibril, which are realized by both intra- and inter-molecular

SUMMARY (continued)

contacts and highly concentrated coordination sites due to the in-register parallel β -sheet arrangements.

In Chapter IV, the redox reactions on Cu^{2+} ion bound to $\text{A}\beta$ fibrils were examined. The interaction of redox-active Cu^{2+} ion with misfolded $\text{A}\beta$ has been linked with the production of ROS, which have been associated with the oxidative stress and neuronal cell damages in Alzheimer's disease (AD). Despite intensive studies, it is still not conclusive how the interaction of Cu^{2+} with misfolded $\text{A}\beta$ leads to ROS production, even at the *in-vitro* level. In this study, we examined the involvement of Cu^{2+} ions bound to $\text{A}\beta(1-40)$ amyloid fibril in the production of ROS and the interaction between reduced Cu^+ and $\text{A}\beta$ fibrils at the *in-vitro* level by SSNMR and other methods. Our photometric studies confirmed the production of $\sim 60 \mu\text{M}$ H_2O_2 from a solution of Cu^{2+} - $\text{A}\beta(1-40)$ fibril complexes at $100 \mu\text{M}$ within 2 hours of incubation after the addition of biological ascorbate at a physiological level ($\sim 1 \text{ mM}$). Our SSNMR ^1H T_1 measurements demonstrated that during the ROS production, the conversion of paramagnetic Cu^{2+} into diamagnetic Cu^+ was likely to take place while the Cu ions remain bound to the amyloid fibrils. ^{13}C SSNMR chemical shift analysis suggested that this conversion to Cu^+ did not alter the overall molecular conformations of $\text{A}\beta(1-40)$ in fibrils. Furthermore, SSNMR ^1H T_1 measurements result showed that O_2 was required for rapid recycling of Cu^+ back to Cu^{2+} , which allows the continuous production of H_2O_2 . ^{13}C SSNMR analysis revealed that Met-35 was not oxidized during the redox cycle, excluding the involvement of Met-35 in ROS production or redox reaction. ^{13}C and ^{15}N SSNMR results show that Cu^+ ions specifically bind His-13 and His-14 of $\text{A}\beta(1-40)$ fibrils. These results present the first detailed evidence on how the full-

SUMMARY (continued)

length A β in amyloid fibrils offers Cu metal centers that continuously produce ROS through redox reactions.

In Chapter V, we studied the molecular level structure of amylospheroid (ASPD) intermediate species associated with AD. Accumulating evidences suggest that many of neurodegenerative diseases including AD are linked with cytotoxic diffusible aggregates of amyloid proteins, which are metastable intermediate species of protein misfolding. This work presents a site-specific structural study on ASPD intermediate species for 42-residue A β (1-42), which is known to correlate with the severity of AD. We demonstrate that detailed structural examination by ^{13}C SSNMR is possible on synthetic ASPD that well mimics morphologies and conformations of native ASPD isolated from an extract of a brain affected by AD. ^{13}C SSNMR chemical shift analysis over 20 residues demonstrated that ASPD is made of a single conformer that is largely composed of β -sheet secondary structure. An inter-strand ^{13}CO - ^{13}CO distance measurement suggests that the ASPD involves a parallel β -sheet arrangement despite the fact that ASPD does not bind to fibril specific dyes such as thioflavin T. (Preliminary comparison of ^{13}C shifts between ASPD and amyloid fibril samples of A β (1-42) suggest that ASPD has distinctive conformation from that of the amyloid fibril). The approach presented here is likely to open an avenue to examine structural details of various amyloid intermediate species pathologically relevant to AD and other amyloid diseases, for which structures have been poorly characterized.

In Chapter VI, we demonstrate the sensitivity and resolution enhancement in SSNMR by paramagnetic relaxation assisted condensed data collection (PACC) and ultra-fast magic angle spinning (UFMAS) in a high magnetic field (18.8 T) with low power decoupling for a metallo-

SUMMARY (continued)

protein and describe the optimal choice of paramagnetic dopants for the PACC approach. One of the main bottlenecks in the field of SSNMR is the limited sensitivity, particularly for biomolecules, which are often available only in minimum amount. To overcome this problem our group recently demonstrated PACC, in which the ^1H T_1 of the sample is reduced to 50-100 ms and the spectrum is acquired by rapid recycle delays without compromising the resolution. In the PACC approach, Cu-EDTA has been used as an effective paramagnetic relaxation agent to decrease the ^1H T_1 for sensitivity enhancement. To apply this technique to a wide variety of systems, it is necessary to have different choices of relaxation agents. Here, we discuss the ^1H T_1 paramagnetic relaxation enhancement effects and line broadening (^{13}C T_2) for proteins doped with various paramagnetic complexes such as Ni(II)-EDTA, Gd(III)-DETPA, and Co(II)-EDTA complexes. We also discuss sensitivity enhancement in ^{13}C SSNMR for Cu^{2+} -A β fibrils with PACC method by taking advantage of short ^1H T_1 for this paramagnetic protein aggregates in an ultra high field (^1H NMR frequency of 800 MHz) under UFMAS of 50 kHz. A comparison of 1D/2D ^{13}C SSNMR of Cu^{2+} -A β fibrils by conventional methods with high-power ^1H decoupling at ^1H frequency of 400 MHz and by PACC methods with low-power decoupling at 800 MHz showed that sensitivity per unit sample can be enhanced by a factor of 4-8 by a combination of an ultra high field and the PACC method. Advantage of low-power decoupling under very fast MAS in an ultra high-field will be discussed.

Finally, in Chapter VII, we present the possibility of enhancing sensitivity of ^{13}C SSNMR for amino acids and proteins by ^1H indirect detection in a high magnetic field by a combination of UFMAS over 70 kHz and stereo-array isotope labeling (SAIL) [Kainosho M. et al., Nature 440, 52-57, 2006]. UFMAS at 78 kHz enhanced the resolution of ^1H line widths for SAIL-Ile

SUMMARY (continued)

(~0.24 ppm) by up to 3-4 folds compared with those for uniformly ^{13}C - and ^{15}N -labeled Ile. ^1H detected 2D $^{13}\text{C}/^1\text{H}$ correlation SSNMR showed improved sensitivity by ~6 and ~3 folds over ^{13}C detected 2D $^{13}\text{C}/^1\text{H}$ correlation and ~1.2-1.4 folds compared with the 1D ^{13}C SSNMR for the SAIL-Ile. Significant sensitivity enhancement was observed by ^1H indirect detection of ^{13}C SSNMR for SAIL-Ubiquitin (Ubq) protein crystals labeled at 7 Ile residues by 2D $^1\text{H}/^{13}\text{C}$ correlation NMR over ^{13}C 1D direct detection demonstrated for the first time enabled us to get high resolution ^1H detected multidimensional experiments. The ^1H detected high resolution 3D $^{13}\text{C}/^{13}\text{C}/^1\text{H}$ correlation experiment for the SAIL-Ubq provided us valuable ^{13}C chemical shift informations for the 7 SAIL-Ile sidechains inspite of overlapping $^{13}\text{C}/^{13}\text{C}$ crosspeaks in the 2D spectrum. The approach is likely applicable to general proteins to examine side chains as well as main-chain for signal assignments and structural elucidation.

I) INTRODUCTION

A) High resolution Solid-State Nuclear Magnetic Resonance of biomolecules

1) General introduction to Nuclear Magnetic Resonance spectroscopy

Over the last fifty years, the Nuclear Magnetic Resonance (NMR) method has become the most powerful spectroscopic technique for molecular characterization.¹ It can provide three-dimensional structural information on any molecule as long as the nuclei of interest in the molecules are NMR active.^{2, 3} NMR is generally a non-destructive technique but requires large amounts of sample than other common spectroscopic techniques. In the case of biological macromolecules either in solution or solid phase, the most common applications involve nuclei such as ¹H, ¹³C, ¹⁵N, ¹⁹F and ³¹P which have a nuclear spin (I) of ½ and are NMR active. In a magnetic field, these nuclei possess 2I+1 spin states and transitions are induced between the energy levels by irradiating the nuclei with electromagnetic waves of appropriate frequency. This condition enables the magnetic component of the radiation to interact with the nuclear dipoles. The transition from the lower energy to higher energy level corresponds to absorption of energy and those in the reverse direction correspond to emission of energy. Due to the excess spin population in the lower energy level, the absorption of energy from the applied secondary electromagnetic field is the dominant process. This process is observed as signal in NMR and the signal intensity is proportional to the total number of spins or simply the concentration of the sample.

2) Solid-State Nuclear Magnetic Resonance spectroscopy

SSNMR using magic angle spinning (MAS) is a powerful technique for the characterization and structural analysis of systems in solids including non-crystalline organic materials and biomolecules.^{4, 5} ¹³C and ¹⁵N SSNMR has been the most widely used methods for

organic solid materials and biomolecules in contrast to the ^1H NMR which is commonly used in solution NMR.⁶⁻⁹ In solids, spatial proximity between two nuclei gives rise to orientation-dependent anisotropic interactions, which modifies the nuclear spin energy levels contributing to severe line broadening in the spectra. These anisotropic features limit the spectral features in biomolecular SSNMR. The anisotropic features in SSNMR can be suppressed by spinning the solid sample in an angle $\theta_m = 54.74^\circ$ oriented with respect to the magnetic field called “magic angle”. In order to have isotropic peak shapes in the SSNMR, the sample needs to be spun on the order of or faster than (several thousands of Hz) the magnitude of the dipolar coupling arising between two nuclei in solid state (see detailed description in Chapter II).

3) **High-resolution Solid-State Nuclear Magnetic Resonance Spectroscopy**

SSNMR spectra of static solid samples are often broad due to the anisotropic or orientation-dependent interactions. High-resolution SSNMR achieved by MAS combined with multiple-pulse sequences that manipulate the nuclear spin interactions can provide similar information that is available from corresponding solution NMR experiments. A number of other methods apart from MAS and multiple-pulse sequences have been developed for attaining high resolution in SSNMR. Cross polarization coupled with MAS is frequently used in biomolecular SSNMR experiments for sensitivity and resolution enhancement.¹⁰ Special sample preparation protocols involving ^1H spin dilution methods (via replacement by ^2H) have been established for biomolecules to remove ^1H heteronuclear dipolar interactions to get high resolution SSNMR spectra.¹¹⁻¹³ The prerequisite for the high-resolution SSNMR of biomolecules requires highly homogeneous sample, and numerous investigations have established that generally long-range structural order in the sample is required to observe the highest resolution in SSNMR of the nano crystalline proteins, the amyloid fibers, and the sample of interest.¹⁴⁻¹⁶

4) Recent applications of biomolecular Solid-State Nuclear Magnetic Resonance

Biomolecular NMR spectroscopy is often associated with biomolecules in solution state. Since late 1980's SSNMR spectroscopy has become a powerful method in biology and is suitable for the characterization of insoluble proteins and protein aggregates such as amyloid fibrils, membrane-lipid complexes, and precipitated proteins. The availability of high-field instruments dedicated for SSNMR, advancement in probe designs, pulse sequences, sample preparation and other areas have greatly expanded the utility of SSNMR in the investigation of large molecular systems to bridge the gap between the traditional structural methods such as X-ray crystallography and solution NMR. SSNMR has become a successful structural method to study the amyloid fibrils. Three-dimensional structures or detailed structural models have been obtained for medium size amyloid proteins such as α -synuclein,¹⁷ full-length HET-s prion,¹⁸ A β (1-40) fibrils.^{19, 20} Apart from the complete structure determination, SSNMR has been widely used for studying the disease related meta-stable intermediate species, which provide crucial insights into the folding of amyloid and other aggregating proteins.²¹⁻²³ Membrane proteins have been the subject of SSNMR investigations, which are hard to study by other structural tools. SSNMR has played a dominant role in the characterization of the structure and function of M2 channel,^{24, 25} histidine kinases,²⁶ ABC transporters,²⁷ bacterial outer-membrane proteins,²⁸ G-protein-coupled receptors.²⁹ SSNMR has been used to study rigid cell walls of bacteria (E.coli peptidoglycal sacculi), bacterial peptidoglycal and its interactions with protein partners under in situ conditions.³⁰ In particular, SSNMR spectroscopy has been very effective in studying the drug interaction with intact cells and cell wall preparations of pathogenic bacteria.³¹⁻³³

B) Amyloid β protein and Alzheimer's Disease

1) Neurodegenerative disorders associated with amyloidosis

Neurons are vital building blocks of the brain and the central nervous system in normal functioning of the human body. When the neurons are damaged, it leads to severe cognitive impairment such as problems in thinking, judgment, memory, issues related to behavior, loss of language function, inability to do calculations, and depression. Progressive loss of the structure and function of neurons in human brains causes neurodegenerative disorders. The damaged neurons are irreparable by the body's defense mechanism and these diseases are commonly not curable.^{34, 35}

Alzheimer's disease (AD), Parkinson's disease (PD), Huntington's disease (HD), Prion diseases are common forms of neurodegenerative disorders, which are associated with the abnormal accumulation of misfolded protein deposit called amyloid.³⁶⁻³⁸ Risks of these neurodegenerative diseases are generally increased upon aging.³⁹ The protein deposits, which are considered to cause the neurodegenerative disease, are mostly insoluble and fibrous in nature commonly referred as misfolded amyloid proteins. Misfolded aggregates of amyloid β ($A\beta$) peptide, α -synuclein, Huntington protein with polyQ expansion are likely responsible for AD, PD and HD. The amyloid protein aggregates share a common β -sheet structural motif conformation, and the aggregation process is seeded by the misfolded proteins.⁴⁰ This is the common hallmark of the neurodegenerative disorders. The proteins in their native state are unfolded and are nontoxic to the neurons.^{41, 42}

2) Alzheimer's disease

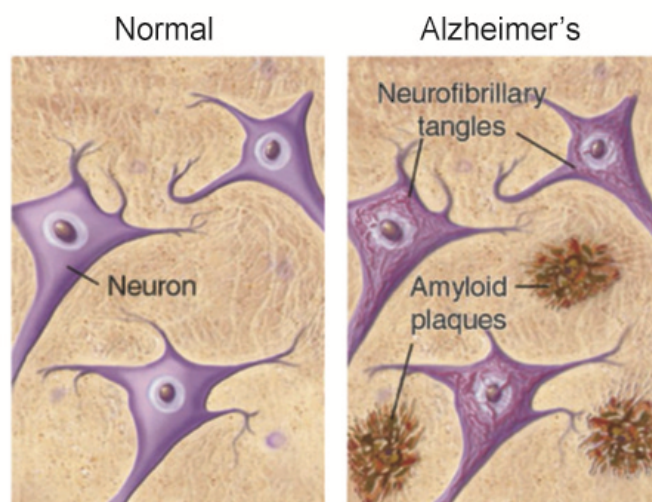
AD is the most common form of neurodegenerative disease, which leads to severe cognitive impairment. The disease was named after German physician Alois Alzheimer who

treated the first documented case of the disease in 1906. AD is found to occur upon aging, and a majority of people with AD are 65 and older. In the early stages of the AD, memory loss is mild, but individuals lose the ability to carry on a conversation and respond to their environment when the disease progresses.⁴³ Those with AD live an average of eight years after their symptoms become noticeable to others, but survival can range from four to 20 years, depending on age and other health conditions (<http://www.health.ny.gov/diseases/conditions/dementia/>). AD is the fifth leading cause of death in the United States over the age of 65 or more.⁴⁴ Worldwide AD cases are currently estimated at 36 million and will triple by 2050.⁴⁵ The total cost in the treatment, research, patient care, etc., for AD are ~ \$ 200 billion annually.⁴⁴ The current treatments cannot stop AD from progression but can temporarily slow the dementia and improve quality of life for those with AD and their caregivers. AD does not just affect the people with the disease but also has a great financial and emotional impact on the family members. There are intensive worldwide efforts under way to find better ways to treat the disease, delay its onset, and prevent it from progression.

3) Neuropathology of AD

The pathological hallmarks of AD are neuronal loss, extracellular senile plaques and neurofibrillary tangles. The neurofibrillary tangles are formed by hyperphosphorylation of microtubule-associated protein “tau”. The aggregates of tau protein form an insoluble intracellular accumulation in human brains of AD patients.³⁶ Senile plaques are characterized by the extracellular deposition of amyloid- β ($A\beta$) peptides^{46, 47} as shown in Figure 1. The $A\beta$ peptides that deposit in the senile plaques are comprised of 39-43 residue isoforms, which are cleaved from the amyloid precursor protein (APP) by β - and γ -secretases. Among the $A\beta$ peptides, 40-residue $A\beta(1-40)$ and 42-residue $A\beta(1-42)$ are the two major species found in the

plaque deposits. The peptides in the plaque deposits are found as insoluble fibrillar aggregates called amyloid fibril. Previous studies indicate that amyloid fibrils of A β showed neural toxicity²¹ and has been long believed that amyloid fibrils of A β are responsible for AD.



The medical illustration is provided by courtesy of Alzheimer's disease research, a program of the American Health Assistance Foundation. (c) 2012 <http://www.ahaf.org/alzheimers>

Figure 1. Cartoon showing the comparison of the healthier neurons in normal human brains and the AD affected human brains.

Most cases of AD are sporadic and ~5 % of cases are of genetic origin with early onset of the AD symptoms and are known as familial AD (FAD).⁴⁸ FAD affects at least two generations of the family and affects people in their early thirties and forties. These are caused by mutations, which change the rate of production or the primary structure of A β . Several FAD related mutations such as English (H6R), Tottori (D7N), Flemish (A21G), Dutch (E22Q), Italian (E22K), Arctic (E22G) and Iowa (D23N) have been extensively studied for the varied

pathogenesis of different forms of FAD.^{49 50-52} Each of these mutations alters peptide assembly or metabolism. N-terminal mutations such as English (H6R) and Tottori (D7N) do not affect the A β production but tend to accelerate fibril assembly in the absence of increased protofibril formation.⁴⁹

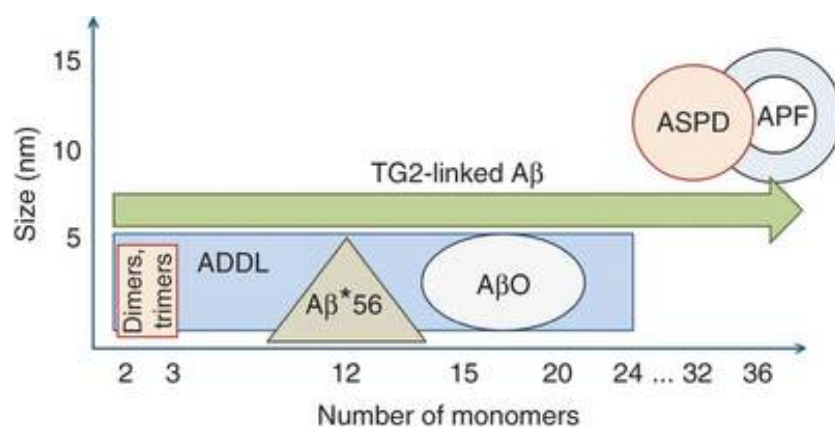
4) Diffusible amyloid intermediate assemblies of A β

Recent studies show that intermediate oligomeric species are more toxic species than later stage fibrils and are considered as potential therapeutic target.⁵³ Various forms of synthetic and natural intermediate assemblies have been reported, ranging from dimeric species to ~1 MDa multimeric toxic species.⁵⁴ The common structural motif present in the self-assembled aggregates of A β has mainly β -sheet conformation; however, the supramolecular structures and their correlation to the neural toxicity are not well understood until now.⁵⁵

The self-assembly of A β peptides into amyloid fibrils in AD is likely to involve a range of differently structured transient assemblies. Shift in research interests from fibrils to these intermediate assemblies was strongly ignited by the *in-vitro* experimental data demonstrating that many amyloid intermediates have higher toxicity to neural cells than amyloid fibrils. Different classes of neurotoxin assemblies have been identified, including oligomers, protofibrils, and high mass assemblies ranging from dimers up to multimers of ~ 1 MDa.⁵⁶ Specific aggregates were shown to disrupt the lipid membrane architecture causing an imbalance in cellular ion homeostasis mechanism leading to cell death. The exact mechanism of neural toxicity of the intermediate A β assemblies is not clearly understood in spite several efforts from various research groups.

The A β assemblies are differentiated according to their sizes. Figure 2 summarizes the size overlap of the natural and synthetic A β oligomers. Dimers and trimers are often called low

molecular weight oligomers,⁵⁷ 3-24 mer A β (1-42) termed as A β -derived diffusible ligands (ADDLs),⁵⁸ 12-mers termed globulomers or A β *56,⁵⁹ 15-20-mer A β assemblies termed A β oligomers,⁶⁰ 150-mer or higher assemblies termed β -sheet intermediates have been reported recently.²¹



Reprinted by permission from Macmillan Publishers Ltd, Nature Neuroscience, 15, 3, March 2012, 349-357, copyright 2012

Figure 2. Size overlap of the natural and synthetic A β oligomers.

5) Amylospheroid (ASPD) intermediate

Recently, Hoshi and co-workers⁶¹ selectively immunisolated intermediate species from AD plaques which tend to coexist along with the fibrils. These amyloid intermediates are highly toxic and exhibit spherical morphology having a diameter of ~10-15 nm, which was defined by transmission electron microscopy (TEM) are termed as Amylospheroids (ASPD). The ASPD's found in the AD are called as native amylospheroids (native ASPDs). The native ASPDs are high mass (> 100kDa) assemblies having a distinct surface tertiary structure different from other

assemblies which induces toxicity to the mature human neurons *in-vitro*. Also, the severity of AD was well correlated with the level of native ASPD found in brains. ASPD is gaining importance as a biomarker and a potential cause of AD, structural details of ASPD are still unknown and are unexplored to a large extent. See Chapter V for detailed description.

6) Accumulation of metal ions in amyloid plaques in AD

AD is characterized by the deposition of amyloid plaques, the plaque deposits encompass metal ions such as copper, iron, zinc, and these metals are strongly coordinated to the A β peptides.^{62, 63} Elevated concentrations of Cu (400 μ M) and Zn (1 mM)⁶³ ions in senile plaques reach \sim 10-fold compared with the regions outside the plaque. Fe is found to be concentrated in the vicinity of amyloid plaques⁶⁴ but the role of Fe in AD is not well established. The normal levels of Cu and Zn in humans are 70 μ M and 350 μ M respectively. The metal ion homeostasis mechanism appears to be severely damaged⁶⁵ in AD leading to the imbalance and accumulation of metal ions in the brain. Significant amount of metal ions in the senile plaques indicates that the metal ions might trigger the promotion of amyloid fibril formation and accumulation in human brains leading to AD. However, the exact mechanism of the metal-ion accumulation has not been understood. Thus, intensive efforts have been made to understand the molecular details of Cu²⁺-binding to A β , which could suggest another potential therapeutic target in AD. On the other hand, most of the structural studies on Cu²⁺-A β binding were performed on soluble model peptides⁶⁶⁻⁷⁰ or monomeric A β ,⁷¹⁻⁷⁵ however, some of these reports are controversial due to the absence of direct site-specific structural evidence of Cu²⁺ binding to A β peptides.

7) Redox reactivity of Cu-A β complex and its role in the oxidative stress

The major pathological event in an AD brain is the excess oxidative stress.^{76, 77} Oxidative stress is a condition in which there is an imbalance between the production of reactive oxygen

species (ROS) and detoxification of ROS by antioxidant defense system. Redox active metal ion Cu^{2+} is found to mediate the production of ROS resulting in oxidative stress leading to the neural cell deaths. It was shown that in association with Cu^{2+} , $\text{A}\beta$ produces ROS such as hydrogen peroxide (H_2O_2), hydroxyl radicals (OH^\bullet) *in-vitro*, reportedly through the reduction of Cu^{2+} to Cu^+ in association with Met-35⁷⁰ and/or biochemical reductants.⁷⁸ The role of these metal ions in the neural toxicity may be highly significant, since trace amounts of metals are believed to be sufficient for the generation of ROS.^{76, 79-81} It was also found that Cu^{2+} bound on the $\text{A}\beta$ fibrils gets reduced to Cu^+ during the ROS production with the involvement of Arg, His, Tyr, Met residues leading to a variety of oxidation products in the presence of biological reductants such as ascorbic acid, cholesterol or dopamine.⁸²

Met-35 residue in the $\text{A}\beta$ peptide has been long suspected to participate in the electron transfer redox reaction along with Cu^{2+} to produce ROS.⁷⁰ Indeed, it was shown in a recent report that $\text{A}\beta$ isolated from plaques contains oxidized form of Met-35.⁶² However, the mechanism of the redox reaction and the involvement of $\text{A}\beta$ in the production of ROS are still unclear. It is known that ascorbic acid is a strong biochemical reducing agent and found in high concentrations ranging from 0.2 to 10 mM in human brains.^{83, 84} Ascorbic acid has dual redox properties which acts as both reducing and oxidizing agent.^{83, 85} A recent *in-vitro* study showed that $\text{Cu-A}\beta$ complex enhances the oxidation of ascorbic acid and generates OH^\bullet radical.⁸⁶ In addition to ascorbate other biological reductants like cholesterol, progesterone, epinephrine, norepinephrine, serotonin, dopamine, L-DOPA, NADPH⁸² could initiate the redox process involving $\text{Cu-A}\beta$ complex. Several research groups have shown the generation of ROS in the presence of Cu^{2+} - $\text{A}\beta$ ^{83, 87, 88} and also linked ROS as the major cause of neural cell loss in AD.^{77,}

II) GENERAL METHODS

A) Nuclear Magnetic Resonance (NMR)

1) Nuclear Spin and Boltzmann Distribution

The phenomenon of NMR was first studied by Zeeman⁹⁰ in 1896 and later the NMR in bulk condensed phased was studied independently by Purcell⁹¹ and Bloch⁹² in 1946. Dramatic progress in the field of NMR started with the development of pulsed Fourier transform NMR spectroscopy by Ernst¹ in 1966. Currently NMR is an indispensable analytical tool in the analysis of molecules in the gas, liquid and solid phase.

The theory of NMR spectroscopy is based on the manifestations of nuclear spin angular momentum (**I**) and it is characterized by nuclear spin quantum number (I). The spin quantum number I value for all the nuclei in atoms may have values equal to or greater than zero. The nuclei with I = 0 has no nuclear spin and are NMR inactive nuclei. Generally, nuclei with an even mass number and even atomic number have no nuclear spin. Nuclei with odd mass numbers have half-integral spin quantum numbers and nuclei with even mass number and odd atomic number have integral spin quantum numbers. For the NMR spectroscopy of organic molecules or bio-molecules, the most important nuclei are ¹H, ¹³C, ¹⁵N, ¹⁹F and ³¹P which possess I = ½ nuclear spin quantum number. The intrinsic angular momentum **I**, is a vector quantity with magnitude given by

$$|\mathbf{I}| = [\mathbf{I} \cdot \mathbf{I}]^{\frac{1}{2}} = \hbar[I(I + 1)]^{\frac{1}{2}}, \quad \dots\dots\dots (1)$$

in which \hbar is the Planck's constant divided by 2π . The z-component of **I** is specified by

$$I_z = \hbar m, \quad \dots\dots\dots (2)$$

where m is the magnetic quantum number which can take values of $m = (-I, -I+1, \dots, I-1, I)$. Thus, for I_z there exist $(2I + 1)$ possible spin states. Nuclei that have non-zero spin angular momentum possess nuclear magnetic moments, μ , which is collinear with the vector representing the nuclear spin angular momentum defined by

$$\mu = \gamma \mathbf{I} \quad \dots\dots\dots (3)$$

γ is the gyromagnetic ratio, which is different for nuclei of different isotopes and atoms. The nuclear spin angular momentum (\mathbf{I}) and the magnetic moment (μ) are vector quantities and in the presence of an external magnetic field, the spin states of the nuclei have energies given by

$$E = -\mu \cdot B_0 \quad \dots\dots\dots (4)$$

where B_0 is the external magnetic field vector. In an NMR spectrometer, the external static magnetic field is along the z -axis and the energy (E) for this geometry reduces to

$$E = -\gamma I_z B_0 = -m \hbar \gamma B_0 \quad \dots\dots\dots (5).$$

So for a spin $\frac{1}{2}$ nuclei such as ^1H or ^{13}C , there are two possible energy states denoted by $+\frac{1}{2}$ and $-\frac{1}{2}$, while for $I = 1$ nuclei (^2H , ^{14}N), the three equally spaced energy states are denoted by $+1$, 0 and -1 as shown in Figure 3. These energy levels which are quantized are known as Zeeman levels. The transition energy between the two Zeeman states is given by

$$\Delta E (+\frac{1}{2} \rightarrow -\frac{1}{2}) = \gamma \hbar B_0 = h(\gamma B_0 / 2\pi), \quad \dots\dots\dots (6)$$

which is directly proportional to the strength of the magnetic field (B_0). By Plank's law, the angular frequency ω and the frequency ν of the NMR transition is given by

$$\omega = \Delta E / \hbar = -\gamma B_0 \quad \dots\dots\dots (7)$$

$$\text{and } \nu = \omega/2\pi = \gamma B_0/2\pi \quad \dots\dots\dots (8)$$

in units of s^{-1} .

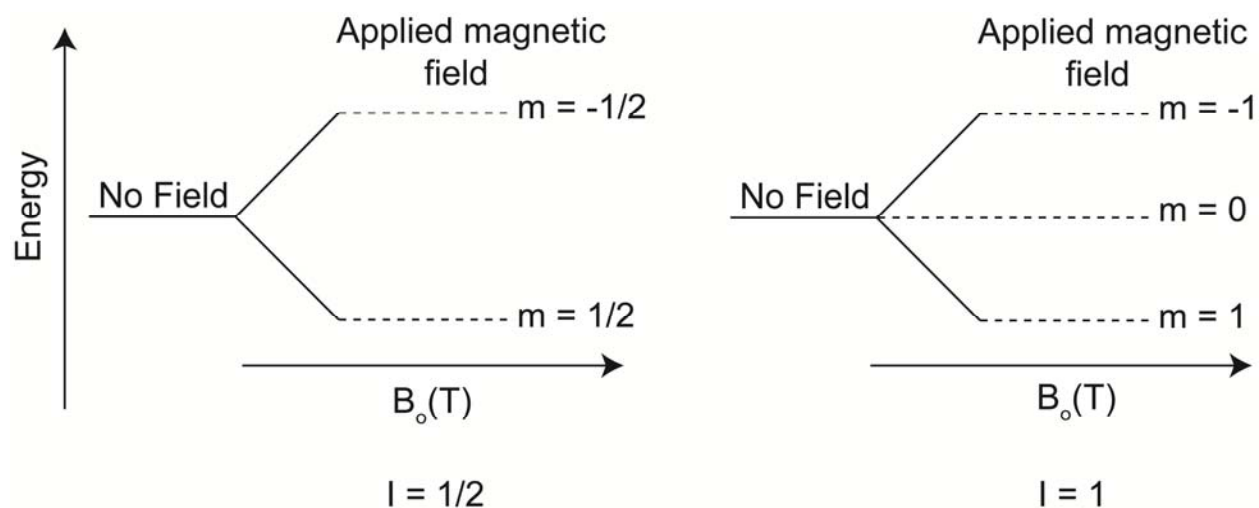


Figure 3. Energy level diagram for $I = 1/2$ and $I = 1$ nuclei in presence of a magnetic field.

Now consider a collection of spin $1/2$ nuclei in an applied external static field. At equilibrium, the $+ 1/2$ and $- 1/2$ states are unequally populated. The orientation of the magnetic dipole vector parallel to the applied magnetic field has slightly lower energy than the vectors in the anti-parallel orientation for nuclei with positive γ . The relative population of the state is given by Boltzmann distribution

$$\frac{N_m}{N} \approx \frac{1}{2I+1} \left(1 + \frac{m\hbar\gamma B_0}{k_B T} \right), \quad \dots\dots\dots (9)$$

in which N_m is the number of nuclei in the m^{th} state and N is the total number of spins, T is the absolute temperature and k_B is the Boltzmann constant. The differences between the Zeeman spin energy states are very small therefore the population differences between them are similarly small. This is why NMR is a very insensitive technique in comparison to other spectroscopic techniques such as IR and UV. The small population excess in the lower energy level gives rise to a resultant magnetization vector M_0 along the z-axis. The static field B_0 imposes a torque on the resultant magnetic moments M_0 along the z-axis; M_0 takes a circular path about the applied magnetic field which is called as precessional frequency or Larmor frequency (ω_0) and is given by

$$\omega_0 = -\gamma B_0. \quad \dots\dots\dots (10)$$

The transition from the lower energy state to the higher energy state for the observation of the NMR signals is achieved by a oscillating secondary magnetic field $B_1(t)$ which will be discussed in the following section.

2) Radiofrequency Pulse

The radio frequency (RF) pulse is simply described as an oscillating magnetic field $B_1(t)$ with an angular frequency ω_{rf} that imposes a tilt on the equilibrium magnetization vector M_0 in the direction that is perpendicular to the direction of the $B_1(t)$ field. Consider an RF pulse applied to a single spin $-1/2$ nuclei in a static field B_0 . The Hamiltonian for the pulse is written as

$$H = -\mu \cdot [B_0 + B_1(t)] = H_z + H_{rf} \quad \dots\dots\dots (11)$$

$$= \omega_0 I_z + \omega_1 [I_x \cos(\omega_{rf}t + \phi) + I_y \sin(\omega_{rf}t + \phi)] \quad \dots\dots\dots (12)$$

where I_x , I_y , and I_z are the spin angular momentum operators along x, y, z axes respectively and ω_0 , ω_1 are given by $-\gamma B_0$ and $-\gamma B_1$. $\omega_0 I_z$ is the precession of the spin under the influence of the static field which is the Zeeman Hamiltonian and the second term in eqn. 12 is the RF pulse.⁹³

3) Chemical Shift

In the presence of an external magnetic field (B_0), currents are induced in the electron cloud, which generates an induced or secondary magnetic field (B_i). The sum of the external magnetic field (B_0) and the secondary magnetic field (B_i) is felt by the nuclei. In a molecule, different nuclei encounter different local magnetic fields, and thus the resonance frequency of each nucleus is different for each chemical species causing dispersion in the NMR spectral frequency which is called the chemical shift.

$$B_i^{\text{loc}} = B_0 + B_i^{\text{induced}} \quad \dots\dots\dots (13)$$

In general, the induced field can be written in the following form:

$$B_i^{\text{induced}} = \delta^j \cdot B_0 \quad \dots\dots\dots (14)$$

δ^j is the second rank chemical shift tensor and is expressed in the following by a 3×3 matrix form as

$$\delta^j = \begin{pmatrix} \delta_{xx}^j & \delta_{xy}^j & \delta_{xz}^j \\ \delta_{yx}^j & \delta_{yy}^j & \delta_{yz}^j \\ \delta_{zx}^j & \delta_{zy}^j & \delta_{zz}^j \end{pmatrix} \quad \dots\dots\dots (15)$$

where x, y and z are the axes of the laboratory frame in which the shielding tensor is expressed. In a high field approximation, the induced field is proportional to the external magnetic field. In this case, assuming B_0 is applied along the z-axis,

$$B_i^{\text{induced}} = \delta_{zz}^j B_0 \quad \dots\dots\dots (16)$$

The shielding tensor matrix can be diagonalized to obtain the chemical shielding tensor principal values (δ_{11}^j , δ_{22}^j , δ_{33}^j). Under isotropic molecular tumbling (i.e. in solution), the observed chemical shift is given by the following form

$$\delta_j^{iso} = \frac{1}{3} (\delta_{xx}^j + \delta_{yy}^j + \delta_{zz}^j) = \frac{1}{3} (\delta_{11}^j + \delta_{22}^j + \delta_{33}^j) \quad \dots\dots\dots (17)$$

Variations in the δ_j^{iso} are observed due to the different electronic environment in the molecule. Typically for an organic molecule δ_j^{iso} varies from 0 - 200 ppm in ^{13}C spectrum or 0 - 15 ppm in a ^1H spectrum.

4) Magic Angle Spinning

In SSNMR, magic angle spinning (MAS) is a technique which is often used to remove chemical shift anisotropy and homo/hetero nuclear dipole-dipole couplings. MAS technique was first demonstrated by Andrew and co-workers in 1958⁵ and independently by Lowe in 1959⁴ by spinning the sample at an angle $\theta_m = 54.74^\circ$ with respect to the static magnetic field. This imposes a cubic symmetry to the solid sample when the movement of the sample over a whole sphere is restricted. Broad resonances on the order of kHz collapse to sharp signals under MAS, dramatically improving the resolution for better identification and analysis of the spectrum. With the advancement in MAS technology commercial, ultra-fast MAS probes which have the capabilities to spin ≥ 80 kHz are available.

In order to understand the MAS experiment, the following Hamiltonian is considered

$$H = H_{CS} + H_D^{IS} + H_D^{II} \quad \dots\dots\dots (18)$$

where H_{CS} is the chemical shielding term, H_D^{IS} and H_D^{II} represents the heteronuclear and homonuclear dipolar couplings. The electrons that surround a nucleus contribute to a secondary field, which changes the resonance frequency of the nucleus. The chemical shielding is determined by the Zeeman interaction between a nuclear magnetic moment (μ) and the external magnetic field (B_0).

$$H_0 = -\mu \cdot B_0 \quad \dots\dots\dots (19)$$

μ is expressed in terms of the nuclear spin operator \mathbf{I} as $\mu = \gamma\hbar\mathbf{I}$ and the eqn. 19 can be rewritten as

$$H_0 = -\gamma\hbar I_z B_0. \quad \dots\dots\dots (20)$$

The Zeeman interaction is the most dominant interaction in the above Hamiltonian. The chemical shielding Hamiltonian is expressed as

$$H_{CS} = \left\{ \sigma_{iso} \gamma B_0 + \frac{1}{2} \delta [3 \cos^2 \theta - 1 - \eta \sin^2 \theta \cos(2\phi)] \right\} I_z \quad \dots\dots\dots (21)$$

$$\sigma_{iso} = \frac{1}{3} (\sigma_{11}^{PAS} + \sigma_{22}^{PAS} + \sigma_{33}^{PAS}) \quad \dots\dots\dots (22)$$

$$\delta = \sigma_{33}^{PAS} - \sigma_{iso} \quad \dots\dots\dots (23)$$

$$\eta = \frac{\sigma_{33}^{PAS} - \sigma_{22}^{PAS}}{\delta} \quad \dots\dots\dots (24)$$

where θ and ϕ describe the orientation of the shielding or dipolar tensor with respect to applied field B_0 . The chemical shielding and anisotropy are represented by a tensor σ that is most conveniently represented in the coordinate system in which it is diagonal. The principal axis system which is an axis frame defined in such a way that the symmetric part of the shielding

tensor is diagonal, and the principal values of the shielding tensor can be given as σ_{iso} (the isotropic value), δ is the anisotropy and η is the asymmetry parameter as shown in eqn. 22 -24.

The hetero-nuclear dipolar Hamiltonian is given by

$$H_D^{IS} = -\frac{\mu_0}{4\pi} \hbar \sum_i \sum_j \frac{\gamma^I \gamma^S}{r_{ij}^3} \frac{1}{2} (3 \cos^2 \theta_{ij} - 1) 2I_z^i S_z^j \quad \dots\dots\dots (25)$$

while the homo-nuclear dipolar Hamiltonian is expressed as

$$H_D^{II} = -\frac{\mu_0}{4\pi} \hbar \sum_i \sum_j \frac{\gamma^2}{r_{ij}^3} \frac{1}{2} (3 \cos^2 \theta_{ij} - 1) (3I_z^i I_z^j - \mathbf{I}^i \cdot \mathbf{I}^j) \quad \dots\dots\dots (26)$$

The molecular orientation dependence in the above equations is expressed in the form of $(3 \cos^2 \theta_{ij} - 1)$ where θ_{ij} is the angle that describes the orientation of the spin interaction tensor, which could be the chemical shielding interaction, or the dipolar coupling tensor in the case of the dipolar coupling interaction and r is the vector between point magnetic dipoles.

The anisotropic interactions described above are averaged out by MAS, producing an isotropic spectrum. The MAS experimental setup is shown in Figure 4, a solid sample is placed in the rotor and mechanically rotated at high spinning frequency about the magic angle $\theta_m = 54.74^\circ$ with respect to the applied magnetic field B_0 which leads to the narrow peaks in the spectrum.⁹⁴

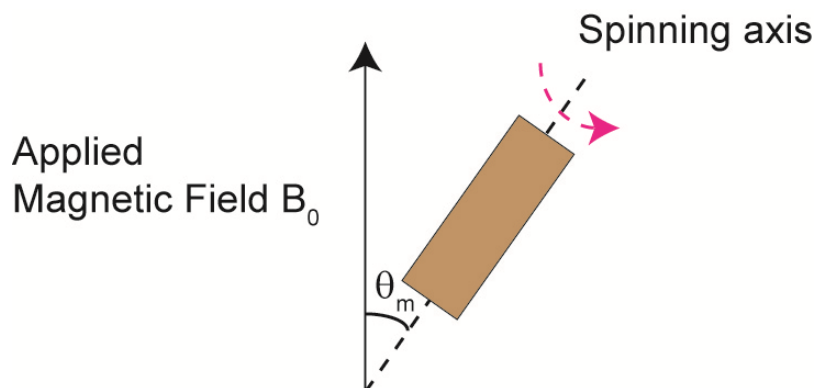


Figure 4. Schematic diagram of the orientation of the sample rotor with respect to the applied magnetic field in a MAS experiment.

B) Fast and Ultra-fast magic angle spinning for sensitivity enhancement in Solid-State NMR

In recent years, SSNMR has advanced greatly as a structural and dynamic probe for biomolecular solids. Two, three or four dimensional homonuclear and heteronuclear correlation experiments have been routinely used for structural and dynamic studies. The recent development of MAS probes capable of spinning so called fast (> 30 kHz) and ultra-fast (> 60 kHz) has revolutionized the SSNMR field. Under ultra-fast MAS (UFMAS) the ^1H dipolar couplings are heavily weakened which facilitates the use of low-power ^1H nuclear decoupling and selective CP opening up various new perspectives in the analysis of a larger range of proteins by high-resolution proton-detection SSNMR methods.⁹⁵⁻¹⁰⁰

Sensitivity enhancement by indirect detection ^{13}C and ^{15}N SSNMR in biological solids and polymers through ^1H signals has been demonstrated more than a decade back by Ishii et al., at fast MAS $\omega_R = 31$ kHz at high magnetic field (17.6 T).^{101, 102} The sensitivity enhancement factor (ξ) by ^1H indirect detection over direct detection of a dilute X-nuclei depends on the line

width in the ^1H dimension W_H as well as the efficiency of polarization transfer (f) between ^{13}C and ^1H for ^1H detection as shown in eqn. (27),^{101, 102}

$$\xi = \frac{f}{\sqrt{2\kappa}} \left(\frac{\gamma_H}{\gamma_X}\right)^{\frac{3}{2}} \left(\frac{W_X}{W_H}\right)^{\frac{1}{2}} \left(\frac{Q_H}{Q_X}\right)^{\frac{1}{2}} \dots\dots\dots (27)$$

where γ_H and γ_X represent the gyromagnetic ratios of the nuclei H and X, W_X and W_H are the line widths observed, Q_H and Q_X is the quality factor for the sample coil for the ^1H detection. f is the polarization transfer efficiency and κ is a constant. The factor $\kappa \sim \pi$ for comparison with 1D ^{13}C CPMAS SSNMR assuming apodization with matched window functions, while $\kappa = 1/2$ for comparison with ^{13}C detected 2D $^{13}\text{C}/^1\text{H}$ correlation. Thus, there is approximately 2.5 times factor difference between ξ values for comparison with 1D and 2D experiments.

C) Solid-State NMR of paramagnetic proteins

Over the last 10 years or so paramagnetic SSNMR has emerged as a powerful tool for the investigation of structure and dynamics of bio-molecules. In particular, use of paramagnetic relaxation enhancement (PRE) and attenuation of NMR signals by paramagnetic metal ions have been used to determine the structure and metal binding sites of microcrystalline proteins, fibrils, membrane proteins and in particular metalloproteins.^{103, 104} The PREs arise from the magnetic dipolar interaction of the nucleus of interest with the unpaired electron of the paramagnetic center. The Hamiltonian for a coupled electron-nucleus system in an external magnetic field B_0 is given by the following equation

$$H = \frac{\beta_e}{\hbar} \mathbf{S} \cdot \mathbf{g} \cdot \mathbf{B}_0 - \frac{g_1 \beta_n}{\hbar} \mathbf{I} \cdot \mathbf{B}_0 + \mathbf{I} \cdot \mathbf{A} \cdot \mathbf{S} \dots\dots\dots (28)$$

where I and S are spin angular momentum operators of nuclear and electron spins. β_e and β_n are the Bohr magneton and nuclear magneton, g_I is the nuclear g-factor specific to nucleus I , \mathbf{g} is the electron g-tensor and \mathbf{A} is the hyperfine coupling tensor which describes the interaction between the electron and nuclear spins and contains a through-space magnetic dipole-dipole contribution as well as the through-bond Fermi contact part. In the above equation, for simplicity, $S = \frac{1}{2}$ and $I = \frac{1}{2}$ are assumed. The Curie spin relaxation mechanism which is observed in paramagnetic systems in solution arising from the interaction of the nuclear spins with the net magnetic moment of the unpaired electrons is absent in solid paramagnetic systems. (See relaxation definition in Chapter VI)

In this thesis, paramagnetic Cu(II) ion binding to A β peptides have been studied extensively due to the biological significance of the system in the AD. Cu(II) has relatively short electron spin relaxation time ($1-5 \times 10^{-9}$ s) and small g-tensor anisotropy which introduces moderate line broadening and small isotropic pseudo contact shifts which enabled us to characterize the Cu(II) binding sites to the A β peptide. The findings are discussed in the Chapter III.

D) The NMR spectrometer

The NMR spectrometer consists of magnet, RF electronics, receiver, transmitter, MAS controller and computer. The magnet consists of a superconducting solenoid immersed in liquid helium, which is surrounded by a thermal radiation shield, a vacuum space, and an outer layer dewar filled with liquid nitrogen. The RF electronics component consists of pulse programmer, frequency synthesizer and an RF transmitter. The RF pulses are fed in to the probe which accommodates the sample, is positioned in the room temperature bore of the magnet in NMR. The NMR signals from the probe are sent to the receiver, which consists of a preamplifier,

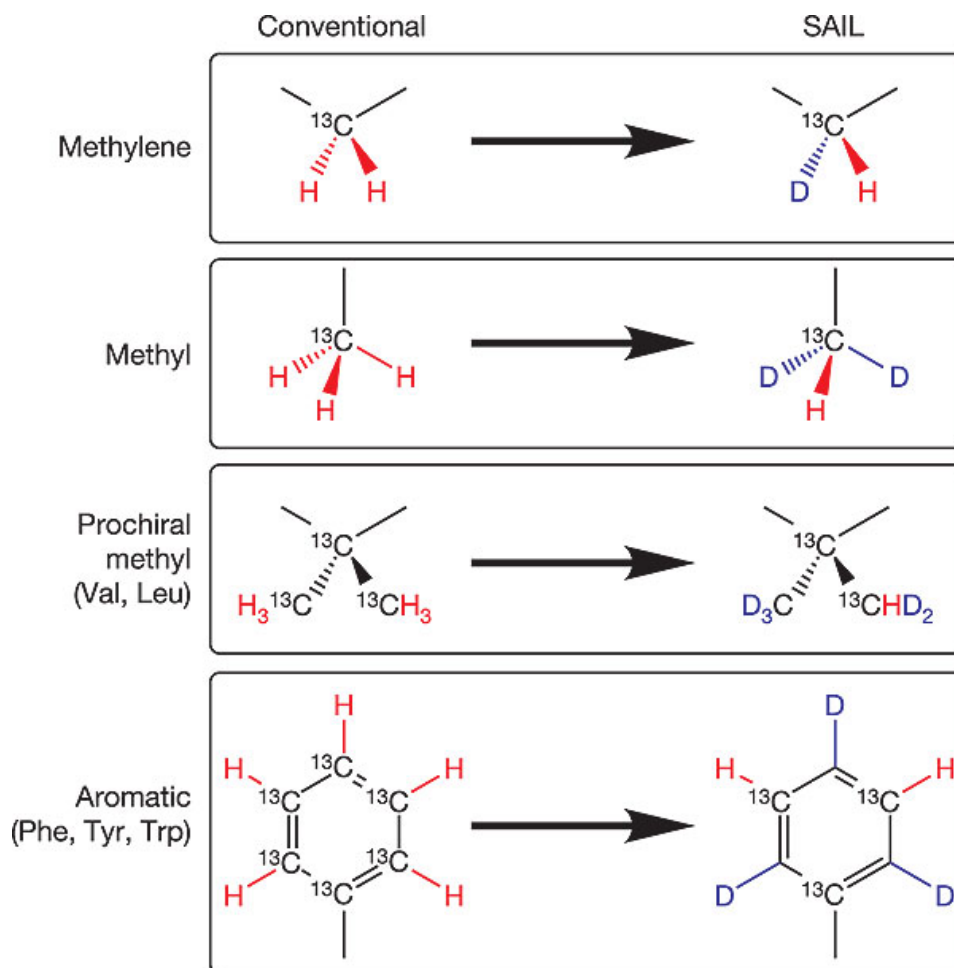
phase-sensitive detector and analog-to-digital converter. The data acquisition and the processing of the signals are done by computer, which controls the various components of the spectrometer.

All the SSNMR experiments in this thesis were performed using a 9.4 T (^1H NMR frequency of 400 MHz) Varian Infinity Plus/Bruker Avance spectrometer and 18.8 T (^1H NMR frequency of 800 MHz) Bruker Avance spectrometer. The probes used for these experiments are, 2.5-mm double/triple probe built in our lab by Drs. Nalinda Wickramasinghe and Yoshitaka Ishii, 1.8-mm double/triple resonance probe purchased from Dr. Ago Samoson in National Institute of Chemical Physics & Biophysics, Tallinn, Estonia and a 1.0-mm double resonance probe provided by JEOL. The numbers 2.5, 1.8 and 1.0 indicate the outer-diameters of the MAS sample rotors. The experimental conditions are presented in this thesis are either indicated in the method section of every chapter or in the figure captions.

E) Stereo array isotope labeling method in ^1H resolution enhancement in Solid-State NMR

^1H SSNMR is primarily hindered by poor resolution due to homo-nuclear dipolar coupling between the ^1H spins in the sample. Though, ultra-fast MAS probes with spinning frequencies exceeding the dipolar couplings ($\text{MAS} \geq 80 \text{ kHz}$) have been developed to significantly improve the ^1H linewidths, ^1H SSNMR still suffers from residual dipolar broadening. Homo-nuclear ^1H - ^1H decoupling pulse sequences have been tried to remove the remaining dipolar coupling at ultra-fast MAS; the pulse sequence requires several conditions to be satisfied.¹⁰⁵ With the advancement in the chemical and bio-synthesis, it is easier to selectively replace the ^1H 's in the sample with heavier isotope Deuterium (^2H) which simplifies the ^1H SSNMR spectrum. Several deuteration labeling strategies have been proposed such as random fractional deuteration,¹⁰⁶ perdeuteration,^{11, 12} residue-selective¹⁰⁷ and segmental labeling.¹⁰⁸ These methods have few drawbacks, random fractional deuteration produces numerous

isotopomers which introduces chemical shift heterogeneity and reduced signal intensities. Perdeuteration protocol removes all the carbon-bound ^1H 's leading to loss of ^{13}C back bone connectivity by ^1H detection, this drawback holds for the residue-selective and segmental labeling strategies. A novel and alternative optimal labeling pattern for protein NMR has been developed by Kainosho and co-workers^{109, 110} in which one ^1H in methylene groups, two ^1H 's in methyl groups are stereo-selectively replaced with ^2H . In the prochiral methyl groups of Leu and Val ^2H is incorporated in the following manner; one methyl group is completely deuterated - $^{12}\text{C}(^2\text{H})_3$ and the other is partially labeled - $^{13}\text{C}^1\text{H}(^2\text{H})_2$. Finally, the aromatic rings are labeled by alternating $^{12}\text{C}-^2\text{H}$ and $^{13}\text{C}-^1\text{H}$ moieties. Figure 5 shows the design concepts embodied in the SAIL amino acid. This labeling strategy was employed in all the 20 amino acids and structures of different proteins have been solved using solution NMR methods.¹¹⁰⁻¹¹⁴ Though the SAIL labeling strategy was successfully used in protein structure analysis by solution NMR, it has not been employed in protein structure determination by SSNMR. SAIL, Ultra-fast MAS and high magnetic field would be an ideal combination for the resolution enhancement in ^1H SSNMR which would help sensitivity enhancement in ^{13}C , ^{15}N SSNMR and eventually in protein structural studies.



Reprinted by permission from Macmillan Publishers Ltd, Nature, 440, 2 March 2006, 52-57, copyright 2006

Figure 5. Design concepts embodied in the SAIL amino acid

III) MOLECULAR-LEVEL EXAMINATION OF Cu^{2+} BINDING STRUCTURE FOR AMYLOID FIBRILS OF 40-RESIDUE ALZHEIMER'S β BY SOLID-STATE NMR SPECTROSCOPY

Adapted with permission from S Parthasarathy, F Long, Y Miller, Y Xiao, D McElheny, K Thurber, B Ma, R Nussinov, Y Ishii, J. Am. Chem. Soc., 2011, 133 (10), 3390-3400. Copyright 2011, American Chemical Society

A) Introduction

AD is characterized by the deposition of senile plaques and neural degeneration. $\text{A}\beta$ peptides are the primary components of senile plaques.^{36, 115} Among $\text{A}\beta$ peptides ranging from 39 to 43 residues, 40-residue $\text{A}\beta(1-40)$ and 42-residue $\text{A}\beta(1-42)$ are the two major species found in plaque.¹¹⁵ In AD, the metal ion homeostasis mechanism appears to be severely damaged, resulting in increased concentrations of Cu and Zn ions in senile plaque, which reach 400 μM and 1 mM respectively⁶³ or ~ 10 -fold excess compared with the region outside the plaque.^{65, 116} More interestingly, it was shown that in association with Cu^{2+} , $\text{A}\beta$ produces ROS such as H_2O_2 *in-vitro*,¹¹⁷ reportedly through the reduction of Cu^{2+} to Cu^+ in association with Met-35 and/or biochemical reductants such as ascorbate.⁷⁸ The toxicity of $\text{A}\beta$ can be greatly attenuated by H_2O_2 scavengers⁸² and metal chelators *in-vitro*.^{117, 118} Indeed $\text{A}\beta$ fibrils strongly bind Cu^{2+} ions.¹¹⁹⁻¹²¹ Although the mechanisms of neural cell deaths and oxidative stress in AD are still debated, these events may be explained by the ROS generated on the redox-active Cu^{2+} ions bound on the $\text{A}\beta$ fibrils which was observed *in-vitro*. Small molecules which target metal- $\text{A}\beta$ interactions have been tested as potential therapeutic agents, including one in a clinical trial.¹²² Thus, intensive efforts have been made to understand the molecular details of Cu^{2+} binding to $\text{A}\beta$.^{66-69, 71-74, 78, 123-}
¹³¹ On the other hand, most structural studies on Cu^{2+} - $\text{A}\beta$ binding were performed on soluble model peptides^{66-69, 125-127} or monomeric $\text{A}\beta$;^{71-73, 131} however, some of these reports are controversial.

Solution NMR studies by Hou and co-workers⁷³ on monomeric A β (1-40) indicated specific binding of Cu²⁺ to sidechains of His-6, His-13 and His-14 by their upfield ¹H shifts, while suggesting the lack of association of Asp-1 and Tyr-10 with Cu²⁺ through the perturbation on their ¹H sidechain shifts.⁷³ The Cu²⁺ binding to the N-terminal region is consistent with a recent NMR study indicating paramagnetic relaxation enhancement on the residue 3-16 upon the addition of Cu²⁺ to monomeric A β (1-40).⁷¹ Electron Paramagnetic Resonance (EPR) spectra of Cu²⁺-bound A β (1-16), A β (1-28) and A β (1-42) monomers show quite similar spectral features for Cu²⁺;⁶⁶⁻⁶⁸ it has been proposed that these EPR spectra suggest the presence of two types of Cu²⁺ binding sites, both of which are likely to have 4-coordination geometries such as 2N/2O and 3N/1O coordination to Cu²⁺.⁶⁶⁻⁶⁸ This is consistent with the solution NMR results⁷³ since two nitrogen's of His imidazole rings typically offer coordination to Cu²⁺.¹³² More detailed isotope-edited EPR studies on A β (1-16) suggested Cu²⁺ coordination to Asp-1, His-6, His-13 (or His-14) for one spectral component (component I; $A_{\parallel} = 162 \pm 3$ G and $g_{\parallel} = 2.272$) and the second Cu²⁺ coordination to Ala-2, His-6, His-13, His-14 for the other minor spectral component at a neutral pH (component II; $A_{\parallel} = 148 \pm 3$ G and $g_{\parallel} = 2.227$).^{66, 67} In contrast, a recent EPR study on monomeric A β (1-28) suggested octahedral coordination by Asp-1, Asp-7, His-6, His-13, His-14 for an EPR spectrum having similar yet distinguishable EPR parameters (component I: $A_{\parallel} = 170$ G and $g_{\parallel} = 2.27$; component II: $A_{\parallel} = 156$ G and $g_{\parallel} = 2.22$).⁶⁸ Although these A β monomer and fragments may have different metal binding modes, a conclusive structural model of Cu²⁺-A β complex has not been established even for the soluble model systems (see Table 1 in Faller et.al.,⁷⁸). More importantly, monomeric A β is nontoxic; a question relevant to the mechanism of AD is, therefore, Cu²⁺ binding structure in A β aggregates. Recent EPR studies on Cu²⁺-bound amyloid fibril of A β (1-40) and A β (1-42) report the presence of, at least, two types of binding

sites that also have 4-coordination geometries.^{68, 74, 127, 129} However, beyond the similarity of the EPR spectra of the A β fibrils with those of more well studied soluble A β fragments, scarce site-specific information on metal binding modes has been obtained for A β fibrils. A recent EPR study on A β (1-28) showed no notable changes in the EPR by H6A or H14A mutations.⁶⁸ Thus, similarity in conventional continuous wave (cw) EPR spectra among Cu²⁺-bound A β with varied sequences may not be sufficient to deduce Cu²⁺ coordination structure uniquely. Rather, coordination to Cu²⁺ involving different His residues and other ligands can yield very similar 1D EPR spectra as long as the local environments around Cu²⁺ are similar. On Cu²⁺ binding to oligomeric A β , there were some interesting studies,^{71, 127} yet the nature of these oligomeric species has not been well-defined. A recent study by SSNMR, a powerful method for structural analysis of protein aggregates^{17, 19, 21, 133-140} and other proteins,^{16, 24, 25, 141-153} indicated Cu²⁺ binding to A β in membrane environments.¹⁵⁴ Despite the broad attention and the intense efforts presented in the previous studies,^{66-69, 71, 73, 74, 78, 123, 125-127, 155} the exact Cu²⁺ binding sites of A β fibrils *have not been identified with any site-specificity*. Lack of site-specific structural information has also severely limited our molecular-level understanding on structural changes of A β fibrils upon Cu²⁺ binding. Such detailed structural information would be highly valuable for revealing still unknown mechanisms of the toxicity for A β aggregates and designing metal binding inhibitors for amyloid aggregates.¹⁵⁶⁻¹⁵⁸

Here, we present the first systematic study to address molecular details of Cu²⁺ binding on amyloid fibrils of full-length A β (1-40) by SSNMR. With the recent advancement in SSNMR for paramagnetic proteins,^{95, 139, 141, 159-161} we examine the possibility of identifying site-specific Cu²⁺ binding to A β (1-40) fibrils and molecular-level structural changes upon the binding. Our SSNMR data show a lack of perturbation to ¹³C chemical shifts by Cu²⁺ binding and for the first

time suggest that the parallel β -sheet structures in the hydrophobic core regions of A β (1-40) fibrils are not reorganized into different structures by Cu²⁺ binding. Molecular dynamics (MD) simulations that take account of the amyloid fibril structure suggest that Cu²⁺ binding to A β in fibril is likely to involve novel binding modes that are not possible in soluble fragments or monomers of A β .

B) Results and Discussion

First, we examined the morphological changes of amyloid fibril after Cu²⁺ binding. Although it has been proposed that Cu²⁺ or Zn²⁺ binding to A β monomers may modulate misfolding kinetics,^{73, 127, 128, 162, 163} in this work, we focus on structural changes due to Cu²⁺ binding after the fibril formation. Figure 6a and b shows transmission electron microscopy (TEM) images of A β fibrils without and with 0.4 mol. eq. CuCl₂, respectively. The fibrils without Cu²⁺ have a diameter of ~9 nm and a length of > 1 μ m, which are consistent with previous reports.¹⁵ The morphology of the A β fibrils is retained after Cu²⁺ was bound to fibrils. Although it is difficult to deduce any molecular-level structural changes from the data, it is likely that Cu²⁺ binding does not substantially destabilize the amyloid fibril structure.

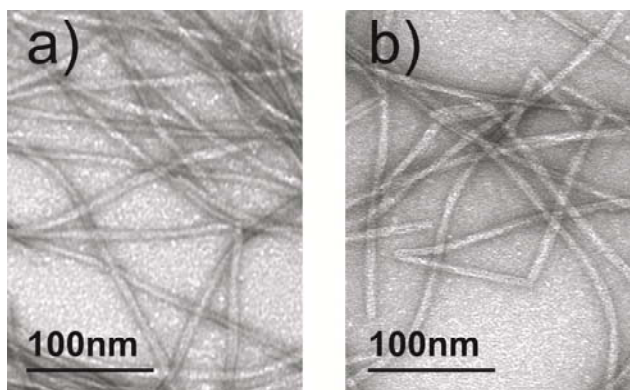


Figure 6. TEM images of A β (1-40) fibrils (a) without and (b) with Cu²⁺, which is 0.4 mol. eq. to A β . Cu²⁺ ions were added after the fibril formation throughout this work.

Binding of Cu²⁺ to A β fibrils was determined by photometric assay using N,N,N',N'-tetraethylthiuram disulfide (TETD) as a Cu²⁺ indicator.¹⁶⁴ We confirmed that less than 5% of Cu²⁺ was unbound to A β (1-40) for both CuCl₂ and CuGly when the ratio of Cu²⁺ to A β ($f_{\text{Cu}/\text{A}\beta}$) was 0.5 or less. However, at $f_{\text{Cu}/\text{A}\beta} = 1.0\%$, 5.3% and 15% of Cu²⁺ ions were not bound to A β fibrils for CuCl₂ and CuGly, respectively, as shown in Figure 7. On the basis of these results, we selected $f_{\text{Cu}/\text{A}\beta} = 0.4$ throughout the following SSNMR study as a condition where nearly all Cu²⁺ ions are strongly bound to A β fibrils.

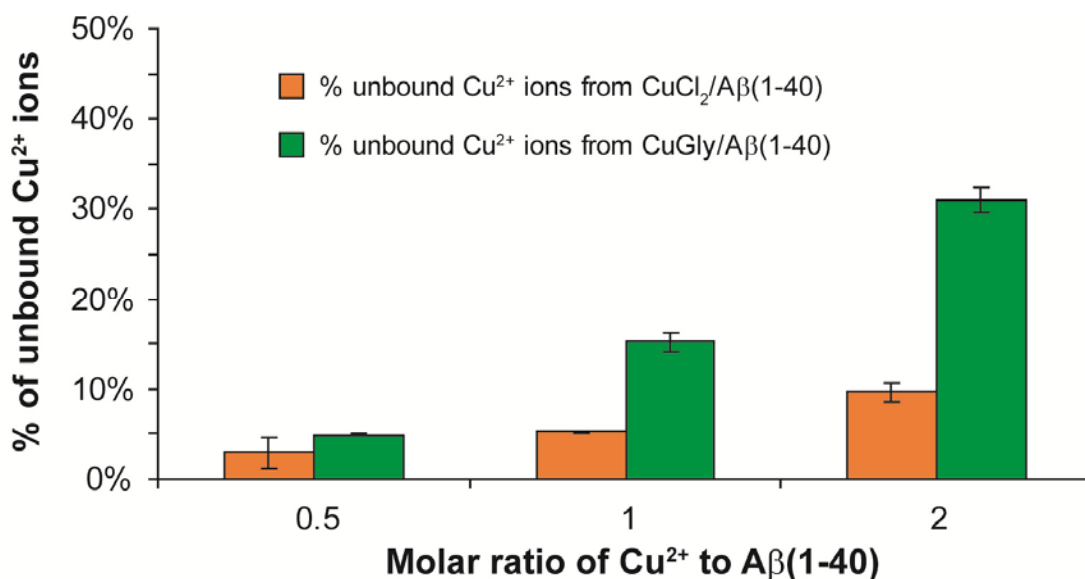


Figure 7. Fractions of Cu²⁺ ions that were not bound to Aβ(1-40) fibrils in a mixture of 500 μM Aβ(1-40) fibril solution with CuGly or CuCl₂ (0.25-1.0 mM) at three molar ratios of Cu²⁺ to Aβ (f_{Cu/Aβ}) of 0.5, 1.0, and 2.0. The unbound Cu²⁺ concentration was photometrically monitored with TETD as a Cu²⁺ indicator for the supernatant obtained after centrifuging the mixture at 16.1 × 10³ g for 30 min.

Next, we examined whether any site-specific binding of Cu²⁺ can be detected by SSNMR for Aβ(1-40) fibrils. Figure 8 show a comparison of the aliphatic region of 1D ¹³C CPMAS SSNMR spectra of Aβ(1-40) amyloid fibrils (black) without and (red) with 0.4 mol. eq. of Cu²⁺ to Aβ. The Aβ(1-40) samples were isotope labeled with uniformly ¹³C- and ¹⁵N-labeled amino acids at Val-12, Phe-20, Ala-21, Ile-31, Gly-33, and ¹³Cε-selectively labeled Met-35 (See materials and methods section for sample preparation, P.51).

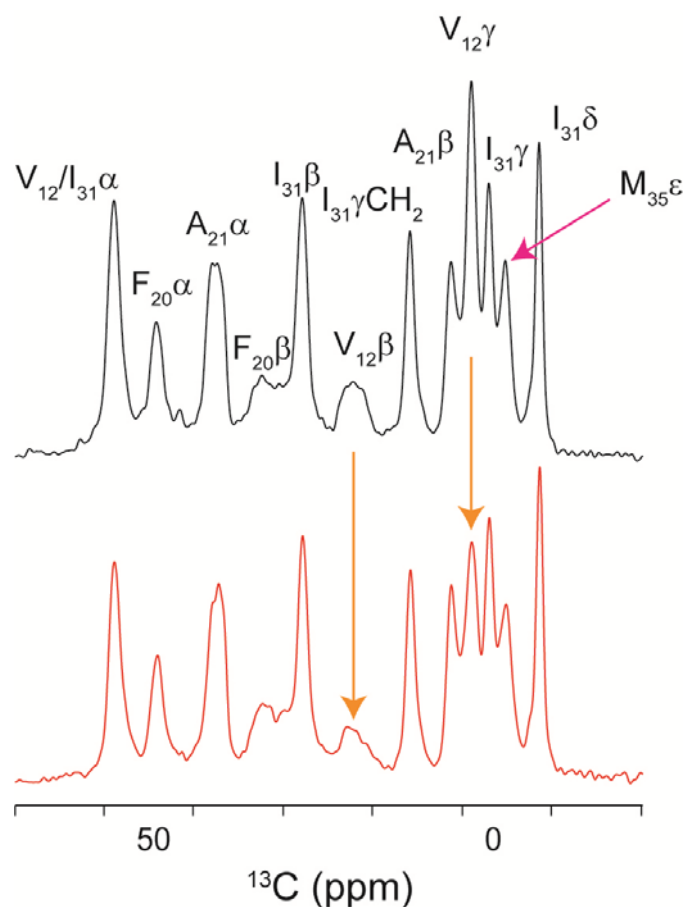


Figure 8. Comparison of 1D ^{13}C CPMAS spectra of $\text{A}\beta(1-40)$ fibrils without (black) and with (red) 0.4 mol. eq. of Cu^{2+} , together with signal assignments. The samples were labeled with uniformly ^{13}C -, ^{15}N -labeled amino acids at Val-12, Phe-20, Ala-21, Ile-31, Gly-33 and with $^{13}\text{C}\epsilon\text{H}_3$ selectively labeled at Met-35.

Interestingly, most sites display no significant changes in the signal intensities. This includes $^{13}\text{C}\epsilon$ of Met-35 (magenta arrow), which has been long suspected as the site that is responsible for the production of H_2O_2 through interactions with Cu^{2+} .^{165, 166} If the Met-35 sidechain ($-\text{SC}\epsilon\text{H}_3$) is oxidized into $-\text{SO}-\text{CH}_3$ as hypothesized previously,⁷⁰ $^{13}\text{C}\epsilon$ shift at 15.6 ppm should be altered to ~ 40 ppm.¹⁶⁷ However, no major changes in the signal intensity or chemical shift were observed for $^{13}\text{C}\epsilon$ Met-35 after a month. In contrast, signal intensities drop

by 36% and 27% selectively for $^{13}\text{C}\gamma$ and $^{13}\text{C}\beta$ of Val-12 (orange arrows), respectively, upon Cu^{2+} binding. The site is nearby to His-13/His-14, which were reported to interact with Cu^{2+} for $\text{A}\beta(1-40)$ monomer.⁷³ These results suggest that the effect of Cu^{2+} binding to fibrils is site-specific, quenching the signals for sites in the vicinity of Cu^{2+} (Val-12 in this case). In a recent SSNMR study of Cu, Zn SOD, signal quenching of ^{13}C within a ~ 5 Å radius of Cu^{2+} was reported.¹⁴¹ Here, we utilize such paramagnetic quenching to identify Cu^{2+} binding sites in the aggregated form of the $\text{A}\beta$ proteins.

Figure 9 shows a comparison of 2D $^{13}\text{C}/^{13}\text{C}$ spectra of the same $\text{A}\beta$ fibril samples (black) without and (red) with Cu^{2+} bound to $\text{A}\beta$ in a superposition. Most of the signals are well resolved without signal overlap. Remarkably, the Cu^{2+} -bound fibrils have nearly identical chemical shift positions (within ± 0.2 ppm) and intensities with those for the Cu^{2+} -free fibrils, except for the Val-12 signals (orange arrows). Since ^{13}C chemical shifts are a probe very sensitive to protein conformations, this presents interesting evidence that the site-specific Cu^{2+} binding does not alter the conformations of $\text{A}\beta$ in the β -sheet cores, including Phe-20, Ala-21, Ile-31. Additional results below support this finding. Thus, we concluded that Cu^{2+} -binding does not introduce major conformation changes except for the N- and C-terminal regions, where binding is likely to take place, as will be discussed.

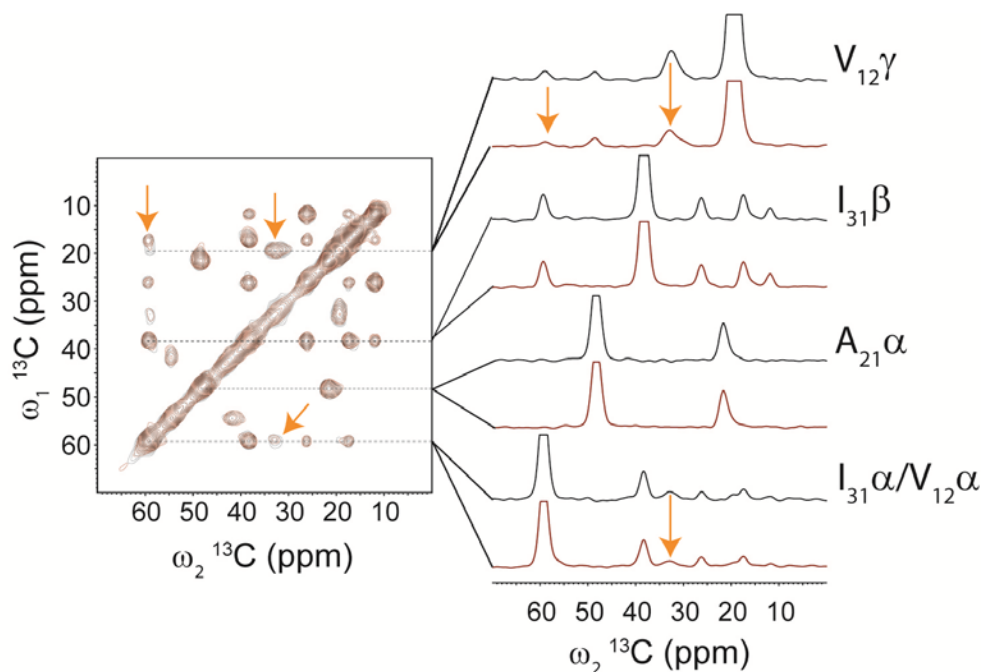


Figure 9. Comparison of 2D $^{13}\text{C}/^{13}\text{C}$ correlation spectra for the same fibril samples as in Figure 8 without (black) and with (red) Cu^{2+} . The spectra were obtained at MAS of 20 kHz with fpRFDR sequence of 1.6 ms during $^{13}\text{C}/^{13}\text{C}$ exchange.¹⁶⁸

On the basis of the above results, we hypothesized that Cu^{2+} ions are interacting with His-13 and His-14 side chains in the $\text{A}\beta$ fibril, and with other neighboring residues. To test this, we performed ^{13}C SSNMR of $\text{A}\beta(1-40)$ fibril samples in which one of these residues was uniformly ^{13}C -labeled. Figure 10a and b show 1D ^{13}C CPMAS spectra of (a) His-13 and (b) His-14 sidechains for $\text{A}\beta$ fibrils (black) without and (red) with Cu^{2+} bound to $\text{A}\beta$, together with signal assignments. Clearly, the signals for both His-13 and His-14 are quenched considerably by Cu^{2+} . Spectral analysis of the aromatic sidechains shows that signals for $^{13}\text{C}\epsilon$ and $^{13}\text{C}\delta$ in His-13/His-14 are quenched by 30-60%, while those for $^{13}\text{C}\gamma$ are quenched less (by <15%) as indicated by orange arrows. This suggests that the Cu^{2+} ion favors coordination to Ne in His-13 and His-14, which is one bond away from $^{13}\text{C}\delta$ and $^{13}\text{C}\epsilon$, over that to N δ . As a control, we examined

paramagnetic quenching for Phe-20 (Figure 10c), which shows nearly no quenching. Previous studies indicated the involvement of the N δ /N ϵ of Histidine in A β (1-40) in Cu²⁺ binding.^{72, 73, 169}

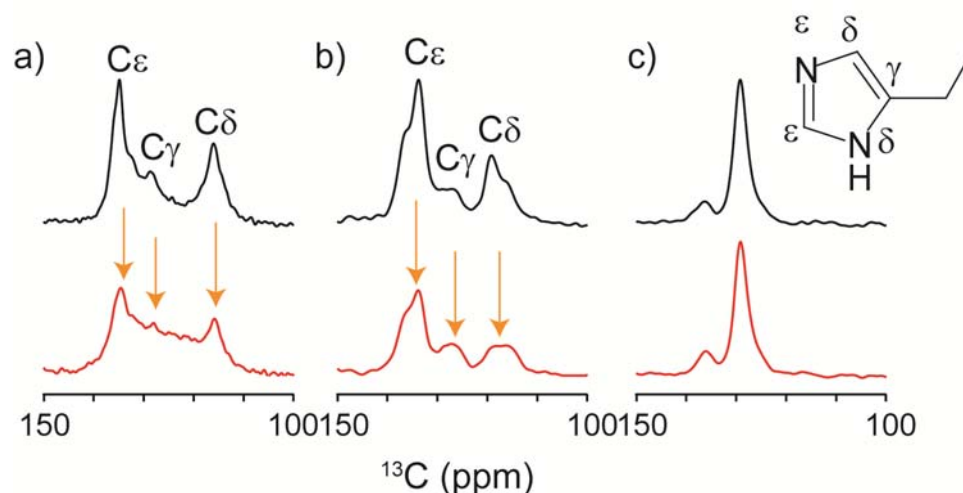


Figure 10. Aromatic regions of ¹³C CPMAS spectra for (a) His-13, (b) His-14, and (c) Phe-20 sidechains for A β (1-40) fibrils in the hydrated state (black) without and (red) with Cu²⁺.

Raman spectroscopic studies⁷² shows that A β (1-40) precipitates obtained by the addition of Cu²⁺ to a A β solution display Cu²⁺ coordination to N ϵ in His, while A β (1-40) monomers in a solution show Cu²⁺ coordination to N δ at pH 7.4. Barnham et al.,¹⁶⁹ reported that A β (1-40) having N-methylated His for N β at position His-6, -13, and -14 has weaker metal-ligand interaction than WT A β or A β (1-40) having N-methylated His for N δ . The results are consistent with our finding. To the best of our knowledge, this is the first experimental data that directly demonstrate the association of Cu²⁺ with His-13 and His-14 of A β (1-40) in amyloid fibrils with site resolution.

Figure 11 shows relative signal intensity for ¹³C resonances of A β (1-40) fibril bound to Cu²⁺ with respect to the corresponding signal intensity for A β without Cu²⁺. The signals are

attenuated as much as by $\sim 60\%$ for the residues in the N-terminus, including Phe-4, Val-12, His-13, His-14, particularly for ^{13}C sites in the side chains. The signals for Val-39 were also quenched probably through the association of Cu^{2+} with the carboxyl terminal of Val-40. More than 20% of the signal intensity was quenched for the side chains of Val-24 ($\text{C}\alpha$, $\text{C}\beta$) and Leu-34 ($\text{C}\delta$). The observed quenching of Val-24 side chain may be attributed to association of Cu^{2+} with Glu-22. The source of the signal quenching at Leu-34 is not clear.

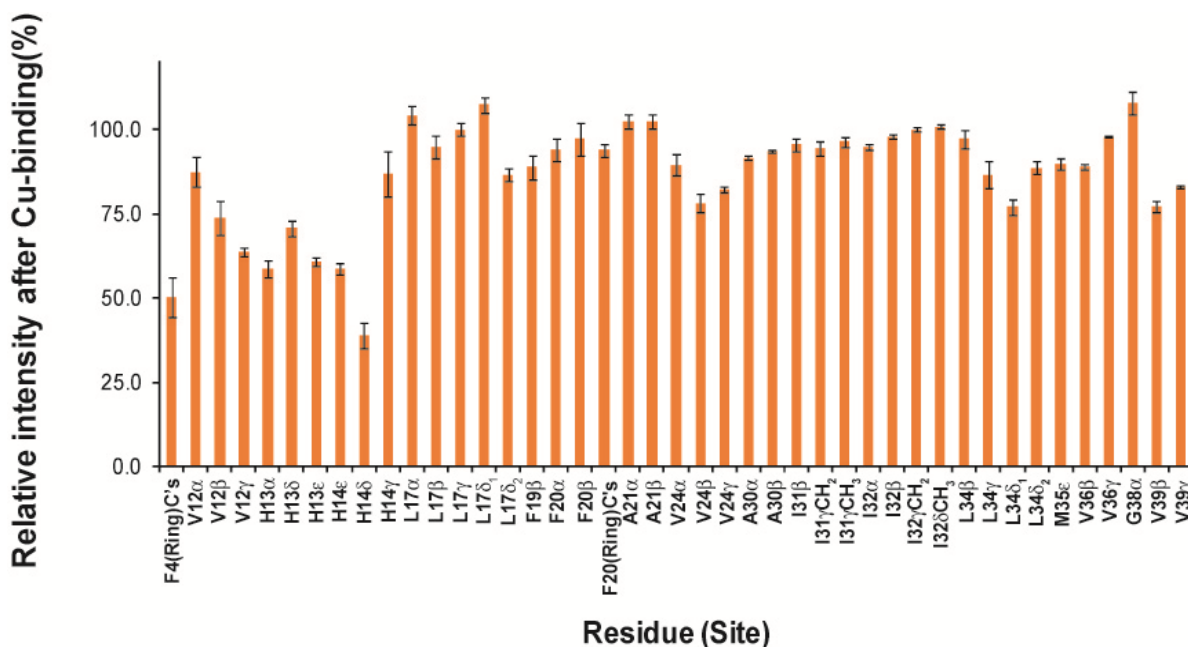


Figure 11. Relative signal intensity of ^{13}C resonances in $\text{A}\beta(1-40)$ fibril after Cu^{2+} binding. The error bars indicate the uncertainty due to the noise level. The intensities were measured from 1D ^{13}C CPMAS for selectively labeled samples.

Figure 12 shows the summary of the residues quenched by Cu^{2+} binding for six $\text{A}\beta$ samples selectively isotope-labeled at different sites. The average of the signal quenching was calculated for each residue from the data, and categorized into three levels. Only a limited

number of aliphatic side chains were quenched by Cu^{2+} bound to $\text{A}\beta$. Apart from the significant changes in the N-terminal region, Val-24, and Val-39, other sites in the residues 17-38 show very limited perturbation from Cu^{2+} on the signal intensities.



Figure 12. Amino acid sequence of $\text{A}\beta(1-40)$ and the extent of signal quenching by Cu^{2+} binding (green $\leq 15\%$; orange 15-25%; red $\geq 25\%$). The quenching is the average of all the observed ^{13}C sites for each residue. The arrows denote β -sheet regions reported in the previous studies by Tycko and co-workers [Proc. Natl. Acad. Sci. U.S.A. 2002, 99,16742–16747].

Importantly, we also found that ^{13}C chemical shifts are not altered upon Cu^{2+} binding by more than 0.2 ppm for the hydrophobic core regions (residues 18-25 and 30-36) except for the moderate perturbation (~ 0.35 ppm) on some sites of Phe-19 and Gly-33 (see Table I). The results provide the first crucial experimental evidence that Cu^{2+} binding does not reorganize or alter the parallel β -sheet structures of the hydrophobic core regions for $\text{A}\beta(1-40)$ fibril with site resolution.

To identify other binding sites, we further performed 2D $^{13}\text{C}/^{13}\text{C}$ correlation SSNMR (Figure 13) of uniformly ^{13}C - and ^{15}N -labeled $\text{A}\beta(1-40)$ fibrils (black) without and (red) with Cu^{2+} . Surprisingly, as shown in the slices (Figure 13a-c), considerable signal quenching by $45 \pm 11\%$ and $59 \pm 9\%$ due to Cu^{2+} (orange arrows) was observed for $^{13}\text{CO}_2^-$ of (c) Val-40 in the C-terminus and (a) Glu side chains, respectively. The extent of the quenching due to Cu^{2+} is

comparable to those for His-13 and His-14. Although Glu signals were not assigned to individual residues, the results clearly suggest Cu^{2+} bindings to the carboxyl terminus of Val-40 and side chains of Glu. Whereas binding to Glu was hypothesized in previous studies,⁷⁸ such Cu^{2+} binding, including that to the C-terminus, has been difficult to examine for $\text{A}\beta$ fibrils until this work. Although site-directed mutations may be effective for short $\text{A}\beta$ fragments,⁷⁵ such mutations on the full-length $\text{A}\beta$ may alter the structure of the amyloid fibril. The data in Figure 13a also indicate signals for other side chain carboxyl groups at 175-180 ppm are likely quenched by Cu^{2+} binding; further studies will be needed for signal assignments and detailed analysis.

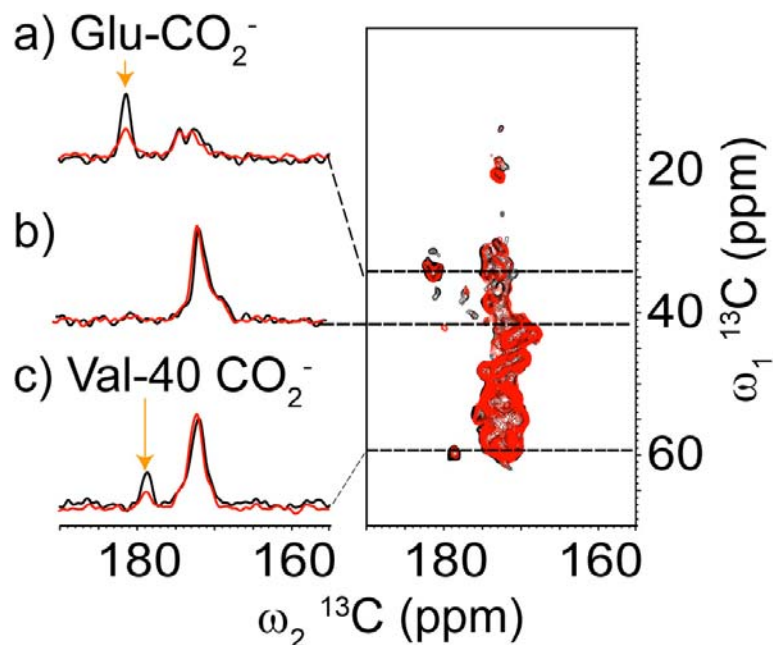


Figure 13. 2D $^{13}\text{C}/^{13}\text{C}$ SSNMR spectra between aliphatic and ^{13}CO regions for uniformly ^{13}C - and ^{15}N -labeled $\text{A}\beta(1-40)$ fibrils (black) without and (red) with Cu^{2+} , with 1D slices at $\omega_1 =$ (a) 34.6, (b) 43.9, and (c) 59.8 ppm. The spectra were obtained at a MAS of 40 kHz with an fpRFDR mixing of 1.6 ms.¹⁶⁸

Multiple Cu^{2+} binding sites in the $\text{A}\beta(1-40)$ fibrils are further confirmed by SSNMR studies of $\text{A}\beta(1-40)$ H14A mutant with and without the addition of the Cu^{2+} ions. Foremost, the TEM analysis of $\text{A}\beta(1-40)$ H14A showed the mutation doesn't alter the fibrillization process. Figure 14 shows the comparison of the $\text{A}\beta(1-40)$ and $\text{A}\beta(1-40)$ H14A fibrils generated under the same condition. (See the materials and methods section for the sample preparation protocol). The morphology of the $\text{A}\beta(1-40)$ H14A fibrils are similar to that of $\text{A}\beta(1-40)$ fibrils with the predominant species being ~ 10 nm diameter but coexistence of ~ 6 nm diameter fibrils is clearly visible in the TEM image indicating heterogeneity of the $\text{A}\beta(1-40)$ H14A fibrils.

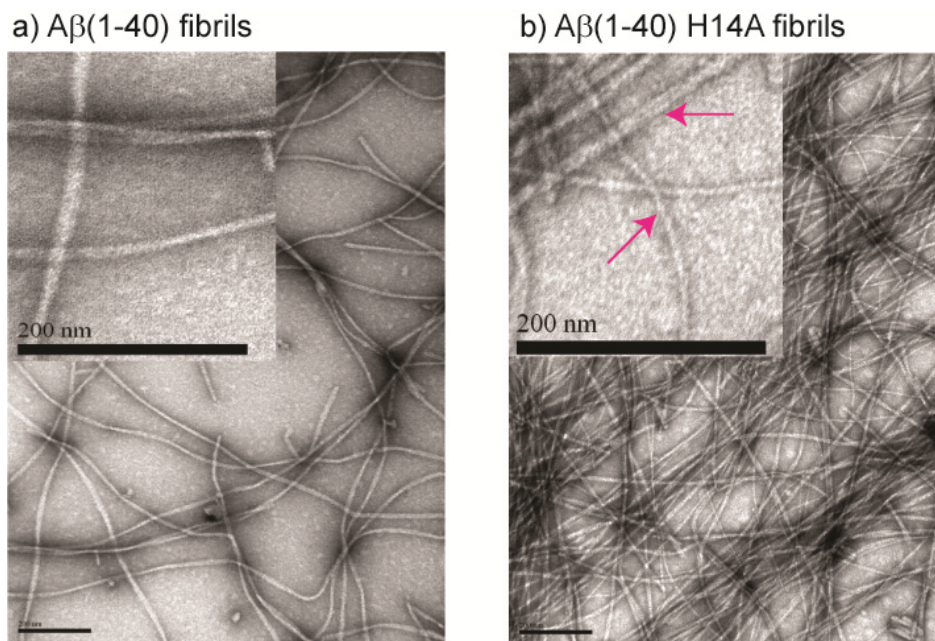


Figure 14. TEM images of (a) A β (1-40) fibrils (b) A β (1-40) H14A fibrils

Figure 15 shows the comparison of the ^{13}C CPMAS spectra of A β (1-40) H14A fibrils labeled at Val-12, Phe-21, Ala-21, Ile-31, Gly-33, and Met-35(ϵ - $^{13}\text{C}\text{H}_3$) with and without Cu^{2+} . The molecular level structure of the A β (1-40)H14A fibril is different from A β (1-40) fibrils generated under same conditions though the morphology was similar from TEM analysis. The difference in the structure is clearly distinguishable from the comparison of the ^{13}C CPMAS spectrum in Figure 15 (black) and Figure 8 (black) of the fibril samples without Cu^{2+} . In spite of the structure of A β (1-40)H14A fibrils being different, the Cu^{2+} ions strongly binds to the fibrils which is clearly seen from the signal quench from the ^{13}C CPMAS spectrum of A β (1-40) H14A fibrils (Figure 15 (red)).

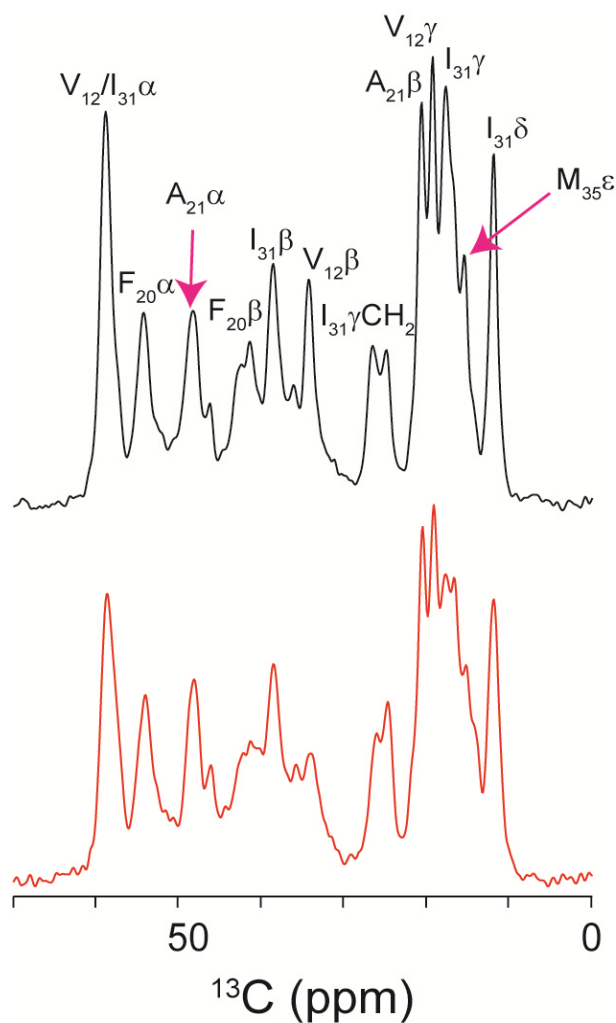


Figure 15. Comparison of 1D ^{13}C CPMAS spectra of A β (1-40) H14A mutation fibrils without (black) and with (red) 0.4 mol. eq. of Cu^{2+} , together with signal assignments. The samples were uniformly labeled with ^{13}C - and ^{15}N - labeled amino acids at Val-12, Phe-20, Ala-21, Ile-31, Gly-33 and with $^{13}\text{C}\epsilon\text{H}_3$ selectively labeled at Met-35.

With these SSNMR results, we conclude that the N-terminal region including His-13, His-14, and Glu sidechains and the CO_2^- in the C-terminus are highly likely to play major roles in Cu^{2+} binding to the A β (1-40) fibril. The Cu^{2+} binding is likely to make very little or no changes on the basic structural units in the hydrophobic cores of the A β amyloid fibril. To elucidate

possible Cu^{2+} binding structures to $\text{A}\beta$, we performed two sets of MD simulations of $\text{A}\beta(1-40)$ fibrils with Cu^{2+} in collaboration with Dr. Dan McElheny at University of Illinois at Chicago (UIC) and Prof. Ruth Nussinov at National Cancer Institute (NCI), Frederick, MD. As the initial structure, we adopted a structural model from Tycko's group²⁰ with a fixed geometry for the residues 15-39 for oligomeric $\text{A}\beta$ with 12 strands. In the first set of the MD simulation, we used cationic dummy atom (CaDa) approach for Cu^{2+} ions in order to identify possible Cu^{2+} binding ligands.¹⁷⁰ On the basis of our SSNMR results, Cu^{2+} ions were non-covalently bound to N ϵ of His-13 (or His-14 in Figure 17) by ionic interactions in the initial structure. Indeed, the final structure with implicit solvents after three thermal annealing cycles demonstrated that CO^{2-}/CO sidechains of Asp-1, Glu-3, Glu-11, Gln-15, and the CO^{2-} terminal of Val-40 coordinate to Cu^{2+} , despite the absence of such interactions in the initial structures (Figure 16). While previous EPR studies for monomeric $\text{A}\beta$ fragments^{66, 67, 73, 78} predicted two major coordination modes, here we suggest that a variety of coordination structures are likely to coexist in the amyloid fibril. Many of these observed binding modes are realized by the parallel β -sheet arrangements, in which Cu^{2+} -coordination sites at the N-terminal are concentrated via aggregation. For example, some Cu^{2+} ions were bridged by two His-13 (or His-14) rings of each two peptides (orange circles in Figures 16a and 17a). Such a binding mode is not possible in a monomer, although the possibility of Cu^{2+} -mediated intermolecular His bridge was proposed for an $\text{A}\beta$ dimer previously.¹⁶³ Also, the Cu^{2+} ions bridge carboxyl terminal of Val-40 and His-13 (or Glu-11); such a binding has not been reported for monomeric $\text{A}\beta$. It should be noted that the above MD simulation results do not necessarily exclude the previously proposed coordination models by EPR and other studies.^{74, 75} Our SSNMR results indeed indicate substantial relaxation on Phe-4, which is consistent with the Cu^{2+} coordination to His-6, which was proposed by the previous

EPR and NMR studies.^{67, 74} In our preliminary MD simulations in Figures 16 and 17, such long-range coordination may not be completely reproduced probably because of the restricted time frame of the simulations (20 ns) and the limited ensemble of the initial structures.

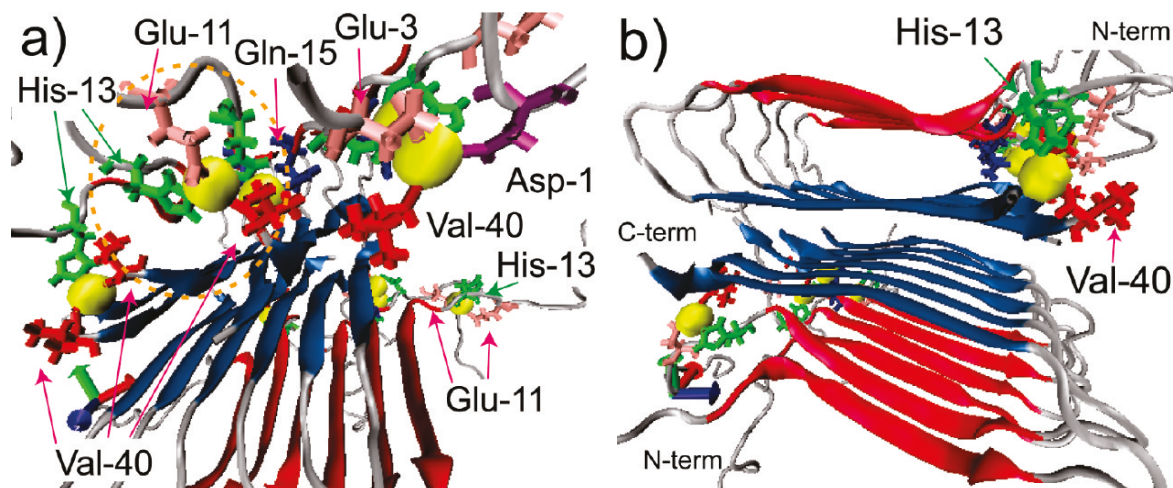


Figure 16. Final MD structure of Cu^{2+} bound $\text{A}\beta(1-40)$ fibril viewed from (a) one of the N-terminal sides and (b) the fibril axis after three thermal annealing cycles. In the initial structures, Cu^{2+} was bound to $\text{N}\epsilon$ of His-13 via non-covalent interactions. Blue and red arrows indicate β -sheet regions in residues 16-24 (red) and 30-39 (blue) of $\text{A}\beta$. The MD structure shows that Cu^{2+} (yellow) are bound to His-13 (green), Glu-3, Glu-11 (pink), Asp-1 (purple), Gln-15 (blue), and Val-40 (red) after the thermal cycles. The radius of the Cu^{2+} ion's sphere is $\sim 2 \text{ \AA}$.

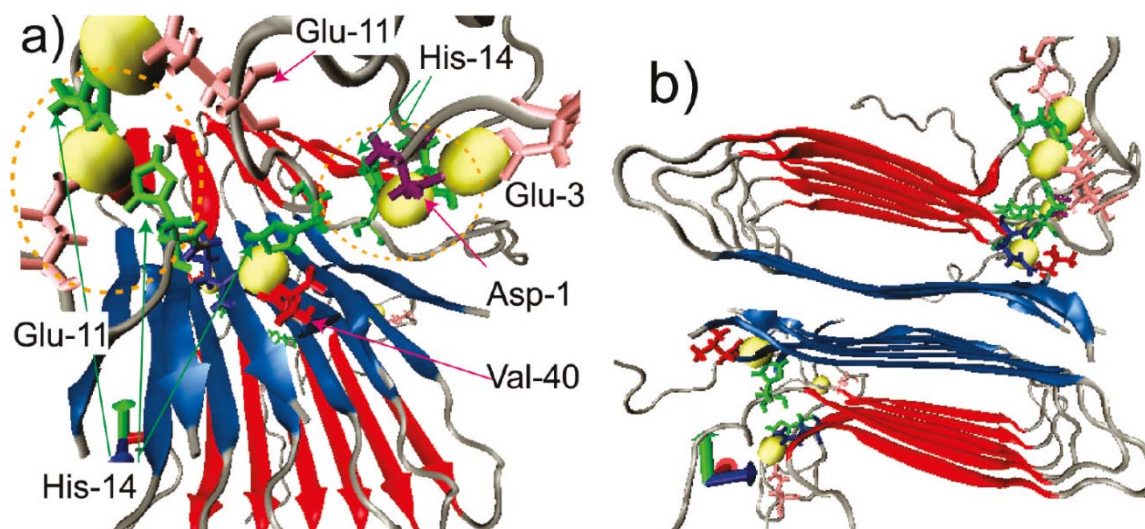


Figure 17. Final MD structure of Cu^{2+} bound $\text{A}\beta(1-40)$ fibril viewed from (a) one of the N-terminal sides and (b) the fibril axis after three thermal annealing cycles. In the initial structures, Cu^{2+} was bound to $\text{N}\epsilon$ of His-14 via non-covalent interactions. Blue and red arrows indicate β -sheet regions in residues 16-24 (red) and 30-39 (blue) of $\text{A}\beta$. The MD structure show that Cu^{2+} (yellow) are bound to His-14 (green), Glu-3, 11 (pink), Asp-1 (purple), Gln-15 (blue), and Val-40 (red) after the thermal cycles. The radius of the yellow sphere is $\sim 2 \text{ \AA}$ from the Cu^{2+} ion.

Our MD simulation starting from a different initial structure with some Cu^{2+} ions coordinated to $\text{N}\epsilon$ of His-6, His-13, His-14 showed that a common Cu^{2+} ion can be coordinated to His-6 and His-14 of $\text{A}\beta$ fibril. The results are consistent with our findings from SSNMR and MD that side chains of His-13 and His-14 and other carboxyl side chains are major coordination sites. It is possible that the various unique coordination modes presented here for the amyloid fibril coexist with those proposed for the monomeric/fragment $\text{A}\beta$ at different population and perhaps in a dynamically exchangeable manner. Figure 18 shows the structural parameters for few selected Cu^{2+} geometries.

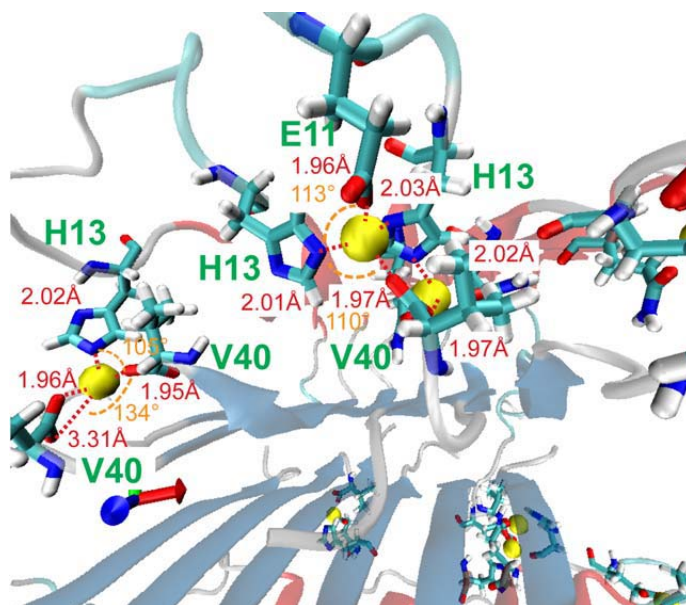


Figure 18. Structural parameters for selected Cu^{2+} coordination geometries in the MD simulation in Figure 16. The color coding of the atoms in the ligands are carbon (cyan), nitrogen (blue), oxygen (red), hydrogen (white).

The simulations presented here are intended to provide insights into the possible ligands coordinated to Cu^{2+} in the A β amyloid fibril. At this point, universal force fields are not available for MD simulations involving Cu^{2+} ions.^{155, 171, 172} Development of more optimized force fields is likely needed to reproduce more accurate coordination geometries for detailed comparison with EPR spectra. Despite the limitation, the MD simulation results allowed for the evaluation of Cu^{2+} coordination modes for more realistic Cu^{2+} -A β fibril model based on our SSNMR results, which suggested that the structural changes by Cu^{2+} binding are restricted to the N-term and C-term regions. It is encouraging that the two separate sets of MD simulations both suggested the previously unexpected unique coordination modes that are consistent with our SSNMR relaxation data.

A schematic of the Cu^{2+} coordination sphere with possible 4-coordination modes involving 1/2 N and 2/3 O are shown in Figure 19 a. Previous studies on various full-length A β peptides in monomeric or fibrillar forms and A β fragment peptides showed Cu^{2+} coordinates to A β either in square-planar, square pyramidal, distorted tetrahedral or octahedral geometry.^{68, 78, 173} Several dynamic Cu^{2+} coordination modes were proposed involving imidazole coordination in both the axial and equatorial positions have emerged as shown in Figure 19 b.¹⁷⁴

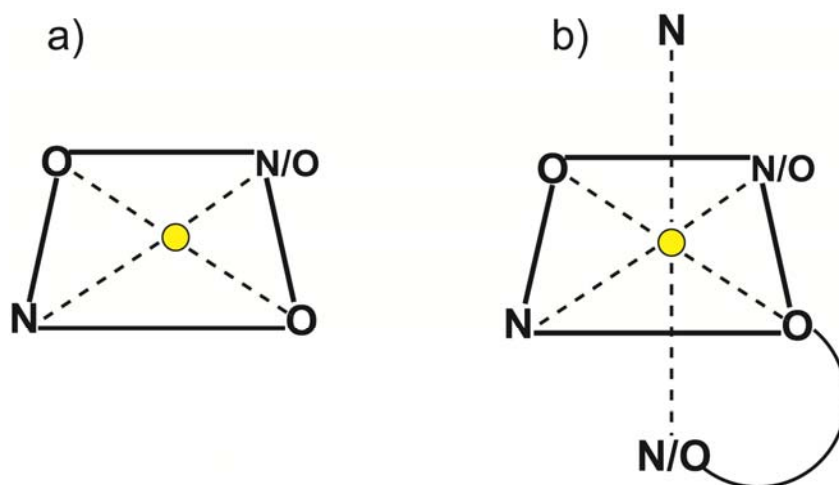


Figure 19. (a) A schematic of 4-coordination Cu^{2+} (yellow sphere) sphere involving 1/2 N and 2/3 O. (b) Cu^{2+} coordination modes involving coordination in both the axial and equatorial positions.

In our studies, four conformers were constructed based on Tycko's fibril model¹⁹ with intra-peptide copper-binding. In Conformer 1, Cu^{2+} binds to His-6, His-13 and His-14 (Figure 20 a) and in Conformer 2, Cu^{2+} binds to Asp-1, His-6 and His-14 (Figure 20 b). In Conformer 3, 4 Cu^{2+} ions interact with Asp-1, His-14 and Val-14 (Figure 20 c) and Asp-1, His-13 and Val-40 (Figure 20 d). The bond angles and lengths suggest that these conformers are consistent with distorted square-planar Cu^{2+} -coordination geometry.

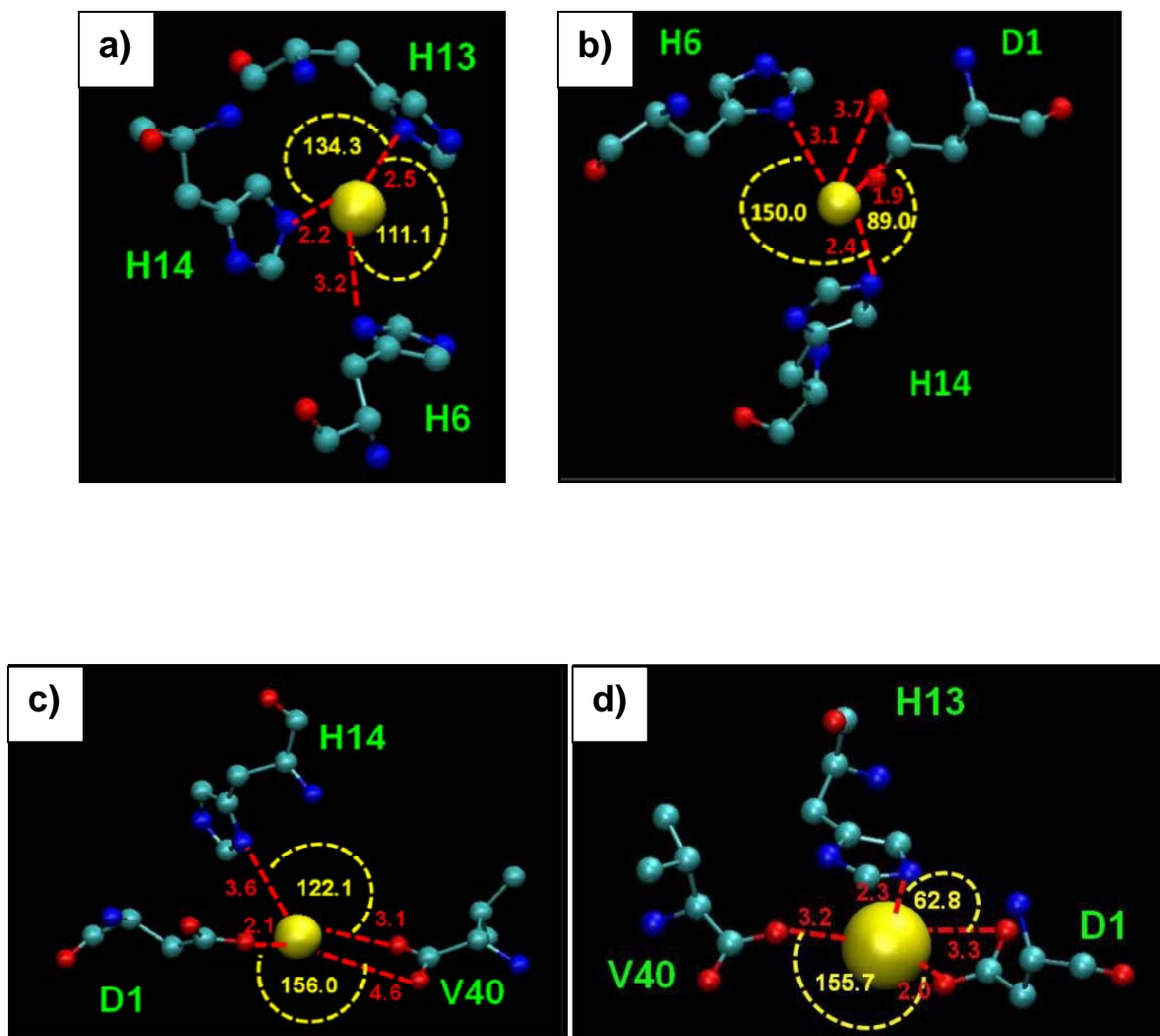


Figure 20. Cu^{2+} coordination geometries to (a) His-6, His-13, His-14, (b) Asp-1, His-6, His-14, (c) Asp-1, His-14, Val-40 (d) Asp-1, His-13, Val-40

i. Structural studies of Cu^{2+} binding to $\text{A}\beta(1-42)$ fibrils

Next we studied the Cu^{2+} binding to the $\text{A}\beta(1-42)$ fibrils. $\text{A}\beta(1-42)$ peptide differs from the $\text{A}\beta(1-40)$ in the C-terminal region with two additional hydrophobic residues Ile-41 and Ala-42. $\text{A}\beta(1-42)$ peptide is highly prone to aggregation and is more neurotoxic than the $\text{A}\beta(1-40)$

fibrils. A β (1-42) peptides are shown to bind Cu²⁺ ions, however the molecular level structure of Cu²⁺-A β (1-42) could be different from Cu²⁺-A β (1-40) complex. Preliminary SSNMR investigations show that the Cu²⁺-A β (1-42) fibrils have similar N-terminal Cu²⁺ coordination as Cu²⁺-A β (1-40) fibrils. Figure 21 shows the comparison of the 1D ¹³C CPMAS spectra of the A β (1-42) fibrils uniformly ¹³C- and ¹⁵N labeled Phe-4, Val-12, Leu-17, Ala-21 and Gly-29. Figure 21 a) is the fibrils without Cu²⁺ and (b) is with 40% mol. eq. of Cu²⁺ with respect to A β (1-42) fibrils. No major spectral changes were observed for Leu-17, Ala-21 and Gly-29 in Cu²⁺-A β (1-42) fibrils. But the Phe-4 and Val-12 residues were quenched ~ 40-50% upon Cu²⁺ binding which is consistent with the signal quenching observed for the Cu²⁺-A β (1-40) fibrils indicating that the N-terminal binding sites are similar as observed for the A β (1-40) fibrils. Figure 22 is the comparison of the ¹³C/¹³C fpRFDR (finite pulse Radio Frequency Driven Dipolar Recoupling) spectra of the same A β (1-42) fibrils described above a) without Cu²⁺ and (b) with 40% mol. eq. Cu²⁺. The ¹³C chemical shifts were not altered upon Cu²⁺ binding suggesting no major alteration of the fibrils structure with the metal binding. The cross peaks for the Phe-4 and Val-12 are diminished in (b) suggesting the possible involvement of N-terminal residues such as Glu-3, His-6, Glu-11, His-13 and His-14. Extensive structural studies are required in order to characterize the Cu²⁺ - binding structure to the A β (1-42) fibrils since the molecular level structure of the fibrils are not known.

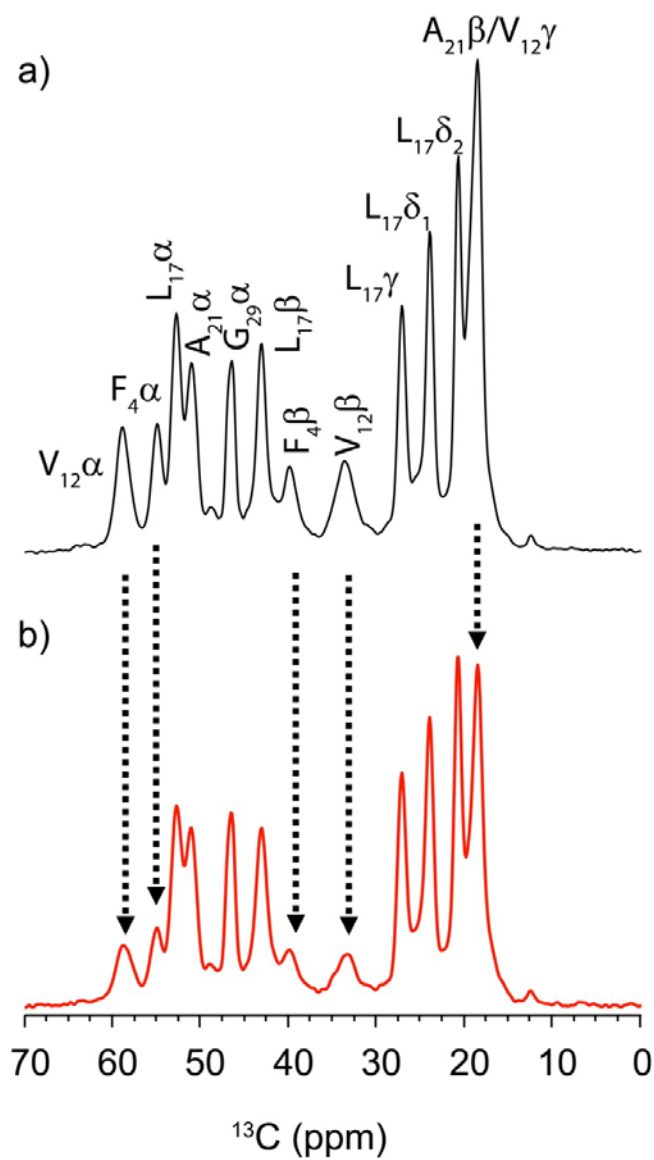


Figure 21. Comparison of 1D ^{13}C CPMAS spectra of $\text{A}\beta(1-42)$ fibrils (a) without (black) and (b) with (red) 0.4 mol. eq. of Cu^{2+} , together with signal assignments. The samples were labeled with uniformly ^{13}C - and ^{15}N -labeled amino acids at Phe-4, Val-12, Leu-17, Ala-21, and Gly-29.

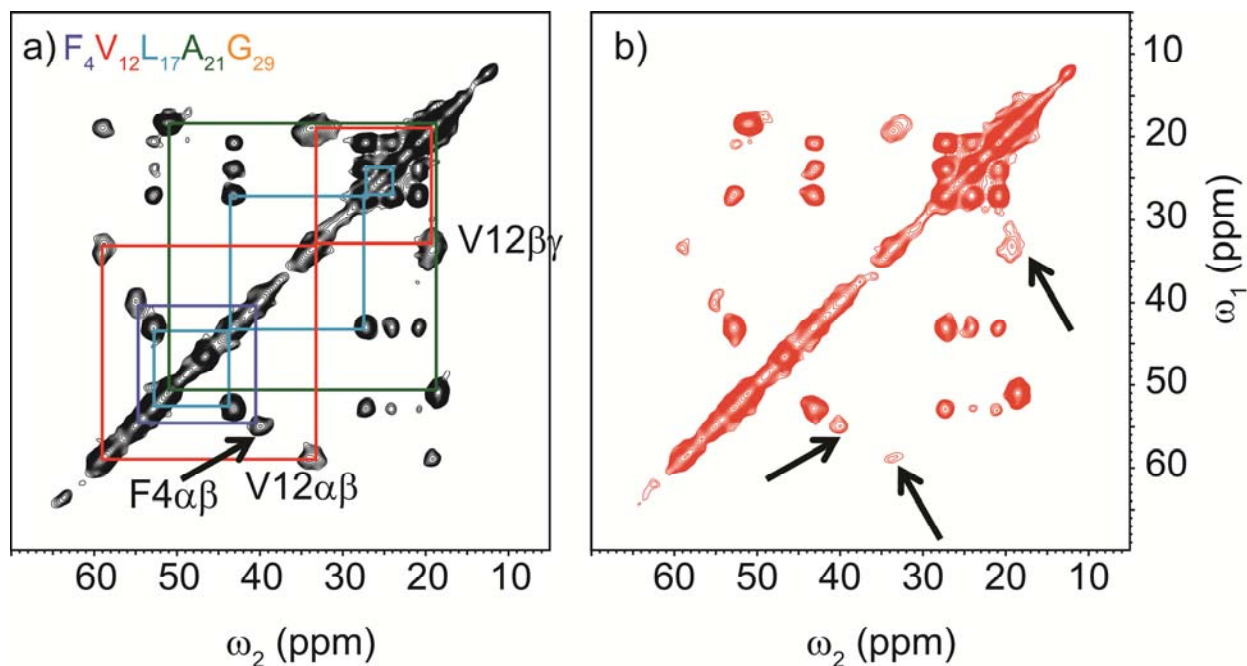


Figure 22. Comparison of 2D $^{13}\text{C}/^{13}\text{C}$ correlation spectra for the same fibrils samples as in Figure 21 (a) without (black) and (b) with (red) Cu^{2+} . The spectra were obtained at MAS of 20 kHz with fpRFDR sequence of 1.6 ms during $^{13}\text{C}/^{13}\text{C}$ exchange.¹⁶⁸

C) Conclusion

In conclusion, this study has presented molecular details of Cu^{2+} -bound $\text{A}\beta(1-40)$ amyloid fibril system by SSNMR. Three chemically and biologically novel aspects are presented in our work. First, this study has demonstrated the first systematic approach to examine binding of Cu^{2+} to insoluble amyloid aggregates at a site-specific level by SSNMR, based on the recent progress in SSNMR for small paramagnetic compounds^{160, 175-178} and for paramagnetic proteins^{139, 141, 142, 161} by our groups and other. We have shown that uses of paramagnetic quenching and chemical-shift perturbation in SSNMR can be effectively employed in order to examine possible Cu^{2+} binding sites and structural changes upon Cu^{2+} binding for insoluble amyloid system. Second, this study has, for the first time, provided detailed site-specific

structural information on Cu^{2+} bound full-length $\text{A}\beta(1-40)$ in amyloid fibrils. Despite the linkage of the Cu^{2+} - $\text{A}\beta$ fibril with AD and its significance as a potential pharmaceutical target,^{122, 157, 158} Cu^{2+} - $\text{A}\beta$ association has been examined mostly for smaller and early stage model systems such as soluble $\text{A}\beta$ fragments or $\text{A}\beta$ monomers. Our study has offered a solution to this situation by overcoming the difficulties in the sample preparation and the lack of suitable structural analysis methods for Cu^{2+} - $\text{A}\beta$ in amyloid fibrils, for which structural information has been very scarce. Third, our SSNMR data experimentally demonstrated various novel features of Cu^{2+} coordination to the $\text{A}\beta$ fibril. Besides offering experimental evidence of the Cu^{2+} coordination to N ϵ of His-13 and His-14, this study has revealed previously unexpected ligands such as the carboxyl group of Val-40 at the C-terminus and Glu sidechains. Our chemical-shift perturbation data suggested very little structural changes for the hydrophobic core regions (residues 18-25 and 30-36) of the $\text{A}\beta$ fibrils upon Cu^{2+} binding. The unique coordination modes suggested by SSNMR were confirmed by the two sets of MD simulations on sophisticated $\text{A}\beta$ oligomer models reflecting realistic amyloid fibril structures. Unlike previous MD studies on Cu^{2+} - $\text{A}\beta$ binding,¹⁵⁵ both MD simulations incorporated intermolecular parallel β -sheet structure that is characteristic of the $\text{A}\beta(1-40)$ amyloid fibril as well as the noncovalent bonding models for Cu^{2+} -ligand interactions. Although further studies are needed to fully understand Cu^{2+} binding structure to $\text{A}\beta$, including its relation to the previous EPR studies and a ROS production mechanism, the combination of SSNMR analyses and MD simulations have provided insights into previously unknown detailed structural features of Cu^{2+} -bound $\text{A}\beta(1-40)$ in amyloid fibrils. The new SSNMR approach presented here may be also applicable to examine binding of small paramagnetic ligands, such as drugs, to amyloid proteins. It has been proposed that metal ions such as Cu^{2+} and Zn^{2+} may trigger the formation of $\text{A}\beta$ oligomer or fibril, modulating

misfolding kinetics and aggregation states of A β .^{71, 128, 162} In this initial work, we focused on establishing SSNMR structural analysis of A β (1-40) fibril upon Cu²⁺ binding after fibril formation. A similar approach is likely useful for SSNMR characterization of the structures of A β oligomer and A β fibril that are formed in the presence of Cu²⁺ or other metal ions.

D) Materials and methods

1) Synthesis and Purification of A β (1-40) Peptide.

A β (1-40) peptide (NH₂-DAEFRHDSGY-EVHHQKLVFF-AEDVGSNKGAIIGLMVGGVV-COOH) was synthesized and purified as reported previously. Briefly, A β (1-40) was synthesized using solid phase peptide synthesis with standard Fmoc synthesis and cleavage protocols.^{15, 21} The crude peptide was purified by HPLC using acetonitrile and water gradient with 0.1% trifluoroacetic acid. ¹³C- and ¹⁵N-labeling was introduced as described previously by incorporating Fmoc-protected uniformly ¹³C- and ¹⁵N-labeled amino acids at selected residues. The Fmoc protection of the uniformly ¹³C- and ¹⁵N-labeled amino acids (Isotec/Sigma-Aldrich, Miamisburg, OH) was performed at the Research Resource Center (RRC) at UIC using the protocol of Fields et al.¹⁷⁹ The purities of the peptide samples were determined by MALDI-TOF mass spectra performed at UIC RRC, and the purities were approximately 95% after the HPLC purification. The purified samples were stored as lyophilized powder at -20 °C before they were used. The labeling schemes for the six samples used are as follows: (1) His-14, Ile-32, Val-36, Gly-37; (2) His-13, Ala-30, Gly-38, Val- 39; (3) Val-12, Phe-20, Ala-21, Ile-31, Gly-33, Met-35(¹³C₆H₃); (4) Phe-4, Gly-9, Val-12, Leu-17, Ala-21; (5) Phe-19, Val-24, Gly-25, Ala-30, Leu-34; (6) Val-18, Phe-19, Ala-21, Ile-31, Gly-33. Uniformly ¹³C- and ¹⁵N-labeled A β (1-40) was prepared by Dr. Fei Long in our group. The sample was expressed as a fusion protein with Glutathione S-Transferase (GST) tag connected by a Factor Xa recognition site (IEGR1) in E.

coli. The GST tag was removed by Factor Xa enzymatic cleavage, and then, the peptide was purified by HPLC as described above. The yield of uniformly ^{15}N - and/or ^{13}C -protein A β (1-40) was ~1.5 mg from 1 L of the cell culture.¹⁸⁰

A β (1-42) peptide (NH₂-DAEFRHDSGY-EVHHQKLVFF-AEDVGSNKGAIIGLMVGGVVIA-COOH) was synthesized by standard Fmoc synthesis and cleavage protocols as described above. The purification of A β (1-42) was performed by following the method from Dr. Hoshi and co-workers.¹⁸¹

2) Preparation of A β (1-40) Fibrils for Cu²⁺-Binding Assay and Solid-State NMR Experiments

For Cu²⁺-binding assay with A β (1-40) fibrils using UV-vis spectroscopy, a solution of 5 mM A β (1-40) was prepared by first dissolving A β (1-40) peptide in 50 mM NaOH.¹³⁹ The peptide mixture was then briefly vortexed and diluted to a final peptide concentration of 500 μM with deionized water containing 0.02 % NaN₃. The pH of the solution was adjusted to 7.4 by using 100 mM HCl. The A β (1-40) solution was sonicated for 5 min in an ice bath, and this solution was then centrifuged at 16.1×10^3 g for 5 min to remove any preformed aggregates. The peptide solution was divided into several 1.5 mL microvials for Cu²⁺-binding assay. The concentration of A β (1-40) was measured using UV-vis spectroscopy.²¹ The A β (1-40) solution was then incubated for 14 days with constant agitation in the sample tube at room temperature. A β (1-40) fibril formation was confirmed by thioflavin T (ThT) fluorescence assay.

For SSNMR studies, amyloid fibril samples were prepared as described above, but with selectively isotope-labeled or uniformly ^{13}C - and ^{15}N -labeled A β (1-40) peptides. For the samples used for Figures 8, 9, 10, 15 after incubation of an A β solution for fibril formation, the A β (1-40) fibril with Cu²⁺ was prepared by adding CuCl₂ solution (pH 7.4) to the A β solution in the mole

ratio of 0.4:1.0 (Cu^{2+} : $\text{A}\beta(1-40)$) and incubated at 4 °C for 24 h with initial vortexing. The control sample without Cu^{2+} was prepared in the same manner except for the addition of CuCl_2 . The samples were then centrifuged at 16.1×10^3 g for about 1 h (20 min at a time), and the supernatant was removed. The gel-like pellet at the bottom was then lyophilized. The lyophilized $\text{A}\beta(1-40)$ fibril samples with and without Cu^{2+} were packed in to 2.5 mm MAS rotors with rubber O-rings on the spacer and cap. The lyophilized samples were rehydrated with deionized water (3 μL water/mg $\text{A}\beta(1-40)$) in the rotor with 3 μL of water added at one time and centrifuged at 2.0×10^3 g for 2 min. The hydrated samples were incubated overnight at 4 °C before running the SSNMR experiments.

For the uniformly ^{13}C - and ^{15}N -labeled $\text{A}\beta(1-40)$ fibril sample used for Figure 13, after incubation for fibril formation, we centrifuged the sample at 16.1×10^3 g for ~ 1.0 h (20 min at a time) and removed the supernatant. The gel-like pellet at the bottom of the centrifugal vial was transferred into the 1.8 mm MAS rotor of 10 μL volume by centrifugation. The fibrils were then packed into a 1.8 mm rotor by fitting a 200 μL pipet tip to the rotor with the fibrils and centrifuging the rotor pipet tip mounted in a microcentrifuge tube with a minimum amount of the supernatant for 2-4 min at 6×10^3 g. Then, the rotor cap was glued with Krazy Glue (Krazy Glue, Columbus OH) with a small piece of Teflon tape between the cap and the sample to avoid interaction of the glue with the peptide. This cap can be removed easily by immersing it in liquid nitrogen. The $\text{A}\beta(1-40)$ fibrils with Cu^{2+} was prepared by adding a 26.5 mM CuCl_2 solution in the mole ratio of 0.4:1.0 (Cu^{2+} : $\text{A}\beta(1-40)$) into the rotor. First, the hydrated $\text{A}\beta(1-40)$ sample in a rotor was lyophilized, and then a CuCl_2 solution was introduced directly into the 1.8 mm rotor by centrifugation and the cap was glued as described above. The rotor was then incubated at 4 °C for 24 h before the SSNMR experiments.

3) Solid-State NMR Experiments

All the SSNMR experiments were performed with an Infinityplus SSNMR spectrometer from Varian (Fort Collins, CO) with a home-built 2.5 mm MAS triple-resonance probe or a 1.8 mm MAS triple-resonance MAS probe developed at Dr. Samoson's lab (National Institutes of Chemical Physics and Biophysics, Tallinn, Estonia) at 9.4 T (^1H frequency of 400.2 MHz) in the double-configuration. For the data in Figures 8, 9, 10 and 15, the spinning speed was set to 20000 ± 3 Hz throughout the experiments with cooling air at -10°C supplied through a Varian VT stack at a flow rate of ~ 140 standard cubic feet per hour (scfh), which kept the sample temperature at $\sim 11^\circ\text{C}$. Approximately, 2.0-3.5 mg of labeled $\text{A}\beta(1-40)$ fibril samples were used. In the 1D ^{13}C CPMAS experiments for Figures 8, 10 and 15 adiabatic CP transfer was used. During the CP period, the ^{13}C RF field amplitude was linearly swept from 45-65 kHz during a contact time of 1.0 ms while the ^1H RF amplitude was kept constant at 75 kHz. During the detection period, ^1H Two Pulse Phase Modulation (TPPM) decoupling of 90 kHz was employed. The recycle delays for the 1D experiments were 1.8 s. The 1D spectra in Figure 8, 10c and 15 were collected with 1024 scans and were processed with Gaussian broadening of 20, 150 and 50 Hz, respectively. The 1D spectra in Figure 10a and b were collected with 4096 scans and processed with Gaussian broadening of 150 Hz. In the 2D experiments for Figure 9, a 2D $^{13}\text{C}/^{13}\text{C}$ correlation pulse sequence with the fpRFDR mixing was used.^{19, 168} After the adiabatic CP, signals were recorded during the t_1 period, and then a real or imaginary component of the magnetization was stored along the z axis. Then, during the mixing period, a fpRFDR $^{13}\text{C}/^{13}\text{C}$ dipolar recoupling sequence with a mixing time of 1.6 ms and a ^{13}C π -pulse width of 15 μs was used. ^1H TPPM decoupling of 90 kHz was employed during the t_1 and t_2 periods, while cw decoupling of the same amplitude was used during the mixing period. For each t_1 point, 192

scans of signals were accumulated with an acquisition period of 10 ms. A total of 180 complex t_1 points were recorded with a t_1 increment of 33.4 μ s. The obtained NMR data were processed by NMRPipe software.¹⁸² Gaussian window functions of 110 and 90 Hz were applied along the t_1 and t_2 time domains. An overall experimental time was 35 h. The experiments were performed for the six A β samples listed above in which different residues are uniformly ^{13}C - and ^{15}N -labeled. ^{15}N -labeling was introduced for experiments to be performed in the future. The spectra in Figure 13 were acquired at a spinning speed of $40\,000 \pm 10$ Hz with cooling air at -20 °C supplied through a Varian VT stack at a flow rate of ~ 140 scfh with cooled bearing air (1 °C), which kept sample temperature at ~ 12 °C. The 2D $^{13}\text{C}/^{13}\text{C}$ correlation spectra were obtained using fpRFDR mixing of 1.6 ms with ^{13}C π - pulse widths of 13 μ s. Approximate amount of the A β fibril sample (excluding water) was ~ 0.6 mg. The $\pi/2$ -pulse for proton excitation was 2.5 μ s. During the 1 ms CP period, the ^{13}C rf field was swept from 48-76 kHz, while the ^1H rf field was kept at 102 kHz. The signal was collected during an acquisition period of 10 ms with low-power TPPM (lpTPPM) ^1H decoupling while the rf field intensity ($\omega_1/2\pi$) at 7 kHz was applied with phase alternation between $\pm 17^\circ$. A total of 126 complex t_1 points were recorded with a t_1 increment 48 μ s. For each t_1 point, 728 scans of signals were accumulated. For the uniformly ^{13}C - and ^{15}N -labeled A β fibril sample without Cu^{2+} , total experimental time was 72 h with recycle delays of 1.4 s. For the sample with 0.4 mol. eq. of Cu^{2+} , the experiment was collected using PACC method¹³⁹ with a total experimental time of 8 h and recycle delays of 150 ms. The details of the pulse program and lpTPPM are described elsewhere.^{139, 183} The obtained NMR data were processed by NMR pipe software. Lorentz to Gaussian window functions with inverse exponential width of 30 Hz and Gaussian broadening of 80 Hz were applied for both t_1 and t_2 time domains.

4) Determination of Cu²⁺ binding to A β (1-40) fibrils using UV-VIS spectroscopy

The A β (1-40) fibrils were mixed with CuCl₂ and Cu-glycinate (CuGly) in the molar ratio of Cu²⁺ to A β monomers in fibrils (i.e. [Cu²⁺]/[A β (1-40)]) of 0.5, 1.0, 2.0. Concentrated solutions of CuCl₂, CuGly at 50 mM were prepared, and 2, 4 or 8 μ L of the solution was added to 500 μ M A β (1-40) fibril solution (concentration in monomer equivalence) of 400 μ L to obtain the required mole ratio of Cu²⁺ to A β (1-40). The solution was vortexed briefly and incubated at 4°C for 24 h. The concentration of Cu²⁺ bound to the A β (1-40) was indirectly determined by the concentration of unbound Cu²⁺ with TETD, which is a photometric indicator of Cu²⁺.^{120, 164} The Cu²⁺ incubated A β (1-40) fibril solution of 0.4 mL was centrifuged in a 1.5 mL centrifuge tube at 16.1×10^3 g for 30 min with Eppendorf 5414D (Hamburg, Germany). The supernatant of 150 μ L was collected from the top of the solution, and mixed with 50 μ L of 2M HCl and allowed to stand for 10 min after brief vortexing. TETD indicator was prepared by mixing 0.04 % TETD solution in acetone and water in the ratio of 4:1. The TETD indicator solution of 25 μ L was added to the acidic peptide supernatant solution. After 15 minutes for the color change, the absorbance at 420 nm of the solution was monitored with a Varian Cary 300 UV-Vis spectrometer (Palo Alto, CA). The unbound Cu²⁺ concentration in the solution was determined by comparison with a calibration curve obtained with a standard CuCl₂ sample.

Figure 7 in Results and Discussion shows the percentage of Cu²⁺ that was not bound to A β (1-40) fibrils for a varied molar ratio of Cu²⁺ to A β ($f_{\text{Cu/A}\beta}$). As indicated above, a solution containing A β (1-40) fibrils (500 μ M at monomer equivalent unit) was mixed with CuCl₂ or CuGly, and the solution was incubated overnight. Then, the concentration of unbound Cu²⁺ was measured for a supernatant after centrifuging the solution. Figure 7 shows that for both CuGly and CuCl₂, less than 5% of Cu²⁺ was unbound to A β (1-40) when $f_{\text{Cu/A}\beta} = 0.5$ (i.e. added Cu²⁺

concentration was 250 μM). However, at $f_{\text{Cu}/\text{A}\beta} = 1.0$, $5.3 \pm 0.1\%$ and $15.2 \pm 1.0\%$ of Cu^{2+} was not bound to A β fibrils for CuCl_2 and CuGly , respectively. Thus, the binding of Cu^{2+} to A β is weaker in the presence of competing glycinate ligand. The concentration of unbound Cu^{2+} was not negligible even for CuCl_2 . The unbound Cu^{2+} ions was increased to $31.1 \pm 1.4\%$ and $9.7 \pm 1.0\%$ at $f_{\text{Cu}/\text{A}\beta} = 2.0$ for CuGly and CuCl_2 , respectively. Based on the results, we selected $f_{\text{Cu}/\text{A}\beta} = 0.4$ as the condition for SSNMR experiments where nearly all Cu^{2+} ions are strongly bound to A β fibrils.

5) Analysis of ^1H T_1 values for Cu^{2+} -bound A β (1-40) fibrils

To examine the possibility of Cu^{2+} binding from NMR parameters, we analyzed ^1H T_1 of the hydrated A β fibril. The ^1H T_1 values of the A β fibril sample was reduced from 401 (± 24) ms down to 77 (± 6) ms after Cu^{2+} binding. Although we reported that doping Cu-EDTA with A β (1-40) fibril significantly reduced ^1H T_1 , selective signal quenching on particular ^{13}C sites was not observed. Moreover, comparable ^1H T_1 value (77 ± 1 ms) was obtained with Cu-EDTA at 200 mM, which is 9 fold higher than the effective Cu^{2+} concentration used here (~ 22 mM). This evidence confirms that unlike Cu-EDTA, Cu^{2+} is likely bound site-specifically to A β in the fibril.

6) Chemical shift analysis of Cu^{2+} -bound and Cu^{2+} -unbound A β (1-40) fibrils

In order to examine the possible structural changes of A β (1-40) in amyloid fibrils upon Cu^{2+} binding, we compared ^{13}C chemical shifts of the A β fibril samples with and without Cu^{2+} . These chemical shifts were measured from 2D $^{13}\text{C}/^{13}\text{C}$ correlation fpRFDR spectra, which were collected in similar conditions to those in Figure 9 with experimental times of 14-57 hours. Interestingly, most of the sites show little chemical shift changes (≤ 0.3 ppm in absolute value) upon Cu^{2+} binding (see Table I). Although Leu-17, Phe-19, and Gly-33, in particular side chains of Leu-17, show notable shifts (0.3-0.7 ppm; highlighted by underline), little structural changes

upon Cu^{2+} binding were suggested from the ^{13}C shift data for other residues in the hydrophobic cores, including Val-18, Phe-20, Ala-21, Val-24, Gly25, Ile-31, 32, Leu-34, Met-35, Val-36. This suggests that parallel β -sheet structure in the $\text{A}\beta(1-40)$ fibrils should be largely retained for these sites after Cu^{2+} binding. The β -sheet core in the $\text{A}\beta(1-40)$ fibrils was confirmed by TALOS dihedral angles predicted using ^{13}C chemical shift information. The data show noticeable but limited shifts (0.3-1.7 ppm) upon Cu^{2+} binding mostly in the N-terminal region (Val-12, His-13, His-14) and the C-terminal region (Gly-37, Gly-38, Val-39), for which Cu^{2+} binding is suggested from our signal quenching data.

TABLE I. ^{13}C CHEMICAL SHIFTS FOR THE A β (1-40) FIBRILS IN THE PRESENCE AND ABSENCE OF Cu^{2+} . THE SHIFTS WERE REFERENCED WITH TMS.

Residues and sites	Chemical shift with Cu^{2+} (ppm) ^{a)}	Chemical Shift without Cu^{2+} (ppm) ^{a)}	Difference (ppm in absolute value) ^{a)}	Dihedral angles from TALOS for Cu^{2+} free sample
Phe-4				-132\pm20, 146\pm13^{c)}
C α	N/A ^{b)}	55.58 (\pm 0.04)	-	
C β	N/A ^{b)}	40.73 (\pm 0.20)	-	
C δ	129.50 (\pm 0.16)	129.53 (\pm 0.03)	0.03 (\pm 0.17)	
Val-12				-118\pm13, 131\pm10
C=O	172.82 (\pm 0.04)	172.58 (\pm 0.07)	0.24 (\pm 0.08)	
C α	58.66 (\pm 0.09)	58.68 (\pm 0.07)	0.02 (\pm 0.11)	
C β	33.19 (\pm 0.10)	32.76 (\pm 0.18)	<u>0.43 (\pm0.21)</u>	
C γ	19.37 (\pm 0.01)	19.40 (\pm 0.00)	0.03 (\pm 0.01)	
His-13				-99\pm12, 143\pm36^{c)}
C α	52.18 (\pm 0.01)	52.11 (\pm 0.20)	0.07 (\pm 0.20)	
C β	29.71 (\pm 0.26)	30.10 (\pm 0.38)	<u>0.40 (\pm0.46)</u>	
C γ	128.80 (\pm 0.05)	29.16 (\pm 0.16)	<u>0.36 (\pm0.17)</u>	
C δ	116.68 (\pm 0.05)	16.68 (\pm 0.09)	0.00 (\pm 0.10)	
C ϵ	135.32 (\pm 0.06)	35.66 (\pm 0.10)	<u>0.34 (\pm0.12)</u>	
His-14				-57\pm7, -43\pm6
C α	b)	58.79 (\pm 0.14)	-	
C β	b)	22.29 (\pm 0.04)	-	
C γ	128.14 (\pm 0.14)	128.90 (\pm 0.05)	<u>0.76 (\pm0.14)</u>	
C δ	117.22 (\pm 0.07)	118.95 (\pm 0.09)	<u>1.72 (\pm0.12)</u>	
C ϵ	133.63 (\pm 0.21)	133.83 (\pm 0.11)	<u>0.20 (\pm0.24)</u>	

TABLE I. ^{13}C CHEMICAL SHIFTS FOR THE A β (1-40) FIBRILS IN THE PRESENCE AND ABSENCE OF Cu^{2+} . THE SHIFTS WERE REFERENCED WITH TMS.

Residues and sites	Chemical shift with Cu^{2+} (ppm) ^{a)}	Chemical Shift without Cu^{2+} (ppm) ^{a)}	Difference (ppm in absolute value) ^{a)}	Dihedral angles from TALOS for Cu^{2+} free sample
Leu-17				-139\pm10, 134\pm12
C=O	172.81 (\pm 0.04)	172.92 (\pm 0.03)	0.10 (\pm 0.05)	
C α	52.52 (\pm 0.08)	52.80 (\pm 0.04)	0.27 (\pm 0.09)	
C β	44.66 (\pm 0.05)	44.06 (\pm 0.08)	<u>0.60 (\pm0.09)</u>	
C γ	26.97 (\pm 0.17)	27.20(\pm 0.03)	0.22 (\pm 0.17)	
C δ 1	24.86 (\pm 0.01)	25.36(\pm 0.02)	<u>0.50 (\pm0.02)</u>	
C δ 2	23.10 (\pm 0.02)	2.47(\pm 0.01)	<u>0.63 (\pm0.03)</u>	
Val-18				-129\pm8, 136\pm13
C α	58.87 (\pm 0.10)	58.75 (\pm 0.06)	0.12 (\pm 0.11)	
C β	32.98 (\pm 0.03)	33.05 (\pm 0.03)	0.08 (\pm 0.04)	
C γ	19.02 (\pm 0.09)	19.06 (\pm 0.09)	0.03 (\pm 0.13)	
Phe-19				-121\pm12, 149\pm11
C=O	172.53 (\pm 0.17)	172.88	<u>0.36</u>	
C α	52.38 (\pm 0.01)	52.60	0.22	
C β	42.67 (\pm 0.07)	42.33	<u>0.34</u>	
C δ	128.76 (\pm 0.05)	128.34	<u>0.42</u>	
Phe-20				-133\pm14, 137\pm14
C=O	170.88 (\pm 0.05)	171.06 (\pm 0.07)	<u>0.18 (\pm0.09)</u>	
C α	54.52 (\pm 0.03)	54.55 (\pm 0.01)	<u>0.03 (\pm0.03)</u>	
C β	41.80 (\pm 0.16)	41.77 (\pm 0.20)	<u>0.03 (\pm0.26)</u>	
C δ	129.48 (\pm 0.02)	129.56 (\pm 0.01)	<u>0.08 (\pm0.02)</u>	

TABLE I. ^{13}C CHEMICAL SHIFTS FOR THE A β (1-40) FIBRILS IN THE PRESENCE AND ABSENCE OF Cu^{2+} . THE SHIFTS WERE REFERENCED WITH TMS.

Residues and sites	Chemical shift with Cu^{2+} (ppm) ^{a)}	Chemical Shift without Cu^{2+} (ppm) ^{a)}	Difference (ppm in absolute value) ^{a)}	Dihedral angles from TALOS for Cu^{2+} free sample
Ala-21				-136\pm16, 143\pm14
C=O	173.22 (\pm 0.05)	173.42 (\pm 0.02)	0.20 (\pm 0.06)	
C α	47.76 (\pm 0.13)	47.91 (\pm 0.03)	0.15 (\pm 0.14)	
C β	21.62 (\pm 0.01)	21.66 (\pm 0.01)	0.04 (\pm 0.01)	
Val-24				-126\pm14, 150\pm9
C=O	174.36 (\pm 0.02)	174.28	0.08 (\pm 0.02)	
C α	57.01 (\pm 0.02)	56.96	0.04 (\pm 0.02)	
C β	33.81 (\pm 0.05)	33.74	0.07 (\pm 0.05)	
C γ	19.53 (\pm 0.01)	19.50	0.03 (\pm 0.01)	
Gly-25				-107\pm22, 165\pm19^{c)}
C α	40.46 (\pm 0.05)	40.42	0.04	
Ala-30				-132\pm16, 156\pm9
C=O	172.17 (\pm 0.02)	172.14	0.03	
C α	47.93 (\pm 0.01)	47.95	0.02	
C β	20.98 (\pm 0.01)	21.20	0.21	
Ile-31				-120\pm18, 127\pm9
C α	59.32 (\pm 0.01)	59.34 (\pm 0.01)	0.02 (\pm 0.01)	
C β	38.22 (\pm 0.00)	38.21 (\pm 0.07)	0.01 (\pm 0.07)	
C γ 1	26.12 (\pm 0.01)	26.24 (\pm 0.02)	0.01 (\pm 0.05)	
C γ 2	17.34 (\pm 0.02)	17.38 (\pm 0.00)	0.04 (\pm 0.02)	
C δ	11.85 (\pm 0.00)	11.87 (\pm 0.01)	0.03 (\pm 0.01)	

TABLE I. ^{13}C CHEMICAL SHIFTS FOR THE A β (1-40) FIBRILS IN THE PRESENCE AND ABSENCE OF Cu^{2+} . THE SHIFTS WERE REFERENCED WITH TMS.

Residues and sites	Chemical shift with Cu^{2+} (ppm) ^{a)}	Chemical Shift without Cu^{2+} (ppm) ^{a)}	Difference (ppm in absolute value) ^{a)}	Dihedral angles from TALOS for Cu^{2+} free sample
Ile-32				-130\pm13, 148\pm15
C α	56.14 (\pm 0.06)	55.91 (\pm 0.10)	0.23 (\pm 0.11)	
C β	40.44 (\pm 0.07)	40.41 (\pm 0.03)	0.04 (\pm 0.08)	
C γ 1	25.10 (\pm 0.01)	25.20 (\pm 0.03)	0.10 (\pm 0.04)	
C γ 2	16.45 (\pm 0.06)	16.42 (\pm 0.04)	0.02 (\pm 0.07)	
C δ	12.47 (\pm 0.01)	12.57 (\pm 0.05)	0.11 (\pm 0.05)	
Gly-33				-149\pm33, 160\pm40^{e)}
C=O	168.96 (\pm 0.02)	169.31 (\pm 0.07)	<u>0.35 (\pm0.07)</u>	
C α	42.96 (\pm 0.03)	43.15 (\pm 0.16)	<u>0.19 (\pm0.16)</u>	
Leu-34				-125\pm25, 138\pm14
C α	52.33 (\pm 0.05)	52.29	0.04 (\pm 0.05)	
C β	44.46 (\pm 0.05)	44.47	0.01 (\pm 0.09)	
C γ	27.01 (\pm 0.18)	27.06	0.05 (\pm 0.18)	
C δ 1	24.45 (\pm 0.01)	24.43	0.02 (\pm 0.01)	
C δ 2	22.40 (\pm 0.00)	22.37	0.03 (\pm 0.00)	
Met-35				N/A
C ϵ	15.60 (\pm 0.01)	15.64 (\pm 0.00)	0.04 (\pm 0.01)	
Val-36				-122\pm9, 134\pm24^{e)}
C=O	173.09 (\pm 0.07)	172.89 (\pm 0.07)	0.20 (\pm 0.10)	
C α	58.73 (\pm 0.08)	58.81 (\pm 0.07)	0.09 (\pm 0.11)	
C β	31.57 (\pm 0.04)	31.56 (\pm 0.01)	0.01 (\pm 0.04)	
C γ	18.98 (\pm 0.0)	18.92 (\pm 0.03)	0.12 (\pm 0.04)	

TABLE I. ^{13}C CHEMICAL SHIFTS FOR THE A β (1-40) FIBRILS IN THE PRESENCE AND ABSENCE OF Cu^{2+} . THE SHIFTS WERE REFERENCED WITH TMS.

Residues and sites	Chemical shift with Cu^{2+} (ppm) ^{a)}	Chemical Shift without Cu^{2+} (ppm) ^{a)}	Difference (ppm in absolute value) ^{a)}	Dihedral angles from TALOS for Cu^{2+} free sample
Gly-37				Not predicted^{c)}
C α	42.66 (± 0.07)	43.22 (± 0.05)	<u>0.56 (± 0.09)</u>	
Gly-38				Not predicted^{c)}
C=O	170.33 (± 0.11)	170.53 (± 0.15)	<u>0.20 (± 0.19)</u>	
C α	42.55 (± 0.10)	43.13 (± 0.09)	<u>0.58 (± 0.14)</u>	
Val-39				-130\pm24, 143\pm16^{c)}
C=O	172.08 (± 0.14)	172.31 (± 0.07)	0.24 (± 0.16)	
C α	59.49 (± 0.03)	59.80 (± 0.10)	<u>0.32 (± 0.10)</u>	
C β	33.39 (± 0.15)	33.29 (± 0.23)	0.10 (± 0.28)	
C γ	19.39 (± 0.02)	19.36 (± 0.00)	0.03 (± 0.02)	

^{a)} The numbers in parentheses denote errors in the measurements. The errors in the shifts were the standard deviation of the chemical shifts from three data sets. The ranges of the error were found to be within 0.15 ppm. For some of the residues, for which the errors are not reported above, the measurements were made only one time. The estimated errors are in a range of ± 0.2 ppm and ± 0.3 ppm for the Cu^{2+} -free and Cu^{2+} -bound samples respectively, based on the above reported standard deviations.

^{b)} The signals were broadened and the chemical shifts are not reported.

^{c)} TALOS predictions for these residues reported 9 or less best matches from the TALOS database; the predictions that report 8 or less best matches are denoted as “Not predicted”.

IV) NMR BASED CHARACTERIZATION OF STRUCTURES, REDOX REACTIONS, AND REACTIVE OXYGEN SPECIES (ROS) PRODUCTION MECHANISM IN Cu-ION BOUND 40-RESIDUE ALZHEIMER'S β AMYLOID FIBRILS

A) Introduction

Progressive accumulation of amyloid plaques in the brain is a major pathogenic event that characterizes the AD,^{184, 185} which is a multi-symptom neural disorder. The primary components of the plaque deposits are amyloid fibrils of 40- and 42-residue A β peptides.¹¹⁵ As misfolded A β has been shown to exhibit cytotoxicity to neuronal cells *in-vitro*, it has been proposed that misfolding of A β triggers the onset of AD.^{55, 115, 186-188} The AD plaques are reported to contain high concentrations of redox-active metals such as Cu²⁺ (~400 μ M) and Fe³⁺ (~950 μ M),⁶³ and A β has been shown to bind these metals with high affinity.^{63, 65} Accumulation of the redox-active metal ions by these aggregates has been proposed to promote the formation of reactive oxygen species (ROS), which may lead to oxidative damages, a common disruption observed in AD brains.^{122, 189-192} Indeed, previous *in-vitro* experiments indicate that Cu²⁺ ions in sub-micromolar concentration along with A β peptide are sufficient for the generation of ROS.^{82, 83, 89, 117, 193, 194} Recent studies demonstrated the redox activity in AD lesions, which was inhibited by prior exposure of the tissue sections to copper and iron chelators.¹⁹⁵⁻¹⁹⁷ Thus, intensive efforts have been made to understand the molecular level structural details and redox reactions of Cu²⁺ bound A β ,^{66-68, 73-75, 78, 104, 123, 124, 198} which can be a potential therapeutic target.

Oxidative stress caused by ROS is believed to be one of the key events in the pathogenesis of AD.^{194, 199, 200} Several reaction mechanisms have been proposed for the ROS generation by Cu-A β , but the exact mechanism is experimentally unknown.⁸⁹ A compelling hypothesis from recent studies by mass spectroscopy and other techniques is that the Cu²⁺ ion

complexed to A β fibrils can be reduced to Cu⁺ by biological reducing agents such as ascorbic acid, cholesterol, or dopamine⁸² and that Cu⁺ may play a vital role for the production of ROS with subsequent oxidation of His or Tyr residue in A β .^{70, 89, 117, 122, 201-203} It was recently proposed that during the production of ROS, redox-active Cu²⁺ ions bound to A β aggregates undergo a redox cycle (i.e., Cu²⁺ ↔ Cu⁺) in the presence of O₂ and biological reductant ascorbate, which is present in brain between 0.2-10 mM.⁸³ Alternatively, it was also suspected that the oxidizable sulfur group on the sidechain of Met-35 in A β aggregates may participate in the electron transfer redox reaction with Cu²⁺ to produce ROS such as H₂O₂, which in turn has been proposed to oxidize the sidechain sulfur group to sulfoxide.^{62, 70, 202, 204} Indeed, it was shown that A β isolated from plaques contains oxidized Met-35.^{62, 205} However, the redox reaction mechanism and associated structural changes involving Cu-bound A β aggregates in the production of ROS are not well understood due to the lack of structural studies correlating the Cu-A β complex to the generation of ROS.

Although a variety of structural studies of aggregated A β by NMR, EPR, X-ray diffraction and other methods have been performed, including those for Cu²⁺-bound A β ,^{20, 68, 74, 75, 104, 133, 206-218} only a few studies focus on the functional aspects of Cu²⁺-bound A β aggregates and the mechanism involved in the ROS production.^{216, 217} It is also imperative to reveal the interaction between less stable Cu⁺ ions and A β in order to understand a detailed redox mechanism of Cu-ion bound A β in the generation of ROS. Thus, in spite of the significance of the problem, only a limited number of such studies have been reported because of the challenges in capturing the transient Cu⁺ species with heterogenous amyloid aggregates for analysis. A recent extended X-ray absorption fine structure spectroscopy (EXAFS) study showed that the N-terminal A β fragments A β (6-14) binds Cu⁺ through two adjacent His residues 13 and 14.²¹⁸

Additional studies by EPR,²¹⁷ molecular dynamics simulation,²¹⁹ and *ab initio* modeling²²⁰ proposed a linear, *bis* coordination of Cu^+ to N δ of the two His-13 and His-14 on the A β peptide.^{221, 222} However, these previous studies have focused mainly on soluble A β monomers or their fragments of A β , rather than physiologically relevant aggregated A β (1-40) or A β (1-42),^{78, 83, 89, 216-218, 223} despite implications of the interactions of the metal ions with A β fibrils in the AD plaques.⁶³ This is largely due to technical difficulties in the analysis of insoluble and non-crystalline A β fibrils with less stable Cu^+ . As a result, direct structural evidence is lacking on the redox reactions and the Cu^+ interaction for Cu-bound A β fibrils.

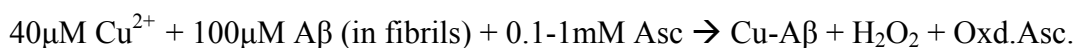
In this study, we present an *in-vitro* study on the structures and functions for Cu-bound A β fibrils in the redox reaction that is responsible for the ROS generation. We show that the A β (1-40) fibril-bound Cu^{2+} produces a major ROS, H_2O_2 , under aerobic conditions with ascorbate. Redox conversions between Cu^{2+} to Cu^+ are clearly demonstrated by SSNMR. SSNMR results also suggest that Cu^+ remains complexed to A β fibrils and that the overall conformations of the A β fibrils is not altered by Cu^+ -binding or the redox reaction. Our results demonstrate the first site-specific structural evidence of Cu^+ binding to A β (1-40) fibrils and its involvement in the redox cycle.

B) Results

1) ROS production by Cu-A β

The production of ROS, such as H_2O_2 , by the redox chemistry of Cu^{2+} -A β complexes was observed when one or more physiological reducing agents is available.^{82, 117} However, only a limited number of previous studies report the interaction between Cu^{2+} and A β fibrils, and their roles in ROS production in the reports are somewhat contradictory.^{83, 89} Thus, we first tested the

redox capability of the Cu^{2+} -A β (1–40) fibril complex in generating H_2O_2 in the presence of a reducing agent ascorbate. The reaction studied is summarized below,



In Figure 23, we monitored the H_2O_2 concentration by incubating Cu^{2+} -bound A β (1–40) fibril sample (100 μM A β and 40 μM Cu^{2+} ions) in the (green bars) presence and (red bars) absence of 1mM ascorbate by photometric assay as described in the materials and method. The data clearly demonstrated the production of $\sim 60 \mu\text{M}$ H_2O_2 within 2 h in the presence of ascorbate. In contrast, in the absence of ascorbate, no detectable H_2O_2 was produced. We previously confirmed 0.4 mol. eq. of Cu^{2+} ions are strongly bound to A β (1–40) fibril.¹⁰⁴ Thus, there is no effect from the excess or unbound free Cu^{2+} in the production of H_2O_2 . The ascorbate concentration at 1 mM was chosen based on the estimated physiological ascorbate concentration of 0.2–10 mM in a brain.^{83, 84} The concentration of Cu^{2+} is one order of magnitude lower than the Cu ion concentration found in the AD plaques (0.4 mM).⁶³ Nevertheless, sub mM level H_2O_2 was generated within several hours by the Cu^{2+} -A β (1–40) fibrils and ascorbate. We also confirmed the generation of another destructive ROS, hydroxyl radicals (Figure 24). Although it is known that free Cu^{2+} ions generate H_2O_2 in the presence of ascorbate, the rate of H_2O_2 production from Cu^{2+} -A β (1–40) fibrils is twice, compared with that from the free Cu^{2+} (Figure 25). Under a physiological environment, high concentration of free Cu^{2+} ions is unlikely to be present. A β 's high affinity to Cu^{2+} is likely to allow the recruitment of trace amounts of free ions up to sub-mM concentrations.

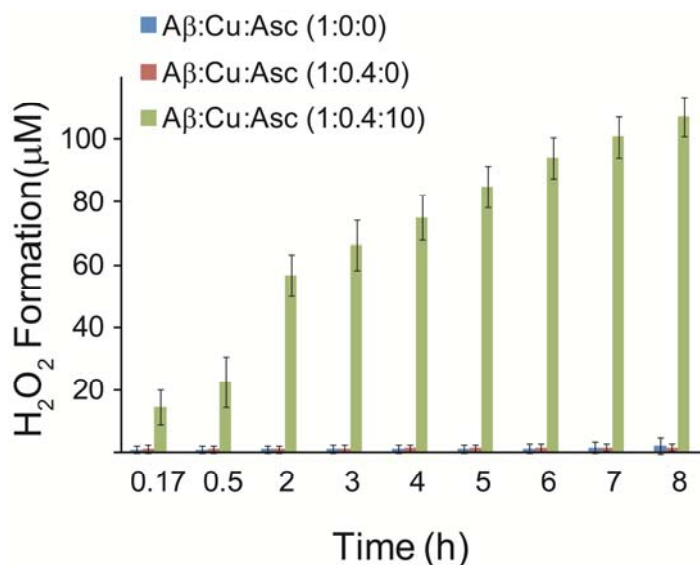


Figure 23. Time-dependent production of ROS H_2O_2 by $A\beta(1-40)$ fibrils alone (blue), with $40 \mu M Cu^{2+}$ (red), and in the presence of $1 mM$ ascorbate (green). The concentration of $A\beta$ fibrils is $100 \mu M$ (based on monomer concentration). With these concentrations of Cu^{2+} and ascorbate available, $A\beta(1-40)$ fibrils can efficiently catalyze the production of $60-70 \mu M H_2O_2$ within the first 4 hours of incubation (green). In the absence of reducing agent ascorbate, both $A\beta$ fibrils with and without Cu^{2+} only generated baseline amount of H_2O_2 (blue and red). The H_2O_2 assay was performed by colorimetric method in which the H_2O_2 generated reacts with horse radish peroxidase (HRP) in presence of OxiRed probe to produce a product with absorption at $570 nm$.

i. Hydroxyl radical detection by fluorescence

A major variant of ROS is OH^\cdot radicals, the free radicals are believed to be intermediates during the ROS production. Several mechanisms showing the involvement of OH^\cdot radicals in the oxidation of $A\beta$ peptides have been proposed earlier. Here in this study, we present the generation OH^\cdot and its interaction with the $A\beta$ peptides. Coumarin-3-carboxylic acid (3-CCA) assay was used to quantify OH^\cdot production. Upon reaction with hydroxyl radicals, the 3-CCA forms a fluorescent active compound, which has a characteristic emission at $450 nm$. The data in Figure 24 clearly shows that in the (a) absence of the $A\beta$ peptides, continuous production of free

radicals were observed but in the (b) presence of A β peptides only a constant amount of OH \cdot radicals were detected by 3-CCA assay indicating the participation of the free radical with A β peptides.

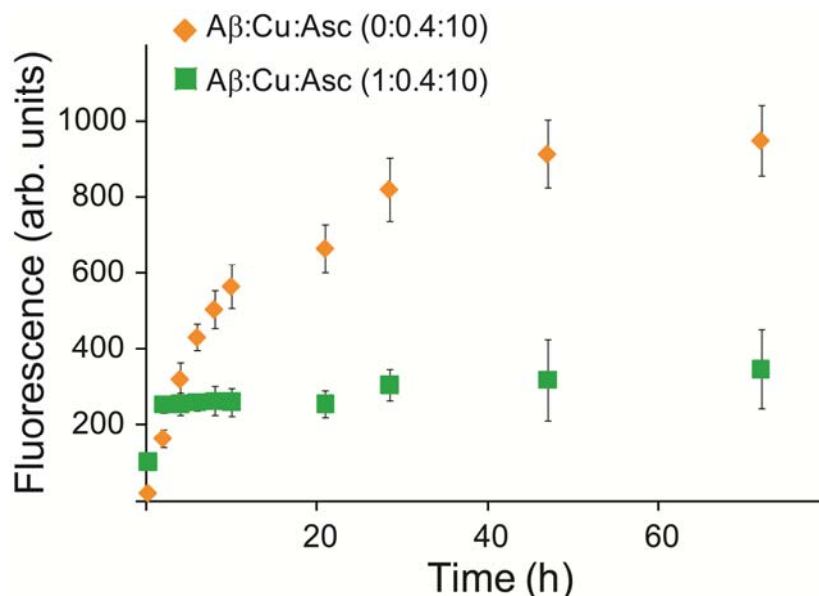


Figure 24. Time-dependent production of hydroxyl radical (OH \cdot) by 40 μ M Cu $^{2+}$ alone (orange) and 100 μ M Cu $^{2+}$ -A β (1-40) fibrils (green) in the presence of 1 mM ascorbate. The generated OH \cdot reacts with 3-CCA to form an adduct that shows fluorescent emission at 450 nm.

ii. Comparison of the ROS production between free Cu $^{2+}$ and Cu $^{2+}$ -A β (1-40) complex

The comparison of the H $_2$ O $_2$ generation by the free Cu $^{2+}$ (orange bars) and Cu $^{2+}$ -A β (1-40) (green bars) complex ions in the presence ascorbate in Figure 25 convincingly proves the participation of the A β (1-40) peptide in the ROS production. Ascorbate is a well known reducing as well oxidizing agent in presence of trace metal ions and is shown to oxidize Met side

chains.⁸⁵ Within the first 3-4 h of the treatment of ascorbate with A β (1-40) peptide produces nearly twice the H₂O₂.

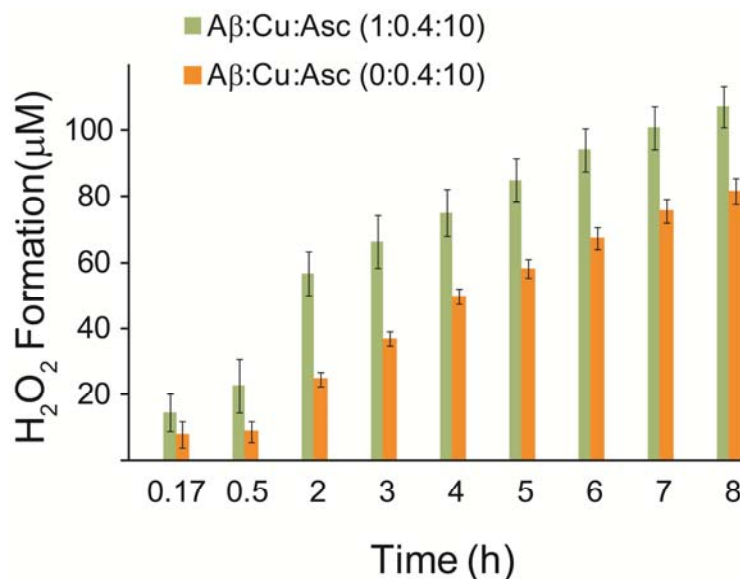


Figure 25. Time-dependent generation of H₂O₂ by 40 μ M Cu²⁺ (orange) and 100 μ M Cu²⁺-A β (1-40) fibrils (green) after the addition of 1 mM ascorbate. The molar ratio between A β fibrils, Cu, and ascorbate is 1:0.4:10, respectively. Cu²⁺ alone can only generate approximately half the amount of H₂O₂, highlighting the involvement of A β fibrils in the production of ROS.

2) In-situ NMR Detection of Redox Cycling for Cu-bound A β fibrils

Mechanistically, the existence of redox cycling between Cu²⁺ and Cu⁺ is a strong evidence for subsequent hydrogenation of molecular oxygen that results in the H₂O₂ generation.^{82, 83, 86, 117, 224} Hence, we next examined the possibility of detecting the redox state of Cu ions after the addition of ascorbate by SSNMR. In general, it is difficult to examine the redox state of a metal ion when the ion is bound to an insoluble protein such as amyloid fibril. SSNMR is one of very few methodologies that provide an access to detailed molecular structures of amyloid fibrils.²²⁵ In addition, NMR relaxation parameters are very sensitive probes of paramagnetic ions

such as Cu^{2+} .²²⁶ By utilizing paramagnetic T_1 and T_2 relaxation enhancements by Cu^{2+} in ^1H and ^{13}C SSNMR, we recently reported that $\text{A}\beta(1-40)$ fibrils bind Cu^{2+} *via* amino acid residues His-13, His-14, Val-40 CO_2^- terminus, and Glu-3/11 CO_2^- side chains.¹⁰⁴ On the other hand, the diamagnetic Cu^+ ions yield no paramagnetic relaxation enhancements. Thus, the redox reaction from Cu^{2+} to Cu^+ can be monitored by examining NMR relaxation parameters. Figure 26 shows incubation-time (t) dependence of ^1H longitudinal relaxation time (T_1) for Cu^{2+} -bound $\text{A}\beta(1-40)$ fibril after the addition of ascorbate in a time span of (a) 6 h and (b) 100 h. The ^1H T_1 relaxation time was monitored by an inversion recovery pulse sequence on ^1H spins followed by a cross-polarization (CP) transfer to detect ^{13}C signals under MAS conditions.²²⁷ The $\text{A}\beta(1-40)$ fibril sample used in the measurements was uniformly ^{13}C - and ^{15}N -labeled at His-14, Ile-32, Val-36, and Gly-37 and was incubated with 0.4 mol. eq. of Cu^{2+} . The initial ^1H T_1 value of hydrated Cu^{2+} - $\text{A}\beta(1-40)$ fibrils without ascorbate was 96 ± 3 ms. When one mol. eq. of ascorbate with respect to $\text{A}\beta$ was added to Cu^{2+} - $\text{A}\beta(1-40)$ fibrils, the ^1H T_1 value showed approximately 6-fold increase to 576 ± 13 ms after the incubation time (t) of 1.5 h (Figure 26 a). The T_1 value at $t = 1.5$ h is comparable to that of Cu^{2+} -free $\text{A}\beta$ fibril. Thus, the data indicate that paramagnetic Cu^{2+} bound to amyloid fibril was completely reduced to diamagnetic Cu^+ by ascorbate. Interestingly, after 70 h, the T_1 value gradually decreased to 60% of the highest value (Figure 26 b). It is likely that Cu^+ was oxidized back to more redox stable Cu^{2+} , when the concentration of ascorbate became gradually decreased. However, we found difficulties in quantitatively reproducing the re-oxidization; the incubation time required for the ^1H T_1 decrease varied considerably in each trial.

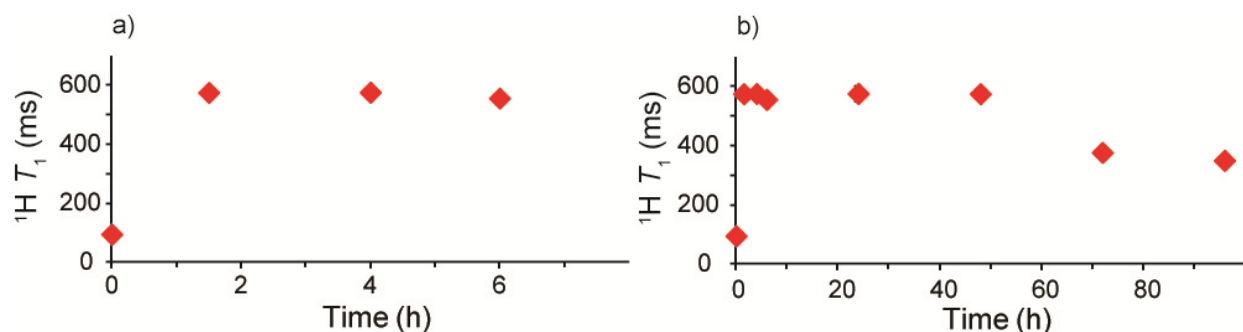


Figure 26. (a) ^1H T_1 of the Cu^{2+} -A β (1-40) in presence of 1 mol. eq. of ascorbate for 8 h. (b) ^1H T_1 of the Cu^{2+} -A β (1-40) in presence of 1 mol. eq. of ascorbate for 100 h. An overall paramagnetic relaxation effect was determined by averaging the observed ^1H T_1 values for several ^{13}C CPMAS signals over the spectral region.

After realizing the possibility that this re-oxidation reaction of Cu^+ may require oxygen from air, we performed a modified experiment shown in Figure 27 with A β (1-40) ^{13}C - and ^{15}N labeled at Val-18, Phe-19, Gly-29, Ile-31. First, to speed up the redox reaction, we used 5 mol. eq. of ascorbate to A β ; the observed ^1H T_1 rapidly increased from 83 ± 3 ms to 577 ± 29 ms in 2 h. Second, in the modified experiment, after observing that the ^1H T_1 reflected the complete conversion of Cu^{2+} to Cu^+ , we made oxygen accessible to the sample by halting the ^1H T_1 measurement, and exposing to air by opening the cap of the MAS rotor. Then, after overnight incubation at 24°C (orange arrows), we resumed the ^1H T_1 measurements. We repeated this process three successive times. As indicated by the orange arrows, the ^1H T_1 dropped considerably to 364 ± 23 ms during the first incubation with oxygen, suggesting that Cu^+ was reoxidized to Cu^{2+} in the presence of oxygen. At this point, the excess ascorbate was still likely to prevent the complete oxidization of Cu^+ ions. Nevertheless, the ^1H T_1 value was reduced much faster than that for Figure 26 without the exposure to air. Subsequent cycles of ^1H T_1 monitoring and exposure to air confirmed the rapid redox recycling between Cu^{2+} and Cu^+ in

association with the amyloid fibrils. As ^1H T_1 of the amyloid fibril is only affected when Cu^{2+} is bound to $\text{A}\beta$, the data clearly suggest that Cu^{2+} is bound to $\text{A}\beta$ throughout the redox cycle.

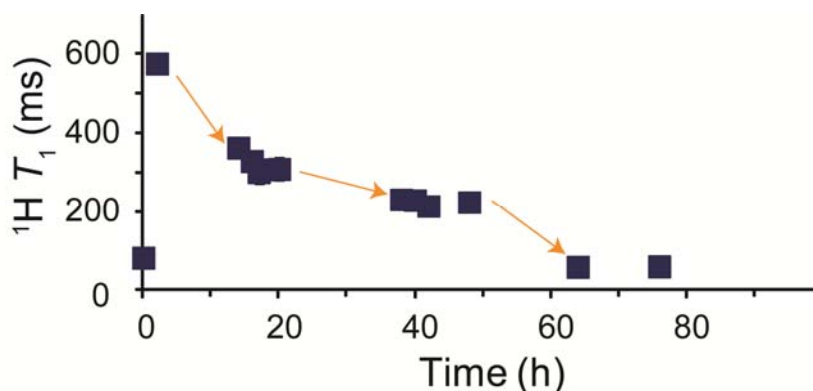


Figure 27. ^1H T_1 of the Cu^{2+} - $\text{A}\beta(1-40)$ in presence of 5 mol. eq. of ascorbate. Orange arrows show the period during the rotor was exposed to the air.

In the above experiment with 5 mol. eq. of ascorbate, we used a considerably higher concentration of ascorbate (~ 487 mM) as a pellet of hydrated amyloid aggregate was used as a sample for the SSNMR analysis. The experiment confirmed the spontaneous reoxidization of Cu^+ to Cu^{2+} even at the high ascorbate concentration. To confirm the reduction from Cu^{2+} to Cu^+ at a physiological ascorbate concentration, we performed a complementary photometric assay with a lower ascorbate concentration (1 mM) for a solution containing suspended Cu^{2+} - $\text{A}\beta$ fibril complex ($f_{\text{Cu}/\text{A}\beta} = 0.4$) at a molar concentration of $\text{A}\beta$ at 100 μM (in monomer equivalence). After 15 min of the incubation of Cu^{2+} - $\text{A}\beta$ with ascorbate, nearly complete reduction of Cu^{2+} to Cu^+ (~ 98 %) was confirmed by BCS, a Cu^+ selective indicator (Figure 28). We also indirectly confirmed that $\sim 97\%$ of Cu^+ was bound to $\text{A}\beta$ fibril by monitoring Cu^+ concentration for the

supernatant after removing the A β fibril from the solution by centrifugation. Although previous studies implied Cu⁺ association with A β , these studies used either fragments of A β or A β in monomeric forms rather than A β aggregates.^{217, 218, 223, 228} To the best of our knowledge, our SSNMR and photometric results demonstrated a continuous redox cycling between Cu²⁺-bound A β fibril and Cu⁺-bound A β fibril for the full-length A β in the presence of ascorbate and oxygen for the first time.

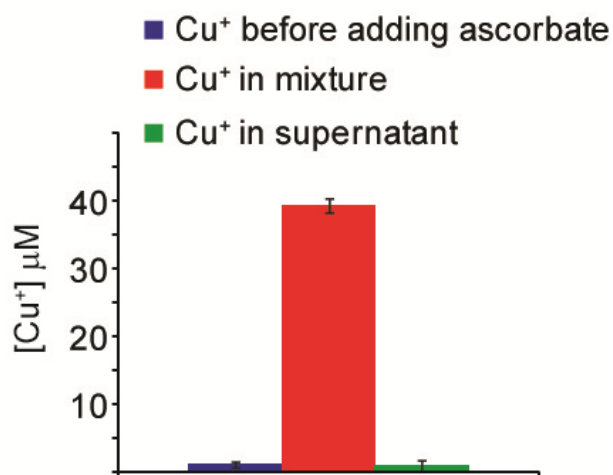


Figure 28. Quantification of Cu⁺-A β (1–40) fibrils resulting from reduction of Cu²⁺ by ascorbate. The concentrations of A β fibrils, Cu²⁺, and ascorbate are 100 μ M, 40 μ M, and 1 mM respectively. The reduced Cu⁺ species was detected by BCS, a Cu⁺-specific indicator that shows a new absorption at 483 nm upon binding. The Cu²⁺-A β fibril sample incubated with ascorbate shows a near complete conversion of Cu²⁺ to Cu⁺ (red) based on UV-vis quantification. Both Cu²⁺-A β (1–40) fibrils (blue) and the supernatant of ascorbate treated Cu²⁺-A β (1–40) fibrils (after A β fibrils have been removed by centrifugation, green) only showed baseline absorbance values or amounts of Cu⁺.

3) Redox reaction and structural information of Cu⁺ binding to A β (1-40) fibrils probed by ¹³C SSNMR

Next, we attempted ¹³C SSNMR experiments in order to reveal molecular-level structural details and dynamics of Cu²⁺-A β (1-40) fibrils during the redox cycling. Figure 29(a, b) shows ¹³C CPMAS spectra of (a) Cu-free and (b) Cu²⁺-bound A β (1-40) in fibrils that were labeled with uniform ¹³C- and ¹⁵N-labeled amino acids at Val-12, Ala-21, Gly-33, and with selectively ¹³C-labeled Met-35 (at ϵ CH₃ position). Compared with the spectrum for the metal-free sample in (a), Figure 29 b showed selective loss in signal intensities of ¹³C α , ¹³C β , and ¹³C γ of Val-12 (blue arrows), while the chemical shifts or signal intensities of Ala-21 and Gly-33 were unaffected. The corresponding ¹H *T*₁ value of Cu²⁺-bound A β (1-40) fibrils were 55 ± 3 ms, which was much shorter than that of A β (1-40) fibrils without Cu²⁺ (370 ± 18 ms). The selective quenching of Val-12 signals (Figure 29 b) and ¹H *T*₁ reduction are consistent with Cu²⁺ binding at the sidechains of His-13, His-14 and other residues of A β in fibrils.¹⁰⁴ Then, we incubated the Cu²⁺-A β fibrils with one mol. eq. of ascorbate with respect to A β at room temperature. After *t* = 1.5 h, we collected a ¹³C CPMAS spectrum for this sample (Figure 29 c). Clearly, ¹³C signals for Val-12 were recovered to the original intensities (~95%) for A β (1-40) fibrils without Cu²⁺ (Figure 29 c, red arrows). We attribute this to the reduction of paramagnetic Cu²⁺ bound to A β to diamagnetic Cu⁺. The ¹H *T*₁ value at 1.5 h after the incubation with ascorbate (351 ± 14 ms) is also consistent with the reduction of Cu²⁺ to Cu⁺. Based on the assumption that paramagnetic relaxation enhancement in ¹H *T*₁ is proportional to Cu²⁺ concentration, approximately 95% of Cu²⁺ was converted to Cu⁺ after incubation with ascorbate. Although it is possible to explain the observation by the removal of Cu²⁺ from A β due to the addition of ascorbate, our ¹³C SSNMR data suggest that this is not the case, as will be discussed below. Thus, it is most likely that Cu ions are subject to redox cycling between Cu²⁺ and Cu⁺ while being coordinated to the A β fibril.

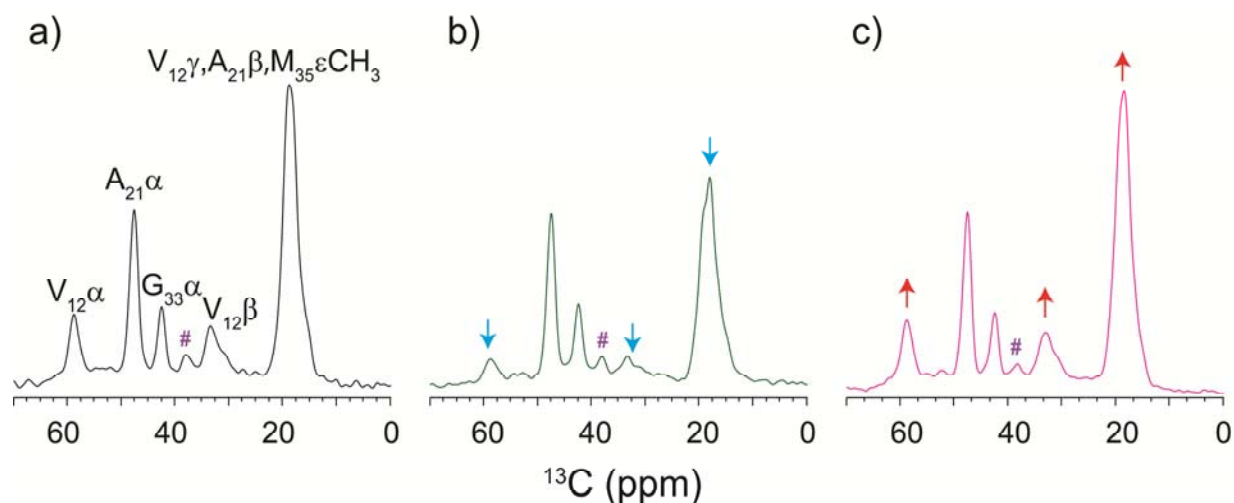


Figure 29. 1D ^{13}C CPMAS SSNMR spectra of (a) A β (1-40) fibrils uniformly ^{13}C - and ^{15}N -labeled at residues Val-12, Ala-21, Gly-33 and selectively ^{13}C labeled Met-35 at (ϵ - $^{13}\text{C}\text{H}_3$) (b) with 0.4 mol. eq. of Cu^{2+} , and (c) with both 0.4 and 1 mol. eq. of Cu^{2+} and ascorbate respectively. The presence of Cu^{2+} attenuates $^{13}\text{C}\alpha$, $^{13}\text{C}\beta$, and $^{13}\text{C}\gamma$ signals of Val-12 (b, blue down arrows), whereas, addition of ascorbate recovers the signal intensities (c, red up arrows). The loss in signal intensities suggests the close proximity of Val-12 to the paramagnetic Cu^{2+} center. However, when Cu^{2+} is converted to diamagnetic Cu^+ by ascorbate, a recovery of signal intensities was observed. In addition, a minor peak at 40 ppm (indicated by #) has been previously assigned to the methyl ^{13}C of the sulfoxide group, an oxidized sidechain of methionine residue.¹⁶⁷

Besides ascorbate, Met-35 has been previously proposed to play a significant role in the redox chemistry of Cu ions and A β .⁷⁰ The methyl $^{13}\text{C}\epsilon$ of Met-35 has been assigned to a signal at ~ 15 ppm,¹⁰⁴ but the signal overlapping with methyl ^{13}C of Val-12 and Ala-21 (Figure 29) did not allow for unambiguous determination of the paramagnetic influence from Cu^{2+} . The fact that the intensity of this signal did not change after the Cu is added to the fibrils suggests no additional oxidation of Met-35 had occurred during the redox cycle (Figure 29 c). This small population of oxidized methionine probably resulted from the initial dissolution of A β peptide in a dilute sodium hydroxide solution (10 mM) or during the incubation period.^{70, 167} In a separate solution NMR experiment, free amino acid methionine was incubated with free Cu^{2+} and

ascorbate; a significant oxidation of free amino acid was observed (Figure 30).⁸⁵ It is possible that the unique structural arrangements of A β fibrils limit solvent accessibility of the Met-35 sidechain,¹⁰⁴ thus preventing its involvement in the redox reaction.

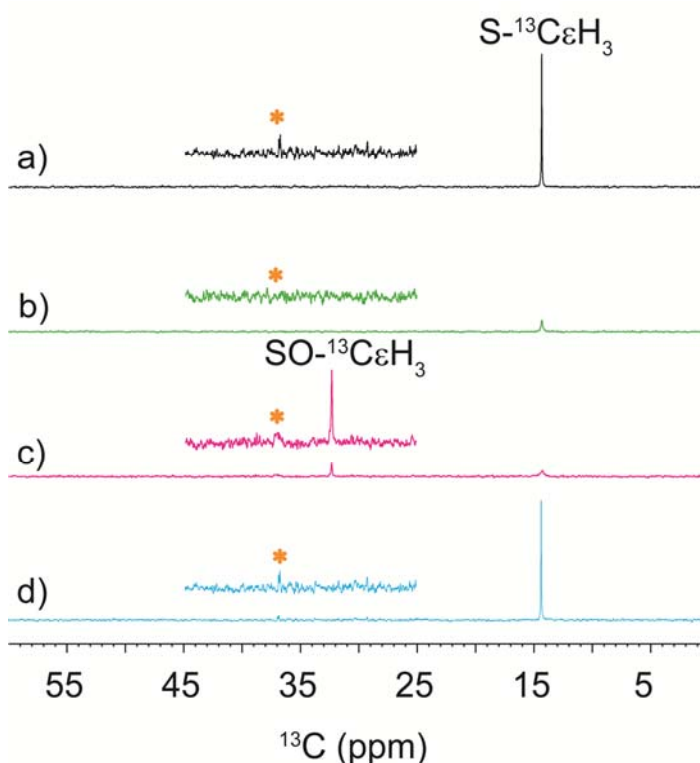


Figure 30. ¹³C DEPT-45 solution state NMR spectra of (a) 2 mM methionine, (b) 2 mM methionine with 0.8 mM CuCl₂, (c) 2 mM methionine with 0.8 mM CuCl₂ and 2 mM ascorbate, and (d) 2 mM methionine with 2 mM ascorbate. The methionine sample was selectively ¹³C labeled at the ϵ -methyl carbon (S-C ϵ H₃). Stock solution of methionine was prepared in 10 mM phosphate buffer at pH 7.4 with 10% D₂O. The samples were incubated at room temperature for 24 h prior to NMR measurements. The S-C ϵ H₃ signal in spectra b and c is weaker due to the presence of paramagnetic Cu²⁺ ions in solution. However, the signal for the methyl ¹³C ϵ attached to the oxidized sulfur group appears only after incubation with ascorbate (c), clearly suggesting the role of ascorbate in promoting the redox reaction of Cu²⁺. (*) represents a minor impurity in the sample. The results here imply that methionine can be oxidized by Cu²⁺ only when it is in direct interaction with the Cu center and when an external reducing agent is present.

Interestingly, ¹³C chemical shifts for Val-12, Ala-21, Ala-30, Ile-32, Gly-33, Val-36, Gly-37, Gly-38 and Val-39 for the Cu⁺-bound A β fibril are essentially unaffected by Cu⁺ binding

(see Figure 31 a, c and ^{13}C Chemical shift Table II). As ^{13}C chemical shifts are sensitive probes to conformations of a protein, the results suggest that the overall A β structures in fibril are largely unaffected by the reduction of Cu^{2+} to Cu^+ . Further analysis of these samples by 2D $^{13}\text{C}/^{13}\text{C}$ fpRFDR¹⁶⁸ experiment showed well resolved, nearly identical chemical shift crosspeaks (± 0.2 ppm) (Figure 31). The lack of change in chemical shifts suggests no significant alterations to the overall structure in the hydrophobic core of the fibril, although the local binding modes and conformations of the residues coordinated to ions may show structural difference at the local level.

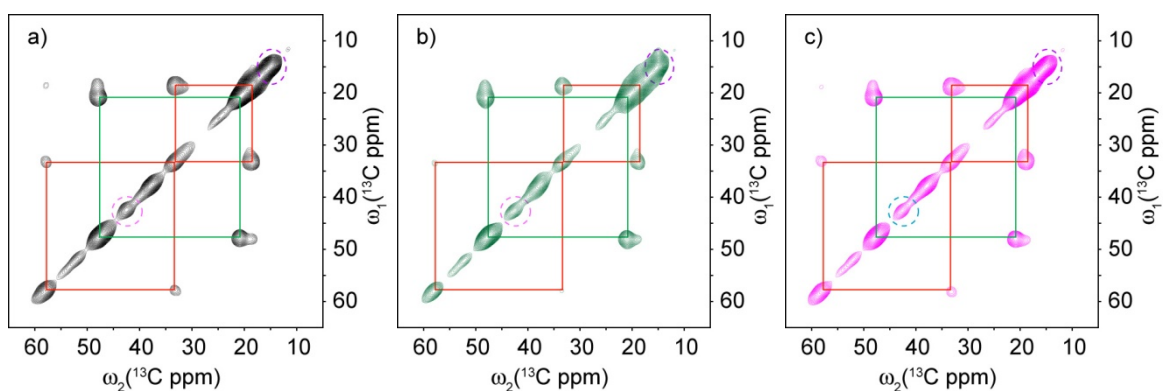


Figure 31. 2D $^{13}\text{C}/^{13}\text{C}$ fpRFDR spectra of (a) 100 μM A β (1–40) fibrils alone, (b) with 0.4 mol. eq. of Cu^{2+} , and (c) with both Cu^{2+} and 1 mol. eq. ascorbate. The A β (1–40) fibril sample was uniformly ^{13}C - and ^{15}N -labeled at Val-12 (Red), Ala-21 (green), Gly-33 (pink), and Met-35 $^{13}\text{C}_\epsilon$. Comparison among the spectra shows no noticeable difference (except for minor attenuation of cross peaks due to paramagnetic Cu^{2+} in (b)) in chemical shifts suggesting lack of significant alteration in secondary structural organization upon Cu^{2+} binding (b) or redox reaction (c).

4) Histidine-coordination to Cu⁺ in A β (1-40) fibrils probed by ¹³C and ¹⁵N SSNMR

In order to understand the redox chemistry of Cu-A β fibrils, we investigated the coordination modality of Cu⁺ on A β fibrils by SSNMR with focus on the coordination to His-13 and His-14 residues. We recently reported that A β (1-40) fibrils bind Cu²⁺ via side chains of His-13, His-14, CO₂⁻ terminus of Val-40, and carboxyl side chains of Glu, based on SSNMR and molecular dynamic simulation studies.¹⁰⁴ As for Cu⁺ binding to A β , several studies using monomeric A β (1-40) and A β (1-42), and shorter fragments have proposed Cu⁺ binding at the histidine residues (i.e. His-6, His-13, and His-14)^{216-219, 223, 228, 229} in the N-terminus region of A β . Nevertheless, no previous studies have demonstrated the interactions between Cu⁺ and A β fibrils. For this purpose, we conducted ¹³C and ¹⁵N SSNMR for A β (1-40) fibrils that were labeled with uniform ¹³C- and ¹⁵N-labeled amino acids at His-13 and His-14.

Figure 32 compares (a, b) 1D ¹³C CPMAS and (c, d) 2D ¹³C/¹³C correlation SSNMR spectra of (a, c) His-13 and (b, d) His-14 for (black) Cu-free, (purple) Cu⁺-bound, and (green) Cu²⁺-bound A β (1-40) fibril, where the data for the Cu²⁺-A β sample were omitted in (c, d) for clarity. The assignments for Cu-free and Cu⁺-bound forms are based on 2D ¹³C/¹³C and ¹³C/¹⁵N correlation SSNMR, as will be discussed below. The 1D ¹³C spectra for Cu-free His-13/14 (black) show two strong peaks for C ϵ (135 ppm) and C δ (116 ppm) with a broad peak for ¹³C γ (~132 ppm) with indications of some minor peaks. Upon Cu²⁺ binding, the imidazole ¹³C signals of His-13/14 were quenched with severe line broadening (Figure 32a, b green) due to Cu²⁺ coordination to His-13/14.¹⁰⁴ After 4-h incubation with ascorbate for the Cu²⁺-bound A β , ¹³C CPMAS spectra (Figure 32 a, b purple) show almost complete recovery of these signals with distinct alterations in the ¹³C chemical shifts from those for the Cu-free A β fibril (black). As the pH was adjusted carefully (see the materials and method), the observed spectral changes are not

attributed to the pH change. The $^{13}\text{C}\epsilon$ and $^{13}\text{C}\gamma$ signals shifted downfield by 1.1-1.8 ppm and 3.1-5.9 ppm in His-13 and His-14, respectively (see Table II). These spectral changes presumably due to Cu^+ -binding are more evident in the respective 2D spectra (Figure 32 c and d). Thus, we identified the samples as Cu^+ -bound $\text{A}\beta$ fibril samples with Cu^+ -coordination to His-13 and His-14. The chemical shift changes are most likely to reflect structural and chemical environment alternations due to Cu^+ binding to these His residues.

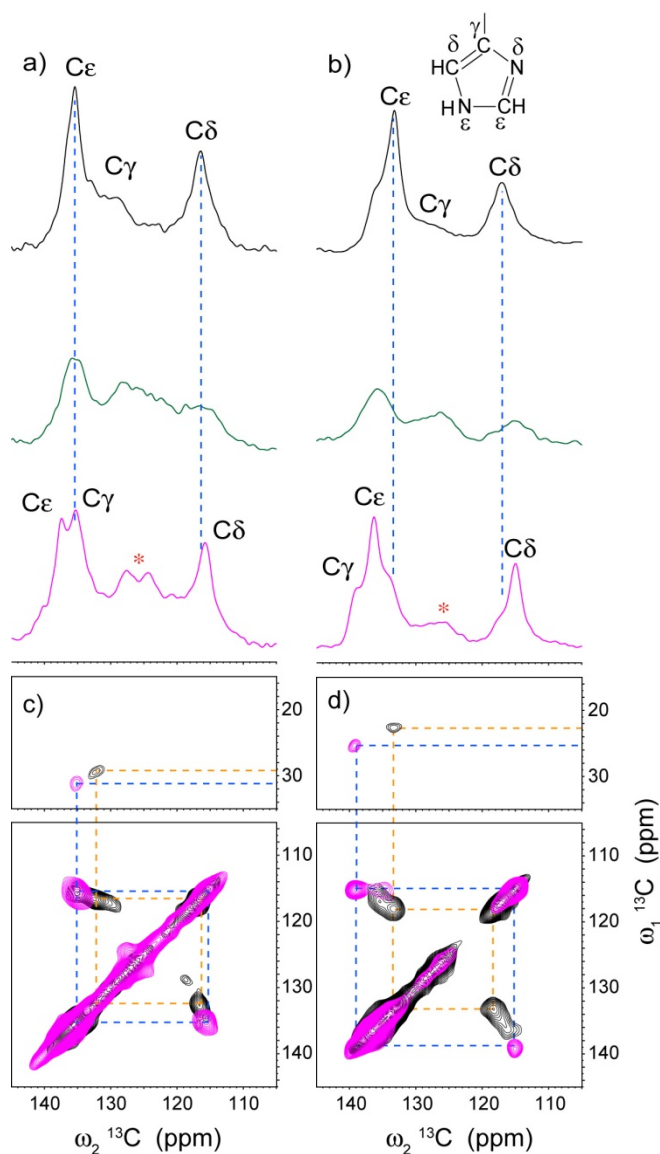


Figure 32. 1D ^{13}C CPMAS (a and b) and 2D $^{13}\text{C}/^{13}\text{C}$ correlation (c and d) spectra of two $\text{A}\beta(1-40)$ fibrils uniformly ^{13}C - and ^{15}N -enriched at residues His-13 (a and c) and His-14 (b and d), respectively, without Cu (black), with Cu^{2+} (green), and with Cu^+ (i.e. after incubation with ascorbate) (purple). While Cu^{2+} considerably broadens the signals (green), reduction to Cu^+ by ascorbate recovers the signals but a small downfield shift of the signals was observed (purple). The assignments for $\text{C}\beta$ - $\text{C}\gamma$ and $\text{C}\gamma$ - $\text{C}\delta$ correlations are shown along the dash lines (orange and blue for $\text{A}\beta(1-40)$ fibrils alone and Cu^+ - $\text{A}\beta(1-40)$ fibrils, respectively) in c and d. For clarity, the 2D spectrum of Cu^{2+} - $\text{A}\beta$ fibrils was not included in c and d

Next, we made signal assignments for ^{13}C resonances. The $\text{C}\beta$, $\text{C}\gamma$, and $\text{C}\delta$ signals of His-13 and His-14 side chains can be assigned readily for the Cu-free and Cu^+ -bound forms from the 2D $^{13}\text{C}/^{13}\text{C}$ chemical-shift correlation SSNMR spectra by tracing single-bond $^{13}\text{C}/^{13}\text{C}$ correlation (Figure 32 c,d). The $\text{C}\epsilon$ signals, which typically appear in a range of 134-138 ppm, were assigned based on the 2D $^{13}\text{C}/^{15}\text{N}$ correlation spectra in Figure 34 a and d, as will be described below. $^{13}\text{C}\delta$ shift is known to be very sensitive to the protonation state of the neighboring $\text{N}\epsilon$. $^{13}\text{C}\delta$ shifts for His having $\text{N}\epsilon\text{H}$ and non-protonated $\text{N}\epsilon$ typically show ~ 115 and ~ 125 ppm, respectively.^{230, 231} As shown in Figure 32(a, b), the Cu-free form at the neutral pH shows $^{13}\text{C}\delta$ shifts of ~ 116 ppm; thus, His-13 and 14 are likely to have τ -tautomer with $\text{N}\epsilon\text{H}$. Histidine having Cu^+ and Zn^{2+} coordinated to $\text{N}\epsilon$ often yields $^{13}\text{C}\delta$ shifts corresponding to non-protonated $\text{N}\epsilon$ (see Table III). Since the Cu^+ -coordinated His-13 and His-14 show $^{13}\text{C}\delta$ shifts of 115-116 ppm, which is consistent with protonated $\text{N}\epsilon$, Cu^+ is likely to be coordinated to $\text{N}\delta$ for both His-13 and His-14. Figure 32(a, b purple) also shows weaker ^{13}C peaks at ~ 125 ppm for the Cu^+ -bound form (indicated by * in a and b bottom). In our preliminary assignments, these peaks are attributed to $^{13}\text{C}\delta$ for a minor histidine species having π -tautomer His with $\text{N}\delta\text{H}$ ²³² or a species having $\text{N}\delta\text{H}$ and $\text{N}\epsilon\text{-Cu}^+$. Overall, the line widths for the His-13,14 residues in the 2D spectra (Figure 32 c, d) are narrower for the Cu^+ -bound form than those for the Cu-free form, suggesting that Cu^+ -coordination may make His coordination states and conformations more homogeneous.

In order to determine which nitrogen ($\text{N}\delta/\text{N}\epsilon$) of the His side chain is involved in the coordination of Cu^+ ions, we performed the 1D ^{15}N CPMAS (Figure 33) and 2D $^{13}\text{C}/^{15}\text{N}$ correlation experiments (Figure 34) on the same set of (a) Cu-free, (b) Cu^{2+} -bound, and (c) Cu^+ -bound ^{13}C - and ^{15}N -labeled A β fibrils. The ^{15}N chemical shifts of the His side chains are highly

dependent on the tautomeric state of the imidazole ring which depends on the pH of the sample.^{103, 230, 232} At neutral pH, the unprotonated N δ and N ϵ in the τ - and π -tautomeric state, respectively, resonate at \sim 250 ppm, whereas their protonated analogues resonate at 160–190 ppm (see Table III).^{231, 232} For the Cu-free A β (1–40) fibrils (Figure 33 a, d), the ^{15}N CPMAS spectra show signals for His-13 at 228 ppm and 172 ppm (Figure 33 a) and those for His-14 at 250 ppm and 164 ppm (Figure 33 d).^{230, 232} Based on ^{13}C shift values, the signals at \sim 172 ppm was assigned as protonated $^{15}\text{N}\epsilon$ in the τ -tautomer while the signals at 228–250 ppm were assigned as non-protonated $^{15}\text{N}\delta$. For His-14, some other minor peaks were observed at 177.9 and 197.7 ppm (* in Figure 33 d). Upon Cu^{2+} binding, the N ϵ signals at \sim 164 ppm in the ^{15}N CPMAS were quenched by \sim 40 %, while the $^{15}\text{N}\delta$ signals at 240–255 ppm were unaffected in the intensities. When Cu^{2+} is reduced to Cu^+ by ascorbate, the N ϵ signals were recovered with new peaks at \sim 210 ppm, which we assigned to Cu^+ -bound $^{15}\text{N}\delta$.

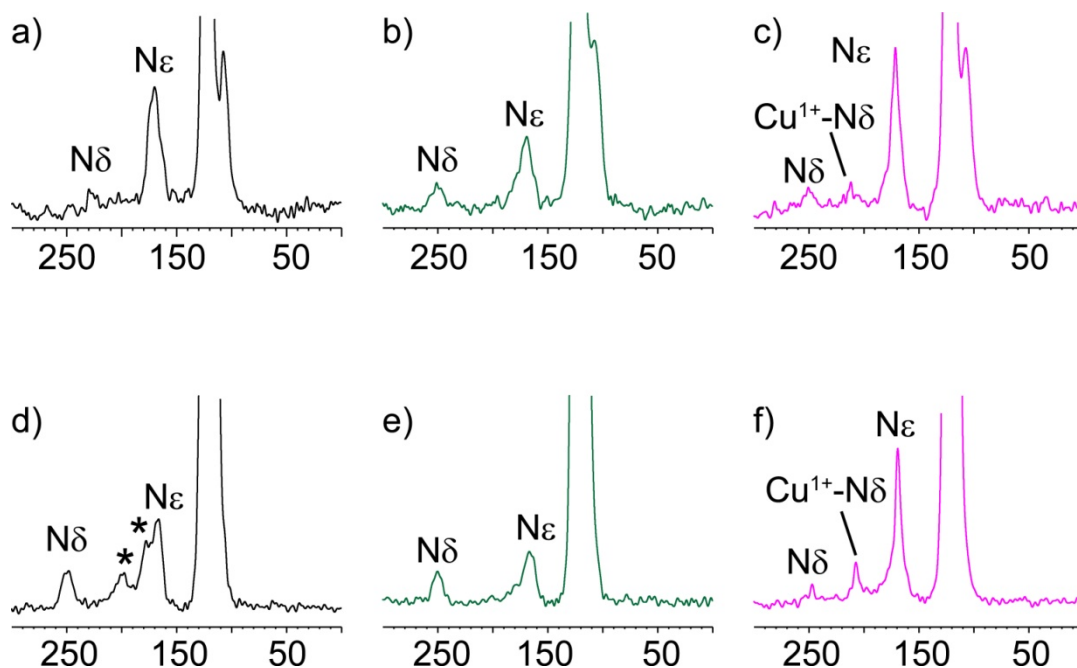


Figure 33. 1D ^{15}N CPMAS spectra of A β (1–40) fibrils (^{15}N -labeled at His-13 (a–c) and His-14 (d–f)) alone (a and d), with Cu^{2+} (b and e), and with Cu^+ (Cu^{2+} and ascorbate, c and f). Addition of Cu^{2+} to A β (1–40) fibrils results in attenuation of the $\text{N}\epsilon$ signal at ~ 170 and ~ 169 ppm in both histidine residues (b and e). Similarly, incubation of Cu^{2+} -A β fibrils with ascorbate recovers the signal intensity of $\text{N}\epsilon$ (c and f) and results in a new signal at ~ 212 and 208 ppm respectively, which is assigned to the Cu^+ - $\text{N}\delta$ species (see text for further explanation). The peaks represented by * in spectrum (d) could be due to $\text{N}\delta$ and $\text{N}\epsilon$ possibly from diprotonated tautomer.

These assignments are consistent with the connectivities observed in 2D $^{13}\text{C}/^{15}\text{N}$ correlation experiments. In the 2D $^{13}\text{C}/^{15}\text{N}$ correlation spectra of Cu-free A β (Figure 34 a, d), the $^{15}\text{N}\epsilon$ signal at 171.5 ppm in His-13 showed strong cross peaks with directly connected $\text{C}\delta$ and $\text{C}\epsilon$, whereas the $^{15}\text{N}\delta$ signal at 227.6 ppm displayed cross peaks only to $\text{C}\gamma$ and $\text{C}\epsilon$. Thus $\text{N}\epsilon\text{H}$ (171.5 ppm) and $\text{N}\delta$ (227.6 ppm) were unambiguously assigned for His-13. However, the 2D $^{13}\text{C}/^{15}\text{N}$ spectrum acquired under identical conditions for the Cu-free A β sample labeled at His-14 (Figure 34 d) showed two sets of cross peaks. The first set of peaks showed correlation of $^{15}\text{N}\epsilon$ shifts of ~ 164 ppm with $^{13}\text{C}\epsilon$ at 136 ppm and $^{13}\text{C}\delta$ of 114 ppm as well as the correlation

of $^{15}\text{N}\delta$ at ~ 250 ppm with $^{13}\text{C}\epsilon$ at 136 ppm. Another set of cross peaks (Figure 34 d orange dashed circles) were observed for the other ^{15}N signals observed in the 1D ^{15}N CPMAS at ~ 178 ppm and at ~ 198 ppm (indicated by * in Figure 33d). The ^{15}N resonance at 178 ppm is connected with $\text{C}\gamma$ (133.4 ppm) as well as $\text{C}\delta$ (117.8 ppm). The ^{15}N signal at ~ 198 ppm shows two overlapping cross peaks to $\text{C}\gamma$ (133.4 ppm), suggesting that the second set of cross peaks that include ^{15}N resonances at ~ 198 ppm could be attributed to biprotonated tautomeric form of imidazole side chain in His-14. Most of these resonances were quenched by Cu^{2+} binding to His-13 and His-14 on $\text{A}\beta(1-40)$ fibrils, which is in agreement with previous studies.¹⁰⁴

Next, we examined 2D $^{15}\text{N}/^{13}\text{C}$ correlation experiments for Cu^+ -bound $\text{A}\beta$. In Figure 34 c, the His-13 shows strong cross peaks connecting the $^{15}\text{N}\epsilon$ signal at 170 ppm with $^{13}\text{C}\delta$ signal at 116 ppm and $^{13}\text{C}\epsilon$ signal at 137 ppm, whereas the $^{15}\text{N}\delta$ resonance at 212 ppm displays cross peaks to $^{13}\text{C}\gamma$ at 136 ppm. The $^{15}\text{N}\delta$ resonance is distinctively shifted from ~ 228 ppm to 212 ppm most likely due to Cu^+ binding to $\text{N}\delta$. Other minor peaks (orange circle) were observed as will be discussed below. Similar patterns were observed, for His-14. The spectrum in Figure 34 f indicate correlation of $^{15}\text{N}\epsilon$ at 169 ppm with $^{13}\text{C}\epsilon$ at 136 ppm and $^{13}\text{C}\delta$ at 115 ppm as well as correlation from $^{15}\text{N}\delta$ at 208 ppm to $^{13}\text{C}\gamma$ at 139 ppm and $^{13}\text{C}\epsilon$ at 136 ppm. $^{15}\text{N}\delta$ signal for His-14 shows a distinctively narrow peak at 208 ppm unlike the broader multiple resonances observed in Figure 34 d. The $^{13}\text{C}\delta$ shift values of ~ 115 ppm are also consistent with Cu^+ coordination to $\text{N}\delta$ for these cross peaks, as discussed above. A recent statistical analysis of the $^{13}\text{C}\delta$ and $^{13}\text{C}\epsilon$ chemical shifts of Zn^{2+} binding proteins²³¹ showed that for histidine residue coordinated to Zn^{2+} via $\text{N}\delta$, the average chemical shifts of $^{13}\text{C}\delta$ and $^{13}\text{C}\epsilon$ are 119.1 ± 1.5 and 138.9 ± 1.3 ppm. In contrast, when His is coordinated to Zn^{2+} via $\text{N}\delta$, the respective values are 127.4 ± 0.8 and 139.7 ± 0.6 ppm. Thus, it was predicted that when $\Delta\epsilon\delta > 17$ ppm, Zn^{2+}

coordination is likely to occur *via* the $N\delta$ ²³¹, where $\Delta\epsilon\delta$ denotes the difference of $^{13}C\epsilon$ and $^{13}C\delta$ shifts. ^{13}C chemical shift data for His coordinated to Cu^+ ^{233, 234} appear to be consistent with this observation for Zn^{2+} coordination to His (see Table III). As $\Delta\epsilon\delta$ is 21.5 ppm for both His-13 and His-14 in Figure 34 (c, f), our data suggest that Cu^+ -coordinates to $^{15}N\delta$ of His. Weak cross peaks were observed in Figure 34 (c, f) at $(\omega_N, \omega_C) = (\sim 170 \text{ ppm}, \sim 125 \text{ ppm})$. The cross peaks are probably attributed to correlation between $^{15}N\delta H$ and $^{13}C\gamma$ or between $^{15}N\delta H$ and $^{13}C\delta$ for a minor species for which Cu^+ is coordinated to $^{15}N\epsilon$, although additional data are needed to confirm the assignments. The data suggest that both $N\delta$ and $N\epsilon$ coordinations to Cu^+ are possible with $^{15}N\delta$ as a primary Cu^+ coordination site. Taken the data together, the SSNMR results provide strong structural evidence that Cu^+ ions site-specifically coordinated to $A\beta$ fibril in the course of redox cycles, which potentially allow for the generation of ROS in AD.

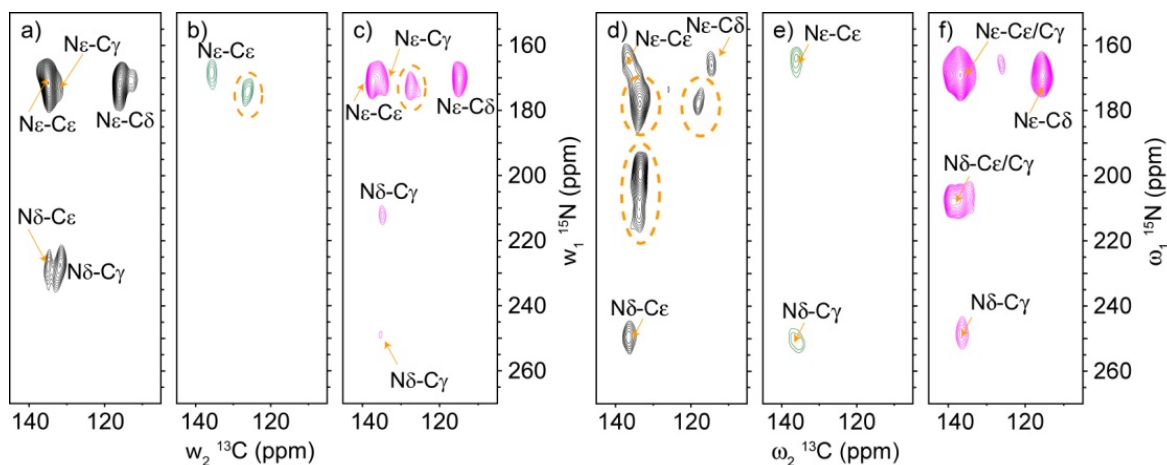


Figure 34. 2D $^{13}\text{C}/^{15}\text{N}$ correlation spectra of $\text{A}\beta(1-40)$ fibrils ^{13}C - and ^{15}N -labeled at His-13 (a-c) and His-14 (d-f) alone (a and d), with Cu^{2+} (b and e), and with Cu^+ (Cu^{2+} and ascorbate, c and f). The cross peaks corresponding to other tautomeric forms of $\text{N}\delta$ and $\text{N}\epsilon$ are shown in orange dashed circles and are easily assigned based on their correlations to ^{13}C neighbors (b and d). The disappearance of the $\text{N}\delta$ cross peaks for the Cu^{2+} -bound $\text{A}\beta$ fibrils is due to the fact that the ^{15}N polarization is transferred to the paramagnetically quenched ^{13}C signals (b and e). The appearance of a new signal (at $\omega_1 = \sim 212$ and 208 ppm and $\omega_2 = \sim 136$ and 139 ppm) in c and f after incubation with ascorbate indicates Cu^+ binding at the $\text{N}\delta$ (based on correlations to $\text{C}\epsilon$ and $\text{C}\gamma$) of the imidazole ring.

5) TEM analysis of the $\text{Cu-A}\beta(1-40)$ fibrils with ascorbate

The H_2O_2 produced locally by Cu^{2+} - $\text{A}\beta(1-40)$ fibrils can potentially inflict oxidative damage on the $\text{A}\beta$ fibrils at the histidine, tyrosine and methionine residues⁷⁰ and disrupt the structural integrity. As a result, any morphological change in the same Cu^{2+} - $\text{A}\beta$ fibrils treated with ascorbate was examined by TEM. Among the samples tested $\text{A}\beta(1-40)$ fibrils alone, Cu^{2+} - $\text{A}\beta(1-40)$ fibrils and Cu^{2+} - $\text{A}\beta(1-40)$ fibrils incubated with ascorbate for 24 h at room temperature, no morphological difference was observed (Figure 35). The TEM images reveal fibrils with diameter of ~ 10 nm and lengths of >1 μM ; these values are consistent with those of previous reports.^{15, 104} Thus, the ROS production by the addition of ascorbate did not yield apparent morphological damage on the $\text{A}\beta$ fibril in Figure 35 c.

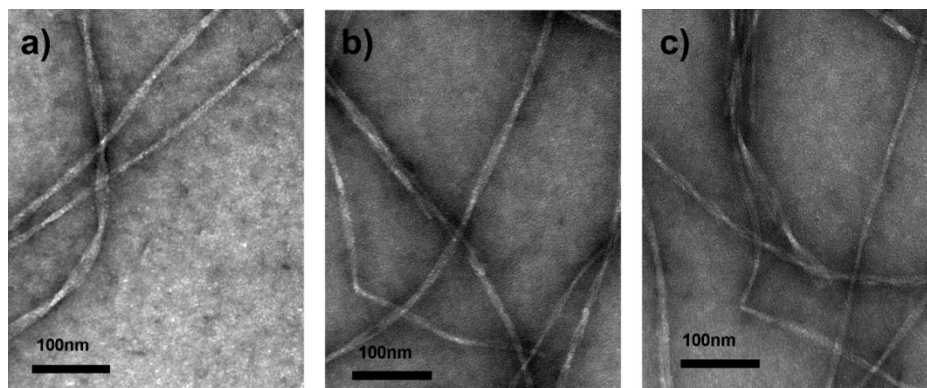


Figure 35. TEM (~10 nm diameter, length > 1 μM) images of the (a) Aβ(1-40) fibrils (100 μM monomer concentration), (b) Aβ(1-40) fibrils incubated with 40 μM Cu²⁺ for 24 h at 4 °C, and (c) Cu²⁺-Aβ(1-40) fibrils incubated with 1 mM ascorbate for 24 h at room temperature. The width of the scale bar represents 100 nm in length. Both Cu-binding and redox reaction upon addition of ascorbate does not alter the overall morphology of the Aβ fibrils.

6) Solution state NMR studies of Cu-Aβ(1-40) monomer

The interaction between Cu⁺ and Aβ(1-40) monomer was assessed by solution state ¹H NMR. Aβ(1-40) monomer and Cu²⁺ in a molar ratio of 1:0.4 was incubated with one mol. eq. of ascorbate (with respect to Aβ concentration) for 30 min at room temperature, and the ¹H NMR spectra were obtained on a 21.2 T Bruker spectrometer. In a previous report by Zagorski et.al.,⁷³ addition of Cu²⁺ to Aβ(1-40) monomers resulted in loss of N-terminal backbone NH (Glu-3–Val-18) and side chain (Arg-5 and Gln-15) signals on the HSQC spectrum. It is likely that Cu²⁺ is bound to Aβ *via* the side chains of histidine (i.e. at positions 6, 13, and 14) and/or acidic (i.e. Asp-1, Glu-3, Asp-7, Glu-11, and Glu-22) amino acid residues on the N-terminus. Particularly, if excess Cu is present, multiple binding modalities are possible; thus, a massive loss of NH signals in the N-terminal region of the peptide is observed. Furthermore, a mere close proximity to the paramagnetic Cu²⁺ center can significantly enhance relaxation of ¹H signals. To mitigate such a global relaxation effect, only 0.4 mol. eq. of Cu²⁺ was used in our studies. The aromatic

region of A β (1–40) monomers with b) and without Cu²⁺ (a) shows a sharp contrast with the spectrum of the former (b) displaying severe line broadening. As anticipated, the side chain signals of His residues are completely abolished, along with those of Tyr-10 and Phe residues. With addition of ascorbate to reduce Cu²⁺ to Cu⁺, most signals except those of His side chains are recovered which imply A β binding of Cu⁺ at the His residues. Thus, the His residues of A β (1–40) are involved in binding of both Cu⁺ and Cu²⁺.

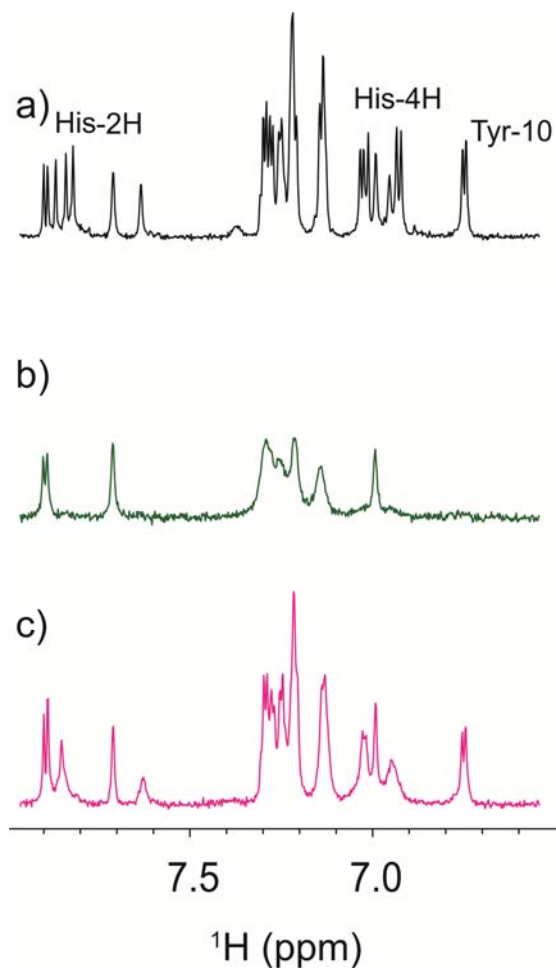


Figure 36. Solution state ^1H NMR spectra (aromatic region) of (a) $92\ \mu\text{M}$ $\text{A}\beta(1-40)$ monomer, (b) with $37\ \mu\text{M}$ Cu^{2+} , and (c) with both Cu^{2+} and 1 mol. eq. of ascorbate. The aromatic side chain ^1H signals of His and Tyr residues of $\text{A}\beta(1-40)$ peptide are easily assigned based on a previous report.⁷³ As expected, Cu^{2+} broadens signals, with some beyond detection (b). The amino acid residues affected by Cu^{2+} include Phe, His, and Tyr. Reduction of Cu^{2+} to Cu^+ by ascorbate recovers majority of the signals but some remained broaden, especially the side chain protons of His residues, indicating the interactions between Cu^+ and histidine amino acids of the $\text{A}\beta(1-40)$ peptide.

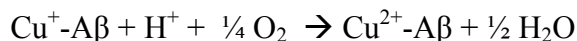
C) Discussion

Redox-active transition metals such as Cu^{2+} and Fe^{3+} have been implicated to be responsible for the extensive oxidative damages observed in the brains of AD victims.^{82, 189, 191,}

^{194, 235} Researchers have exhaustively studied the interactions between these metals and AD-

associated A β peptides.^{74, 82, 117, 121, 122, 163, 189, 191, 235, 236} Nonetheless, a critical question remains unanswered, given that these metals are isolated along with aggregated plaques/fibrils of A β . *What is the role of these metal ions complexed to aggregated A β fibrils in regard to the oxidative stress in AD?* In this study, we have shown the ability of Cu⁺/Cu²⁺ to complex with A β (1–40) fibrils in order to generate harmful ROS such as H₂O₂ and hydroxyl radical by photometric assay and SSNMR. To the best of our knowledge, this study has showed the unique redox properties and structure of Cu⁺-bound A β fibrils, which are likely to have relevance to the pathogenesis of AD, for the first time. Quantitative analysis based on photometric assay suggest sub mM of H₂O₂ generation for a 100- μ M A β (1–40) fibrils with only 0.4 mol. eq. of Cu²⁺ in the presence of ascorbate. Then, we have utilized various SSNMR experiments to show that the electron transfer between Cu, ascorbate, and oxygen does occur and that both Cu²⁺ and Cu⁺ remain bound to the fibrils during the redox reaction.

A generalized mechanism of the redox reaction entails initial reduction of Cu²⁺ to Cu⁺ by ascorbate, resulting in the H₂O₂ formation; this is followed by an electron transfer from Cu⁺ to O₂ to oxidize back to Cu²⁺. The redox cycle indicated by our study is as follows:



In the process, each O₂ can accept two electrons to generate H₂O₂. As a result, in the presence of excess ascorbate and O₂, a significant amount of H₂O₂ can be accrued locally, potentially inflicting oxidative damage. The requirements of cellular reductant and molecular oxygen for the ROS production imply that diffusible A β aggregates, rather than immobile fibril, may be more efficient agent for catalyzing such a reaction in terms of accessibility to cellular reducing

agent. Such diffusible aggregates of A β have been reported to be more toxic to neural cells.²¹ Furthermore, based on SSNMR data, we propose that the Met-35 residue on A β is not involved in the redox cycle and that His-13 and His-14 of A β (1–40) fibrils may bind to Cu²⁺ and Cu⁺ in different coordination modes through N ϵ and N δ , respectively. Overall, the results in this report indicate that A β (1–40) fibrils become a strong catalyst that attracts Cu ions and introduce cyclic redox reactions involving Cu ions in a continuous manner, which may contribute to the oxidative stress and a cascade of the downstream events in AD.

TABLE II. ^{13}C CHEMICAL SHIFTS OF THE $\text{A}\beta(1-40)$ FIBRILS, Cu^{2+} - $\text{A}\beta(1-40)$ FIBRILS, AND Cu^{2+} - $\text{A}\beta(1-40)$ FIBRILS INCUBATED WITH ASCORBATE (Cu^{+} - $\text{A}\beta(1-40)$ FIBRILS). THE CHEMICAL SHIFTS WERE REFERENCED TO TETRAMETHYLSILANE (TMS).

Residues	$\text{A}\beta(1-40)$ fibrils (ppm) ^{a)}	Cu^{2+} - $\text{A}\beta(1-40)$ fibrils (ppm) ^{a)}	Cu^{+} - $\text{A}\beta(1-40)$ fibrils (ppm) ^{a)}	Difference Δ (ppm) ^{a)} $\Delta = \text{A}\beta(1-40)$ fibrils – Cu^{+} - $\text{A}\beta(1-40)$ fibrils
Val-12				
C=O	172.3	172.3	172.2	0.1
C α	57.8	58.1	58.1	-0.3
C β	33.2	33.5	33.2	0.0
C γ	18.6	18.6	18.8	-0.2
His-13				
C α	52.0		51.6	0.4
C β	29.7		31.2	-1.5
C γ	132.4		135.5	-3.1
C δ	116.0		115.6	0.4
C ϵ	135.5	135.8	137.3	-1.8
N δ	227.6	250.3	212.3, 248.2 ^{b)}	15.3
N ϵ	171.5	168.4	170.3	1.2
His-14				
C α	58.9		59.6	-0.7
C β	22.4		25.2	-2.8
C γ	133.4		139.3	-5.9
C δ	116.9	116.0	115.2	1.7
C ϵ	135.3	136.3	136.4	-1.1
N δ	249.5	251.4	207.9, 248.5 ^{b)}	41.6
N ϵ	164.4	163.8	169.3	-4.9

TABLE II. ^{13}C CHEMICAL SHIFTS OF THE $\text{A}\beta(1-40)$ FIBRILS, Cu^{2+} - $\text{A}\beta(1-40)$ FIBRILS, AND Cu^{2+} - $\text{A}\beta(1-40)$ FIBRILS INCUBATED WITH ASCORBATE (Cu^{+} - $\text{A}\beta(1-40)$ FIBRILS). THE CHEMICAL SHIFTS WERE REFERENCED TO TETRAMETHYLSILANE (TMS).

Residues	$\text{A}\beta(1-40)$ fibrils (ppm) ^{a)}	Cu^{2+} - $\text{A}\beta(1-40)$ fibrils (ppm) ^{a)}	Cu^{+} - $\text{A}\beta(1-40)$ fibrils (ppm) ^{a)}	Difference Δ (ppm) ^{a)} $\Delta = \text{A}\beta(1-40)$ fibrils - Cu^{+} - $\text{A}\beta(1-40)$ fibrils
Ala-21				
C=O	173.1	173.2	173.2	-0.1
C α	47.8	48.0	48.0	-0.2
C β	20.6	20.8	20.9	-0.3
Ala-30				
C=O	173.4	17.4	173.4	0
C α	50.0	49.9	50.0	0
C β	17.4	17.9	17.4	0
Ile-32				
C α	56.4	56.0	56.0	0.4
C β	40.3	40.3	39.9	0.4
C γ 1	25.3	25.0	24.9	0.4
C γ 2	15.7	15.9	15.9	-0.2
C δ	12.5	12.3	12.3	0.2
Gly-33				
C=O	168.2	168.4	168.4	-0.2
C α	42.4	42.7	42.6	-0.2
Met-35				
C ϵ	15.1	15.3	15.2	-0.1
Val-36				
C α	58.8	58.5	58.5	0.3
C β	32.1	31.7	31.3	0.8
C γ	19.2	18.7	18.7	0.5

TABLE II. ^{13}C CHEMICAL SHIFTS OF THE $\text{A}\beta(1-40)$ FIBRILS, Cu^{2+} - $\text{A}\beta(1-40)$ FIBRILS, AND Cu^{2+} - $\text{A}\beta(1-40)$ FIBRILS INCUBATED WITH ASCORBATE (Cu^{+} - $\text{A}\beta(1-40)$ FIBRILS). THE CHEMICAL SHIFTS WERE REFERENCED TO TETRAMETHYLSILANE (TMS).

Residues	$\text{A}\beta(1-40)$ fibrils (ppm) ^{a)}	Cu^{2+} - $\text{A}\beta(1-40)$ fibrils (ppm) ^{a)}	Cu^{+} - $\text{A}\beta(1-40)$ fibrils (ppm) ^{a)}	Difference Δ (ppm) ^{a)} $\Delta = \text{A}\beta(1-40)$ fibrils – Cu^{+} - $\text{A}\beta(1-40)$ fibrils
Gly-37				
C=O	169.6	169.5	170.1	-0.5
C α	42.9	42.5	43.1	-0.2
Gly-38				
C=O	170.1	169.2	169.9	0.2
C α	42.5	42.6	42.5	0
Val-39				
C=O	172.0	172.4	171.9	0.1
C α	59.5	59.0	59.2	0.3
C β	33.5	33.6	33.5	0
C γ	19.4	19.4	19.5	-0.1

^{a)} Referenced to TMS.

^{b)} Unbound N δ form in the His side chains

TABLE III. SURVEY OF THE ^{13}C , ^{15}N CHEMICAL SHIFTS OF Cu^+ AND Zn^{2+} BOUND TO HISTIDINE RESIDUES ALONG WITH THE ^{13}C , ^{15}N CHEMICAL SHIFTS OF HISTIDINE TAUTOMERS

a) Cu,Zn Superoxide dismutase (SOD); PDB ID; 2k4w, BMRB Entry 15112; Citation ²³³								
Residues	Coordination		$^{13}\text{C}\gamma$ (ppm)	$^{13}\text{C}\epsilon$ (ppm)	$^{13}\text{C}\delta$ (ppm)	$\Delta = \text{C}\epsilon - \text{C}\delta$ (ppm)	N δ	N ϵ
	N δ	N ϵ						
His 67	N δ -Cu $^+$	*	135.2	136.1	117.3	18.8	*	166.3
His 69	*	N ϵ -Cu $^+$	130.0	134.6	126.2	8.4	169.4	*
His 92	N δ -Zn $^{2+}$	N ϵ -Cu $^+$	135.0	134.5	114.7	19.8	*	*
His 147	*	N ϵ -Cu $^+$	126.6	137.3	126.3	11.0		*
b) ba3 oxidase subunit II of Thermus thermophilus in the reduced state; BMRB Entry 5819; Citation ²³⁴								
His 82	N δ -Cu $^+$	N ϵ -H	133.5	135.9	118.2	17.7	224.6	163.0
His 125	N δ -Cu $^+$	*	134.5	134.5	117.0	17.5	218.1	162.3
c) Histidine tautomers ²³⁰								
Anionic- π	N δ -H	N ϵ	129.2	135.8	125.4	10.4	171.8	248.2
Neutral- τ	N δ	N ϵ -H	137.7	135.3	113.6	21.7	249.4	171.1
Anionic- τ	N δ	N ϵ -H	136.8	135.6	113.0	22.6	252.7	167.3
Biprotonated	N δ -H	N ϵ -H	128.7	136.3	119.4	16.9	190.0	176.3
d) ^{13}C chemical shift analysis of Ensemble of Zn$^{2+}$ bound to His residues reported by Barraud ²³¹								
Zn $^{2+}$ -His N ϵ	*	N ϵ -Zn $^{2+}$	*	137.7	125.4	12.3	*	*
Zn $^{2+}$ -His N δ	N δ -Zn $^{2+}$	*	*	136.9	117.1	19.8	*	*
e) Cu$^+$ bound on Aβ(1-40) fibrils (Current study)								
His-13	N δ -Cu $^+$	N ϵ -H	135.5	137.3	115.6	21.7	212.3	170.3
His-14	N δ -Cu $^+$	N ϵ -H	139.3	136.4	115.2	21.2	207.9	169.3

* Not known

Yellow highlight - Cu $^+$ bound to N δ

D) Materials and Methods

1) Chemicals and reagents

Wang resin, fmoc protected aminoacids, and 2-(6-Chloro-1H-benzotriazole-1-yl)-1,1,3,3-tetramethylammonium hexafluorophosphate (HCTU) were purchased from Peptide International (Louisville, KY). N,N-Diisopropylethylamine, N-Methylpyrrolidone, and Dichloromethane were purchased from Applied Biosystems (Foster City, CA). Piperidine, bathocuproine disulfonic acid disodium salt (BCS), ascorbic acid, coumarin-3-carboxylic acid (3-CCA), sodium azide, thioflavin-T, and selectively ^{13}C -labeled methionine were obtained from Sigma-Aldrich (St. Louis, MO). Sodium hydroxide, potassium phosphate, and sodium phosphate were acquired from Fischer Scientific (Hanover Park, IL). D_2O was purchased from Cambridge Isotope laboratories (Andover, MA). ^{13}C - and ^{15}N -labeled amino acids were purchased from Isotec/Sigma-Aldrich (Miamisburg, OH). H_2O_2 assay kit (#K265-200) was purchased from Biovision (Mountain view, CA).

2) Synthesis and purification of A β (1-40) peptide

A β (1-40) peptide was synthesized as reported in materials and methods section in Chapter III, P.51. The ^{13}C - and ^{15}N -labeling schemes used for SSNMR experiments are (a) Val-12, Ala-21, Gly-33, Met-35 (ϵ - $^{13}\text{C}\text{H}_3$), (b) His-13, Ala-30, Gly-38, Val-39, (c) His-14, Ile-32, Val-36, Gly-37, and (d) Val-18, Phe-19, Gly-29, Ile-31.

3) Photometric hydrogen peroxide (H_2O_2) quantification

The quantification of H_2O_2 was performed as per the instructions given in the assay kit. A 50- μl aliquot of 100 μM Cu^{2+} -A β (1-40) fibrils ($f_{\text{Cu}/\text{A}\beta} = 0.4$) was gently mixed with 1 mM ascorbate solution. Then, 50 μl of the peroxide detection reagent mixture (46 μl assay buffer, 2 μl OxiRed probe solution, 2 μl horse radish peroxidase (HRP)) was immediately added and

incubated at room temperature for 10 min, according to the manufacture's instruction. In the presence of HRP, the OxiRed probe reacts with H_2O_2 to produce a product that can be detected at $\lambda_{\text{max}} = 570$ nm. The product was quantified by a Dynex microplate reader. Six duplicates were performed for each trial. The concentration of H_2O_2 produced from Cu^{2+} -A β (1–40) fibrils and ascorbate was determined from the H_2O_2 calibration curve.

4) Hydroxyl radical detection by fluorescence

Coumarin-3-carboxylic acid (3-CCA) assay was used to quantify hydroxyl radical production. Upon reaction with hydroxyl radicals, the 3-CCA forms a fluorescent active compound, which has a characteristic emission at 450 nm. The emission measurements were done on a Fluorescence Hitachi F7000 spectrophotometer at the excitation wavelength of 388 nm. The emission spectra were recorded from 410–550 nm with the slit widths of 5 nm for both excitation and emission. The assay constituted 100 μM A β (1-40) fibrils, 40 μM Cu^{2+} , 1 mM ascorbate, and 2 mM 3-CCA and performed in 10 mM phosphate buffer at pH 7.4. For the control experiment, the 10 mM phosphate buffer (pH 7.4) was used instead of A β fibrils under identical conditions. At least three replicates were performed for each time point.

5) Solution-state NMR

The solution ^1H NMR studies were performed on a Bruker Avance 900-MHz spectrometer equipped with a cryoprobe at the UIC Center of Structural Biology. The sample temperature was set to 10° C in all the experiments. A β (1–40) monomer solution at pH 7.4 was incubated with CuCl_2 for 15 min at 4 °C. Then, ascorbate was added to the mixture and incubated for another 15 min. The mole ratios were $f_{\text{Cu}/\text{A}\beta} = 0.4$ and $f_{\text{asc}/\text{A}\beta} = 1$. ^1H NMR and ^1H T_1 measurements were performed for the all the samples. ^1H T_1 measurements were performed to confirm the formation of Cu^+ from Cu^{2+} ions. Three samples were prepared for the regular ^1H

and ^1H T_1 NMR measurements: (a) $\text{A}\beta(1-40)$ monomers, (b) Cu^{2+} - $\text{A}\beta(1-40)$, and (c) Cu^{2+} - $\text{A}\beta(1-40)$ with ascorbate.

6) Transmission electron microscopy (TEM)

A JEOL JEM-1220 transmission electron microscope (TEM) at an accelerating voltage of 120 kV was used for the morphological analysis of $\text{A}\beta(1-40)$ fibrils with Cu^{2+} and ascorbate. A 10- μl aliquot of sample was spotted on a carbon-coated Formvar 200-mesh copper grid (Electron Microscopy Sciences, Hatfield, PA) for 30 sec and wicked dry with a tissue paper. Then, the grid was negatively stained with ~ 10 μl of 2% uranyl acetate solution for 1 min and again wicked dry. Finally, the grid was air-dried and analyzed at the UIC RRC.

7) Solid-state NMR

All SSNMR experiments were performed on Varian Infinity Plus and Bruker Avance spectrometers with a home-built 2.5-mm MAS triple-resonance probe at 9.4 T (^1H frequency of 400.2 MHz) in a triple configuration. The spinning speed was set to $20,000 \pm 3$ Hz throughout all experiments. Approximately 2.5–4.0 mg of labeled $\text{A}\beta(1-40)$ fibril samples were used in each experiment. In 1D ^{13}C CPMAS experiments, adiabatic CP transfer was used. During the CP period, the ^{13}C RF field amplitude was linearly swept from 45–65 kHz during a contact time of 1.0 ms, while the ^1H RF amplitude was kept constant at 75 kHz. During the detection period, ^1H TPPM decoupling of 90 kHz was employed. 1D spectra in Figure 29 (a-c) and Figure 32 (a,b) were collected with 512 and 1024 scans, and were processed with Gaussian broadening of 100 and 50 Hz respectively. The 1D ^{15}N CPMAS spectra were measured with the ^1H spin-lock field strength of $\omega_1/2\pi = 50$ kHz. During the CP period, the ^{15}N RF field was linearly swept from 25–35 kHz during a contact time of 900 μs . The spectra in Figure 33 were obtained with

15360 scans and were processed with Gaussian broadening of (a-c) 2 and (d-f) 1 ppm respectively.

For the 2D $^{13}\text{C}/^{13}\text{C}$ correlation experiments in Figure 32 c, d, fpRFDR pulse sequence with a mixing time of 1.6 ms and a ^{13}C π -pulse width of 15 μs was used¹⁶⁸. After the adiabatic CP, the FID was recorded during the t_1 period, and a real or imaginary component of the magnetization was stored along the z-axis. For each t_1 point, 128 scans of FID were accumulated with an acquisition period of 10 ms. A total of 100 complex t_1 points was recorded with a t_1 increment of 38.1 μs . The overall acquisition time was 6 h. Similarly, the 2D $^{15}\text{N}/^{13}\text{C}$ correlation spectra in Figure 34 were measured by preparing the initial ^{15}N magnetization by adiabatic CP. After the t_1 evolution period, the real or imaginary component of ^{15}N magnetization was transferred to ^{13}C by $^{13}\text{C}/^{15}\text{N}$ CP, in which the sum of ω_{C} and ω_{N} was matched to twice the spinning frequency. The ^{13}C signals were detected during t_2 period. ^1H TPPM decoupling of 90 kHz was employed during the t_1 and t_2 periods, while cw decoupling of the same amplitude was used during the mixing period or 2nd CP period for the $^{13}\text{C}/^{13}\text{C}$ and $^{13}\text{C}/^{15}\text{N}$ experiment, respectively. For each t_1 point, 1496 scans of FID were accumulated with an acquisition period of 10 ms. A total of 70 complex t_1 points was recorded with a t_1 increment of 35.7 μs . The FID was processed by NMRPipe software¹⁸² with Gaussian window function of 150 Hz applied along the t_1 and t_2 time domains. The overall acquisition time was 49 h. The A β (1-40) fibril samples analyzed were uniformly ^{13}C - and ^{15}N -labeled at A) Val-12, Ala-21, Gly33, Met-35(ϵ - $^{13}\text{CH}_3$), B) His-13, Ala-30, Gly-38, Val-39, and C) His-14, Ile-32, Val-36, Gly-37.

8) Sample preparation for SSNMR

A solution of 1 mM A β (1-40) was prepared by first dissolving the A β (1-40) peptide in 10 mM NaOH by a brief vortexing. Then, the peptide solution was diluted to a final concentration

of 100 μM with 10 mM phosphate buffer containing 0.02 % NaN_3 , sonicated for 30 s in an ice bath, and filtered through an Amicon Ultra centrifugal filter (MWCO = 50 kDa) at 3200 g and -5°C to remove pre-existing aggregates.^{21, 133} The final pH of the $\text{A}\beta(1-40)$ solution was ~ 7.4 . The concentration of $\text{A}\beta(1-40)$ was determined based on the UV-Vis absorbance at $\lambda = 280$ nm and $\epsilon = 1280 \text{ M}^{-1}\text{cm}^{-1}$.²¹ The $\text{A}\beta(1-40)$ fibril was prepared by incubating the filtered solution at room temperature with constant agitation for 2 weeks. The fibril formation was monitored by thioflavin-T (ThT) fluorescence assay.^{21, 139}

The $\text{A}\beta(1-40)$ fibrils were recovered by centrifuging the sample at 3200 g for 1.5 h (30 min at a time) at -5°C . The supernatant was removed, and the recovered fibrils were frozen in liquid N_2 and lyophilized. The lyophilized sample was then packed into a 2.5-mm MAS rotor for SSNMR experiments. The powder sample in the rotor was rehydrated by adding the supernatant buffer (2 μL per mg of fibrils) and centrifuging down at 2000 g for 2 min. The rehydrated sample was incubated overnight at 4°C before data acquisition.

For the Cu^{2+} - $\text{A}\beta(1-40)$ fibril sample, 2 μL of a concentrated CuCl_2 solution (300 mM, pH 7.4) was added to 15 mL of the fibril solution (100 μM in monomer equivalence) to give a final mole ratio $f_{\text{Cu}/\text{A}\beta} = 0.4$, and incubated at 4°C for 24 h with a brief vortexing to mix the sample. Then, the Cu^{2+} -bound $\text{A}\beta(1-40)$ fibril was recovered by centrifugation at 3200 g for 1.5 h (30 min at a time) at -5°C . The supernatant was discarded, and the resulting fibril pellet was frozen in liquid N_2 , lyophilized, and packed into a 2.5-mm MAS rotor for SSNMR analysis.

For the preparation of the Cu^{2+} - $\text{A}\beta$ fibril sample incubated with ascorbate, a 340 mM ascorbate solution (0.7 μL per mg of fibrils) was added to a 2.5-mm MAS rotor packed with ~ 3 mg of Cu^{2+} - $\text{A}\beta(1-40)$ fibrils by centrifuging at 6000 g for 15 min. In order to avoid pH-induced chemical shift changes in the sample, the ascorbic acid solution was neutralized in equimolar

NaOH before introducing into the rotor. The sample was then used for SSNMR experiments. For the 1D and 2D experiments in Figure 29, 31-34, the mole ratio of A β fibrils to ascorbate is $f_{\text{asc}/\text{A}\beta} = 1$. The sample temperature was set to 12 °C during the SSNMR experiments. For the ^1H T_1 measurements that require sample exposure to O $_2$ in the air in Figure 27, the SSNMR rotor containing the Cu $^{2+}$ -A β fibrils and ascorbate with the rotor cap removed was placed in a centrifuge tube with a tiny hole on the cap and incubated at room temperature for 14 h with a gentle shaking at 100 rpm on a New Brunswick Scientific Excella E24 Incubator shaker. In subsequent ^1H T_1 SSNMR measurements, the temperature was set to 24° C. The sample was exposed to air three times.

V) MOLECULAR-LEVEL STRUCTURAL INSIGHT INTO A PATHOLOGICALLY RELEVANT AMYLOID INTERMEDIATE OF ALZHEIMER'S β BY SOLID-STATE NMR SPECTROSCOPY

A) Introduction

A variety of neurological disorders such as AD, PD are associated with misfolding of disease-specific amyloid proteins. It has been long believed that neural dysfunctions identified in such “amyloid diseases” are caused by amyloid fibrils of amyloid proteins, which are often neurotoxic. Recent evidences, however, have indentified diffusible amyloid aggregates, intermediate species in amyloid misfolding, as a more potent toxin in amyloid diseases.^{115, 181, 237} Despite their increasing importance, intrinsically unstable and heterogeneous natures of these amyloid intermediates have made it an intractable problem to define their detailed structural features, relationship with amyloid fibril, and pathogenic functions. To date, no atomic-level structures are obtained for toxic amyloid intermediates of disease-specific amyloid proteins. Early TEM and atomic-force microscopy (AFM) studies identified spherical assemblies ranging in a diameter of 5–20 nm for amyloid proteins such as A β and α -synuclein, which are associated with AD and PD, respectively.^{181, 238-240} Recent studies showed that an amyloid intermediate of A β (1–40) have a parallel β -sheet structure by site-specific analysis using SSNMR.²⁴¹ Parallel cross- β structure is a ribbon-like β -sheet that extends over the length of the fibril and comprises of β -strands that run approximately perpendicular to the long axis of the fibril. Backbone hydrogen bonds that link the β -strands are nearly parallel to the long axis. More recently, a cross β -sheet structure, which may involve anti-parallel β -sheet, was identified for oligomeric species of A β (1–42) (~20 mer) by X-ray power diffraction, FT-IR, and CD.²⁴² Anti-parallel β -sheet arrangement involves stacking of β -strands as shown in Figure 37 a. Structurally less ordered disk-like oligomer was also identified for A β (1–42) by a SSNMR and AFM study.²⁴⁰ For a

nontoxic tetramer of A β (1–40) that was stabilized in SDS, a mixed parallel and anti-parallel β -sheet structure was identified by solution NMR.²³⁹ For a model system of 11-residue fragment of α β -crystalline, a tetramer that mimics amyloid intermediate was shown to have anti-parallel β -sheet by X-ray crystallography.²⁴³ There are also an increased number of structural studies on oligomeric species of other proteins such as α -synuclein,²³ and Human Serum Albumin²⁴⁴. Even with these efforts, structures of amyloid intermediates are poorly understood for a majority of species, which include biochemically well characterized intermediates for A β such as ADDL,²⁴⁵ A β *56,⁵⁹ and globulomer.²³⁹ More importantly, the structural details of pathogenic or pathogenically relevant amyloid intermediates have been missing in the past studies. The difficulties of such studies are attributed to the low abundance of such species in tissues and heterogeneous nature of amyloid intermediates. Also, lacking is a suitable approach to isolate or reproduce such amyloid species associated with AD pathology for detailed structural analysis. These factors have made structural studies of pathologically relevant amyloid intermediates extremely challenging.



This figure was reprinted from Qiang and co-workers, Proc. Natl. Acad. Sci. U. S. A, 2012 109 (12) 4443-4448

Figure 37. (a) Schematic representation of the double-layered antiparallel cross- β motif (Left), showing β -strands in yellow, the intervening loop in red, and groups of hydrophobic side chains as light green and dark green blocks. (b) Schematic representation of the double-layered parallel cross- β motif identified in WT-A β 1–40 fibrils by Tycko and co-workers.^{15, 19, 20}

In order to define structures of amyloid intermediates relevant to AD, we present an approach to study site-specific structure of highly toxic amyloid intermediate called amylo-spheroid (ASPD) for 42-residue A β .¹⁸¹ ASPD represents a class of highly toxic amyloid intermediates that exhibit spherical morphology having a diameter of ~ 10-18 nm.^{54, 181} A recent study has indicated that ASPD is structurally similar to a spherical amyloid intermediate of A β found in brain affected by AD (termed as “native ASPD”). The similarities of ASPD and native ASPD in structural and morphological aspects were confirmed by “conformational” monoclonal antibodies targeting ASPD and electron micrograph studies by Dr. Minako Hoshi’s group at Institute of Biomedical Research and Innovation, Kobe Hybrid Business Center, Japan.⁵⁴ Also, the severity of AD was well correlated with the level of native ASPD found in brains. Although ASPD is gaining importance as a biomarker and a potential cause of AD, structural details of ASPD are still unknown and unexplored largely. Here, for the ASPD sample prepared *in-vitro*, we perform an analysis of detailed structural features on the ASPD amyloid intermediate that is most likely relevant to AD pathologies by SSNMR, a vital tool for structural analysis of insoluble proteins. The study presents evidence that the oligomeric A β has well defined secondary structure and supramolecular molecular assembly, which potentially make ASPD an excellent therapeutic target for AD.

B) Results

ASPD samples were prepared in collaboration with Hoshi’s group. ASPD’s were obtained by incubating synthetic A β (1–42) in a F12 medium as described previously.⁵⁴ For samples used for the SSNMR analysis, the A β peptides were prepared from A β (1–42) that was isotope labeled with uniformly ¹³C- and ¹⁵N-labeled amino acids at selected sites.²⁴¹ As established in previous structural studies for synthetic amyloid intermediates by SSNMR,^{240, 241}

the samples were quick frozen in liquid nitrogen, and subsequently lyophilized to trap the metastable intermediate state. The TEM analysis on an ASPD sample for isotope labeled A β (Figure 38) showed spherical morphology having a diameter of \sim 10 nm, which is consistent with the previous study.

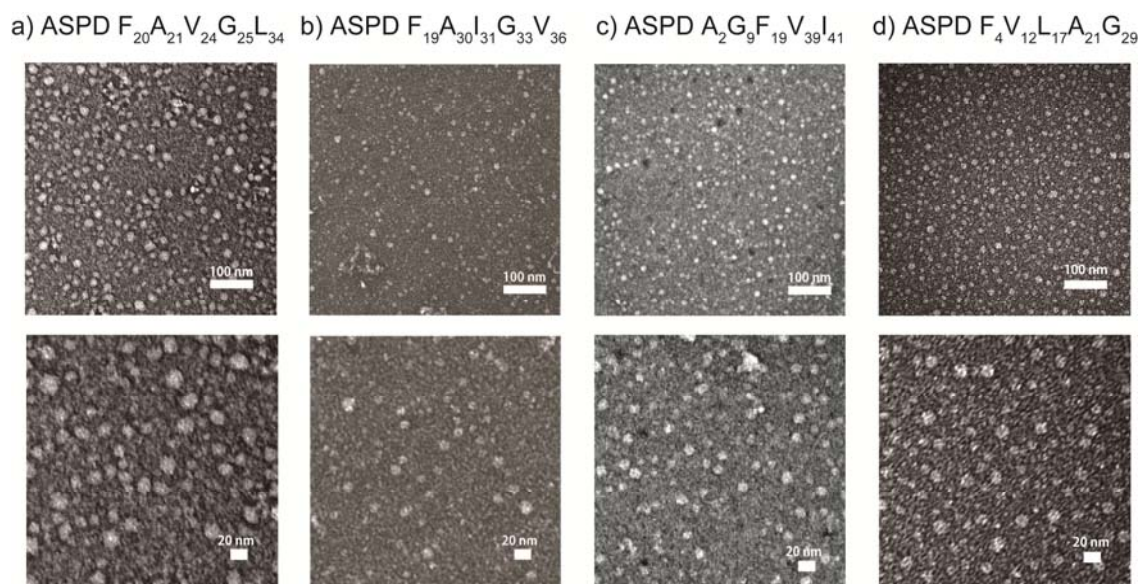


Figure 38. Transmission electron micrograph for the entire ASPD sample used for the NMR analysis in Figure 40. The images show spherical morphologies of ASPD having diameter of 10–18 nm morphologies.

The functional and structural similarity between the ASPD sample analyzed here and native ASPD were confirmed by Hoshi's group with monoclonal antibody assay (which specifically recognizes ASPD), TEM, CD, and cytotoxicity assay. The amino acid sequence of A β (1–42) is listed with the isotope labeled sites to be inspected in the NMR analysis are discussed in Figure 39.



Figure 39. Amino acid sequence of A β (1-42), where the residue names are color coded by type of amino acids as follows: negatively charged (red), positively charged (blue), hydrophilic (cyan), and hydrophobic (green) residues. The underlined residues represent those inspected in the present SSNMR analysis of ASPD.

1) A β (1-42) misfolds into a highly ordered conformer in ASPD

In an effort to seek the site-specific structural features of ASPD, we performed 2D $^{13}\text{C}/^{13}\text{C}$ correlation SSNMR experiments on four ASPD samples having different ^{13}C -labeling schemes (Figure 40 a-d; see Table IV for the list of samples). Previous studies using ASPD specific conformational antibody indicated unique structural folds of ASPD, which are commonly recognized by the antibody for both native ASPD and ASPD.⁵⁴ As discussed above, no secondary structure or site-specific structures have been available for ASPD. Likewise, there is currently no direct evidence that ordered secondary or tertiary structure exists in any pathogenically relevant amyloid intermediates at the site-specific level. The 2D $^{13}\text{C}/^{13}\text{C}$ spectra (Figure 40 a-d) show promising results for the first attempt of structural analysis of ASPD. All the ^{13}C -labeled sites were successfully assigned based on amino-acid specific exchange patterns, as shown by the color coded lines. The spectra display reasonably narrow line widths (1.9-3.7 ppm) even after considerable Gaussian convolution (1.3-1.5 ppm) for sensitivity enhancement. The natural line widths are comparable to or slightly broader than those observed for lyophilized amyloid fibril.^{20, 21, 133, 246} As a line width or a distribution of chemical shift reflects conformational heterogeneity, the reasonably narrow line widths suggest that ASPD is likely to have a well ordered structure comparable to amyloid fibril, the structure of which is known to be highly ordered. Except for some residues such as Leu-17 and Ile-31, most of the residues have a single set of cross peaks for a directly bonded ^{13}C - ^{13}C pair. The SSNMR suggests that A β in

ASPD has a well defined *single* conformer for most of the residues. This also confirms good homogeneity of the ASPD samples analyzed for this study. The result is surprising as amyloid intermediates are generally only metastable species. Even amyloid fibrils of A β , the final product in misfolding, often involve polymorphs, which cannot be easily detected by traditional spectroscopic analysis such as FT-IR or CD. A previous SSNMR study on toxic A β (1–42) indicated somewhat disordered structure.²⁴⁰ Although the recognition of ASPD by conformational antibodies was reported, it does not guarantee that the epitope structures are homogeneous. Overall, the results, for the first time, present direct evidence of a well ordered conformer in the amyloid intermediate that is pathologically relevant to AD. The N-terminal residues (Ala-2, Phe-4) have weaker signal intensities, compared with those for corresponding amino acids in other sites such as Phe-19 and Ala-21 (Figure 40 a, b). This finding indicates that the N-terminal region of A β in ASPD may be disordered with some residual structural order.

i. Sample analyzed using SSNMR

TABLE IV. A LIST OF THE ASPD SAMPLES USED FOR THIS STUDY

Sample in Figure 37	Uniformly ¹³ C ¹⁵ N labeled sites/residues	Total sample in the rotor (mg)	Peptide amount by amino-acid analysis (mg)
A	F20, A21, V24, G25, L34	38	2.7
B	F19, A30, I31, G33, V36	24.9	3.5
C	A2, G9, F19, V39, I41	30	2.4
D	F4, V12, L17, A21, G29	11	1.8

The ASPD samples (10-40mg) as received from Dr. Hoshi's group were packed in a 2.5 mm 20 μ L volume SSNMR rotor in a glove box under inert nitrogen environment with the humidity level as low as 11-13 %.

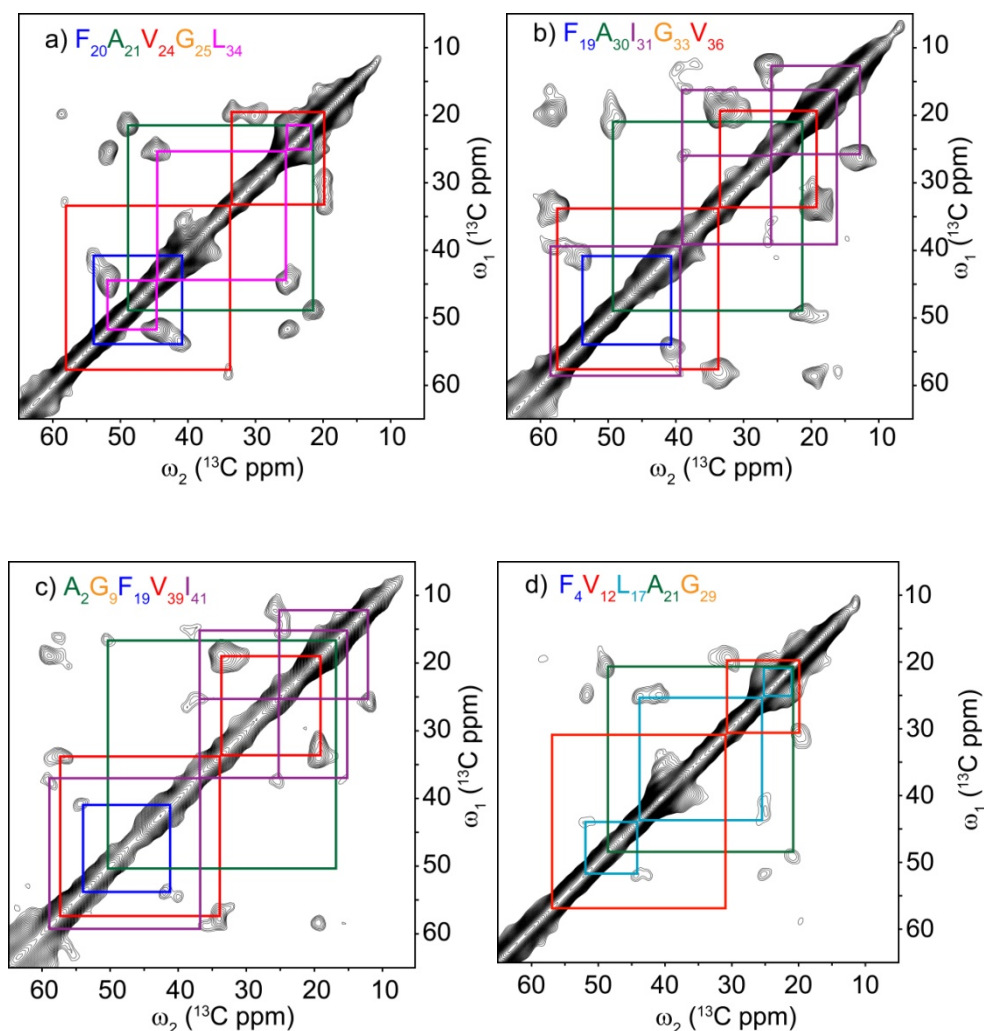


Figure 40. 2D $^{13}\text{C}/^{13}\text{C}$ SSNMR spectra of ASPD for A β (1-42) with a short-range mixing (DARR mixing time of 50 ms)²⁴⁷ at a spinning speed of 20 kHz. The A β (1-42) samples were labeled with uniformly ^{13}C - and ^{15}N -labeled amino acids (a) Phe-20, Ala-21, Val-24, Gly-25, Lue-34, (b) Phe-19, Ala-30, Ile-31, Gly-33, Val-36, (c) Ala-2, Gly-9, Phe-19, Val-39, Ile-41, and (d) Phe-4, Val-12, Leu-17, Ala-21, Gly-29. The signals were collected with a t_1 period of (a) 5 ms (b, c) 4ms (d) 3ms and a t_2 period of 10 ms. The spectrum was processed with Gaussian line broadening of (a, d) 1.3 or (b, c) 1.5 ppm on both dimensions with linear prediction on t_1 to 6 ms. The experimental times were (a, b) 4.9 days, (c) 5.5 days, (d) 8.2 days.

2) Conformational analysis of ASPD

Based on the collected ^{13}C chemical shifts (Table V), we performed an analysis of the secondary chemical shifts of the inspected residues of A β (1-42) for ASPD (Figure 41). The red

and blue bars respectively show the secondary chemical shifts of $^{13}\text{C}\alpha$ and $^{13}\text{C}\beta$, which represent deviations from the corresponding chemical shifts for model peptides in random-coil structures. It is empirically well established that a region in β -sheet structure respectively shows negative and positive secondary shifts for $^{13}\text{C}\alpha$ (blue) and $^{13}\text{C}\beta$ (red), whereas an opposite trend is observed for a helical region. The analysis in Figure 41 clearly indicates that the ASPD involves β -sheet conformations. The majority of the residues studied here are in the hydrophobic core (residues 17-24) or C-terminus regions (residues 30-42) of A β with few residues in the N-terminal region. To elucidate the conformations of ASPD, we performed the torsion angle analysis using the ^{13}C chemical shifts obtained from SSNMR experiments with TALOS software (Figure 42). The predicted torsion angles suggest that the ASPD involves a β -sheet motif to a large extent. Specifically, the hydrophobic core (residues 17-24) and the C-terminal region (residues 30-41) of the ASPD constitute the β -sheet regions.

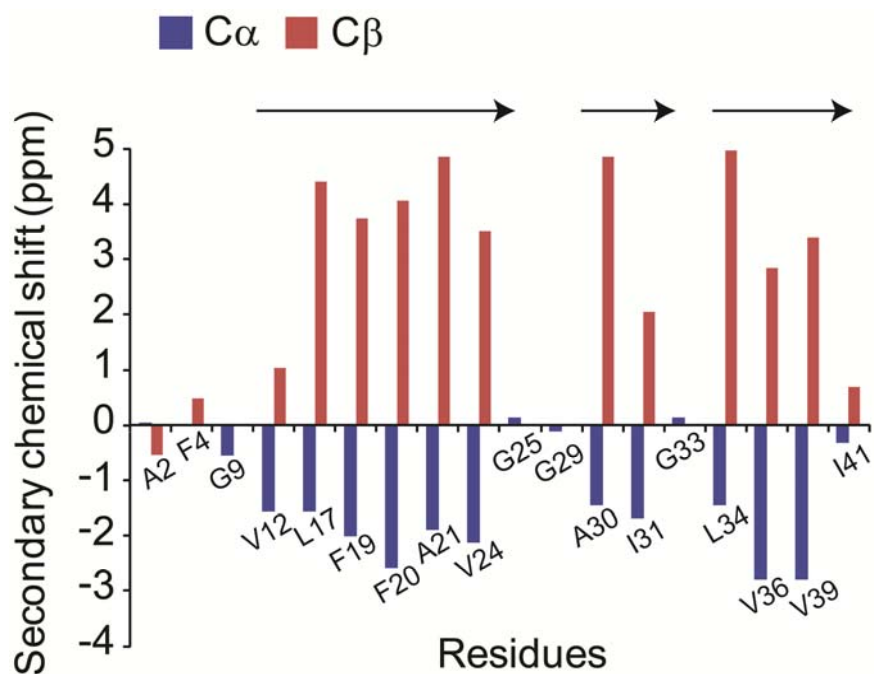


Figure 41. Secondary chemical shift analysis for the 18 residues from four different ASPD samples. The arrows indicate the β -sheet region and other residues studied are disordered.

TABLE V. ^{13}C CHEMICAL SHIFTS ASSIGNED FOR THE ASPD SAMPLES WITH PREDICTED TORSION ANGLES

Residues	Chemical shift (ppm) ¹⁾							Torsion angle(degrees)	
	CO	C α	C β	C γ	C γ 1	C γ 2	C δ	Ψ	ϕ
Ala-2		50.5	16.6						
Phe-4			38.0 ²⁾				129.2 ¹⁾		
Gly-9	170.7 ³⁾	42.6 ³⁾							
Val-12	172.5	58.8	31.8		20.1			129(\pm 11)	-120(\pm 11)
Leu-17	173.1	51.7 53.3*	44.3 42.4*	25.6				134(\pm 14)	-124(\pm 16)
Phe-19	171.3	53.9	40.9	137.0			128.9	137(\pm 23)	-129(\pm 16)
Phe-20		53.4	41.2	136.5			129.6	136(\pm 11)	-130(\pm 9)
Ala-21	172.9	48.8	21.4					146(\pm 10)	-142(\pm 12)
Val-24	172.3	58.3 59.0*	34.0 29.9*		19.9 19.6*			151(\pm 16)	-133(\pm 13)
Gly-25	169.9 ³⁾	43.2 ³⁾							
Gly-29	170.0 ³⁾	43.0 ³⁾							
Ala-30	173.2	49.2	21.4					146(\pm 10)	-130(\pm 21)
Ile-31	173.2	57.6	38.6 35.9* 41.1*		26.5 26.0* 25.2*	14.7	12.8	132(\pm 12)	-122(\pm 10)
Gly-33	169 ³⁾	43.2 ³⁾							
Leu-34	172.5	51.8	44.8	25.4				139(\pm 16)	-133(\pm 14)
Val-36	172.5	57.7	33.4		19.4			153(\pm 16)	-123(\pm 13)
Val-39		57.7	33.9		19.3			149(\pm 12)	-138(\pm 6)
Ile-41		58.8	37.4		15.1	25.9	12		

¹⁾ Referenced to TMS.

²⁾ Assigned from the side chain correlation between $^{13}\text{C}\beta$ and $^{13}\text{C}\gamma$.

³⁾ Assigned from the correlation between $^{13}\text{C}\alpha$ and ^{13}CO . * represent minor species, which were not used for the TALOS and secondary chemical shift analysis.

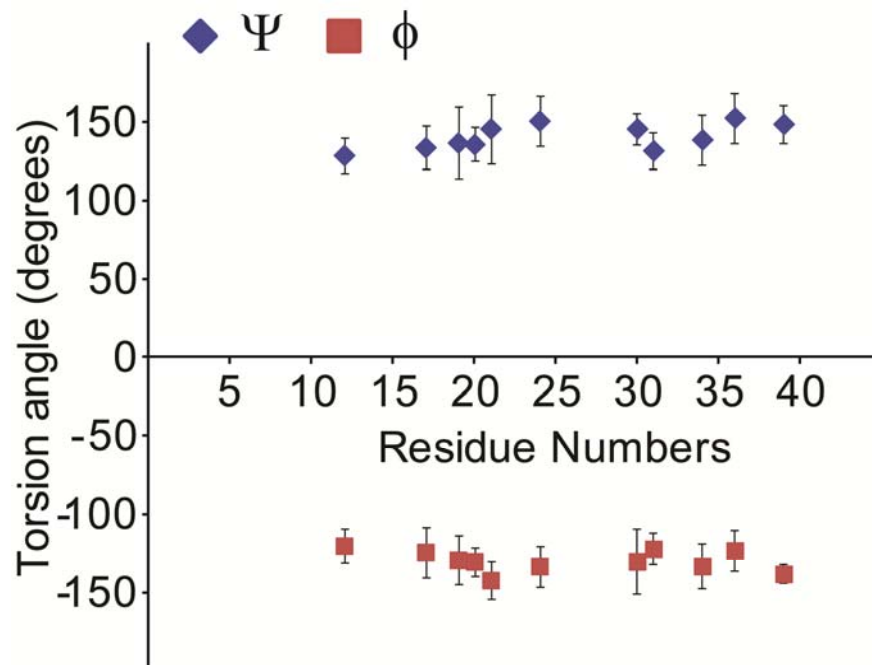


Figure 42. Torsion angle prediction using TALOS software. The predicted torsion angles suggest that $(\phi, \psi) \sim (-120^\circ, 130^\circ)$, which is consistent with β -sheet structure.

3) ASPD has a parallel β -sheet arrangement

The above results suggest that the structural motif of $A\beta$ in ASPD may be similar to those for the previously reported molecular models for $A\beta$ fibrils as well as that for the β -sheet intermediate (I_β) for $A\beta(1-40)$.^{20, 207, 225, 248, 249} These previous studies for $A\beta$ aggregates show that $A\beta$ in the fibrils and the I_β intermediates are likely to misfold into parallel β -sheet arrangements having β -turn- β motifs. On the other hand, a recent X-ray crystallography study of a 11 residue fragment of $\alpha\beta$ -crystalline showed the possibility of anti-parallel β -sheet formation in oligomeric amyloid intermediates. A recent FT-IR study implies the presence of anti-parallel β -sheet for oligomeric species of $A\beta(1-40)$, although no site-specific structural information was

obtained for the species and FT-IR analysis on heterogeneous amyloid systems are sometime contradictory.

In order to examine the supramolecular arrangement for the pathogenically relevant amyloid intermediate, we performed inter-strand ^{13}C - ^{13}C distance measurement for the ASPD sample prepared with $\text{A}\beta(1-42)$ selectively labeled at ^{13}C in Ala-30 (Figure 43). The obtained distance ($\sim 5.8 \text{ \AA}$) is consistent with parallel β -sheet arrangement. Thus, the present SSNMR data have clearly demonstrated that the pathologically relevant $\text{A}\beta$ intermediate has highly homogeneous parallel β sheet architecture for the first time. It is noteworthy that it was not expected that ASPD has a parallel β -sheet structure like amyloid fibril as ASPD does not bind to ThT, which is an indicator of amyloid. Although it is possible that the $\text{A}\beta$ in the ASPD intermediate has more complex supramolecular arrangement such as a mixed parallel and anti-parallel β -sheet arrangement, it is encouraging that this SSNMR study revealed the presence of well defined parallel β -sheet in ASPD.

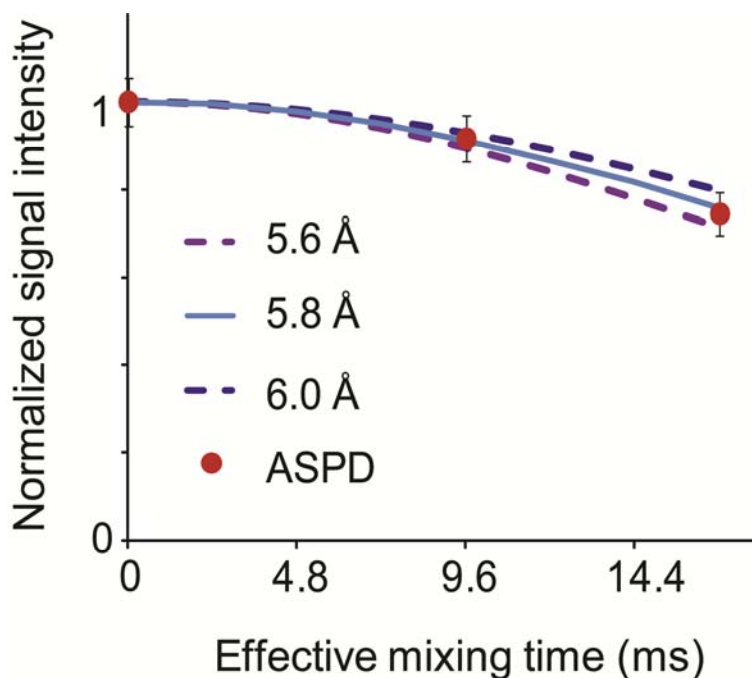


Figure 43. ^{13}CO - ^{13}CO interstrand distance measurement (solid circle) for Ala-30 by CT-fpRFDR measurement with simulated dephasing curves for 5.6 Å (purple), 5.8 Å (cyan), and 6.0 Å (blue).

4) ASPD Misfolds Differently from Fibril

Our remaining question is whether the structure of A β (1-42) in ASPD is notably different from that in amyloid fibril, which was previously proposed to have a β -turn- β structure.^{21, 22, 207, 246, 248} Figure 44 shows the tentative cartoon showing secondary structure of ASPD derived from ^{13}C chemical shifts. The arrows indicate the β -sheet region of ASPD.

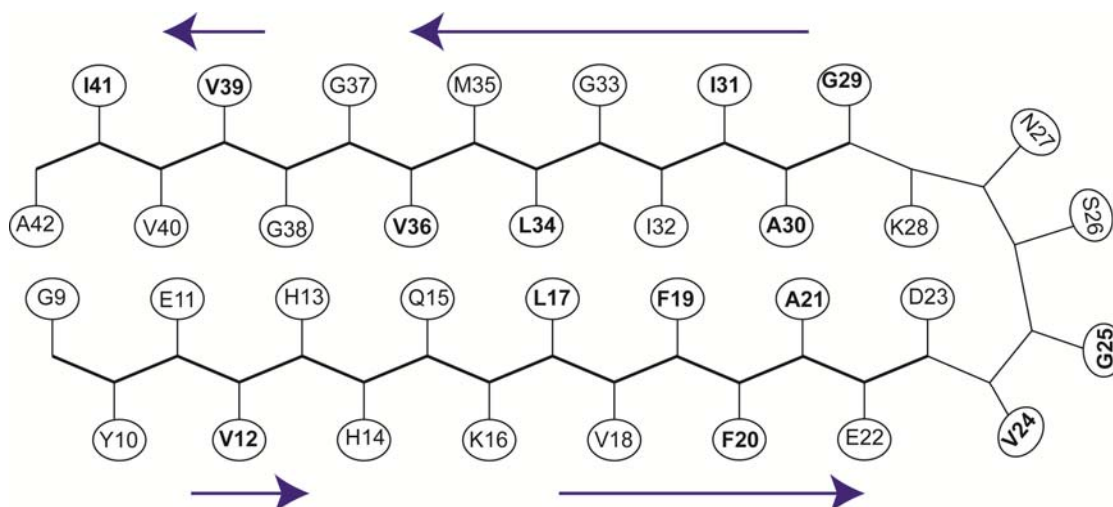


Figure 44. A possible structural model based on the present data. The residues inspected by SSNMR are in bold. The β -sheet regions indicated in Figure 41 and 42 are represented by blue arrows.

Figure 45 shows the β -sheet region of ASPD (magenta) on the $A\beta(1-42)$ fibril structural model obtained by H/D exchange NMR. While the region identified as β -sheet in ASPD in the present study overall agrees with that of the $A\beta(1-42)$ fibril structure, the β -sheet region for ASPD includes Ala-30, which was identified as the loop region of the fibril.

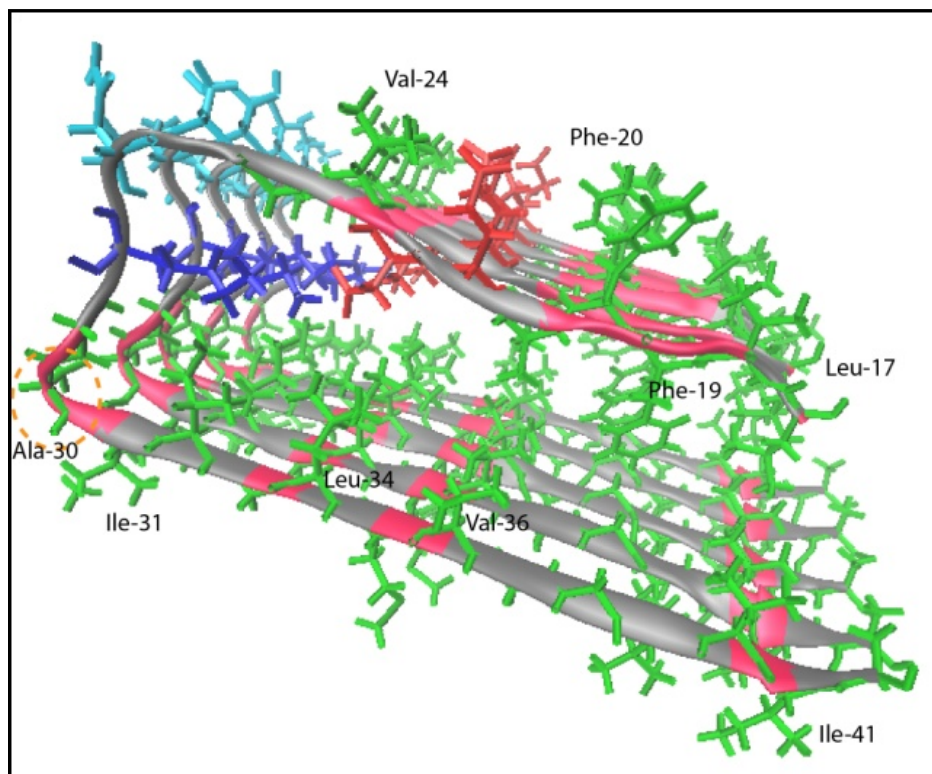


Figure 45. Overlay of the β -sheet region (magenta) on amyloid fibril structure of $A\beta(1-42)$ obtained by H/D exchange NMR, where the side chains are color coded following that in Figure 41. The residues 1-16 are omitted in the structure as these residues are disordered in the fibril structure.

Also, our preliminary $^{13}\text{C}/^{13}\text{C}$ SSNMR data of amyloid fibril of $A\beta(1-42)$ as shown in Figure 46 b show considerably different chemical shifts from the corresponding shifts of ASPD in Figure 46 a. Thus, the conformations and possibly overall packing of $A\beta(1-42)$ of ASPD are considerably different from those of the corresponding fibril sample. Further analysis and detailed comparison between ASPD and amyloid fibril is required for identifying complete structural differences.

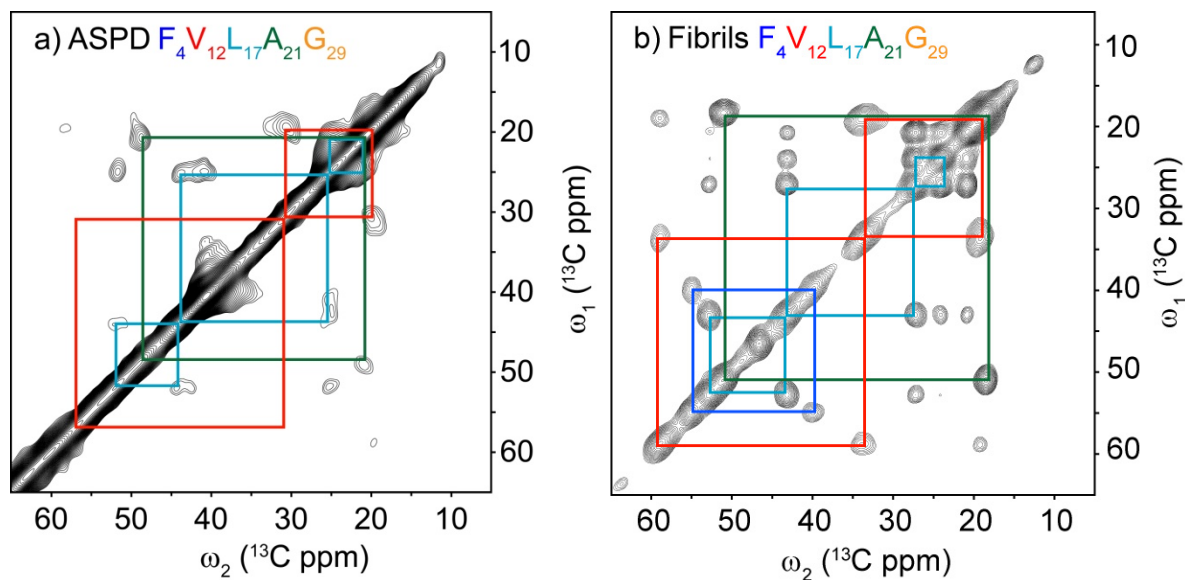


Figure 46. Comparison of the 2D $^{13}\text{C}/^{13}\text{C}$ SSNMR spectra of (a) ASPD and (b) Fibrils for A β (1-42) with a short-range mixing (DARR mixing time of 50 ms). The A β (1-42) was uniformly ^{13}C - ^{15}N -labeled at Phe-4, Val-12, Leu-17, Ala-21 and Gly-29.

Thus, the conformations and possibly the packing of A β (1-42) of ASPD could be considerably different from those of the corresponding fibril sample. Further analysis and detailed comparison between ASPD and amyloid fibril will be required for a complete molecular level analysis.

C) Discussion

1) Structural Features of ASPD and Significance

The present study revealed that ASPD contains a parallel β -sheet structure as a primary structural motif. Unlike other diffusible oligomer systems for which detailed structures were previously studied, the presence of native ASPD in human AD brains exhibits a correlation with the severity of AD as discussed above.⁶¹ Thus, this study presents the first molecular-level structural evidence that A β (1-42) is likely to misfold into diffusible aggregates, which have a

well defined single conformer made of a parallel β -sheet motif for the pathologically relevant ASPD species. As described above, it has been generally very difficult to study detailed molecular structures of amyloid intermediates due to difficulties of sample preparation and other factors. Our study presents a novel approach to examine a molecular structure of a pathologically relevant amyloid intermediate through examining a synthetic intermediate species, for which conformational and biochemical similarity to a native amyloid intermediate is established. Unlike many structural studies on model amyloid peptides, our study focused on the full-length $A\beta(1-42)$, which is known to be more pathogenic than $A\beta(1-40)$, but has been difficult to study even for more stable amyloid fibrils. Although structural information is still limited, the present study yielded the most detailed structural features among the previously published works for amyloid intermediate of $A\beta(1-42)$.

2) Difference from other Amyloid aggregates for $A\beta$

For diffusible aggregates of the full-length $A\beta$, there have been very limited structural studies. Our group previously reported that spherical aggregates of $A\beta(1-40)$ called I_β having a diameter of ~ 20 nm.²¹ Our SSNMR data showed that I_β is likely to have a β -turn- β motif that is very similar to that for $A\beta(1-40)$ fibril. Based on ^{13}C SSNMR data, the molecular conformations of $A\beta$ in I_β are likely very similar to those in fibril. As I_β is observed at the late stage of misfolding right before the conversion to fibril, this may be reasonable. Olejniczak, et.al²⁴⁹ studied SDS-stabilized non-toxic spherical oligomers for $A\beta(1-42)$ with diameters of 1-2 nm (2-6 mer), which are called preglobulomers. It was reported that the preglobulomers also show a β -turn- β motif in which two β -strands (residues 18-23 and 29-40) are connected by a loop (residues 22-28). Interestingly, they reported that in the preglobulomer, the β -strand in residues 18-22

form intra-molecular anti-parallel β -sheet with the strand in residues 29-32 whereas the strand in residues 34-40 form intermolecular parallel β -sheet. Although Olejniczak, et.al reported the presence of larger globulomer having a diameter of 4-5 nm, its structure was not identified. More recently, Smith.et.al reported that $A\beta(1-42)$ forms stable disk-like oligomers at low temperature. Although a hypothetical packing was proposed for the disk-like oligomer, the secondary structure and supermolecular arrangements of the disk-like oligomers are largely unknown.²²

3) Transition to a Toxic Amyloid Intermediate

It is currently not well understood how $A\beta$ or other amyloid protein gains cytotoxicity through a structural transition along the misfolding path from non-toxic monomers. It was proposed by Chimon et.al., that β -sheet formation triggers the onset of cytotoxicity for amyloid intermediates.²⁴¹ The hypothesis has been largely supported by various previous studies on amyloid intermediates for $A\beta$ and other proteins. The present study also supports the hypothesis for the pathogenically relevant amyloid aggregates. Except for a few examples, small oligomers (< 10 mer), which are typically less ordered, exhibit no toxicity. It was recently proposed that amyloid protein undergoes a transition from anti-parallel β -sheet configuration to parallel β -sheet configuration in the course of misfolding toward fibril formation.²⁴³ In this work, we did not observe evidence that ASPD involves any anti-parallel β -sheet structure. As this is the first structural study of a pathogenically relevant amyloid intermediate, it is not clear whether there are any other types of toxic amyloid intermediates relevant to the onset of AD. Further studies of other pathogenically relevant amyloid aggregates will be needed to identify a misfolding pathway of $A\beta$ in AD. An excellent study was recently reported for amyloid fibril of $A\beta(1-40)$ prepared with “seed” fibril using amyloid aggregates from a brain affected by AD.²⁵⁰ Our

approach provides a novel means to examine other pathogenically relevant amyloid intermediates, for which “seeding” has not been effective.

D) Materials and Methods

ASPD sample was prepared as described previously by Dr. Hoshi's group.⁵⁴ Briefly, A β (1-42) was synthesized and purified as described previously using solid-phase synthesis with standard Fmoc synthesis and cleavage protocols and HPLC purification.¹⁸¹ The synthesis was performed with an ABI 433 peptide synthesizer at UIC with Fmoc protected ¹³C- and ¹⁵N-labeled amino acids at selected sites. Fmoc protection of the labeled amino acids was performed at the UIC RRC.²³⁸ The peptide was purified by reverse-phase HPLC with a Agilent Zorbax column at the UIC Department of Chemistry. Purity of the A β samples was determined based on the MALDI-TOF mass spectra collected at the UIC RRC to be approximately 90 % and 95 % before and after the HPLC purification, respectively.

All the SSNMR experiments were performed with a Varian Infinity-plus or Bruker Avance III SSNMR spectrometer with a homebuilt 2.5-mm triple-resonance MAS probe at 9.4 T (¹H frequency of 400.2 MHz) in the double- or triple-resonance configuration. The lyophilized ASPD samples (10-40 mg) were packed in a 2.5 mm 20 μ L volume SSNMR rotor in a glove box under inert nitrogen environment with the humidity level as low as 11-13 %. The spinning speed was set to 20,000 \pm 3 Hz throughout the experiments. In the 2D ¹³C/¹³C correlation experiments with DARR mixing²⁴⁷ in Figure 40, 1.8-3.5 mg of isotope labeled A β (1-42) ASPD samples were used. The SSNMR experiments were performed following the established procedures used for amyloid intermediates of A β (1-40).²⁴¹ (See materials and methods section in Chapter III and IV.)

VI) CHOICE OF DOPANTS FOR PARAMAGNETIC RELAXATION-ASSISTED CONDENSED DATA COLLECTION METHOD AND ITS APPLICATION AT HIGH MAGNETIC FIELD

A) Introduction

One of the major drawbacks in the field of biological SSNMR is poor sensitivity, which requires enormous amount of machine time to acquire good quality multidimensional NMR spectra. Recently, sensitivity enhancement in SSNMR was achieved by higher magnetic fields, better instrumentation, probes and through improved pulse sequences. Under the conditions mentioned above, a majority of biomolecular SSNMR experiments are performed by cross polarization magic angle spinning (CPMAS) conditions to gain sensitivity and resolution enhancement. During the cross polarization (CP), the magnetization is transferred from ^1H nuclei to either ^{13}C or ^{15}N for sensitivity enhancement followed by other RF pulses depending on the need of the information which needs to be extracted. Since the polarization transfer is from the abundant ^1H spins in the CP experiments, for each repetition of the scan during the signal averaging, it is necessary to wait for the ^1H magnetization to relax back to equilibrium. Typically, the pulse delay or the repetition time is set three to five times the ^1H T_1 for the recovery of ^1H magnetization. Consequently, 95-99% of the experimental time, the NMR instrument is idle during long recycle delays to protect the probe from arcing due to RF irradiation, or to avoid sample degradation due to heating in conventional SSNMR. To overcome this problem, Ishii and co-workers¹⁰⁴ have developed a method by which the ^1H T_1 's can be reduced to the order of 50-100 ms by careful selection of paramagnetic relaxation agents or paramagnetic dopants by PRE. The paramagnetic Cu(II)-EDTA complex was used in this method to reduce the ^1H T_1 by several orders of magnitude. Thus, the experimental times in biomolecular SSNMR were reduced by several orders of magnitude by faster pulse delays. The

concentration of the paramagnetic dopant used in our studies for the reduction in ^1H T_1 were minimal and the effect on transverse relaxation rate (T_2) were negligible. Thus the resolution in ^{13}C and ^{15}N SSNMR were not compromised. Reduction of ^1H T_1 by Cu(II)-EDTA was successfully tested on amorphous A β fibrils and protein micro-crystals and demonstrated an acceleration of 5-20 fold in the data acquisition in comparison to the traditional method. This method was termed as paramagnetic relaxation-assisted condensed data collection (PACC). However, the Cu(II)-EDTA complex used in this method may not be an universal paramagnetic dopant suitable for wide variety of biological systems such as RNA, DNA protein complex, membrane proteins or other bio-polymers. These biomolecules could be subjected to oxidation in presence of Cu(II)-EDTA. Therefore, it is necessary to have different choice of paramagnetic dopants for this method.

One of the key requirements for the implementation of PACC method is the fast MAS and low-power ^1H decoupling during the signal acquisition. Traditionally, at moderate MAS (≤ 20 kHz) the ^1H heteronuclear couplings were not averaged out and require high power (~ 100 kHz) ^1H decoupling during acquisition to gain resolution enhancement. High power ^1H decoupling limits the acquisition time and requires long pulse delays to compensate for the heat generated and to keep the biological samples from degradation. ^1H homonuclear or the heteronuclear couplings can be suppressed by spinning the sample at high frequencies. Commercial probes with MAS rates that exceed the dipolar coupling strength are available which do not require high power decoupling for gaining resolution in the spectrum. A relatively low power 8-12 kHz ^1H IpTPPM decoupling field is sufficient for removing the residual dipolar coupling significantly improving the resolution.¹⁸³ This decoupling sequence was successfully tested in high-resolution SSNMR in a 9.4 T magnet at 40 kHz MAS. At higher field, 18.8 T or

above, the ^1H lpTPPM was not tested at ultra-fast MAS (≥ 70 kHz) until recently, since the ^1H bandwidth is twice as large when compared to the 9.4 T magnet. Here in this chapter we will demonstrate the use of ^1H lpTPPM decoupling at a high magnetic field (18.8 T) and ultra-fast MAS conditions for the sensitivity enhancement using PACC method for the metal bound biological solids.

B) Results and Discussion

1) Choice of paramagnetic dopants

The PRE arising from an unpaired electron in the paramagnetic metal ion is primarily dependent on the electronic correlation time (τ_c), electron spin number (S), electron nuclear spin interaction properties, the electron g-tensor. The presence of the paramagnetic metal ions enhances longitudinal (R_1) and transverse (R_2) nuclear spin relaxation in the solid-state and the dipolar relaxation mechanism is given by the Solomon equation as shown in eqn. 29 and 30.

$$R_1 \approx \frac{2}{15} \left(\frac{\mu_0}{4\pi} \right)^2 \frac{\gamma_I^2 g_e^2 \beta_e^2 S(S+1)}{r^6} \left(\frac{3\tau_c}{1+\omega_I^2\tau_c^2} + \frac{7\tau_c}{1+\omega_e^2\tau_c^2} \right) \dots\dots\dots (29)$$

$$R_2 \approx \frac{1}{15} \left(\frac{\mu_0}{4\pi} \right)^2 \frac{\gamma_I^2 g_e^2 \beta_e^2 S(S+1)}{r^6} \left(4\tau_c + \frac{3\tau_c}{1+\omega_I^2\tau_c^2} + \frac{13\tau_c}{1+\omega_e^2\tau_c^2} \right) \dots\dots\dots (30)$$

where β_e is Bohr magneton, γ_I is the nuclear gyromagnetic ratio, S electron spin number, g_e is the free spin electron g factor, ω_I and ω_e are the angular frequencies of the nucleus and electron respectively. $\omega_I = -\gamma_I B_0$ and $\omega_e = -\gamma_e B_0 = 658 (\omega_I)$ for protons.

The longitudinal PRE (R_1) and transverse PRE (R_2) are proportional to the square of the electron-nucleus dipolar interaction i.e., the PRE arises from the magnetic dipolar interactions between a nucleus and an unpaired electron in the paramagnetic metal center. This interaction is

distance dependant $\langle r^{-6} \rangle$ which provides quantitative structural information of the metallo proteins. The paramagnetic metal ions used for PRE measurements in these studies are selected based on the g-tensor. Nitroxide spin labels, Cu^{2+} , Mn^{2+} complexes with EDTA and Gd^{3+} have nearly isotropic g tensors, which do not contribute to the pseudo-contact shifts. These dopants are considered versatile dopants for characterization of the biomolecules using PRE in NMR. Lanthanide metal ions except Gd^{3+} have strong anisotropic g tensor inducing pseudocontact shifts. These shifts have typical magnitudes on the order of a few ppm to tens of ppm depending on the distance between the paramagnetic metal center and nuclei.

In this study, we are interested in searching substitutes for Cu(II)-EDTA in the application for PACC method. It has been clearly demonstrated that Cu(II)-EDTA significantly reduces the ^1H T_1 without affecting the spectral quality. It is very important to have different choices of paramagnetic relaxation agents, in the case Cu(II)-EDTA is not suitable for some specific systems. Ni(II), Gd(III) and Co(II) paramagnetic complexes are found to be alternative choice of paramagnetic dopants for the PACC method. These complexes were incubated with lysozyme microcrystals and the ^{13}C CPMAS spectral features and the effect on ^1H T_1 's were examined. The ideal condition is that the dopants should reduce the ^1H T_1 by 10 fold to 50-100 ms without degrading the spectral resolution or inducing any changes in the peak positions. It was confirmed that the ^1H T_1 for lysozyme microcrystals doped with 3 mM Ni(II)-EDTA was reduced to 88 ms from 530 ms observed for an undoped sample (Figure 47 a,b). The ^1H T_1 value is comparable to 73 ms for 10 mM Cu(II)-EDTA doped lysozyme obtained for the same microcrystal sample (Figure 47 c). A ^{13}C CPMAS spectrum of lysozyme doped with 3 mM Ni-EDTA (Figure 47 b) showed no major spectral degradation, compared with that of undoped lysozyme (a) and lysozyme doped with 10 mM Cu(II)-EDTA (c). The spectral data indicates that

Ni(II)-EDTA is one of the alternative dopants which can be used in the PACC method. The concentration of Ni(II)-EDTA was approximately 3 times lesser than 10 mM Cu(II)-EDTA which is consistent with spin quantum number (S) value of 1 for Ni and $\frac{1}{2}$ for Cu. The relaxation depends on S by $2S(S+1)$ as given in eqn. 29.

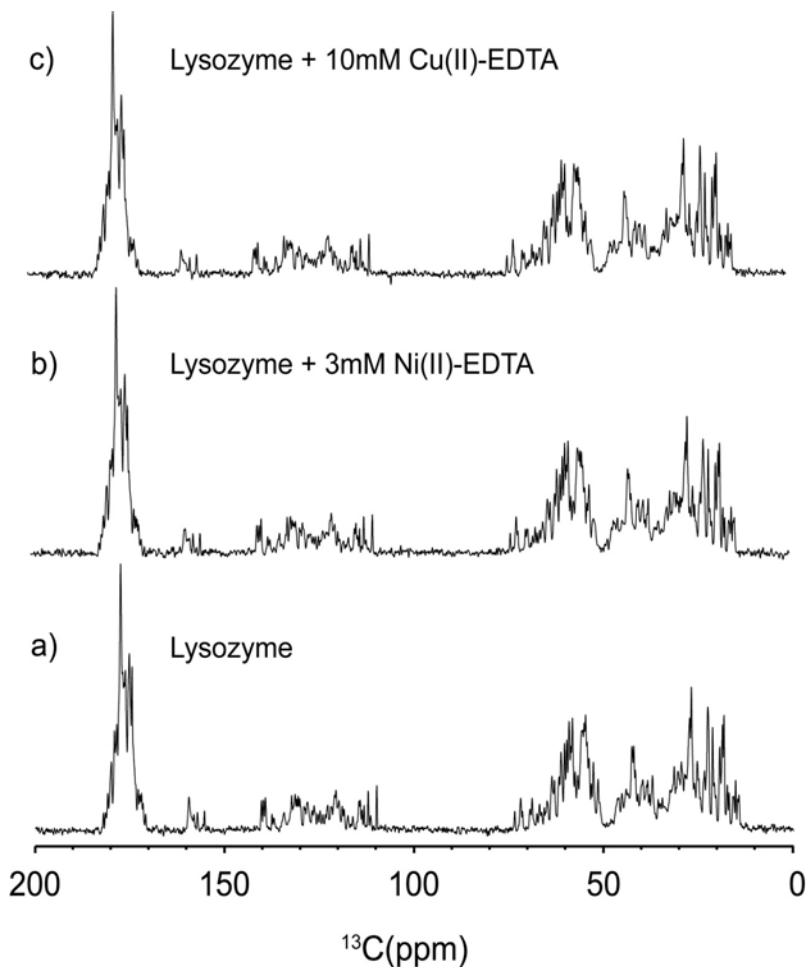


Figure 47. The comparison of ^{13}C CPMAS spectra of unlabeled lysozyme (a) without dopants (b) with 3 mM Ni(II)-EDTA, and (c) with 10 mM Cu(II)-EDTA. A total of 41 k scans were collected for each spectrum at a spinning speed for 40 kHz. Approximately 6 mg of the protein sample was used for each spectrum. The recycle delays of (a) 1.55 s, (b) 260 ms, (c) 220 ms were matched to $3\ ^1\text{H}$ T_1 . The total experimental time is (a) 18.9 h (b) 3.5 h (c) 2.9 h.

We also tested Ni(II)-DO2A, a macromolecular complex of Ni which has been successfully tested in solution NMR for PRE measurement.²⁵¹ For the lysozyme sample doped with Ni(II)-DO2A, we obtained a comparable ^1H T_1 reduction (^1H $T_1 \sim 96$ ms), but at a higher concentration (20 mM) than the amount of Ni(II)-EDTA. The electron correlation time of Ni in Ni(II)-DO2A could be different in comparison with Ni(II)-EDTA; this could be the probable reason for the increase in dopant concentration. Increased metal ion concentration up to 20 mM of Ni(II)-DO2A shows similar effect in relaxation compared to Ni(II)-EDTA, but we observed some site-specific line broadening in the aromatic regions of the lysozyme ^{13}C CPMAS spectrum as shown in Figure 48 a,c. The inset in Figure 48 shows the aromatic region expansion of the ^{13}C CPMAS spectra. See materials and methods section for the synthesis of Ni(II)-DO2A complex.

Other alternatives such as Gd(III) and Mn(II) compounds, which have been popular as relaxation and contrast agents for NMR and magnetic resonance imaging, such paramagnetic metal ions having relatively long τ_c ($\tau_c > 10^{-9}$ s) are probably not suitable for our purpose since these ions have more pronounced effects on R_2 rather than R_1 , causing line broadening and a loss of resolution. For demonstration purposes, we tested Gd(III)-DETPA to examine its relaxation properties, where DETPA is an analog of EDTA. Although we found that doping of 1 mM Gd(III)-DEPTA reduces ^1H T_1 of lysozyme to 100 ms, lines of a ^{13}C CPMAS spectrum of the Gd-DETPA doped sample were subject to considerable broadening (~ 2.5 times) as shown in Figure 48 b. A total of 203 k scans were collected for the spectrum in Figure 48 b to get equivalent sensitivity to that of the undoped lysozyme sample in Figure 48 a, since the lines were severely broadened out by Gd(III)-DEPTA.

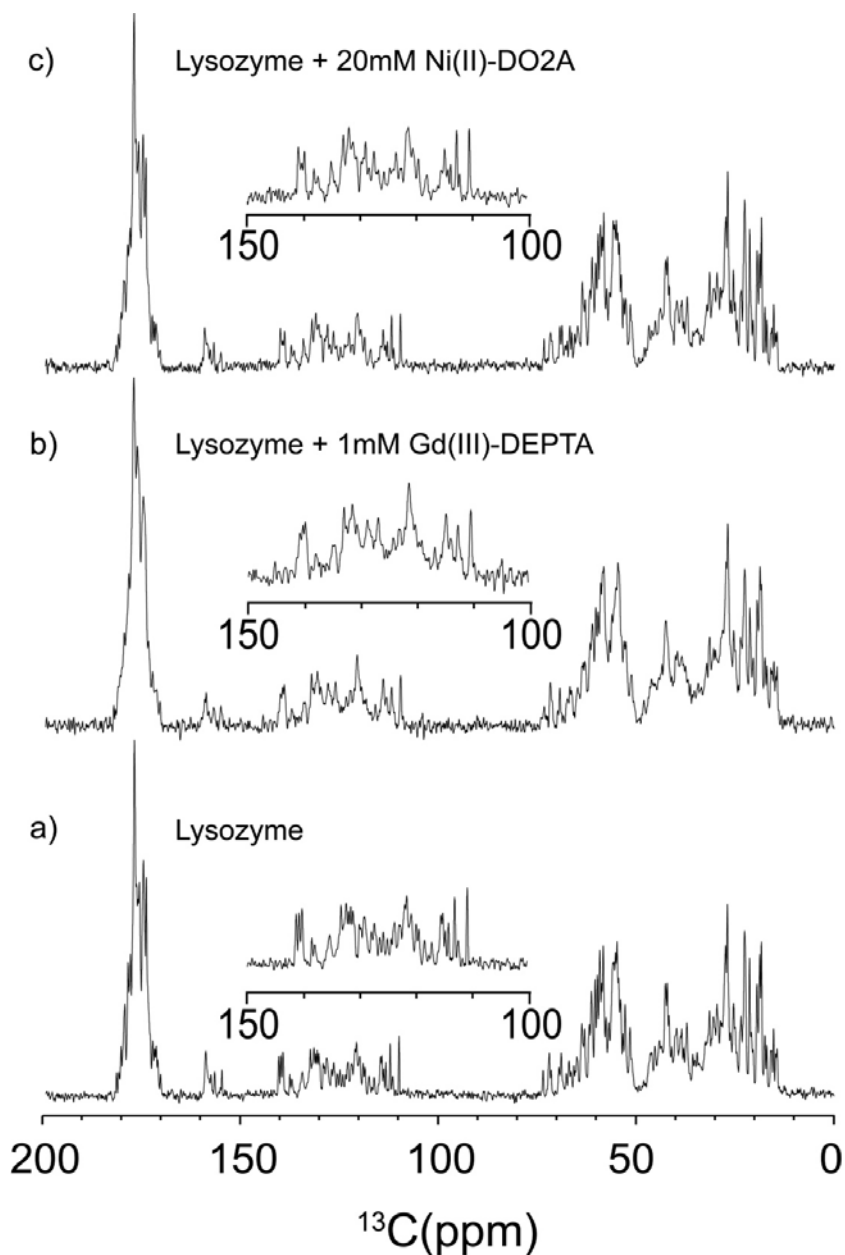


Figure 48. The comparison of ^{13}C CPMAS spectra of unlabeled lysozyme (a) without dopants (b) with 1mM Gd(III)-DEPTA, and (c) with 20 mM Ni(II)-DO2A. A total of 41 k scans were collected for spectrum in (a) and (c) and 203 k scans for the spectrum in (b) at a spinning speed for 40 kHz. Approximately 6 mg of the protein sample was used for each spectrum. The recycle delays of (a) 1.55 s, (b) 300 ms, (c) 288 ms were matched to $3\ ^1\text{H}\ T_1$. The total experimental time is (a) 18.9 h (b) 17.3 h (c) 3.4 h.

The reduction in the $^1\text{H } T_1$ depends on the concentration of the paramagnetic dopants. The Ni(II)-EDTA and Cu(II)-EDTA concentration dependence in the tuning of $^1\text{H } T_1$ was tested with the ^{13}C CPMAS of lysozyme. Figure 49 shows the comparison of the ^{13}C CPMAS obtained with PACC method using (a) 10 mM Cu(II)-EDTA with that of the ^{13}C CPMAS obtained with (b) 6mM Ni(II)-EDTA and (c) 20 mM Cu(II)-EDTA. At higher concentrations of the paramagnetic dopants, the $^1\text{H } T_1$'s were short but the resolution is moderately affected which can be clearly seen in the spectra. The comparison of different paramagnetic dopants in reducing the $^1\text{H } T_1$, the dopant concentration required and resulting ^{13}C linewidths were summarized in Table VI. We also think that paramagnetic ions having large g-anisotropy such as many lanthanide ions may introduce detectable changes in the shift positions through pseudo contact interactions. Cu(II) and 5-6 coordinate Ni(II) compounds are suitable dopants for the bio-molecular SSNMR experiments because τ_c for these compounds are in a range of $10^{-10} - 10^{-9}$ s and the g-anisotropy for these metal ions are typically small. Further investigation is likely to offer various paramagnetic compounds suitable for the PACC approach. Other relaxation agents such as Co(II)-EDTA have been tested for the relaxation enhancement. Co(II)-EDTA doesn't reduce the $^1\text{H } T_1$ considerably though the electron spin correlation time ($\sim 10^{-11}$ s) is very short for high spin Co(II) coordinated complex.

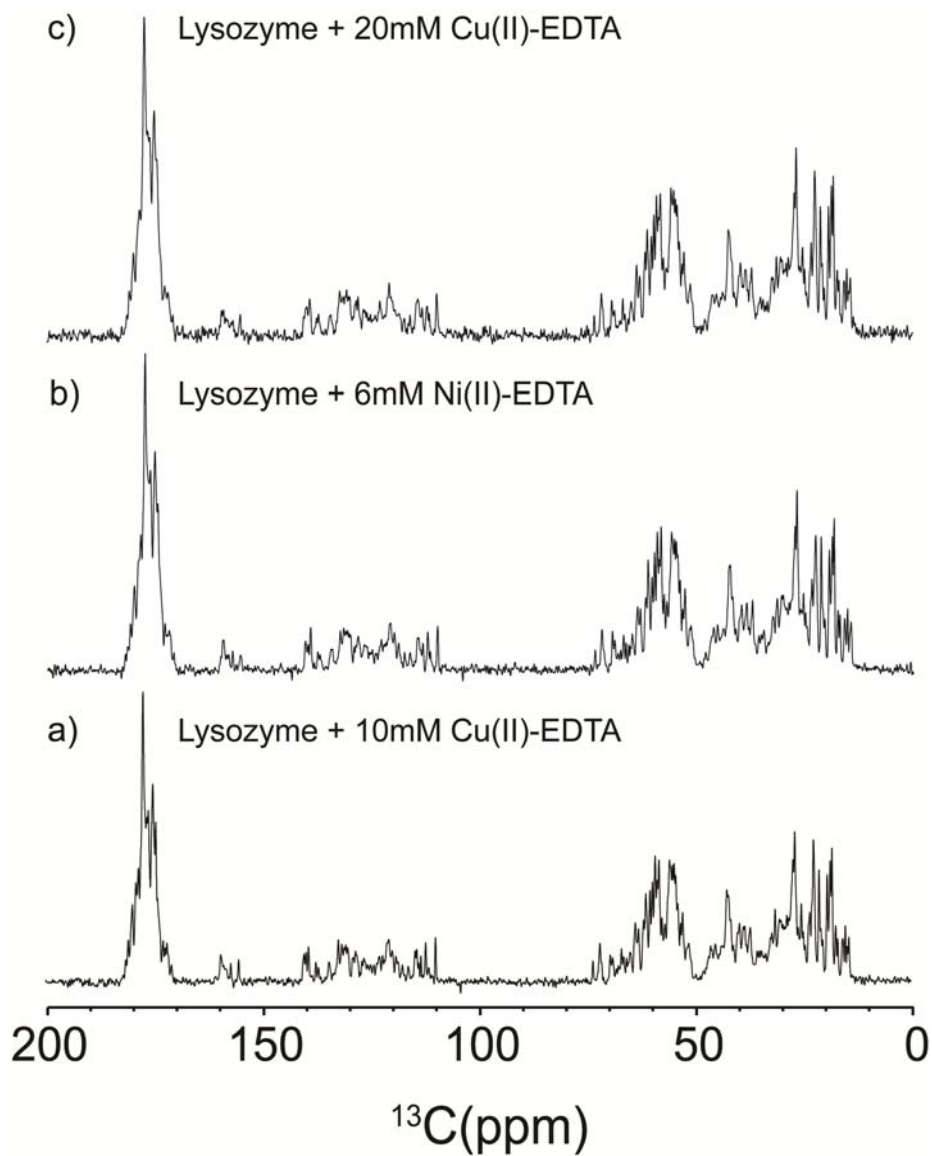


Figure 49. Comparison of ^{13}C CPMAS spectra of lysozyme (a) with 10 mM Cu(II)-EDTA (b) with 6 mM Ni(II)-EDTA, and (c) with 20 mM Cu(II)-EDTA. A total of 41k scans were collected for each spectrum at a spinning speed for 40 kHz. Approximately 6mg of the protein sample was used for each spectrum. The recycle delays of (a) 220 ms, (b) 177 ms, (c) 165 ms were mated to $3\ ^1\text{H}\ T_1$. The total experimental time is (a) 2.9 h (b) 2.1 h (c) 1.9 h.

TABLE VI. COMPARISON OF THE EFFECT OF DIFFERENT PARAMAGNETIC RELAXATION DOPANTS AND THEIR CONCENTRATION DEPENDENCE ON ^1H T_1 AND ^{13}C LINE BROADENING. THE LINE WIDTHS WERE MEASURED ONLY FOR THE SPECTRA WHICH SHOWED CONSIDERABLY SHORT ^1H T_1 'S WHICH WERE USED FOR THE PACC METHOD.

Dopents	Gd(III)- DETPA	Co(II)-EDTA		Ni(II)-DO2A				Cu(II)-EDTA		Ni(II)-EDTA			
[Dopents]mM	1	1	5	5	10	15	20	10	20	1	2	3	6
$^1\text{H}T_1$ (Error) ms	99 (± 11)	430 (± 7)	279 (± 9)	214 (± 4)	139 (± 3)	96 (± 4)	75 (± 6)	73 (± 4)	52 (± 4)	171 (± 3)	129 (± 5)	88 (± 5)	59 (± 4)
R1 (Error) (s^{-1})	10.1 (± 1.1)	2.3 (± 0.04)	3.6 (± 0.1)	4.7 (± 0.1)	7.2 (± 0.2)	10.4 (± 0.4)	13.3 (± 1.1)	13.7 (± 0.8)	19.2 (± 1.5)	5.8 (± 0.1)	7.8 (± 0.3)	11.4 (± 0.6)	16.9 (± 0.6)
Line Broadening (Hz)	21-27	-	-	-	-	-	2-12	6-10	3-23	-	-	3-9	7-17
τ_c (s) [#]	$10^{-8} - 10^{-9}$	$5 \times 10^{-12} - 10^{-13}$		Nk				$(1-5) \times 10^{-9}$		10^{-10}			
S	7/2	3/2		1				1/2		1			

^{nk} represents not known.

[#] represents the τ_c values taken from Current methods in Inorganic chemistry, Vol 2, Solution NMR of Paramagnetic NMR²²⁶

2) ^{13}C SSNMR by PACC for α -spectrin II (Sp α II 1-147) microcrystals

We present a comparison of ^{13}C CPMAS spectra for uniformly ^{13}C - and ^{15}N -labeled 147-residue recombinant protein of the cytoskeletal protein α -spectrin II (Sp α II(1-147)) in Figure 50 (a) in the presence of 50 mM Cu(II)-EDTA dopant and (b) absence of the dopant. The molecular mass of this system is ~ 19 kDa, which is larger than that of ubiquitin or A β (1-40) fibrils. The system is expected to be highly helical protein. Indeed, ^{13}C O shifts in the Figure 50 suggest that the system is highly helical. ^1H T_1 values for the undoped and doped samples were 530 ms and 120 ms, respectively. The spectral features in Figure 50 (a) and (b) are nearly identical. The difference spectrum in (c) shows that no additional chemical shifts or line broadening is detectable from the 1D spectra, despite the considerable reduction in ^1H T_1 by ~ 4.5 fold with the paramagnetic doping. The 2D $^{13}\text{C}/^{13}\text{C}$ correlation spectra for the Sp α II sample, also showed nearly identical spectra for the doped and undoped Sp α II samples as shown in Figure 51. The spectrum obtained by PACC method is in red and the spectrum corresponding to traditional acquisition method is in black. The spectra were overlaid on top of each other and the results indicate that the spectra were identical with respect to each other. The results experimentally show that the PACC approach can be effectively implemented for globular proteins of moderate molecular masses.

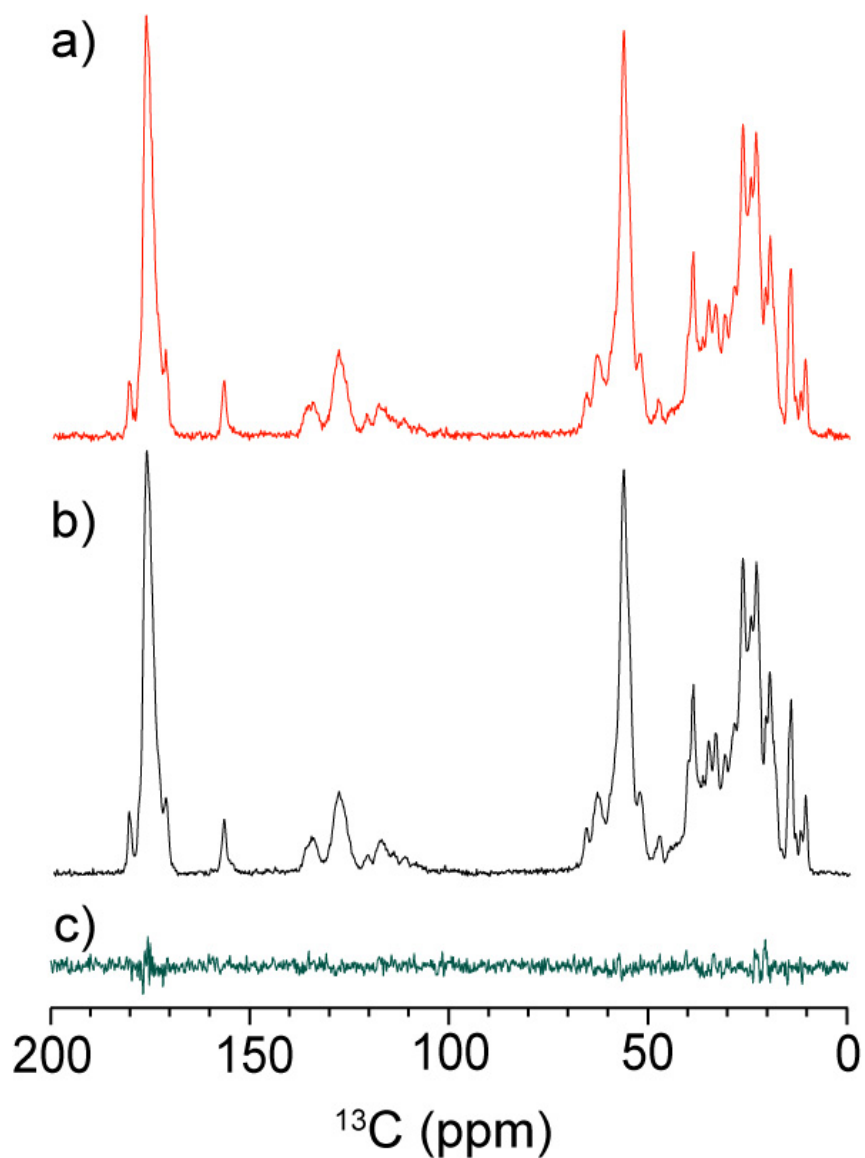


Figure 50. Comparison of ^{13}C CPMAS spectra of 147-residue recombinant protein of the cytoskeletal protein α -spectrin II (SpaII(1-147)) (a) with 50 mM Cu(II)-EDTA and (b) without doping, together with (c) a difference spectrum. The samples are uniformly ^{13}C - and ^{15}N -labeled. The ^{13}C shifts are referenced to DSS. A total of 128 scans were collected for each spectrum of in (a, b) at a spinning speed of 40 kHz. Approximately 2.5 mg of the protein sample was used for each spectrum of (a, b). The recycle delays were (a) 1.6 s and (b) 360 ms.

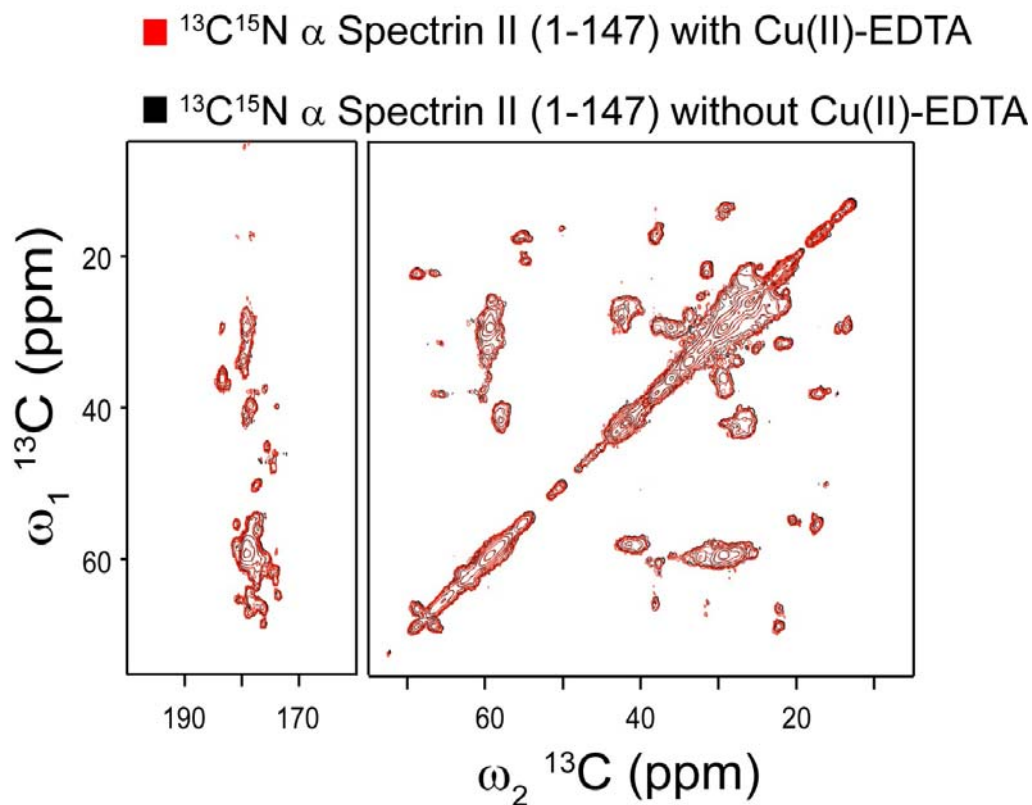


Figure 51. Comparison of $^{13}\text{C}/^{13}\text{C}$ fpRFDR 2D spectra of 147-residue recombinant protein of the cytoskeletal protein α -spectrin II (Sp α II(1-147)) without and with 50 mM Cu(II)-EDTA doping. The samples are uniformly ^{13}C and ^{15}N -labeled. The ^{13}C shifts are referenced to DSS.

3) Spinning speed dependence of ^1H T_1

Wickramasinghe et.al proposed the relaxation mechanism for the PACC method.¹³⁹ The ^1H polarization relaxed on protein surface by paramagnetic dopants is transferred to ^1H spins inside the proteins via ^1H spin diffusion suggesting the surface specific relaxation is most likely to take place. Although homogeneous ^1H T_1 indicates the effect of spin diffusion, we further tested whether ^1H spin diffusion is a key element in ^1H T_1 relaxation in the PACC approach by measuring the spinning-speed dependence of ^1H T_1 for (a) Cu(II)-EDTA doped and (b) undoped

ubiquitin samples. Since it is known that fast spinning considerably suppresses ^1H spin diffusion, it is expected that faster spinning slows down the relaxation process. As shown in the Figure 52, for the Cu-EDTA doped sample in (a), ^1H T_1 values increased considerably at faster spinning, while the ^1H T_1 values were not affected by spinning for the undoped sample in (b). The data clearly demonstrate that the time required for the ^1H spin-diffusion process is likely to contribute substantially to ^1H T_1 values in the PACC approach.

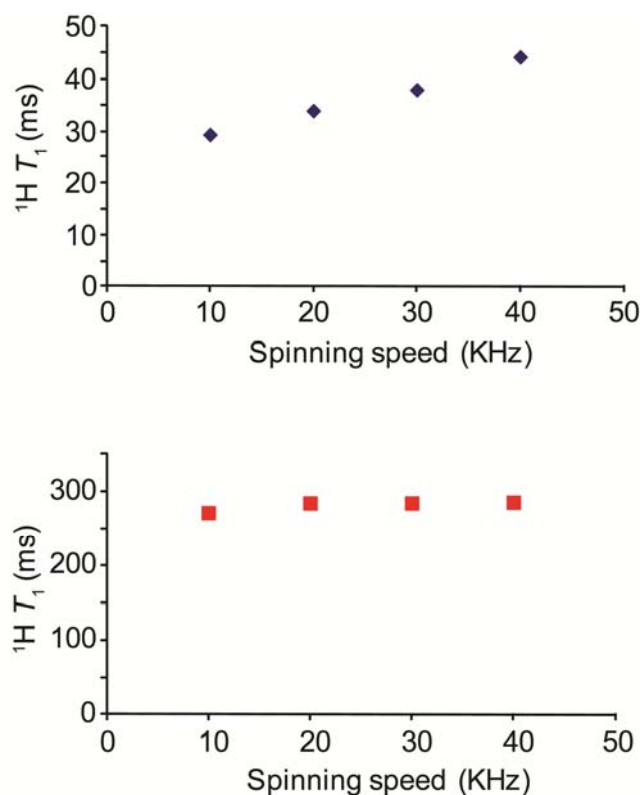


Figure 52. Spinning-speed dependence of ^1H T_1 values for Cu(II)-EDTA doped (a) and undoped (b) uniformly ^{13}C - and ^{15}N -labeled ubiquitin samples. The sample temperature was kept at ~ 15 $^{\circ}\text{C}$ by using different temperatures for cooling air, depending on the spinning speeds.

4) Low power decoupling at Ultra-fast MAS

lpTPPM decoupling has been successfully tested at 400 MHz with 40kHz fast MAS, however at ultra high magnetic field 18.8 T (^1H frequency of 800 MHz) and for MAS exceeding 40 kHz, the application of lpTPPM has not been studied extensively, and it is not guaranteed to work due to the larger ^1H bandwidth compared to 400MHz. In this study, we have successfully tested the use of lpTPPM ^1H decoupling at ultra-fast MAS (≥ 70 kHz) in an ultra high magnetic field 18.8 T. Figure 53 is the comparison of the 1D ^{13}C CPMAS of uniformly ^{13}C - ^{15}N - labeled Alanine sample at (a) MAS 19 kHz with high power ^1H 100 kHz decoupling (b) MAS 78kHz with low power TPPM 7.8 kHz decoupling. Inset in the Figure 53 a, b shows the $^{13}\text{C}=\text{O}$ region expansion. Significant resolution enhancement was observed at MAS 78 kHz with 7.8 kHz low power ^1H lpTPPM decoupling at ultra-fast MAS. Careful optimization of CP conditions and further studies are required for greater sensitivity enhancement at ultra-fast MAS conditions since the spin dynamics are considerably altered at such a high MAS.

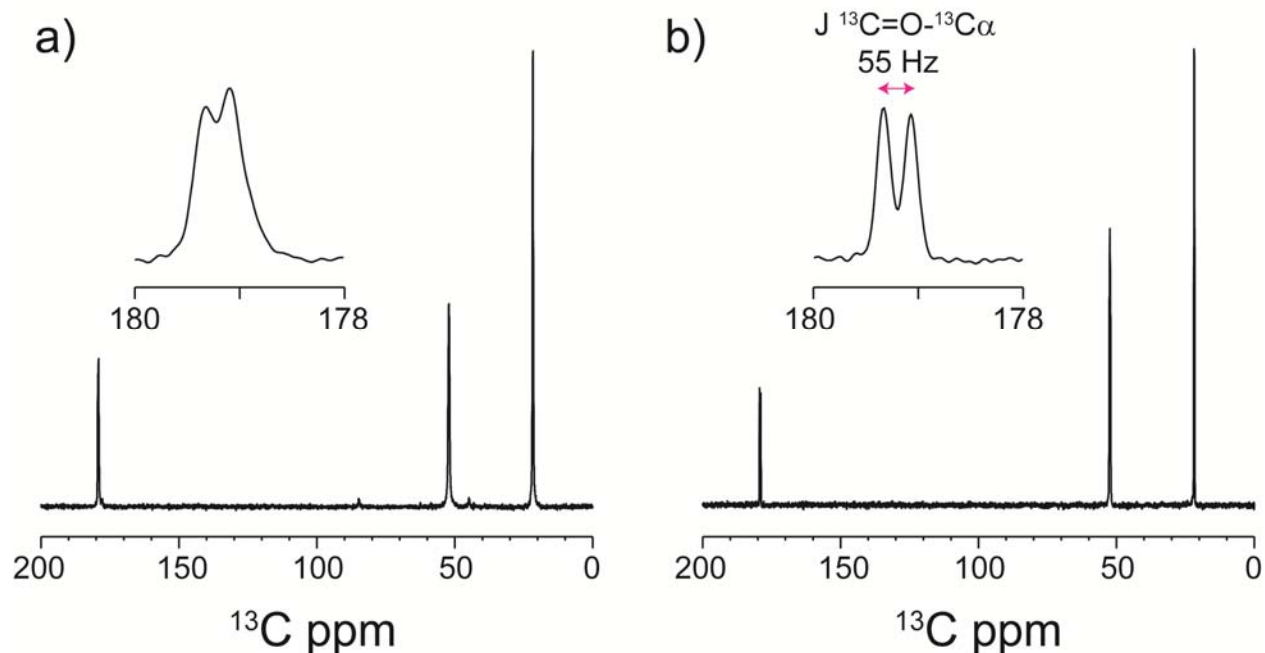


Figure 53. Comparison of the performance of the (a) high power 100 kHz TPPM decoupling at 19 kHz MAS with (b) 8 kHz lpTPPM at 78 kHz ultra-fast MAS in ^{13}C - and ^{15}N - uniformly labeled Alanine sample. Inset is the $^{13}\text{C}=\text{O}$ peak expansion showing the ($J=55\text{Hz}$) scalar coupling between $^{13}\text{C}=\text{O}$ and $^{13}\text{C}\alpha$.

The ^1H lpTPPM decoupling was tested at various spinning speeds for the ^{13}C - and ^{15}N - Isoleucine sample. Figure 54 shows the comparison of the signal intensities in ^{13}C CPMAS spectra for $^{13}\text{C}\alpha$, $^{13}\text{C}\beta$, $^{13}\text{C}\gamma_1$, $^{13}\text{C}\gamma_2$ at four different spinning speeds with variable low power decoupling rf field (ω_1) strengths. The signal intensities and the resolution improve when the $\omega_1 = \omega_R/n$ where ω_R is the MAS frequency and $n = 1, 2, 3, \dots$ which is very consistent with the results by Kotecha et.al.¹⁸³

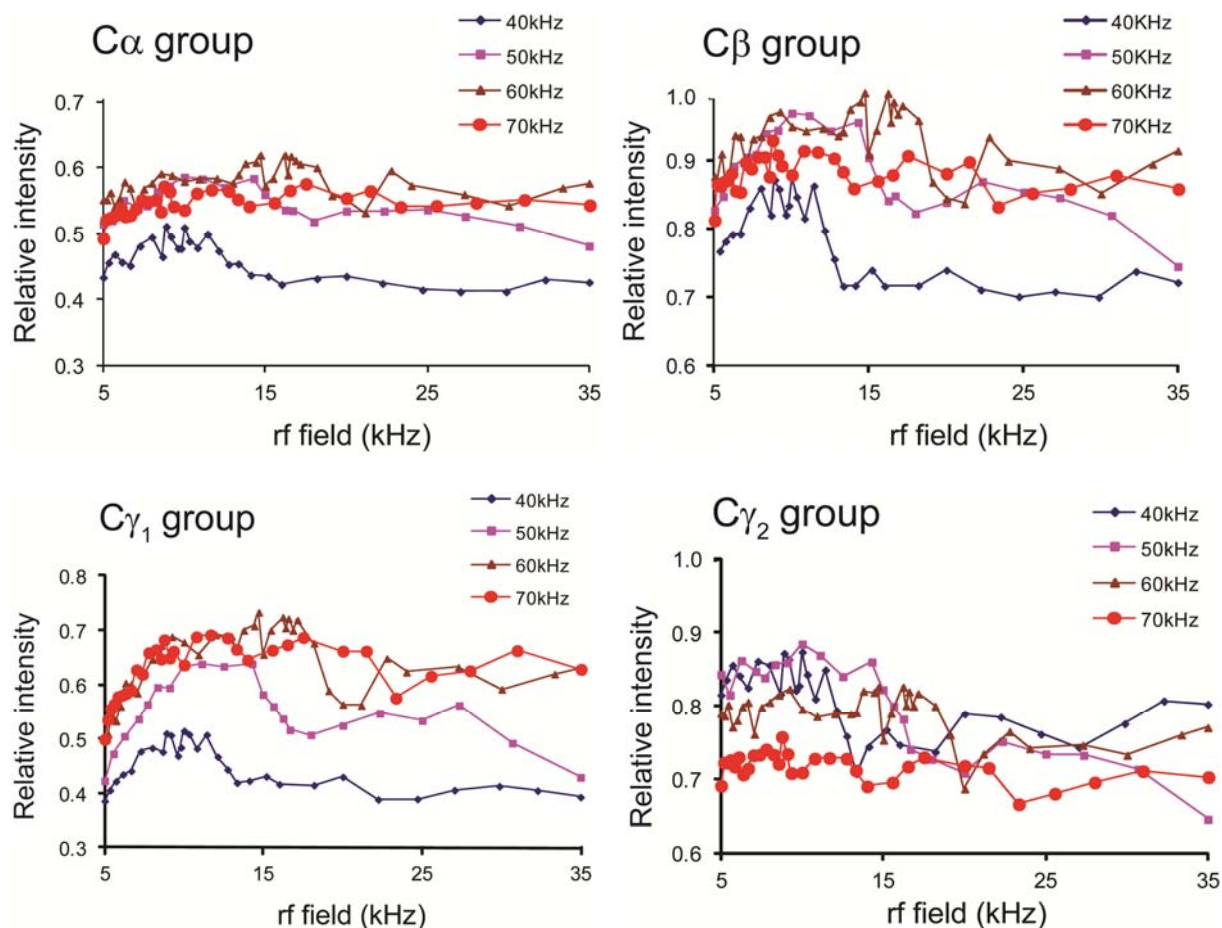


Figure 54. ^1H decoupling field dependence of ^{13}C CPMAS signal intensities under TPPM decoupling for $^{13}\text{C}\alpha$, $^{13}\text{C}\beta$, $^{13}\text{C}\gamma_1$, $^{13}\text{C}\gamma_2$ groups of uniformly ^{13}C - and ^{15}N -labeled L-Isoleucine.

5) PACC at Ultra-fast MAS

Figure 55 is the 2D $^{13}\text{C}/^{13}\text{C}$ fpRFDR SSNMR spectrum of uniformly ^{13}C - and ^{15}N -labeled Alanine sample at MAS 78 kHz collected with rapid pulse delays without paramagnetic dopants in 2 min. One and two bond cross peaks are observed in the spectrum without any loss of the structural information. The condensed pulse delays in the experiment were made possible by the application of ^1H lpTPPM decoupling at ultra-fast MAS. A short pulse delay of 300 ms was used in this experiment and it was not matched to $3 \times ^1\text{H } T_1$. The information content in the

spectrum was not diminished by such a short pulse delay indicating the applicability of the condensed data collection approach for small organic molecules or pharmaceuticals at ultra-fast MAS.

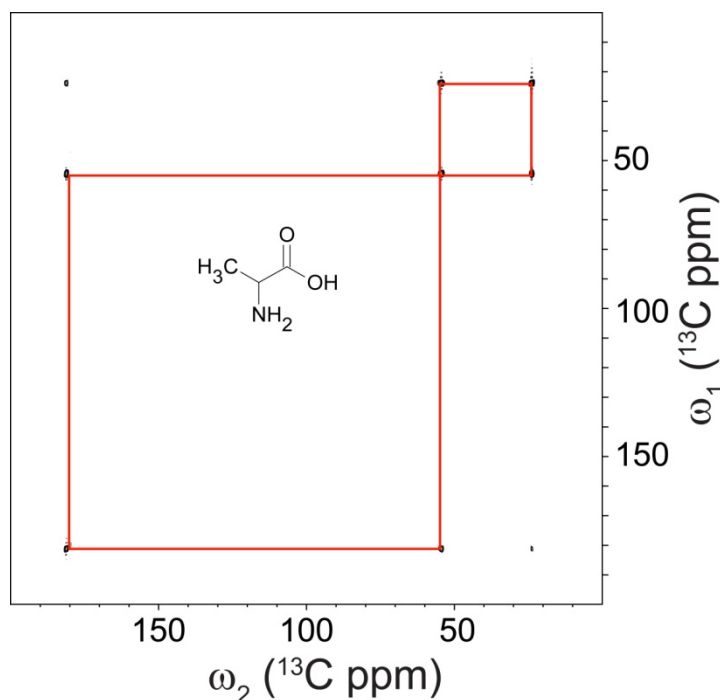


Figure 55. Two dimensional $^{13}\text{C}/^{13}\text{C}$ fpRFDR SSNMR spectrum of uniformly ^{13}C - and ^{15}N -labeled Alanine sample at MAS 78 kHz. Inset is the chemical structure of Alanine and red squares indicate the one bond connectivity. A ^{13}C - ^{13}C fpRFDR mixing period of 1.6 ms was used in this experiment.

Figure 56 is the comparison of the ^{13}C CPMAS of Cu^{2+} -A β (1-40) fibrils uniformly ^{13}C - and ^{15}N - labeled at sites Phe-4, Gly-9, Val-12, Leu-17 and Ala-21 collected at (a) 9.4 T with 3 mg fibrils at MAS 20 kHz with 90 kHz TPPM ^1H decoupling and (b) at 18.8 T magnet with 1 mg fibrils at MAS 50 kHz with 10 kHz ^1H lpTPPM decoupling. The signal assignments are shown in (b). Both the spectra were collected with 1024 scans, the spectra in (a) was collected in a

traditional approach with 1.8 s pulse delay and (b) was collected with PACC approach with 0.2 s pulse delay. The experimental times were for (a) 35 min and (b) 5 min respectively. Analysis of the signal intensities from the 1D spectrum showed a sensitivity enhancement factor for 4 for the $^{13}\text{C}=\text{O}$ group and 6-8 for the $^{13}\text{C}\alpha$ and $^{13}\text{C}\beta$ groups in the Cu^{2+} -A β (1-40) sample with $\sim 1/3^{\text{rd}}$ of the sample amount. Then we compared the sensitivity enhancement in the two dimensional SSNMR spectra collected at 9.4 T and 18.8 T.

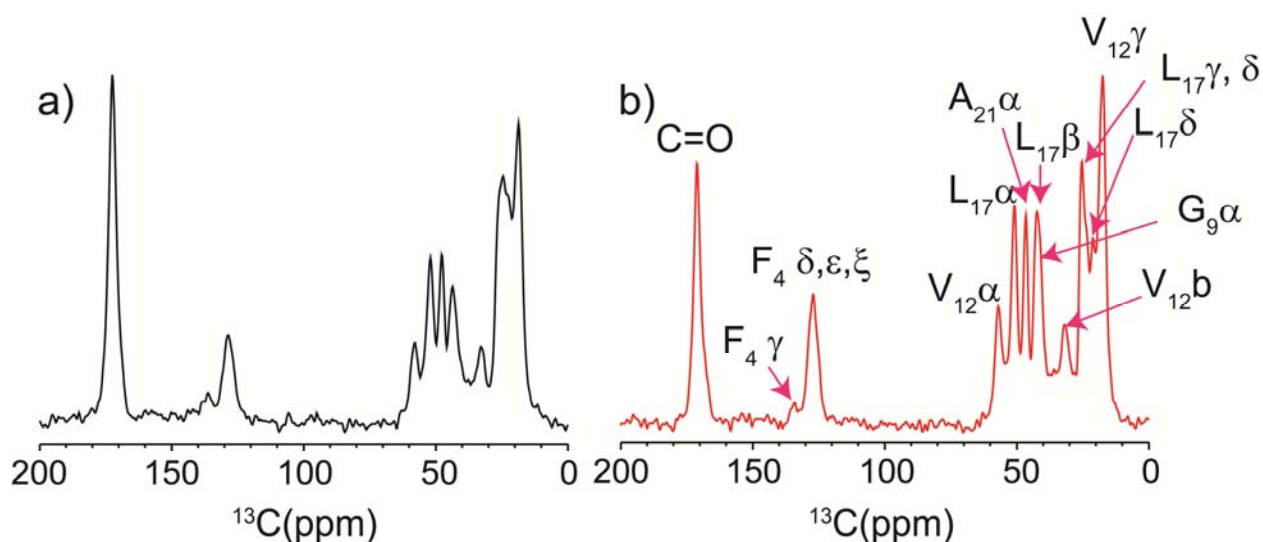


Figure 56. Comparison of the 1D ^{13}C CPMAS of Cu^{2+} -A β (1-40) fibrils uniformly ^{13}C - and ^{15}N -labeled at sites Phe-4, Gly-9, Val-12, Leu-17 and Ala-21 collected at (a) 9.4 T magnet with 3 mg fibrils at MAS 20 kHz with 90 kHz TPPM ^1H decoupling and 1.8 s pulse delay (b) 18.8 T magnet with 1 mg fibrils at MAS 50 kHz with 10 kHz low power TPPM ^1H decoupling and 0.3 s pulse delay. Both the spectra were collected with 1024 scans.

Figure 57 is the comparison of the 2D $^{13}\text{C}/^{13}\text{C}$ fpRFDR SSNMR spectra of the same Cu^{2+} -A β (1-40) fibrils sample described above. The spectrum in (a) was collected with traditional data collection approach with a total experimental time of 65 h in 9.4 T (^1H frequency of 400

MHz) and (b) was collected with PACC approach in 3.4 h in 18.8 T (^1H frequency of 800 MHz). The 2D experiment acquired by PACC method is comparable to the 2D acquired by traditional method and the experiment in (b) was ~ 19 times faster than the traditional approach. The comparison of 1D-slices for the Val-12 γ , Ala-21 α and Leu-17 α from PACC (red) and traditional (black) are shown in (c), indicating no major spectral alteration in the spectrum. The PACC approach opens up the possibility of exploring metallo proteins, which do not require external dopants for PRE.

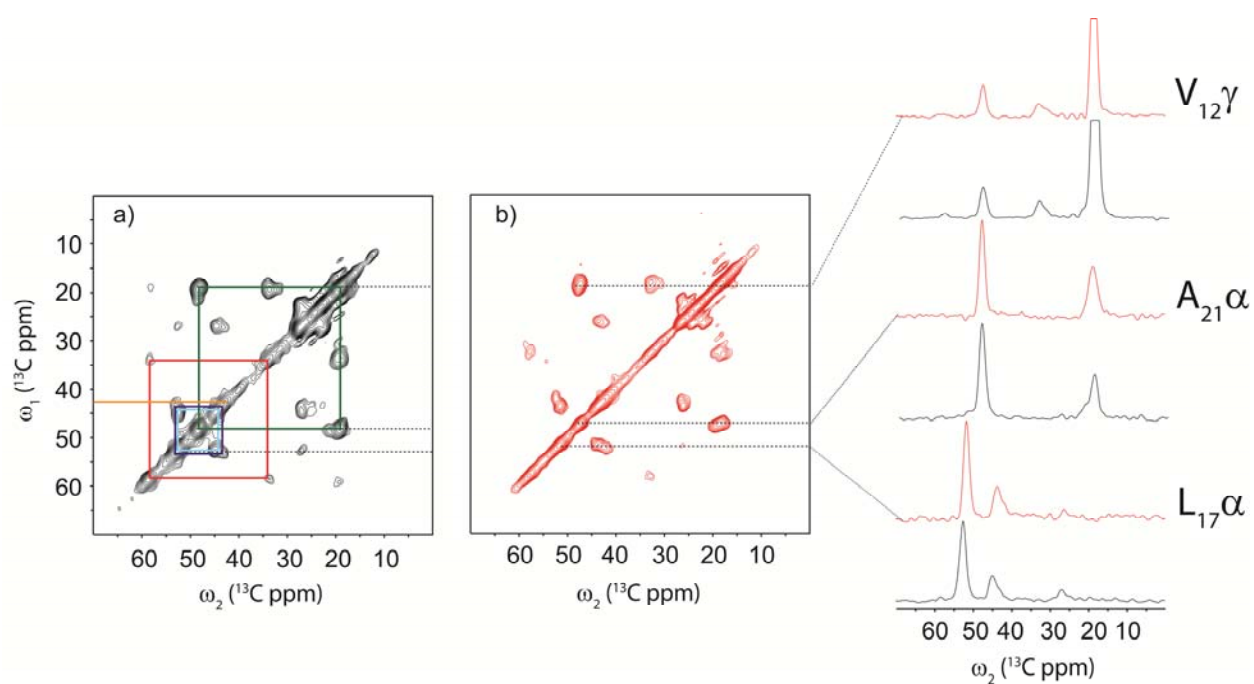


Figure 57. Comparison of the 2D $^{13}\text{C}/^{13}\text{C}$ fpRFDR spectra of Cu^{2+} -A β (1-40) fibrils uniformly ^{13}C - and ^{15}N - labeled at sites Phe-4(Blue), Gly-9(Orange), Val-12(Red), Leu-17(Cyan) and Ala-21(Green) collected at (a) 9.4 T magnet with 3 mg fibrils at MAS 20 kHz with 90 kHz TPPM ^1H decoupling and 1.8 s pulse delay (b) 18.8 T magnet with 1mg fibrils at MAS 50 kHz with 10 kHz lpTPPM ^1H decoupling and 0.28 s pulse delay. The experimental times for (a) 65 h and (b) 3.4 h.

C) Materials and Methods

Lysozyme from chicken egg white, sodium acetate, NiCl₂, Cu(II)-EDTA, Gd(III)-DEPTA was purchased from Sigma-Aldrich (St. Louis, MO). Sodium Chloride was purchased from Fischer Scientific, polyethyleneglycol (PEG) 2000 was purchased from Fluka. Ni(II)-EDTA, Co(II)-EDTA was purchased from Tokyo Chemical Industry, America. Purified water (double deionized and distilled) was prepared using a High-Q 103 S water still system (High-Q Corp., Wilmette, IL). The purified water was used for preparation of all the protein microcrystals and A β fibrils.

1) Lysozyme crystallization

Lysozyme microcrystals were prepared by using the protocol established by Wickramasinghe et al.²⁵² An equal volume mixture of lysozyme stock solution in sodium acetate buffer pH 4.5 (25 mg protein/ml) and the crystallization solution (12% w/v PEG 2000 and 75 mM sodium chloride in 100 mM sodium acetate buffer pH 4.5) was concentrated to approximately half the starting volume using SpeedVac concentrator (Savant, Farmingdale, NY). The concentrated lysozyme solution of ~ 0.5 mL was incubated in a microcentrifuge tube at 4 °C for 12 h to obtain protein microcrystals. The crystals were centrifuged at 1.5×10^3 g for 5 min using an Eppendorf 5414D micro-centrifuge (Eppendorf, Westbury, NY).

2) Incubation with paramagnetic reagents

The lysozyme microcrystals containing the paramagnetic complexes were prepared by separating the supernatant from the protein crystal by centrifugation. Stock solution of the paramagnetic complexes were prepared in the protein mother liquor and diluted to the required concentration. Then, the solution was kept at 4 °C for about 2-4 h, and centrifuged to remove any precipitated protein due to the salts. The mother liquor containing the paramagnetic complexes

is then added to the protein micro crystals. The crystals containing paramagnetic complexes were then briefly vortexed and left at 4°C for 3-4 days to dope the complexes into protein crystals. The control sample was prepared in the same way except for the addition of paramagnetic complexes.

Figure 58 is the comparison showing the images of the lysozyme microcrystals (a) without dopants and (b) with 3mM Ni(II)-EDTA. The crystal shapes are identical and no damage or degradation of the crystals upon the addition of the dopants.

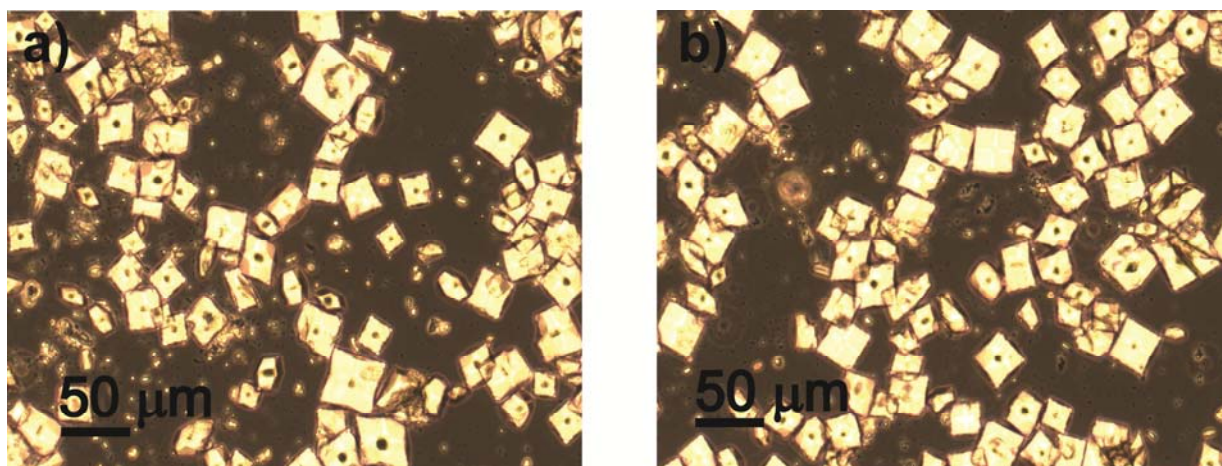


Figure 58. Comparison showing the microscope images of lysozyme microcrystals (a) without dopants and (b) with 3 mM Ni(II)-EDTA. The crystals shapes were identical after the addition of the dopants.

3) Synthesis of Ni(II)-DO2A

The ester hydrolysis was performed by refluxing 1,4,7,10-Tetraazacyclododecane-1,7-bis(t-butyl acetate) (DO2A t-butyl acetate) in 4ml of 20% HCl at 120 °C. Water was removed by high vacuum using rotavapor. The compound was treated with ether followed by ethanol, a white solid was observed after the workup and the solid was kept at high vacuum for 2 hours. NiCl₂ is

used as complexing agent with 1, 4, 7, 10-tetra-azacyclododecane-1,4,7,10-1,7-bis(acetic acid) (DO2A). NiCl₂ and DO2A are added in equimolar ratio and dissolved in water. Few drops of ammonium hydroxide is added to the aqueous solution. Purple color was observed immediately after adding ammonium hydroxide. The final solid was kept under high vacuum to remove water. Ni-DO2A complex was allowed to pass in to DOWEX Cl⁻ ion exchange resin column to remove Cl⁻ ions. Final compound was sent for elemental analysis to Desert Analytics, Inc., AZ.

4) SSNMR experiments

SSNMR experiments were performed at 9.4 T (¹H NMR frequency of 400.2MHz) with a Varian Infinity plus 400 MHz spectrometer using a 1.8-mm double/triple-resonance MAS NMR probe developed at Dr. Samoson's lab. All the data were acquired at the spinning speed of 40,000 ± 10 Hz with a cooling air at -20 °C supplied through a Varian VT stack at a flow rate of ~ 66 L/min (~140 cubic-feet/h). The sample temperature was maintained approximately at 15 °C by this condition, which compensates the frictional heating generated by fast MAS. The sample temperature was calibrated using standard samples Cu(II)(DL-alanine)₂ and Pb(II)(NO₃)₂. All the spectra were referenced externally to TMS using the secondary reference of ¹³C adamantane methylene peak at 38.56 ppm, and then, the reference was readjusted to DSS with a 1.7 ppm chemical shift difference between TMS and DSS. The crystals were packed in to 1.8 mm Rotor by centrifuging the crystals through a pipette tip fitted on to the top of the rotor. The rotor cap was sealed with instant adhesive Krazy Glue (Krazy Glue, Columbus OH) to avoid any leakage of water at high spinning speed. The rotor was left to stand for ~ 10-12 h before starting the spinning. The rotor caps are removed safely after the experiments by immersing the rotor in to the liquid nitrogen.

The ultra-fast MAS experiments were carried out on a Bruker-800MHz spectrometer, using a JEOL double resonance MAS probe with rotor diameter of 1mm. The samples were cooled using FTS unit with nitrogen gas. The sample temperature at 78 kHz was kept 15°C using a home built VT stack which connects the probe head and FTS outlet.

VII) ^1H INDIRECT DETECTION FOR ^{13}C BIOMOLECULAR SOLID-STATE NMR: ENHANCED SENSITIVITY AND RESOLUTION BY A COMBINED USE OF ULTRA-FAST MAGIC ANGLE SPINNING, HIGH FIELD AND STEREO ARRAY ISOTOPE LABELING

A) Introduction

^1H indirect detection of ^{13}C and ^{15}N has been an indispensable tool for biomolecular solution NMR. In biomolecular SSNMR, ^1H indirect detection was introduced about a decade ago.^{101, 102} Nevertheless, ^1H detected SSNMR has not gained a widespread usage because of limited ^1H resolution even under fast MAS and lack of sensitivity advantage over more common ^{13}C direct detection. Recent introduction of ^1H dilution by high level of deuteration and partial back exchange of amide ^1H (~ 10%) has greatly improved the resolution of ^1H SSNMR for biomolecules,^{110, 253} offering a practical protocol for ^1H indirect detection in SSNMR. However, the method is coupled to a significant loss of ^1H intensity for a majority of the amide sites (~90%) due to extensive deuteration. Also, very sparse ^1H spins make it difficult for one to incorporate ^1H detection experiments in standard 3D SSNMR schemes such as NCOCA or NCA for sequential assignments or to collect structural information from ^1H - ^1H contact. ^1H detection experiments for fully protonated proteins at very fast MAS (~40 kHz) has been proposed to obtain signal assignments for a model protein.²⁵⁴ This method, however, is still hampered by limited ^1H resolution,²⁵⁵ the ^1H spectral line widths of ~ 1 ppm reported in this study have not been sufficient even for small proteins. More importantly, with the resolution, it has been difficult to enhance sensitivity by ^1H indirect detection over standard 1D ^{13}C direct detected SSNMR. More recently, ^1H indirect detection under ultra-fast MAS (UFMAS) at spinning frequencies of ~ 60 kHz was reported,²⁵⁶ resulting in well resolved amide ^1H resonances for fully deuterated protein with fully back exchanged amide ^1H . The sensitivity and resolution advantage of ^1H detection method over traditional ^{13}C direct detection methods have not been established

even for such a high quality data. In this study, we examine the possibility of sensitivity and resolution enhanced ^1H -detected ^{13}C SSNMR by a combination of UFMAS (≥ 70 kHz),^{256, 257} and a novel labeling strategy. As a highly effective labeling scheme that is suited for ^1H detected SSNMR, we propose use of stereo-array isotope labeling (SAIL) for amino acids and proteins. SAIL scheme was originally introduced to overcome the size limitation of biomolecular solution NMR for large proteins by incorporating stereoselective deuteration to achieve isolated ^1H throughout all the side chains of a protein.¹¹⁰ Despite previous attempts,²⁵⁸ successful use of SAIL labeling was difficult for biomolecular SSNMR. We demonstrate that a combination of UFMAS and SAIL selective deuteration provides distinctive sensitivity enhancement by ^1H -detected ^{13}C SSNMR spectroscopy of biomolecules over ^{13}C direct detection. Our motivation is to demonstrate that ^1H detection can be implemented into conventional multi-dimensional ^{13}C detected NMR for enhancing sensitivity as well as resolution. Our goal also includes achieving high ^1H resolution as well as assignments through sensitivity and resolution enhanced ^{13}C SSNMR by ^1H detection for a protein sample.

B) Results and Discussion

1) Resolution enhancement in ^1H SSNMR by UFMAS and SAIL

First, we examine the effectiveness of combination of the SAIL labeling with UFMAS in a high magnetic field of 18.8 T (^1H frequency of 800 MHz) on ^1H SSNMR through experiments on amino acid samples. Figure 59 (a, b) shows chemical structures and labeling schemes for (a) uniformly ^{13}C -, ^{15}N -labeled isoleucine (UL-Ile) and (b) SAIL- isoleucine (SAIL-Ile). Unlike high-level of random deuteration, in SAIL labeling, all the ^{13}C groups are connected to a single ^1H species. This feature also allows one to prepare strong ^{13}C magnetization for all the ^{13}C species via efficient cross polarization from ^1H nuclei. More importantly, isolated ^1H spins allow

us to achieve very high resolution without the effects of strong ^1H - ^1H dipolar couplings. Figure 59 (c, d) shows spinning speed dependence of ^1H SSNMR of (c) UL-Ile and (d) SAIL-Ile with signal assignments in (d). Significant enhancement in the resolution and sensitivity was obtained at the faster spinning speed (ω_R). Resolution enhancements on the order of a factor of ~ 2 -3 times were observed at $\omega_R = 78$ kHz in (d) over the data at $\omega_R = 30$ kHz, which was used in previous studies of ^1H SSNMR on SAIL-valine.²⁵⁸ Clearly, SAIL-Ile shows higher resolution in Figure 59 d at $\omega_R = 78$ kHz, compared with the corresponding spectrum for the UL-Ile in Figure 59 c. In particular, for the $\text{H}\beta$, $\text{H}\gamma_1$, $\text{H}\delta$ groups, the spectrum for SAIL-Ile indicates dramatic resolution enhancement by a factor of 3-4 over the resolution for UL-Ile, showing ^1H widths of ~ 0.24 ppm. This narrowing is likely attributed to the features of SAIL, isolated ^1H in methylene and methyl groups by stereo-specific deuteration.^{109, 110} Much broader ^1H line widths (0.7-1.0 ppm) for these groups in UL-Ile demonstrate that UFMAS itself is still not sufficient to remove broadening due to strong ^1H - ^1H dipolar couplings within the CH_2 and CH_3 groups even at $\nu_R \sim 80$ kHz. The ^1H line widths for O-H, and $^{13}\text{C}\alpha$ - ^1H in Figure 59 d also showed distinctive resolution enhancements (14-19%) by a combination of SAIL and UFMAS over the data in Figure 59 c although the line width for amino ^1H was only comparable in Figure 59 c and d. Compared with the resolution for UL-Ile at $\omega_R = 40$ kHz, which is similar to the condition used in a previous study on ^1H detected SSNMR on proteins,²⁵⁹ the resolution enhancements for CHD and CHD_2 groups are as much as a factor of 5-6 for the SAIL sample at $\omega_R = 78$ kHz.

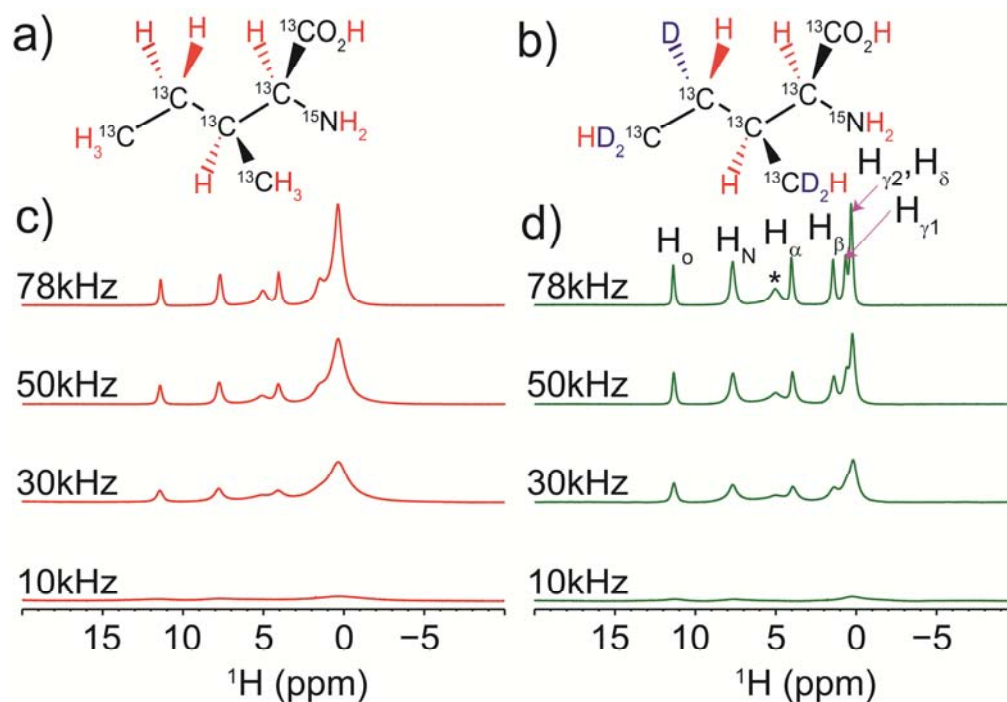


Figure 59. (a, b) The chemical structures of (a) UL-Ile and (b) SAIL-Ile. (c, d) Spinning dependence of ^1H MAS SSNMR spectra of (c) the UL-Ile and (d) SAIL-Ile. A peak at 4.8 ppm indicated by * is likely attributed to ^1H from HCl salts incorporated into the crystal lattice.^{260, 261} No window functions were applied for data processing. The SAIL-Ile and UL-Ile used for these experiments were recrystallized in 20% DCl in D_2O and the recrystallized samples were packed in to the 1mm rotor.

Next, we compared the resolution enhancement by UFMAS and SAIL of another amino acid, Threonine, by UFMAS and SAIL. SAIL-Thr powder was recrystallized by dissolving 3.7 mg of the amino acid in 35 μL D_2O followed by the addition of 55 μL d_4 -methanol. Precipitate was observed after the addition of d_4 -methanol and it was allowed to stand at room temperature for slow evaporation. The dry crystals were recovered after 2 weeks and were used for the SSNMR measurements. Figure 60 shows the comparison of ^1H SSNMR spectra of SAIL-Thr sample at various spinning speeds. At 78 kHz MAS the ^1H line widths for H_α , H_β were 0.22 ppm, H_γ was 0.24 ppm and OH/NH were 0.20 ppm comparable to the ^1H line widths observed for the SAIL-Ile at 78 kHz.

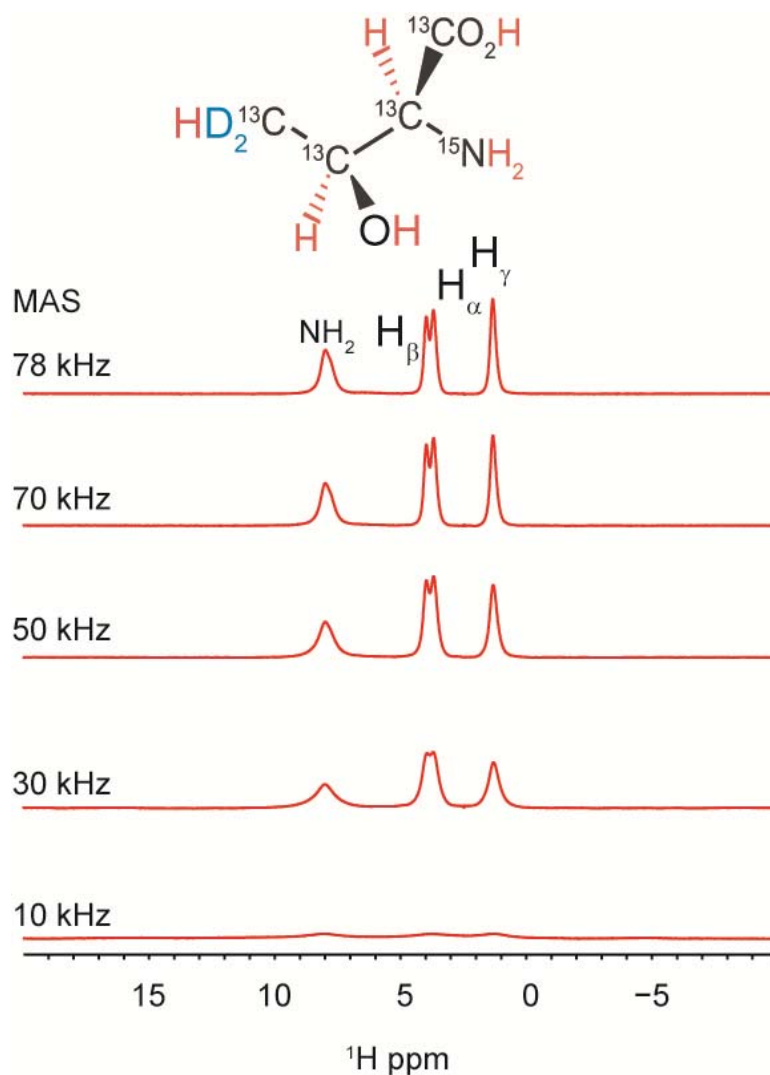


Figure 60. ^1H SSNMR of SAIL-Thr (Chemical structure at the top) at various spinning speeds. The ^1H NMR spectra were obtained with 10 kHz WALTZ-16 ^{13}C decoupling. All the spectra were obtained with 2 scans with a pulse delay of 15 s and were processed without any window function. The ^1H line widths for H_α , H_β were 0.22 ppm, H_γ 0.24 ppm and OH/NH 0.20 ppm.

2) Sensitivity enhancement in ^{13}C SSNMR by ^1H detection experiments using UFMAS and SAIL

Next, we demonstrate sensitivity and resolution enhancement by ^1H indirect detection for the SAIL-Ile and SAIL-Thr crystalline samples. The sensitivity enhancement factor (ξ) by ^1H

indirect detection over direct detection of a dilute X-nuclei depends on the line width in the ^1H dimension W_{H} as well as the efficiency of polarization transfer (f) between ^{13}C and ^1H for ^1H detection as shown in eqn. 31.^{101, 102}

$$\xi = \frac{f}{\sqrt{2\kappa}} \left(\frac{\gamma_{\text{H}}}{\gamma_{\text{X}}}\right)^{\frac{3}{2}} \left(\frac{W_{\text{X}}}{W_{\text{H}}}\right)^{\frac{1}{2}} \left(\frac{Q_{\text{H}}}{Q_{\text{X}}}\right)^{\frac{1}{2}} \dots\dots\dots (31)$$

where γ_{H} and γ_{X} represent the gyromagnetic ratios of the nuclei H and X, W_{X} and W_{H} are the line widths observed, Q_{H} and Q_{X} is the quality factor for the sample coil for the ^1H detection. The factor $\kappa \sim \pi$ for comparison with 1D ^{13}C CPMAS SSNMR assuming apodization with matched window functions, while $\kappa = 1/2$ for comparison with ^{13}C detected 2D $^{13}\text{C}/^1\text{H}$ correlation. Thus, there is approximately 2.5 times factor difference between ξ values for comparison with 1D and 2D experiments. As discussed above, SAIL labeling ensures efficient CP transfer between ^1H and ^{13}C even under UFMAS as all the aliphatic ^{13}C species are directly bonded to ^1H . Figure 61(a-c) shows (a) ^1H -detected 2D $^{13}\text{C}/^1\text{H}$ correlation spectrum, (b) the corresponding ^{13}C -detected 2D $^{13}\text{C}/^1\text{H}$ correlation spectrum, and (c) a 1D ^{13}C CPMAS spectrum of the SAIL-IIe. For sensitivity comparison, all the spectra in Figure 61 (a-c) were collected with a common scan numbers (1960 total scans each or ~ 11 min each) at $\nu_{\text{R}} = 78$ kHz and at a ^1H NMR frequency of 800 MHz. Figure 61 (d, e) respectively shows slices from Figure 61 (a, b) for the ^1H shift for $^1\text{H}\alpha$ (4.1 ppm); the noise (scaled 20 times) in Figure 61 (c-e) are displayed above each 1D slice for sensitivity comparison. It is clear that drastic sensitivity enhancement is achieved by ^1H detection. The sensitivity enhancement factors by ^1H detection over the ^{13}C detected 2D data in Figure 61 b are in a range of 5.6-6.1 for the ^{13}CH and ^{13}CHD groups, while the factors were 2.8-3.0 for the $^{13}\text{CHD}_2$. Significant but lower sensitivity enhancement factors observed for the CHD_2 groups are attributed to lower cross polarization transfer efficiency ($f \sim 1.2$) for the CHD_2 groups, compared with that for ^{13}CH and ^{13}CHD groups ($f \sim 2.3$).

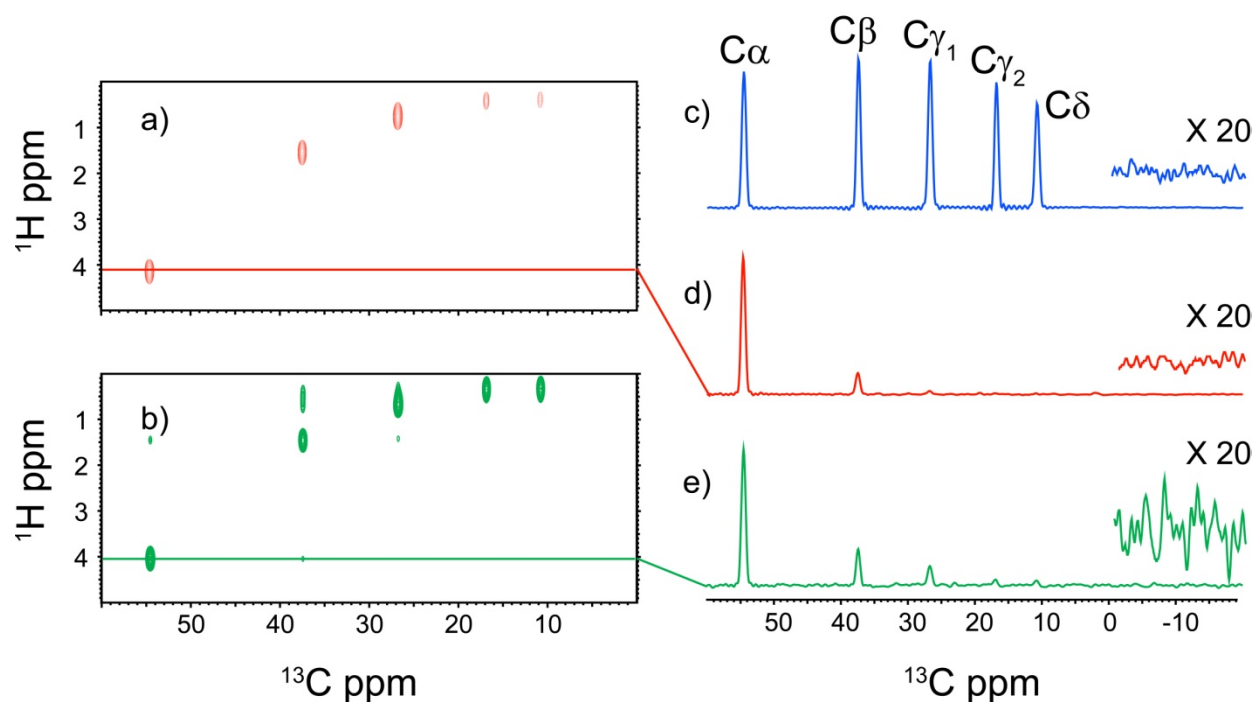


Figure 61. (a) ^1H detected and (b) ^{13}C detected $^{13}\text{C}/^1\text{H}$ 2D experiment (c) 1D CPMAS of SAIL-Ile at MAS 78kHz d,e) 1D slice along the ^1H chemical shift of 4.1 ppm from (d) the ^1H detected and (e) ^{13}C detected 2D $^{13}\text{C}/^1\text{H}$ correlation SSNMR. All the spectra were processed with matched window functions using Gaussian broadening of 200 Hz and 100 Hz for ^1H and ^{13}C respectively.

Notable sensitivity enhancements were observed by ^1H detection in Figure 61 a even when the sensitivity was compared with that for the 1D ^{13}C CPMAS experiment in Figure 61 c. We observed experimental enhancement factor ξ of 1.2-1.4 for the CH and CHD groups. The enhancement was confirmed by a comparison of the slice from the ^1H detected experiment in Figure 61 d with a 1D ^{13}C CPMAS spectrum in Figure 61 c, which indicates ξ of 1.4 for the $^{13}\text{C}\alpha$ signal at 54.5 ppm by ^1H detection. For CHD₂, marginal enhancements were observed ($\xi \sim 0.75$). In addition to the enhanced sensitivity, ^1H indirect detection provides improved spectral resolution by the added ^1H dimension. Next the ^{13}C sensitivity enhancement by UFMAS and SAIL was tested on SAIL-Thr sample, the sensitivity enhancement factors observed for the

SAIL-Thr sample as shown in Figure 62 (a-e) were comparable to the SAIL-Ile results as shown in Figure 62 (a-e).

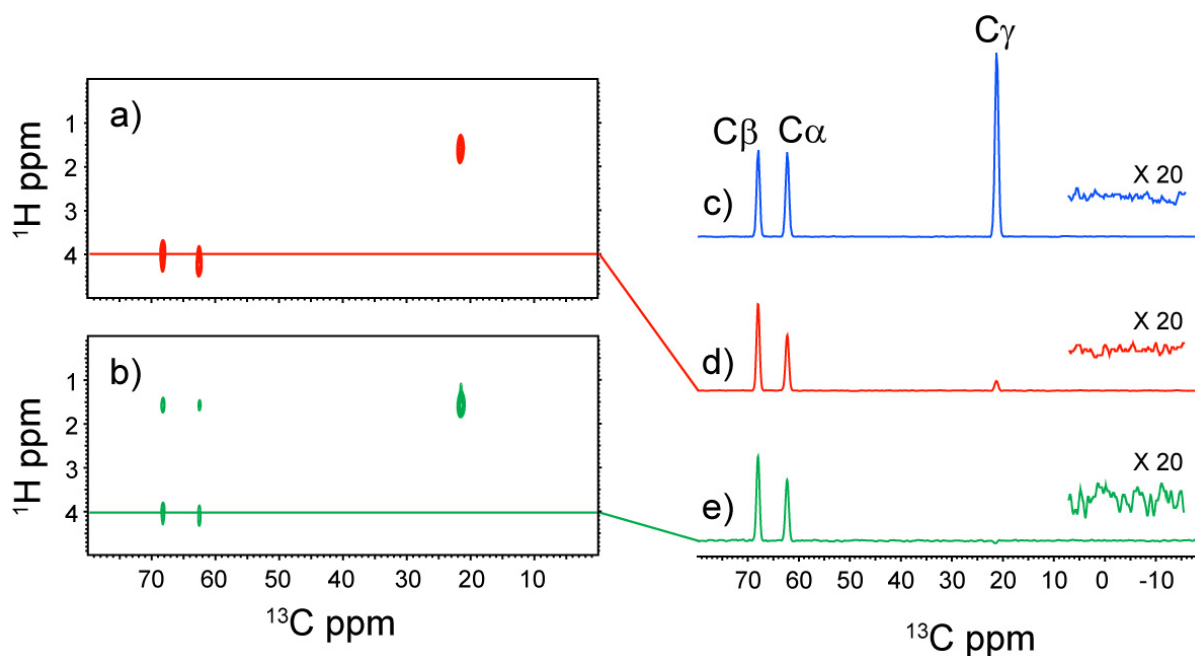


Figure 62.(a) ^1H detected (b) ^{13}C detected $^{13}\text{C}/^1\text{H}$ 2D experiment (c) 1D CPMAS of SAIL-Thr at MAS 78kHz. (d,e) 1D slice along the ^1H chemical shift of 4.1 ppm from (d) the ^1H detected and (e) ^{13}C detected 2D $^{13}\text{C}/^1\text{H}$ correlation SSNMR. All the spectra were processed with matched window functions using Gaussian broadening of 200 Hz and 100 Hz for ^1H and ^{13}C respectively.

Next, we explore the possibility of sensitivity and resolution enhancement of ^{13}C SSNMR for SAIL proteins. As a suitable benchmark system, we selected micro crystals of ubiquitin that was labeled selectively with SAIL-Ile in order to compare the resolution with that for the amino acid data. As there are as many as 7 Ile in ubiquitin (Ubq), the system is also suited for testing the effectiveness for ^1H detection for resolution enhancements. Another major challenge is the limited sample amount. As the engineering needs for UFMAS at 78 kHz limit the sample volume to only $\sim 1 \mu\text{L}$, there was a concern that sufficient sensitivity could be obtained in multi-

dimensional SSNMR for the protein sample even in a high magnetic field. Figure 63 (a, b) shows (a) ^1H -detected and (b) ^{13}C -detected 2D $^{13}\text{C}/^1\text{H}$ correlation spectra of the SAIL-ubiquitin sample.

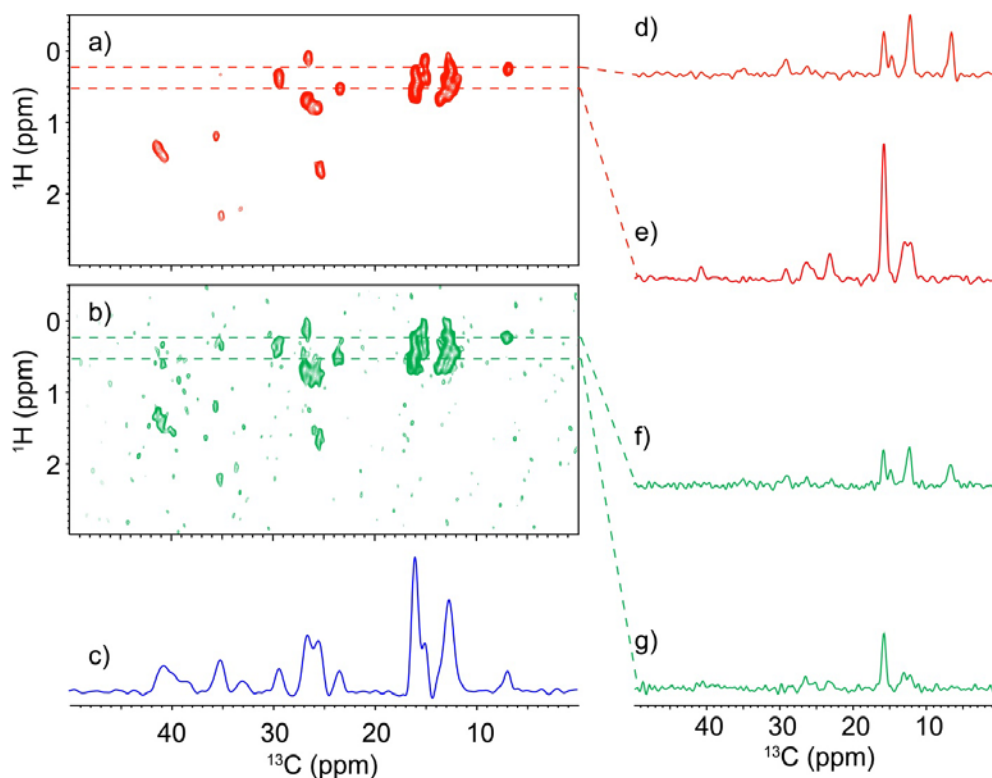


Figure 63.(a) ^1H detected and (b) ^{13}C detected $^{13}\text{C}/^1\text{H}$ 2D experiment (c) 1D CPMAS of SAIL-Ubq at MAS 78kHz (d-g) 1D slices from ^1H shifts of (d, f) 0.27 ppm and (e, g) 0.58 ppm from (d, f) ^1H detected and (e, g) ^{13}C detected experiments. All the spectra were processed with 45° and 60° shifted sinebell window function on ^1H and ^{13}C dimensions respectively. The ^1H and ^{13}C linewidths were found to be 0.20-0.25 ppm and 0.65-0.92 ppm without any window functions.

Excellent sensitivity enhancements by a factor of 6.3-9.5 were observed for the ^1H detected 2D spectrum in Figure 63 a over the ^{13}C detected 2D data in b), as shown from the comparison of the corresponding slices in (d-g). As a result of the distinctive enhancement, the

2D spectrum was obtained in Figure 63 a only after 50 minutes with ~0.5 mg of the protein sample (~60 nmol). In contrast, the ^{13}C detected 2D spectrum in Figure 63 b was obtained in 250 minutes with much less signal-to-noise ratio. Because of the spectral dispersion along the ^1H dimension, most of the resonances are well separated in the ^1H detected 2D spectrum in Figure 63 a while many of the resonances are overlapping in the 1D ^{13}C SSNMR in (c). The ^1H line widths for the SAIL-Ubq were found to be 0.20-0.25 ppm. Clearly, our approach is useful for characterization of a mass limited protein sample. The sensitivity enhancement factors in comparison with 1D ^{13}C CPMAS in (c) is 1.2-2.2 for the resolved two ^{13}CHD signals (29.3 and 23.4 ppm) and a $^{13}\text{CHD}_2$ signal (6.8 ppm) in 1D NMR. The factors are lower than the theoretical factor 2.5-3.8, which was obtained by multiplying $1/\sqrt{2\pi}$ to ξ for comparison with ^{13}C detected 2D experiment. The lower enhancement factor is likely attributed to the effects of the t_1 noise, which probably arose for limited temperature stability for our prototype VT system. Thus, higher sensitivity enhancements could be attained with improved instrumental stability. Nevertheless, to the best of our knowledge, this is the first case that significant sensitivity enhancement was observed by ^1H indirect detection of ^{13}C SSNMR for a protein by 2D $^1\text{H}/^{13}\text{C}$ correlation NMR over ^{13}C 1D direct detection with ^1H chemical shift information.

Lastly, we performed $^{13}\text{C}/^{13}\text{C}/^1\text{H}$ 3D experiment with ^1H detection for the SAIL-Ubq microcrystals. Figure 64 (a) shows the 2D projection of (a) $^{13}\text{C}/^1\text{H}$ 2D (b) is the secondary structure of Ubq protein showing the only the 7 Ile residues which are SAIL, (c-e) are $^{13}\text{C}/^{13}\text{C}$ 2D slices corresponding to ^1H chemical shifts of (c) 0.16 ppm, (d) 0.35 ppm (e) 0.48 ppm respectively with the assignments. The 3D experiment in Figure 64 was obtained in ~21 h. The $^{13}\text{C}/^{13}\text{C}$ side chains signals were assigned from the spin connectivities from the 2D slices based on previous studies^{139, 262} for this model protein. The overlapped sidechain $^{13}\text{C}/^{13}\text{C}$ cross peaks

in the 2D were resolved by the additional ^1H dimension. The back bone $^1\text{H}\alpha$'s were replaced by ^2H in the protein expression by E-Coli in D_2O , hence the backbone $^{13}\text{C}\alpha$ signals were weak. Uniformly or partly SAIL labeling the residues in a protein sample combination with UFMAS in a high magnetic field under ^1H detection experiments would be ideal in identifying the structure, dynamics of large protein crystals.

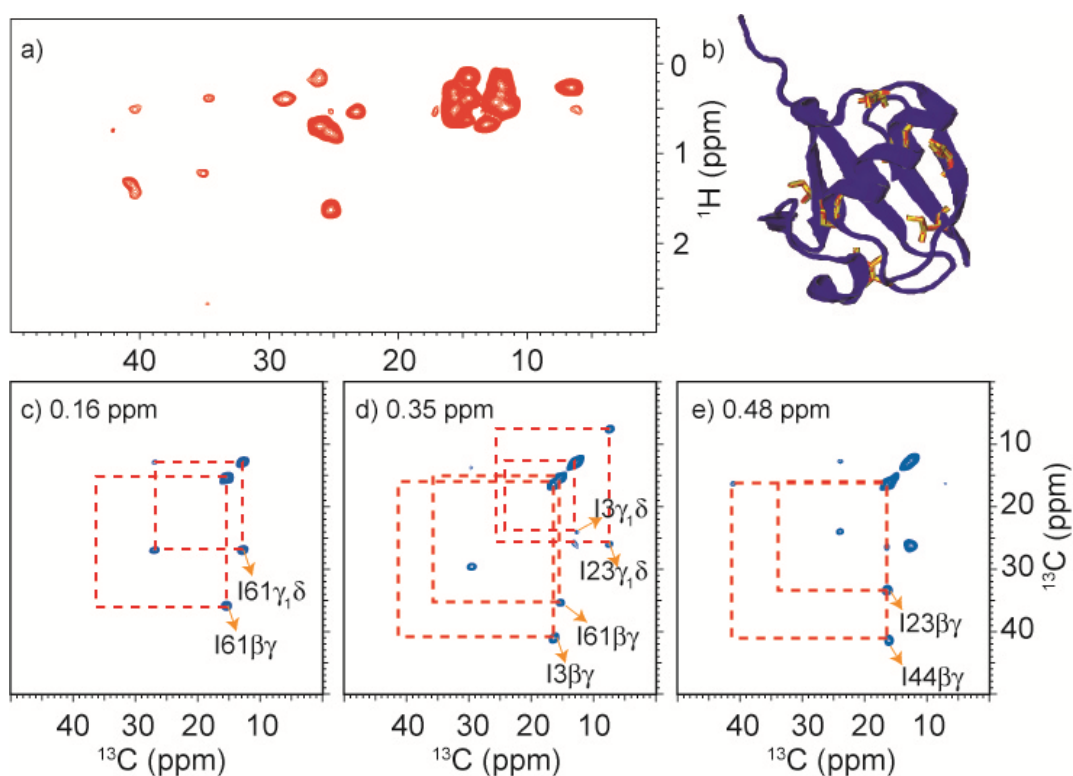


Figure 64. (a) $^{13}\text{C}/^1\text{H}$ 2D projection from the 3D $^{13}\text{C}/^{13}\text{C}/^1\text{H}$ experiment (b) the secondary structure of Ubq showing the Ile residues which are SAIL labeled (See experimental section for the aminoacid sequence) (c-e) are the representative 2D $^{13}\text{C}/^{13}\text{C}$ slices corresponding to ^1H chemical shifts of (c) 0.16 ppm and (d) 0.35 ppm and (e) 0.48 ppm from the 3D experiment. The spectrum was processed with 45° and 60° shifted sinebell window function on ^1H and both ^{13}C dimensions.

In conclusion, we have successfully demonstrated sensitivity and resolution advantage of our new approach for 2D ^1H detected ^{13}C SSNMR experiment on SAIL-labeled amino-acid and protein samples for the first time over 1D and 2D ^{13}C direct detection SSNMR. Well resolved 2D correlation SSNMR was shown for only ~ 60 nmole of the protein sample in one hour. Extension of this approach to various 3D and 4D experiments for mass limited protein samples is feasible with demonstrated sensitivity enhancements especially in combination with additional time-saving techniques such as PACC method¹³⁹ and non-uniform sampling.^{263, 264} Second, the method can be applied to a variety of proteins that are selectively labeled with a set of different SAIL amino acids. In spite the sample volume limitation, 2D and 3D analysis for a 50-kDa protein is feasible within a few days. Thirdly, by combining SAIL method with UFMAS, we could get ^1H resolution of 0.20-0.25 ppm at 800MHz for the amino acids and protein microcrystal samples. The ^1H line widths observed for the SAIL-Ile in the ^1H SSNMR could be attributed to ^1H - ^2D dipolar coupling.²⁶⁵ Thus, further resolution and sensitivity enhancement may be possible by adequate ^2D decoupling. As ^1H line widths under UFMAS are limited by residual dipolar couplings, an even higher magnetic field would also improve the ^1H resolution. Such experiments under UFMAS will be tested in our future studies.

C) Experimental section

The experiments were carried out on a Bruker-800MHz spectrometer, using a JEOL double resonance MAS probe with rotor diameter of 1mm. The samples were cooled using FTS unit with nitrogen gas. The sample temperature at 78 kHz was kept 15°C using a home built VT stack which connects the probe head and FTS outlet. The SAIL-Ile and UL-Ile used for these experiments were recrystallized in 20% DCI in D_2O and the recrystallized samples were packed into the 1mm rotor. SAIL-Ubiquitin samples were recrystallized by dissolving 2 mg of the

lyophilized powder in 160 μL citrate buffer in D_2O and precipitating with 240 μL $\text{d}_{12}\text{-MPD}$. Sequence of Ubiquitin: MQI₃FVKTLTG-KTI₁₃TLEVEPS-DTI₂₃ENVKAKI₃₀-QDKEGI₃₆PPDQ-QRLI₄₄FAGKQL-EDGRTLSDYN-I₆₁QKESTLHLV-LRLRGG. The pulse sequence used for the ^1H detected and ^{13}C detected $^{13}\text{C}/^1\text{H}$ 2D experiments are shown in Figure 65 and 66. The ^1H detected 3D $^{13}\text{C}/^{13}\text{C}/^1\text{H}$ pulse sequence is shown in Figure 67.

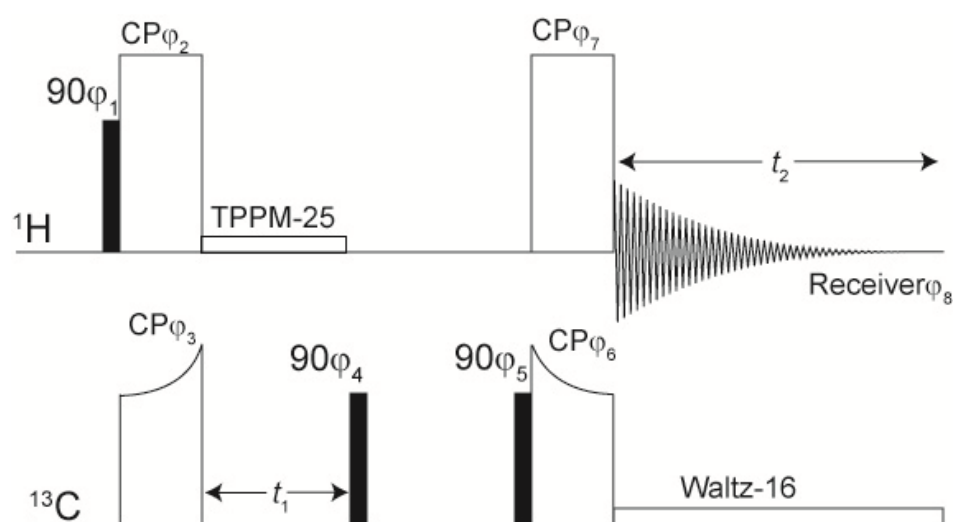


Figure 65. Pulse sequence for ^1H -detected 2D $^1\text{H}/^{13}\text{C}$ correlation spectroscopy. Magnetization of ^{13}C spins is prepared with adiabatic cross polarization using a tangential shaped pulse at the ^{13}C frequency. During the t_1 period, a low-power TPPM-25 ^1H decoupling field is applied. After the t_1 period, a pair of 90° pulses is applied to select the real or imaginary component of the ^{13}C magnetization, which is transferred back to ^1H spins with the reversed tangential pulse. During the t_2 period 10 kHz Waltz-16 decoupling was applied on the ^{13}C channel. The phase cycle for the pulse sequence are $\phi_1 = y, -y$; $\phi_2 = x$; $\phi_3 = x, x, -x, -x$; $\phi_4 = y, y, y, y, -y, -y, -y, -y$; $\phi_5 = y$; $\phi_6 = -x, -x, -x, -x$; $\phi_7 = -x, -x, -x, -x, -x, -x, -x, -x, x, x, x, x, x, x, x, x$; $\phi_8 = x, -x, -x, x, -x, x, x, -x, x, x, -x, x, -x, -x, x$.

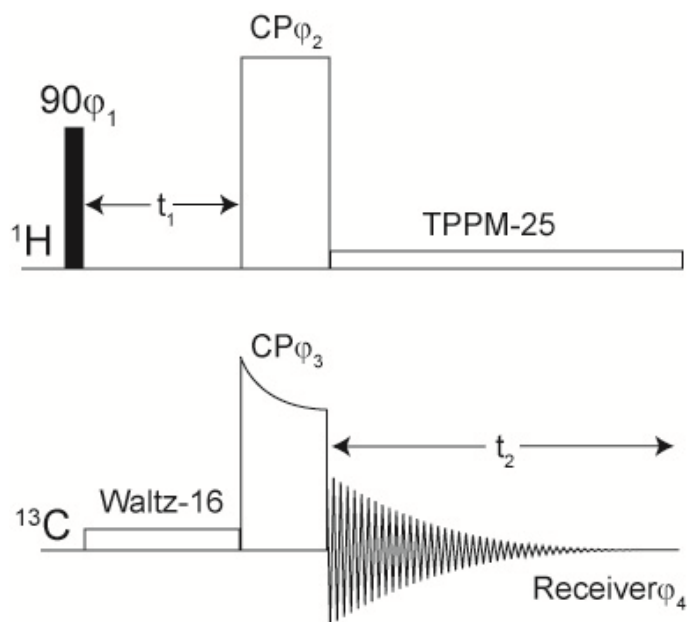


Figure 66. Pulse sequence for ^{13}C -detected 2D $^1\text{H}/^{13}\text{C}$ correlation spectroscopy. ^1H magnetization evolves during t_1 period with 10 kHz Waltz-16 ^{13}C decoupling after the initial excitation 90° pulse. The ^1H magnetization is transferred to the ^{13}C nuclei by adiabatic tangential CP and detected during the t_2 period with low power ^1H decoupling. The phase cycle for the pulse sequence are $\phi_1 = y, -y$; $\phi_2 = x$; $\phi_3 = x, x, -x, -x$; $\phi_4 = x, -x, -x, x$.

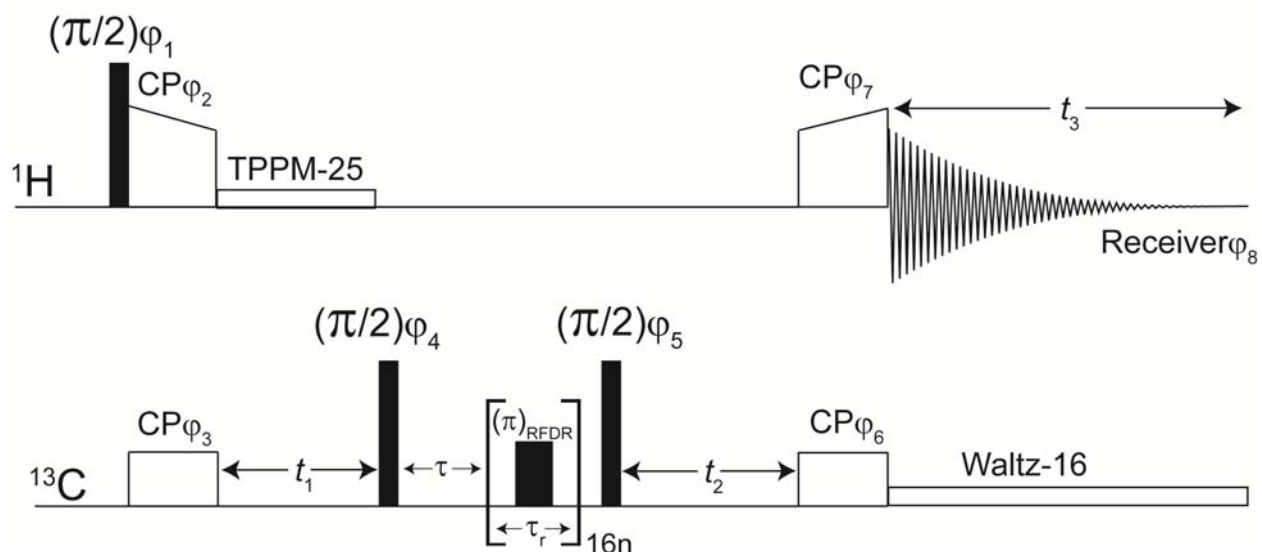


Figure 67. Pulse sequence for ^1H -detected 3D $^{13}\text{C}/^{13}\text{C}/^1\text{H}$ correlation spectroscopy. Magnetization of ^{13}C spins is prepared by CP using a ramp pulse at the ^1H frequency. During the t_1 period, a low-power TPPM-25 ^1H decoupling field is applied. After the t_1 period, the magnetization is stored along the z-axis and the unnecessary components in the transverse plane are dephased during a period of τ , ^{13}C - ^{13}C dipolar couplings were restored by the fpRFDR sequence without ^1H rf irradiation. XY-16 pulse sequence was rotor-synchronously applied so that a π -pulse is applied at the center of every rotor cycle. The magnetization is transferred back to ^1H spins by a $\pi/2$ -pulse on the ^{13}C followed by a CP with the reversed tangential pulse on ^1H channel. During the t_2 period 10 kHz Waltz-16 decoupling was applied on the ^{13}C channel. The phase cycle for the pulse sequence are $\phi_1 = y, -y$; $\phi_2 = x$; $\phi_3 = x, x, -x, -x$; $\phi_4 = y, y, y, y, -y, -y, -y, -y$; $\phi_5 = y$; $\phi_6 = -x, -x, -x, -x$; $\phi_7 = -x, -x, -x, -x, -x, -x, -x, -x, x, x, x, x, x, x, x, x$; $\phi_8 = x, -x, -x, x, -x, x, x, -x, x, x, -x, x, -x, x$.

The ^1H NMR spectra in Figure 59, 60 were collected with a 1 pulse excitation with 10 kHz Waltz-16 ^{13}C decoupling with a pulse delay of 10 s at various spinning conditions. Figure (61, 62) (a) are the ^1H detected $^{13}\text{C}/^1\text{H}$ 2D correlation spectra and Figure (61, 62) (b) are the ^{13}C detected $^{13}\text{C}/^1\text{H}$ 2D correlation spectra obtained by the pulse programs shown in Figure 65 and Figure 66. The ^{13}C magnetization was prepared by adiabatic cross-polarization CP transfer with a constant amplitude on ^1H matched to ~ 2.5 spinning speed (v_R) and the ^{13}C matching condition was $\sim 1.5 v_R$. The effective t_1 and t_2 period for Figure 61 (a) (^1H detection) were 5.0 and 2.5 ms

and it is the exact reverse for the Figure 61 (b) (^{13}C detection). The spectra in Figure 61 (a,b) were processed with a matched Gaussian window function of 200 Hz on ^1H and 100 Hz ^{13}C dimension. The pulse delays were set to 0.31 s with a contact times of 2.6 ms and 0.5 ms during the 1st and 2nd CP period in Figure 61. Similar processing parameters used for Figure 62. The spectra in Figure 63 (a) was acquired with a t_1 and t_2 of 7.5 and 7.0 ms and Figure 63 (b) was collected with a t_1 and t_2 periods of 7.0 and 7.5 ms respectively. The pulse delays were 1.5 s with contact times of 4.0 ms and 2.7 ms during the 1st and 2nd CP in Figure 63. All the spectra in Figure 63 were processed with 45° and 60° shifted sinebell window function on ^1H and ^{13}C dimensions respectively. The spectrum in Figure 64 was obtained with the pulse program shown in Figure 67. The 3D experiment (Figure 64) was obtained with a low-power CP, in which the ^{13}C amplitude was set constant ($\frac{1}{4}^{\text{th}} v_R$) with a linear ramp (100-75%) on ^1H averaging ($\frac{3}{4}^{\text{th}} v_R$). The experiment in Figure 64 was acquired with a t_1 and t_2 period of 3.5 ms and t_3 10.6 ms. The spectrum in Figure 64 was linear predicted to 6.6 ms in t_1 and t_2 and was processed in the same way as Figure 63.

VIII) CITED LITERATURE

1. Ernst, R. R., Anderson, W. A., Application of Fourier Transform Spectroscopy to Magnetic Resonance. *Rev. Sci. Instrum.* **1966**, 37.
2. Riek, R.; Fiaux, J.; Bertelsen, E. B.; Horwich, A. L.; Wuthrich, K., Solution NMR techniques for large molecular and supramolecular structures. *J. Am. Chem. Soc.* **2002**, 124, (41), 12144-12153.
3. Fiaux, J.; Bertelsen, E. B.; Horwich, A. L.; Wuthrich, K., NMR analysis of a 900K GroEL-GroES complex. *Nature* **2002**, 418, (6894), 207-211.
4. Lowe, I. J., Free Induction Decays of Rotating Solids. *Phys. Rev. Lett.* **1959**, 2, (7), 285-287.
5. E. R. Andrew, A. B., R. G. Eades, Nuclear magnetic resonance spectra from a crystal rotated at high speed. *Nature* **1958**, 182, 1659.
6. Degroot, H. J. M.; Smith, S. O.; Courtin, J.; Vandenberg, E.; Winkel, C.; Lugtenburg, J.; Griffin, R. G.; Herzfeld, J., Solid-state ^{13}C and ^{15}N NMR study of the low pH forms of bacteriorhodopsin. *Biochemistry* **1990**, 29, (29), 6873-6883.
7. Schaefer, J.; Kramer, K. J.; Garbow, J. R.; Jacob, G. S.; Stejskal, E. O.; Hopkins, T. L.; Speirs, R. D., Aromatic cross-links in insect cuticle - detection by solid-state ^{13}C and ^{15}N NMR. *Science* **1987**, 235, (4793), 1200-1204.
8. Gu, Z. T.; Opella, S. J., Three-dimensional ^{13}C shift/ ^1H - ^{15}N Coupling/ ^{15}N shift solid-state NMR correlation spectroscopy. *J. Magn. Reson.* **1999**, 138, (2), 193-198.
9. Tan, W. M.; Gu, Z. T.; Zeri, A. C.; Opella, S. J., Solid-state NMR triple-resonance backbone assignments in a protein. *J. Biomol. NMR* **1999**, 13, (4), 337-342.
10. Hartmann, S. R. H., E. L., Nuclear Double Resonance in the Rotating Frame. *Phys. Rev.* **1962**, 128, (5), 2042-2053.
11. Gardner, K. H.; Kay, L. E., The use of H-2, C-13, N-15 multidimensional NMR to study the structure and dynamics of proteins. *Annu. Rev. Biophys. Biomol. Struct.* **1998**, 27, 357-406.
12. Goto, N. K.; Kay, L. E., New developments in isotope labeling strategies for protein solution NMR spectroscopy. *Curr. Opin. Struct. Biol.* **2000**, 10, (5), 585-592.
13. Hologne, M.; Chevelkov, V.; Reif, B., Deuterated peptides and proteins in MAS solid-state NMR. *Prog. Nucl. Magn. Reson. Spectrosc.* **2006**, 48, (4), 211-232.
14. Paravastu, A. K.; Leapman, R. D.; Yau, W. M.; Tycko, R., Molecular structural basis for polymorphism in Alzheimer's beta-amyloid fibrils. *Proc. Natl. Acad. Sci. U. S. A.* **2008**, 105, (47), 18349-18354.

15. Petkova, A. T.; Leapman, R. D.; Guo, Z. H.; Yau, W. M.; Mattson, M. P.; Tycko, R., Self-propagating, molecular-level polymorphism in Alzheimer's beta-amyloid fibrils. *Science* **2005**, 307, (5707), 262-265.
16. Morcombe, C. R.; Gaponenko, V.; Byrd, R. A.; Zilm, K. W., C-13 CPMAS spectroscopy of deuterated proteins: CP dynamics, line shapes, and T-1 relaxation. *J. Am. Chem. Soc.* **2005**, 127, (1), 397-404.
17. Heise, H.; Hoyer, W.; Becker, S.; Andronesi, O. C.; Riedel, D.; Baldus, M., Molecular-level secondary structure, polymorphism, and dynamics of full-length alpha-synuclein fibrils studied by solid-state NMR. *Proc. Natl. Acad. Sci. U. S. A.* **2005**, 102, (44), 15871-15876.
18. Wasmer, C.; Schuetz, A.; Loquet, A.; Buhtz, C.; Greenwald, J.; Riek, R.; Boeckmann, A.; Meier, B. H., The Molecular Organization of the Fungal Prion HET-s in Its Amyloid Form. *J. Mol. Biol.* **2009**, 394, (1), 119-127.
19. Petkova, A. T.; Ishii, Y.; Balbach, J. J.; Antzutkin, O. N.; Leapman, R. D.; Delaglio, F.; Tycko, R., A structural model for Alzheimer's beta-amyloid fibrils based on experimental constraints from solid state NMR. *Proc. Natl. Acad. Sci. U. S. A.* **2002**, 99, (26), 16742-16747.
20. Petkova, A. T.; Yau, W. M.; Tycko, R., Experimental constraints on quaternary structure in Alzheimer's beta-amyloid fibrils. *Biochemistry* **2006**, 45, (2), 498-512.
21. Chimon, S.; Shaibat, M. A.; Jones, C. R.; Calero, D. C.; Aizezi, B.; Ishii, Y., Evidence of fibril-like beta-sheet structures in a neurotoxic amyloid intermediate of Alzheimer's beta-amyloid. *Nat. Struct. Mol. Biol.* **2007**, 14, (12), 1157-1164.
22. Ahmed, M.; Davis, J.; Aucoin, D.; Sato, T.; Ahuja, S.; Aimoto, S.; Elliott, J. I.; Van Nostrand, W. E.; Smith, S. O., Structural conversion of neurotoxic amyloid-beta(1-42) oligomers to fibrils. *Nat. Struct. Mol. Biol.* **2010**, 17, (5), 561-567.
23. Comellas, G.; Lemkau, L. R.; Zhou, D. H.; George, J. M.; Rienstra, C. M., Structural Intermediates during alpha-Synuclein Fibrillogenesis on Phospholipid Vesicles. *J. Am. Chem. Soc.* **2012**, 134, (11), 5090-5099.
24. Cady, S. D.; Schmidt-Rohr, K.; Wang, J.; Soto, C. S.; DeGrado, W. F.; Hong, M., Structure of the amantadine binding site of influenza M2 proton channels in lipid bilayers. *Nature* **2010**, 463, (7281), 689-692.
25. Hu, F.; Luo, W.; Hong, M., Mechanisms of Proton Conduction and Gating in Influenza M2 Proton Channels from Solid-State NMR. *Science* **2010**, 330, (6003), 505-508.
26. Etzkorn, M.; Kneuper, H.; Duennwald, P.; Vijayan, V.; Kraemer, J.; Griesinger, C.; Becker, S.; Unden, G.; Baldus, M., Plasticity of the PAS domain and a potential role for signal transduction in the histidine kinase DcuS. *Nat. Struct. Mol. Biol.* **2008**, 15, (10), 1031-1039.

27. Lange, V.; Becker-Baldus, J.; Kunert, B.; van Rossum, B.-J.; Casagrande, F.; Engel, A.; Roske, Y.; Scheffel, F. M.; Schneider, E.; Oschkinat, H., A MAS NMR Study of the Bacterial ABC Transporter ArtMP. *ChemBioChem* **2010**, 11, (4), 547-555.
28. Hiller, M.; Higman, V. A.; Jehle, S.; van Rossum, B.-J.; Kuehlbrandt, W.; Oschkinat, H., 2,3-C-13 -labeling of aromatic residues-getting a head start in the magic-angle-spinning NMR assignment of membrane proteins. *J. Am. Chem. Soc.* **2008**, 130, (2), 408-409.
29. Luca, S.; White, J. F.; Sohal, A. K.; Filippov, D. V.; van Boom, J. H.; Grisshammer, R.; Baldus, M., The conformation of neurotensin bound to its G protein-coupled receptor. *Proc. Natl. Acad. Sci. U. S. A.* **2003**, 100, (19), 10706-10711.
30. Kern, T.; Hediger, S.; Mueller, P.; Giustini, C.; Joris, B.; Bougault, C.; Vollmer, W.; Simorre, J.-P., Toward the characterization of peptidoglycan structure and protein - Peptidoglycan interactions by solid-state NMR Spectroscopy. *J. Am. Chem. Soc.* **2008**, 130, (17), 5618-5619.
31. Kim, S. J.; Schaefer, J., Hydrophobic side-chain length determines activity and conformational heterogeneity of a vancomycin derivative bound to the cell wall of *Staphylococcus aureus*. *Biochemistry* **2008**, 47, (38), 10155-10161.
32. Kim, S. J.; Singh, M.; Schaefer, J., Oritavancin Binds to Isolated Protoplast Membranes but not Intact Protoplasts of *Staphylococcus aureus*. *J. Mol. Biol.* **2009**, 391, (2), 414-425.
33. Sharif, S.; Singh, M.; Kim, S. J.; Schaefer, J., *Staphylococcus aureus* Peptidoglycan Tertiary Structure from Carbon-13 Spin Diffusion. *J. Am. Chem. Soc.* **2009**, 131, (20), 7023-7030.
34. Rubinsztein, D. C., The roles of intracellular protein-degradation pathways in neurodegeneration. *Nature* **2006**, 443, (7113), 780-786.
35. Bredesen, D.; Rao, R.; Mehlen, P., Cell death in the nervous system. *Nature* **2006**, 443, (7113), 796-802.
36. Mattson, M. P., Pathways towards and away from Alzheimer's disease. *Nature* **2004**, 430, (7000), 631-639.
37. Prusiner, S. B., Prions. *Proc. Natl. Acad. Sci. U. S. A.* **1998**, 95, (23), 13363-13383.
38. Burre, J.; Sharma, M.; Tsetsenis, T.; Buchman, V.; Etherton, M. R.; Suedhof, T. C., alpha-Synuclein Promotes SNARE-Complex Assembly in Vivo and in Vitro. *Science* **2010**, 329, (5999), 1663-1667.
39. Bucciantini, M.; Giannoni, E.; Chiti, F.; Baroni, F.; Formigli, L.; Zurdo, J. S.; Taddei, N.; Ramponi, G.; Dobson, C. M.; Stefani, M., Inherent toxicity of aggregates implies a common mechanism for protein misfolding diseases. *Nature* **2002**, 416, (6880), 507-511.

40. Tycko, R., Solid-State NMR Studies of Amyloid Fibril Structure. In *Ann. Rev. Phys. Chem. Vol 62*, Leone, S. R.; Cremer, P. S.; Groves, J. T.; Johnson, M. A., Eds. 2011; Vol. 62, pp 279-299.
41. Jellinger, K., The role of alpha-synuclein in neurodegeneration - An update. *Trans. Neur.* **2012**, 3, (2), 75-122.
42. Neudecker, P.; Robustelli, P.; Cavalli, A.; Walsh, P.; Lundstrom, P.; Zarrine-Afsar, A.; Sharpe, S.; Vendruscolo, M.; Kay, L. E., Structure of an Intermediate State in Protein Folding and Aggregation. *Science* **2012**, 336, (6079), 362-366.
43. Mohs, R. C., The clinical syndrome of Alzheimer's disease: aspects particularly relevant to clinical trials. *Gen. Bra. Beha.* **2005**, 4, (3), 129-133.
44. Alzheimers, A., 2012 Alzheimer's disease facts and figures. *Alzheimers & Dementia* **2012**, 8, (2), 131-168.
45. Cumming, T.; Brodtmann, A., Dementia and stroke: the present and future epidemic. *Int. J. Stroke* **2010**, 5, (6), 453-454.
46. Perl, D. P., Neuropathology of Alzheimer's Disease. *Mt. Sinai J. Med.* **2010**, 77, (1), 32-42.
47. Duyckaerts, C.; Delatour, B.; Potier, M.-C., Classification and basic pathology of Alzheimer disease. *Acta Neuropathol. (Berl)*. **2009**, 118, (1), 5-36.
48. Megan Murray Gessel, S. B., Martin Kemper, David B. Teplow, Michael T. Bowers, Familial Alzheimer's Disease Mutations Differentially Alter Amyloid β -Protein Oligomerization. *ACS Chem. Neuroscience* **2012**, 3, (11), 909-918.
49. Kenjiro Ono, M. M. C., David B. Teplow, Effects of the English (H6R) and Tottori (D7N) Familial Alzheimer Disease Mutations on Amyloid-Protein Assembly and Toxicity. *The J. Biol. Chem.* **2010**, 285, (30), 23186-23197.
50. Wei-Ting Chen, C.-J. H., Ya-Tzu Lin, Wen-Han Chang, He-Ting Huang, Jhih-Ying Liao, Yu-Jen hang,; Yi-Fang Hsieh, C.-Y. C., Hsiu-Chih Liu, Yun-Ru Chen, Irene H. Cheng, Amyloid-Beta ($A\beta$) D7H Mutation Increases Oligomeric $A\beta_{42}$ and Alters Properties of $A\beta$ -Zinc/Copper Assemblies. *PLoS One* **2012**, 7, (4), 1-12
51. Hilal A. Lashuel, D. M. H., Benjamin M. Petre, Joseph S. Wall, Martha N. Simon, Thomas Walz, Peter T. Lansbury Jr, Mixtures of Wild-type and a Pathogenic (E22G) Form of Ab40 in Vitro Accumulate Protofibrils, Including Amyloid Pores. *J. Mol. Biol.* **2003**, 332, 795-808.
52. William E. Van Nostrand, J. P. M., Hyun Soon Cho, Steven M. Greenberg, G. William Rebeck, Pathogenic Effects of D23N Iowa Mutant Amyloid β -Protein. *J. Biol. Chem.* **2001**, 276, (35), 32860-32866.

53. Roychaudhuri, R.; Yang, M.; Hoshi, M. M.; Teplow, D. B., Amyloid beta-Protein Assembly and Alzheimer Disease. *J. Biol. Chem.* **2009**, 284, (8), 4749-4753.
54. Noguchi, A.; Matsumura, S.; Dezawa, M.; Tada, M.; Yanazawa, M.; Ito, A.; Akioka, M.; Kikuchi, S.; Sato, M.; Ideno, S.; Noda, M.; Fukunari, A.; Muramatsu, S.; Itokazu, Y.; Sato, K.; Takahashi, H.; Teplow, D. B.; Nabeshima, Y.; Kakita, A.; Imahori, K.; Hoshi, M., Isolation and Characterization of Patient-derived, Toxic, High Mass Amyloid beta-Protein (A beta) Assembly from Alzheimer Disease Brains. *J. Biol. Chem.* **2009**, 284, (47), 32895-32905.
55. Kaye, R.; Head, E.; Thompson, J. L.; McIntire, T. M.; Milton, S. C.; Cotman, C. W.; Glabe, C. G., Common structure of soluble amyloid oligomers implies common mechanism of pathogenesis. *Science* **2003**, 300, (5618), 486-489.
56. Benilova, I.; Karran, E.; De Strooper, B., The toxic A beta oligomer and Alzheimer's disease: an emperor in need of clothes. *Nat. Neurosci.* **2012**, 15, (3), 349-357.
57. Podlisny, M. B.; Ostaszewski, B. L.; Squazzo, S. L.; Koo, E. H.; Rydell, R. E.; Teplow, D. B.; Selkoe, D. J., Aggregation of secreted Amyloid beta-protein into sodium dodecyl sulfate-stable oligomers in cell-culture. *J. Biol. Chem.* **1995**, 270, (16), 9564-9570.
58. Lambert, M. P.; Barlow, A. K.; Chromy, B. A.; Edwards, C.; Freed, R.; Liosatos, M.; Morgan, T. E.; Rozovsky, I.; Trommer, B.; Viola, K. L.; Wals, P.; Zhang, C.; Finch, C. E.; Krafft, G. A.; Klein, W. L., Diffusible, nonfibrillar ligands derived from A beta(1-42) are potent central nervous system neurotoxins. *Proc. Natl. Acad. Sci. U. S. A.* **1998**, 95, (11), 6448-6453.
59. Lesne, S.; Koh, M. T.; Kotilinek, L.; Kaye, R.; Glabe, C. G.; Yang, A.; Gallagher, M.; Ashe, K. H., A specific amyloid-beta protein assembly in the brain impairs memory. *Nature* **2006**, 440, (7082), 352-357.
60. Deshpande, A.; Mina, E.; Glabe, C.; Busciglio, J., Different conformations of amyloid beta induce neurotoxicity by distinct mechanisms in human cortical neurons. *J. Neurosci.* **2006**, 26, (22), 6011-6018.
61. Noguchi, A.; Matsumura, S.; Dezawa, M.; Tada, M.; Yanazawa, M.; Ito, A.; Akioka, M.; Kikuchi, S.; Sato, M.; Ideno, S.; Noda, M.; Fukunari, A.; Muramatsu, S.; Itokazu, Y.; Sato, K.; Takahashi, H.; Teplow, D. B.; Nabeshima, Y.; Kakita, A.; Imahori, K.; Hoshi, M., Isolation and Characterization of Patient-derived, Toxic, High Mass Amyloid beta-Protein (A beta) Assembly from Alzheimer Disease Brains. *J. Biol. Chem.* **2009**, 284, (47), 32895-32905.
62. Dong, J.; Atwood, C. S.; Anderson, V. E.; Siedlak, S. L.; Smith, M. A.; Perry, G.; Carey, P. R., Metal binding and oxidation of amyloid-beta within isolated senile plaque cores: Raman microscopic evidence. *Biochemistry* **2003**, 42, (10), 2768-2773.
63. Lovell, M. A.; Robertson, J. D.; Teesdale, W. J.; Campbell, J. L.; Markesbery, W. R., Copper, iron and zinc in Alzheimer's disease senile plaques. *J. Neurol. Sci.* **1998**, 158, (1), 47-52.
64. Zecca, L.; Youdim, M. B. H.; Riederer, P.; Connor, J. R.; Crichton, R. R., Iron, brain ageing and neurodegenerative disorders. *Nat. Rev. Neurosci.* **2004**, 5, (11), 863-873.

65. Miller, L. M.; Wang, Q.; Telivala, T. P.; Smith, R. J.; Lanzirrotti, A.; Miklossy, J., Synchrotron-based infrared and X-ray imaging shows focalized accumulation of Cu and Zn co-localized with beta-amyloid deposits in Alzheimer's disease. *J. Struct. Biol.* **2006**, 155, (1), 30-37.
66. Drew, S. C.; Masters, C. L.; Barnham, K. J., Alanine-2 Carbonyl is an Oxygen Ligand in Cu²⁺ Coordination of Alzheimer's Disease Amyloid-beta Peptide - Relevance to N-Terminally Truncated Forms. *J. Am. Chem. Soc.* **2009**, 131, (25), 8760-8761.
67. Drew, S. C.; Noble, C. J.; Masters, C. L.; Hanson, G. R.; Barnham, K. J., Pleomorphic Copper Coordination by Alzheimer's Disease Amyloid-beta Peptide. *J. Am. Chem. Soc.* **2009**, 131, (3), 1195-1207.
68. Sarell, C. J.; Syme, C. D.; Rigby, S. E. J.; Viles, J. H., Copper(II) Binding to Amyloid-beta Fibrils of Alzheimer's Disease Reveals a Picomolar Affinity: Stoichiometry and Coordination Geometry Are Independent of A beta Oligomeric Form. *Biochemistry* **2009**, 48, (20), 4388-4402.
69. Minicozzi, V.; Stellato, F.; Comai, M.; Dalla Serra, M.; Potrich, C.; Meyer-Klaucke, W.; Morante, S., Identifying the minimal copper- and zinc-binding site sequence in amyloid-beta peptides. *J. Biol. Chem.* **2008**, 283, (16), 10784-10792.
70. Ali, F. E.; Separovic, F.; Barrow, C. J.; Cherny, R. A.; Fraser, F.; Bush, A. I.; Masters, C. L.; Barnham, K. J., Methionine regulates copper/hydrogen peroxide oxidation products of A beta. *J. Pept. Sci.* **2005**, 11, (6), 353-360.
71. Lim, K. H.; Kim, Y. K.; Chang, Y.-T., Investigations of the molecular mechanism of metal-induced A beta (1-40) amyloidogenesis. *Biochemistry* **2007**, 46, (47), 13523-13532.
72. Miura, T.; Suzuki, K.; Kohata, N.; Takeuchi, H., Metal binding modes of Alzheimer's amyloid beta-peptide in insoluble aggregates and soluble complexes. *Biochemistry* **2000**, 39, (23), 7024-7031.
73. Hou, L. M.; Zagorski, M. G., NMR reveals anomalous copper(II) binding to the amyloid A beta peptide of Alzheimer's disease. *J. Am. Chem. Soc.* **2006**, 128, (29), 9260-9261.
74. Karr, J. W.; Kaupp, L. J.; Szalai, V. A., Amyloid-beta binds Cu²⁺ in a mononuclear metal ion binding site. *J. Am. Chem. Soc.* **2004**, 126, (41), 13534-13538.
75. Karr, J. W.; Szalai, V. A., Cu(II) binding to monomeric, oligomeric, and fibrillar forms of the Alzheimer's disease amyloid-beta peptide. *Biochemistry* **2008**, 47, (17), 5006-5016.
76. Atwood, C. S.; Huang, X. D.; Moir, R. D.; Tanzi, R. E.; Bush, A. I., Role of free radicals and metal ions in the pathogenesis of Alzheimer's disease. *Metal Ions in Biological Systems, Vol 36* **1999**, 36, 309-364.
77. Barnham, K. J.; Masters, C. L.; Bush, A. I., Neurodegenerative diseases and oxidative stress. *Nat. Rev. Drug Discov.* **2004**, 3, (3), 205-214.

78. Faller, P., Copper and Zinc Binding to Amyloid-beta: Coordination, Dynamics, Aggregation, Reactivity and Metal-Ion Transfer. *ChemBioChem* **2009**, 10, (18), 2837-2845.
79. Dikalov, S. I.; Vitek, M. P.; Maples, K. R.; Mason, R. P., Amyloid beta peptides do not form peptide-derived free radicals spontaneously, but can enhance metal-catalyzed oxidation of hydroxylamines to nitroxides. *J. Biol. Chem.* **1999**, 274, (14), 9392-9399.
80. Turnbull, S.; Tabner, B. J.; El-Agnaf, O. M. A.; Twyman, L. J.; Allsop, D., New evidence that the Alzheimer beta-amyloid peptide does not spontaneously form free radicals: An ESR study using a series of spin-traps. *Free Radical Biol. Med.* **2001**, 30, (10), 1154-1162.
81. Campbell, A.; Smith, M. A.; Sayre, L. M.; Bondy, S. C.; Perry, G., Mechanisms by which metals promote events connected to neurodegenerative diseases. *Brain Res. Bull.* **2001**, 55, (2), 125-132.
82. Opazo, C.; Huang, X. D.; Cherny, R. A.; Moir, R. D.; Roher, A. E.; White, A. R.; Cappai, R.; Masters, C. L.; Tanzi, R. E.; Inestrosa, N. C.; Bush, A. I., Metalloenzyme-like activity of Alzheimer's disease beta-amyloid - Cu-dependent catalytic conversion of dopamine, cholesterol, and biological reducing agents to neurotoxic H₂O₂. *J. Biol. Chem.* **2002**, 277, (43), 40302-40308.
83. Guilloreau, L.; Combalbert, S.; Sournia-Saquet, A.; Mazarguil, H.; Faller, P., Redox chemistry of copper-amyloid-beta: The generation of hydroxyl radical in the presence of ascorbate is linked to redox-potentials and aggregation state. *ChemBiochem* **2007**, 8, (11), 1317-1325.
84. Rice, M. E., Ascorbate regulation and its neuroprotective role in the brain. *Trends Neurosci.* **2000**, 23, (5), 209-216.
85. Aksnes, A.; Njaa, L. R., Oxidation of Methionine-Effect of ascorbic-acid autooxidation. *Food Chem.* **1981**, 7, (4), 305-310.
86. Dikalov, S. I.; Vitek, M. P.; Mason, R. P., Cupric-amyloid beta peptide complex stimulates oxidation of ascorbate and generation of hydroxyl radical. *Free Radical Biol. Med.* **2004**, 36, (3), 340-347.
87. Jiang, D.; Li, X.; Liu, L.; Yagnik, G. B.; Zhou, F., Reaction Rates and Mechanism of the Ascorbic Acid Oxidation by Molecular Oxygen Facilitated by Cu(II)-Containing Amyloid-beta Complexes and Aggregates. *J. Phys. Chem. B* **2010**, 114, (14), 4896-4903.
88. Tabner, B. J.; Turnbull, S.; El-Agnaf, O. M. A.; Allsop, D., Formation of hydrogen peroxide and hydroxyl radicals from A beta and alpha-synuclein as a possible mechanism of cell death in Alzheimer's disease and Parkinson's disease. *Free Radical Biol. Med.* **2002**, 32, (11), 1076-1083.
89. Hureau, C.; Faller, P., A beta-mediated ROS production by Cu ions: Structural insights, mechanisms and relevance to Alzheimer's disease. *Biochimie* **2009**, 91, (10), 1212-1217.

90. Zeeman, P., The Influence of a Magnetic Field on Radiation Frequency. *Proceedings of the Royal Society of London* **1896**, 60, 513-514.
91. Purcell, E. M., Torrey, H.C, Pound, R.V, Resonance absorption by Nuclear Magnetic Moments in a Solid. *Physical Review* **1945**, 69, (1-2), 2.
92. Bloch, F., Nuclear Induction. *Physical Review* **1946**, 70, (7-8), 15.
93. John Cavanagh, W. J. F., Arthur G. Palmer III, Mark Rance and Nicholas J. Skelton *Protein NMR Spectroscopy Principles and Practice*. 2nd ed.; Elsevier Academic Press: 2007.
94. Duer, M. J., *Introduction to Solid-State NMR Spectroscopy*. 2004.
95. Bertini, I.; Emsley, L.; Lelli, M.; Luchinat, C.; Mao, J.; Pintacuda, G., Ultrafast MAS Solid-State NMR Permits Extensive (¹³C and (¹H) Detection in Paramagnetic Metalloproteins. *J. Am. Chem. Soc.* **2010**, 132, (16), 5558-5559.
96. Knight, M. J.; Felli, I. C.; Pierattelli, R.; Bertini, I.; Emsley, L.; Herrmann, T.; Pintacuda, G., Rapid Measurement of Pseudocontact Shifts in Metalloproteins by Proton-Detected Solid-State NMR Spectroscopy. *J. Am. Chem. Soc.* **2012**, 134, (36), 14730-14733.
97. Knight, M. J.; Pell, A. J.; Bertini, I.; Felli, I. C.; Gonnelli, L.; Pierattelli, R.; Herrmann, T.; Emsley, L.; Pintacuda, G., Structure and backbone dynamics of a microcrystalline metalloprotein by solid-state NMR. *Proc. Natl. Acad. Sci. U. S. A.* **2012**, 109, (28), 11095-11100.
98. Knight, M. J.; Webber, A. L.; Pell, A. J.; Guerry, P.; Barbet-Massin, E.; Bertini, I.; Felli, I. C.; Gonnelli, L.; Pierattelli, R.; Emsley, L.; Lesage, A.; Herrmann, T.; Pintacuda, G., Fast Resonance Assignment and Fold Determination of Human Superoxide Dismutase by High-Resolution Proton-Detected Solid-State MAS NMR Spectroscopy. *Angew. Chem. Int. Ed* **2011**, 50, (49), 11697-11701.
99. Marchetti, A.; Jehle, S.; Felletti, M.; Knight, M. J.; Wang, Y.; Xu, Z.-Q.; Park, A. Y.; Otting, G.; Lesage, A.; Emsley, L.; Dixon, N. E.; Pintacuda, G., Backbone Assignment of Fully Protonated Solid Proteins by ¹H Detection and Ultrafast Magic-Angle-Spinning NMR Spectroscopy. *Angew. Chem. Int. Ed* **2012**, 51, (43), 10756-10759.
100. Lewandowski, J. R.; Dumez, J.-N.; Akbey, U.; Lange, S.; Emsley, L.; Oschkinat, H., Enhanced Resolution and Coherence Lifetimes in the Solid-State NMR Spectroscopy of Perdeuterated Proteins under Ultrafast Magic-Angle Spinning. *J. Phys. Chem. Lett.* **2011**, 2, (17), 2205-2211.
101. Ishii, Y.; Tycko, R., Sensitivity enhancement in solid state N-15 NMR by indirect detection with high-speed magic angle spinning. *J. Magn. Reson.* **2000**, 142, (1), 199-204.
102. Ishii, Y.; Yesinowski, J. P.; Tycko, R., Sensitivity enhancement in solid-state ¹³C NMR of synthetic polymers and biopolymers by ¹H NMR detection with high-speed magic angle spinning. *J. Am. Chem. Soc.* **2001**, 123, (12), 2921-2922.

103. Su, Y.; Hu, F.; Hong, M., Paramagnetic Cu(II) for Probing Membrane Protein Structure and Function: Inhibition Mechanism of the Influenza M2 Proton Channel. *J. Am. Chem. Soc.* **2012**, 134, (20), 8693-8702.
104. Parthasarathy, S.; Long, F.; Miller, Y.; Xiao, Y.; McElheny, D.; Thurber, K.; Ma, B.; Nussinov, R.; Ishii, Y., Molecular-Level Examination of Cu²⁺ Binding Structure for Amyloid Fibrils of 40-Residue Alzheimer's beta by Solid-State NMR Spectroscopy. *J. Am. Chem. Soc.* **2011**, 133, (10), 3390-3400.
105. Nishiyama, Y.; Lu, X. Y.; Trebosc, J.; Lafon, O.; Gan, Z. H.; Madhu, P. K.; Amoureux, J. P., Practical choice of ¹H-¹H decoupling schemes in through-bond ¹H-{X} HMQC experiments at ultra-fast MAS. *J. Magn. Reson.* **2012**, 214, 151-158.
106. Lemaster, D. M., Chiral-beta and random fractional deuteration for the determination of protein side-chain conformation by NMR. *FEBS Lett.* **1987**, 223, (1), 191-196.
107. Arata, Y.; Kato, K.; Takahashi, H.; Shimada, I., Nuclear-Magnetic-Resonance study of antibodies-a multinuclear approach. *Nuclear Magnetic Resonance, Pt C* **1994**, 239, 440-464.
108. Yamazaki, T.; Otomo, T.; Oda, N.; Kyogoku, Y.; Uegaki, K.; Ito, N.; Ishino, Y.; Nakamura, H., Segmental isotope labeling for protein NMR using peptide splicing. *J. Am. Chem. Soc.* **1998**, 120, (22), 5591-5592.
109. Kainosho, M.; Guentert, P., SAIL - stereo-array isotope labeling. *Q. Rev. Biophys.* **2009**, 42, (4), 247-300.
110. Kainosho, M.; Torizawa, T.; Iwashita, Y.; Terauchi, T.; Ono, A. M.; Guentert, P., Optimal isotope labelling for NMR protein structure determinations. *Nature* **2006**, 440, (7080), 52-57.
111. Miyanoiri, Y.; Takeda, M.; Jee, J.; Ono, A. M.; Okuma, K.; Terauchi, T.; Kainosho, M., Alternative SAIL-Trp for robust aromatic signal assignment and determination of the chi(2) conformation by intra-residue NOEs. *J. Biomol. NMR* **2011**, 51, (4), 425-435.
112. Miyanoiri, Y.; Takeda, M.; Kainosho, M., Stereo-array isotope labeling method for studying protein structure and dynamics. *Adv. Exp. Med. Biol.* **2012**, 992, 83-93.
113. Ikeya, T.; Takeda, M.; Yoshida, H.; Terauchi, T.; Jee, J.-G.; Kainosho, M.; Guentert, P., Automated NMR structure determination of stereo-array isotope labeled ubiquitin from minimal sets of spectra using the SAIL-FLYA system. *J. Biomol. NMR* **2009**, 44, (4), 261-272.
114. Takeda, M.; Ono, A. M.; Terauchi, T.; Kainosho, M., Application of SAIL phenylalanine and tyrosine with alternative isotope-labeling patterns for protein structure determination. *J. Biomol. NMR* **2010**, 46, (1), 45-49.
115. Selkoe, D. J., Cell biology of protein misfolding: The examples of Alzheimer's and Parkinson's diseases. *Nat. Cell Biol.* **2004**, 6, (11), 1054-1061.

116. Leszczyszyn, O. I.; Schmid, R.; Blindauer, C. A., Toward a property/function relationship for metallothioneins: Histidine coordination and unusual cluster composition in a zinc-metal lothionein from plants. *Prot. Stru. Func. Bioinform.* **2007**, 68, (4), 922-935.
117. Huang, X. D.; Atwood, C. S.; Hartshorn, M. A.; Multhaup, G.; Goldstein, L. E.; Scarpa, R. C.; Cuajungco, M. P.; Gray, D. N.; Lim, J.; Moir, R. D.; Tanzi, R. E.; Bush, A. I., The A beta peptide of Alzheimer's disease directly produces hydrogen peroxide through metal ion reduction. *Biochemistry* **1999**, 38, (24), 7609-7616.
118. Scott, L. E.; Orvig, C., Medicinal Inorganic Chemistry Approaches to Passivation and Removal of Aberrant Metal Ions in Disease. *Chem. Rev.* **2009**, 109, (10), 4885-4910.
119. Atwood, C. S.; Scarpa, R. C.; Huang, X. D.; Moir, R. D.; Jones, W. D.; Fairlie, D. P.; Tanzi, R. E.; Bush, A. I., Characterization of copper interactions with Alzheimer amyloid beta peptides: Identification of an attomolar-affinity copper binding site on amyloid beta 1-42. *J. Neurochem.* **2000**, 75, (3), 1219-1233.
120. Atwood, C. S.; Moir, R. D.; Huang, X. D.; Scarpa, R. C.; Bacarra, N. M. E.; Romano, D. M.; Hartshorn, M. K.; Tanzi, R. E.; Bush, A. I., Dramatic aggregation of Alzheimer A beta by Cu(II) is induced by conditions representing physiological acidosis. *J. Biol. Chem.* **1998**, 273, (21), 12817-12826.
121. Bush, A. I.; Tanzi, R. E., The galvanization of beta-amyloid in Alzheimer's disease. *Proc. Natl. Acad. Sci. U. S. A.* **2002**, 99, (11), 7317-7319.
122. Bush, A. I.; Tanzi, R. E., Therapeutics for Alzheimer's disease based on the Metal Hypothesis. *Neurotherapeutics* **2008**, 5, (3), 421-432.
123. Jun, S.; Gillespie, J. R.; Shin, B.-k.; Saxena, S., The Second Cu(II)-Binding Site in a Proton-Rich Environment Interferes with the Aggregation of Amyloid-beta(1-40) into Amyloid Fibrils. *Biochemistry* **2009**, 48, (45), 10724-10732.
124. Mantri, Y.; Fioroni, M.; Baik, M. H., Computational study of the binding of Cu-II to Alzheimer's amyloid-beta peptide: Do A beta 42 and A beta 40 bind copper in identical fashion? *J. Biol. Inorg. Chem.* **2008**, 13, (8), 1197-1204.
125. Ali, F. E.; Separovic, F.; Barrow, C. J.; Yao, S. G.; Barnham, K. J., Copper and zinc mediated oligomerisation of A beta peptides. *Int. J. Pep. Res. Thera.* **2006**, 12, (2), 153-164.
126. Gaggelli, E.; Grzonka, Z.; Kozlowski, H.; Migliorini, C.; Molteni, E.; Valensin, D.; Valensin, G., Structural features of the Cu(II) complex with the rat A beta(1-28) fragment. *Chem. Commun.* **2008**, (3), 341-343.
127. Karr, J. W.; Szalai, V. A., Role of aspartate-1 in Cu(II) binding to the amyloid-beta peptide of Alzheimer's disease. *J. Am. Chem. Soc.* **2007**, 129, (13), 3796-+.

128. Liu, S. T.; Howlett, G.; Barrow, C. J., Histidine-13 is a crucial residue in the zinc ion-induced aggregation of the A beta peptide of Alzheimer's disease. *Biochemistry* **1999**, 38, (29), 9373-9378.
129. Antzutkin, O. N.; Balbach, J. J.; Leapman, R. D.; Rizzo, N. W.; Reed, J.; Tycko, R., Multiple quantum solid-state NMR indicates a parallel, not antiparallel, organization of beta-sheets in Alzheimer's beta-amyloid fibrils. *Proc. Natl. Acad. Sci. U. S. A.* **2000**, 97, (24), 13045-13050.
130. Hindo, S. S.; Mancino, A. M.; Braymer, J. J.; Liu, Y.; Vivekanandan, S.; Ramamoorthy, A.; Lim, M. H., Small Molecule Modulators of Copper-Induced A beta Aggregation. *J. Am. Chem. Soc.* **2009**, 131, (46), 16663-16665.
131. Olofsson, A.; Lindhagen-Persson, M.; Vestling, M.; Sauer-Eriksson, A. E.; Ohman, A., Quenched hydrogen/deuterium exchange NMR characterization of amyloid-beta peptide aggregates formed in the presence of Cu²⁺ or Zn²⁺. *FEBS J.* **2009**, 276, (15), 4051-4060.
132. Zoroddu, M. A.; Medici, S.; Peana, M., Copper and nickel binding in multi-histidinic peptide fragments. *J. Inorg. Biochem.* **2009**, 103, (9), 1214-1220.
133. Chimon, S.; Ishii, Y., Capturing intermediate structures of Alzheimer's beta-amyloid, A beta(1-40), by solid-state NMR spectroscopy. *J. Am. Chem. Soc.* **2005**, 127, (39), 13472-13473.
134. Sciarretta, K. L.; Gordon, D. J.; Petkova, A. T.; Tycko, R.; Meredith, S. C., A beta 40-Lactam(D23/K28) models a conformation highly favorable for nucleation of amyloid. *Biochemistry* **2005**, 44, (16), 6003-6014.
135. Wasmer, C.; Soragni, A.; Sabate, R.; Lange, A.; Riek, R.; Meier, B. H., Infectious and noninfectious amyloids of the HET-s(218-289) prion have different NMR spectra. *Angew. Chem. Int. Ed* **2008**, 47, (31), 5839-5841.
136. Helmus, J. J.; Surewicz, K.; Nadaud, P. S.; Surewicz, W. K.; Jaroniec, C. P., Molecular conformation and dynamics of the Y145Stop variant of human prion protein. *Proc. Natl. Acad. Sci. U. S. A.* **2008**, 105, (17), 6284-6289.
137. Curtis-Fisk, J.; Spencer, R. M.; Weliky, D. P., Native conformation at specific residues in recombinant inclusion body protein in whole cells determined with solid-state NMR spectroscopy. *J. Am. Chem. Soc.* **2008**, 130, (38), 12568-12569.
138. Jaroniec, C. P.; MacPhee, C. E.; Astrof, N. S.; Dobson, C. M.; Griffin, R. G., Molecular conformation of a peptide fragment of transthyretin in an amyloid fibril. *Proc. Natl. Acad. Sci. U. S. A.* **2002**, 99, (26), 16748-16753.
139. Wickramasinghe, N. P.; Parthasarathy, S.; Jones, C. R.; Bhardwaj, C.; Long, F.; Kotecha, M.; Mehboob, S.; Fung, L. W. M.; Past, J.; Samoson, A.; Ishii, Y., Nanomole-scale protein solid-state NMR by breaking intrinsic ¹H T₁ boundaries. *Nat. Methods* **2009**, 6, (3), 215-218.

140. Masuda, Y.; Uemura, S.; Ohashi, R.; Nakanishi, A.; Takegoshi, K.; Shimizu, T.; Shirasawa, T.; Irie, K., Identification of Physiological and Toxic Conformations in A beta 42 Aggregates. *ChemBioChem* **2009**, 10, (2), 287-295.
141. Pintacuda, G.; Giraud, N.; Pierattelli, R.; Bockmann, A.; Bertini, I.; Emsley, L., Solid-state NMR spectroscopy of a paramagnetic protein: Assignment and study of human dimeric oxidized Cu-II-Zn-II superoxide dismutase (SOD). *Angew. Chem. Int. Ed* **2007**, 46, (7), 1079-1082.
142. Balayssac, S.; Bertini, I.; Bhaumik, A.; Lelli, M.; Luchinat, C., Paramagnetic shifts in solid-state NMR of proteins to elicit structural information. *Proc. Natl. Acad. Sci. U. S. A.* **2008**, 105, (45), 17284-17289.
143. Balayssac, S.; Bertini, I.; Lelli, M.; Luchinat, C.; Maletta, M., Paramagnetic ions provide structural restraints in solid-state NMR of proteins. *J. Am. Chem. Soc.* **2007**, 129, (8), 2218-2219.
144. Pooransingh-Margolis, N.; Renirie, R.; Hasan, Z.; Wever, R.; Vega, A. J.; Polenova, T., V-51 solid-state magic angle spinning NMR spectroscopy of vanadium chloroperoxidase. *J. Am. Chem. Soc.* **2006**, 128, (15), 5190-5208.
145. Castellani, F.; van Rossum, B.; Diehl, A.; Schubert, M.; Rehbein, K.; Oschkinat, H., Structure of a protein determined by solid-state magic-angle-spinning NMR spectroscopy. *Nature* **2002**, 420, (6911), 98-102.
146. Lorieau, J. L.; Day, L. A.; McDermott, A. E., Conformational dynamics of an intact virus: Order parameters for the coat protein of Pfl bacteriophage. *Proc. Natl. Acad. Sci. U. S. A.* **2008**, 105, (30), 10366-10371.
147. Qiang, W.; Bodner, M. L.; Weliky, D. P., Solid-state NMR Spectroscopy of human immunodeficiency virus fusion peptides associated with host-cell-like membranes: 2D correlation spectra and distance measurements support a fully extended conformation and models for specific antiparallel strand registries. *J. Am. Chem. Soc.* **2008**, 130, (16), 5459-5471.
148. Lange, A.; Giller, K.; Hornig, S.; Martin-Eauclaire, M. F.; Pongs, O.; Becker, S.; Baldus, M., Toxin-induced conformational changes in a potassium channel revealed by solid-state NMR. *Nature* **2006**, 440, (7086), 959-962.
149. Sharma, M.; Yi, M.; Dong, H.; Qin, H.; Peterson, E.; Busath, D. D.; Zhou, H.-X.; Cross, T. A., Insight into the Mechanism of the Influenza A Proton Channel from a Structure in a Lipid Bilayer. *Science* **2010**, 330, (6003), 509-512.
150. Griffin, R. G., Dipolar recoupling in MAS spectra of biological solids. *Nat. Struct. Biol.* **1998**, 5, 508-512.
151. Opella, S. J., NMR and membrane proteins. *Nat. Struct. Biol.* **1997**, 4, 845-848.
152. McDermott, A. E., Structural and dynamic studies of proteins by solid-state NMR spectroscopy: rapid movement forward. *Curr. Opin. Struct. Biol.* **2004**, 14, (5), 554-561.

153. Baldus, M., Molecular interactions investigated by multi-dimensional solid-state NMR. *Curr. Opin. Struct. Biol.* **2006**, 16, (5), 618-623.
154. Gehman, J. D.; O'Brien, C. C.; Shabanpoor, F.; Wade, J. D.; Separovic, F., Metal effects on the membrane interactions of amyloid-beta peptides. *Eur. Biophys. J. Biophys. Lett* **2008**, 37, (3), 333-344.
155. Mantri, Y.; Fioroni, M.; Baik, M.-H., Computational study of the binding of Cu(II) to Alzheimer's amyloid-beta peptide: Do A beta 42 and A beta 40 bind copper in identical fashion? *J. Biol. Inorg. Chem.* **2008**, 13, (8), 1197-1204.
156. Bush, A. I., Drug Development Based on the Metals Hypothesis of Alzheimer's Disease. *J. Alz. Dis.* **2008**, 15, (2), 223-240.
157. Barnham, K. J.; Kenche, V. B.; Ciccotosto, G. D.; Smith, D. P.; Tew, D. J.; Liu, X.; Perez, K.; Cranston, G. A.; Johanssen, T. J.; Volitakis, I.; Bush, A. I.; Masters, C. L.; White, A. R.; Smith, J. P.; Cherny, R. A.; Cappai, R., Platinum-based inhibitors of amyloid-beta as therapeutic agents for Alzheimer's disease. *Proc. Natl. Acad. Sci. U. S. A.* **2008**, 105, (19), 6813-6818.
158. Choi, J.-S.; Braymer, J. J.; Nanga, R. P. R.; Ramamoorthy, A.; Lim, M. H., Design of small molecules that target metal-A beta species and regulate metal-induced A beta aggregation and neurotoxicity. *Proc. Natl. Acad. Sci. U. S. A.* **2010**, 107, (51), 21990-21995.
159. Jovanovic, T.; McDermott, A. E., Observation of ligand binding to cytochrome P450-BM-3 by means of solid-state NMR spectroscopy. *J. Am. Chem. Soc.* **2005**, 127, (40), 13816-13821.
160. Wickramasinghe, N. P.; Shaibat, M. A.; Ishii, Y., Elucidating connectivity and metal-binding structures of unlabeled paramagnetic complexes by C-13 and H-1 solid-state NMR under fast magic angle spinning. *J. Phys. Chem. B* **2007**, 111, (33), 9693-9696.
161. Nadaud, P. S.; Helmus, J. J.; Kall, S. L.; Jaroniec, C. P., Paramagnetic Ions Enable Tuning of Nuclear Relaxation Rates and Provide Long-Range Structural Restraints in Solid-State NMR of Proteins. *J. Am. Chem. Soc.* **2009**, 131, (23), 8108-8120.
162. Miller, Y.; Ma, B.; Nussinov, R., Polymorphism in Alzheimer A beta Amyloid Organization Reflects Conformational Selection in a Rugged Energy Landscape. *Chem. Rev.* **2010**, 110, (8), 4820-4838.
163. Smith, D. P.; Smith, D. G.; Curtain, C. C.; Boas, J. F.; Pilbrow, J. R.; Ciccotosto, G. D.; Lau, T. L.; Tew, D. J.; Perez, K.; Wade, J. D.; Bush, A. I.; Drew, S. C.; Separovic, F.; Masters, C. L.; Cappai, R.; Barnham, K. J., Copper-mediated amyloid-beta toxicity is associated with an intermolecular histidine bridge. *J. Biol. Chem.* **2006**, 281, (22), 15145-15154.
164. Matsuba, Y.; Takahash, Y., Spectrophotometric determination of Copper with N,N,N',N'-Tetraethylthiuram disulfide and an application of this method for studies on subcellular distribution of Copper in Rat Brain. *Anal. Biochem.* **1970**, 36, (1), 182-191.

165. Varadarajan, S.; Kanski, J.; Aksenova, M.; Lauderback, C.; Butterfield, D. A., Different mechanisms of oxidative stress and neurotoxicity for Alzheimer's A beta(1-42) and A beta(25-35). *J. Am. Chem. Soc.* **2001**, 123, (24), 5625-5631.
166. Schoneich, C.; Pogocki, D.; Hug, G. L.; Bobrowski, K., Free radical reactions of methionine in peptides: Mechanisms relevant to beta-amyloid oxidation and Alzheimer's disease. *J. Am. Chem. Soc.* **2003**, 125, (45), 13700-13713.
167. Barnham, K. J.; Ciccotosto, G. D.; Tickler, A. K.; Ali, F. E.; Smith, D. G.; Williamson, N. A.; Lam, Y. H.; Carrington, D.; Tew, D.; Kocak, G.; Volitakis, I.; Separovic, F.; Barrow, C. J.; Wade, J. D.; Masters, C. L.; Cherny, R. A.; Curtain, C. C.; Bush, A. I.; Cappai, R., Neurotoxic, redox-competent Alzheimer's beta-amyloid is released from lipid membrane by methionine oxidation. *J. Biol. Chem.* **2003**, 278, (44), 42959-42965.
168. Ishii, Y., ^{13}C - ^{13}C dipolar recoupling under very fast magic angle spinning in solid-state nuclear magnetic resonance: Applications to distance measurements, spectral assignments, and high-throughput secondary-structure determination. *J. Chem. Phys.*, 2001; Vol. 114, pp 8473-8483.
169. Tickler, A. K.; Smith, D. G.; Ciccotosto, G. D.; Tew, D. J.; Curtain, C. C.; Carrington, D.; Masters, C. L.; Bush, A. I.; Cherny, R. A.; Cappai, R.; Wade, J. D.; Barnham, K. J., Methylation of the imidazole side chains of the Alzheimer disease amyloid-beta peptide results in abolition of superoxide dismutaselike structures and inhibition of neurotoxicity. *J. Biol. Chem.* **2005**, 280, (14), 13355-13363.
170. Pang, Y. P., Novel zinc protein molecular dynamics simulations: Steps toward antiangiogenesis for cancer treatment. *J. Mol. Model.* **1999**, 5, (10), 196-202.
171. Branco, R. J. F.; Fernandes, P. A.; Ramos, M. J., Molecular dynamics simulations of the enzyme Cu, Zn superoxide dismutase. *J. Phys. Chem. B* **2006**, 110, (33), 16754-16762.
172. Peters, M. B.; Yang, Y.; Wang, B.; Fuesti-Molnar, L.; Weaver, M. N.; Merz, K. M., Jr., Structural Survey of Zinc-Containing Proteins and Development of the Zinc AMBER Force Field (ZAFF). *J. Chem. Theo. Comp.* **2010**, 6, (9), 2935-2947.
173. Dorlet, P.; Gambarelli, S.; Faller, P.; Hureau, C., Pulse EPR Spectroscopy Reveals the Coordination Sphere of Copper(II) Ions in the 1-16 Amyloid-beta Peptide: A Key Role of the First Two N-Terminus Residues. *Angew. Chem. Int. Ed.* **2009**, 48, (49), 9273-9276.
174. Viles, J. H., Metal ions and amyloid fiber formation in neurodegenerative diseases. Copper, zinc and iron in Alzheimer's, Parkinson's and prion diseases. *Coord. Chem. Rev.* **2012**, 256, 2271-2284.
175. Ishii, Y.; Wickramasinghe, N. P.; Chimon, S., A new approach in 1D and 2D ^{13}C high-resolution solid-state NMR spectroscopy of paramagnetic organometallic complexes by very fast magic-angle spinning. *J. Am. Chem. Soc.* **2003**, 125, (12), 3438-3439.

176. Wickramasinghe, N. P.; Shaibat, M.; Ishii, Y., Enhanced sensitivity and resolution in ^1H solid-state NMR spectroscopy of paramagnetic complexes under very fast magic angle spinning. *J. Am. Chem. Soc.* **2005**, 127, (16), 5796-5797.
177. Shaibat, M. A.; Casabianca, L. B.; Wickramasinghe, N. P.; Guggenheim, S.; de Dios, A. C.; Ishii, Y., Characterization of polymorphs and solid-state reactions for paramagnetic systems by ^{13}C solid-state NMR and ab initio calculations. *J. Am. Chem. Soc.* **2007**, 129, (36), 10968-10969.
178. Kervern, G.; Pintacuda, G.; Zhang, Y.; Oldfield, E.; Roukoss, C.; Kuntz, E.; Herdtweck, E.; Basset, J.-M.; Cadars, S.; Lesage, A.; Coperet, C.; Emsley, L., Solid-state NMR of a paramagnetic DIAD-Fe-II catalyst: Sensitivity, resolution enhancement, and structure-based assignments. *J. Am. Chem. Soc.* **2006**, 128, (41), 13545-13552.
179. Fields, C. G.; Fields, G. B.; Noble, R. L.; Cross, T. A., Solid-Phase peptide-synthesis of ^{15}N -Gramicidin-A, ^{15}N -Gramicidin-B, and ^{15}N -Gramicidin-C and high-performance liquid-chromatographic purification. *Int. J. Pept. Protein Res.* **1989**, 33, (4), 298-303.
180. Long, F.; Cho, W.; Ishii, Y., Expression and purification of ^{15}N - and ^{13}C -isotope labeled 40-residue human Alzheimer's beta-amyloid peptide for NMR-based structural analysis. *Protein Expression Purif.* **2011**, 79, (1), 16-24.
181. Hoshi, M.; Sato, M.; Matsumoto, S.; Noguchi, A.; Yasutake, K.; Yoshida, N.; Sato, K., Spherical aggregates of beta-amyloid (amylospheroid) show high neurotoxicity and activate tau protein kinase I/glycogen synthase kinase-3 beta. *Proc. Natl. Acad. Sci. U. S. A.* **2003**, 100, (11), 6370-6375.
182. Delaglio, F.; Grzesiek, S.; Vuister, G. W.; Zhu, G.; Pfeifer, J.; Bax, A., NMRPIPE - A multidimensional spectral processing system based on UNIX pipes. *J. Biomol. NMR* **1995**, 6, (3), 277-293.
183. Kotecha, M.; Wickramasinghe, N. P.; Ishii, Y., Efficient low-power heteronuclear decoupling in ^{13}C high-resolution solid-state NMR under fast magic angle spinning. *Magn. Reson. Chem.* **2007**, 45, S221-S230.
184. De Felice, F. G.; Ferreira, S. T., beta-amyloid production, aggregation, and clearance as targets for therapy in Alzheimer's disease. *Cell. Mol. Neurobiol.* **2002**, 22, (5-6), 545-563.
185. Selkoe, D. J., The origins of Alzheimer disease - A is for amyloid. *J. Am. Med. Assoc.* **2000**, 283, (12), 1615-1617.
186. Rijal Upadhaya, A.; Capetillo-Zarate, E.; Kosterin, I.; Abramowski, D.; Kumar, S.; Yamaguchi, H.; Walter, J.; Fandrich, M.; Staufenbiel, M.; Thal, D. R., Dispersible amyloid beta-protein oligomers, protofibrils, and fibrils represent diffusible but not soluble aggregates: their role in neurodegeneration in amyloid precursor protein (APP) transgenic mice. *Neurobiol. Aging* **2012**, 33, (11), 2641-60.

187. Harper, J. D.; Wong, S. S.; Lieber, C. M.; Lansbury, P. T., Observation of metastable A beta amyloid protofibrils by atomic force microscopy. *Chem. Biol.* **1997**, 4, (2), 119-125.
188. Glabe, C. G.; Kaye, R., Common structure and toxic function of amyloid oligomers implies a common mechanism of pathogenesis. *Neurology* **2006**, 66, S74-S78.
189. Hung, Y. H.; Bush, A. I.; Cherny, R. A., Copper in the brain and Alzheimer's disease. *J. Biol. Inorg. Chem.* **2010**, 15, (1), 61-76.
190. Zhu, X.; Su, B.; Wang, X.; Smith, M. A.; Perry, G., Causes of oxidative stress in Alzheimer disease. *Cell. Mol. Life Sci.* **2007**, 64, (17), 2202-2210.
191. Bush, A. I., The metallobiology of Alzheimer's disease. *Trends Neurosci.* **2003**, 26, (4), 207-214.
192. Atwood, C. S.; Obrenovich, M. E.; Liu, T. B.; Chan, H.; Perry, G.; Smith, M. A.; Martins, R. N., Amyloid-beta: a chameleon walking in two worlds: a review of the trophic and toxic properties of amyloid-beta. *Brain Res. Rev.* **2003**, 43, (1), 1-16.
193. Huang, X. D.; Cuajungco, M. P.; Atwood, C. S.; Hartshorn, M. A.; Tyndall, J. D. A.; Hanson, G. R.; Stokes, K. C.; Leopold, M.; Multhaup, G.; Goldstein, L. E.; Scarpa, R. C.; Saunders, A. J.; Lim, J.; Moir, R. D.; Glabe, C.; Bowden, E. F.; Masters, C. L.; Fairlie, D. P.; Tanzi, R. E.; Bush, A. I., Cu(II) potentiation of Alzheimer A beta neurotoxicity - Correlation with cell-free hydrogen peroxide production and metal reduction. *J. Biol. Chem.* **1999**, 274, (52), 37111-37116.
194. Atwood, C. S.; Huang, X. D.; Moir, R. D.; Tanzi, R. E.; Bush, A. I., Role of free radicals and metal ions in the pathogenesis of Alzheimer's disease. *Met. Ions Biol. Syst.* **1999**, 36, 309-364.
195. Castellani, R. J.; Honda, K.; Zhu, X. W.; Cash, A. D.; Nunomura, A.; Perry, G.; Smith, M. A., Contribution of redox-active iron and copper to oxidative damage in Alzheimer disease. *Ageing Research Reviews* **2004**, 3, (3), 319-326.
196. Perry, G., Cash, Adam D, Smith, Mark A, Alzheimer Disease and Oxidative Stress. *J. Biomed. Biotech.* **2002**, 2, (3), 120-123
197. Sayre, L. M.; Zelasko, D. A.; Harris, P. L. R.; Perry, G.; Salomon, R. G.; Smith, M. A., 4-hydroxynonenal-derived advanced lipid peroxidation end products are increased in Alzheimer's disease. *J. Neurochem.* **1997**, 68, (5), 2092-2097.
198. Ali, F. E.; Separovic, F.; Barrow, C. J.; Yao, S. G.; Barnham, K. J., Copper and zinc mediated oligomerisation of A beta peptides. *Int. J. Pept. Res. Thera.* **2006**, 12, (2), 153-164.
199. Federico, A.; Cardaioli, E.; Da Pozzo, P.; Formichi, P.; Gallus, G. N.; Radi, E., Mitochondria, oxidative stress and neurodegeneration. *J. Neurol. Sci.* **2012**, 322, (1-2), 254-62.

200. Barnham, K. J.; Masters, C. L.; Bush, A. I., Neurodegenerative diseases and oxidative stress. *Nat. Rev. Drug Discov.* **2004**, 3, (3), 205-214.
201. Schoneich, C.; Williams, T. D., Cu(II)-catalyzed oxidation of beta-amyloid peptide targets His(13) and His(14) over His(6): Detection of 2-oxo-histidine by HPLC-MS/MS. *Chem. Res. Toxicol.* **2002**, 15, (5), 717-722.
202. Schiewe, A. J.; Margol, L.; Soreghan, B. A.; Thomas, S. N.; Yang, A. J., Rapid characterization of amyloid-beta side-chain oxidation by tandem mass spectrometry and the scoring algorithm for spectral analysis. *Pharm. Res.* **2004**, 21, (7), 1094-1102.
203. Atwood, C. S.; Huang, X. D.; Khatri, A.; Scarpa, R. C.; Kim, Y. S.; Moir, R. D.; Tanzi, R. E.; Roher, A. E.; Bush, A. I., Copper catalyzed oxidation of alzheimer A beta. *Cell. Mol. Biol.* **2000**, 46, (4), 777-783.
204. Butterfield, D. A., Amyloid beta-peptide (1-42)-induced oxidative stress and neurotoxicity: Implications for neurodegeneration in Alzheimer's disease brain. A review. *Free Radical Res.* **2002**, 36, (12), 1307-1313.
205. Naslund, J.; Schierhorn, A.; Hellman, U.; Lannfelt, L.; Roses, A. D.; Tjernberg, L. O.; Silberring, J.; Gandy, S. E.; Winblad, B.; Greengard, P.; Nordstedt, C.; Terenius, L., Relative abundance of Alzheimer A-beta Amyloid peptide variants in Alzheimer-disease and normal aging. *Proc. Natl. Acad. Sci. U. S. A.* **1994**, 91, (18), 8378-8382.
206. Li, H., Rahimi, F., Sinha, S., Maiti, P., Bitan, G., Murakami, K., Amyloids and Protein Aggregation-Analytical Methods. In *Encyc. Anal. Chem.*, 2009.
207. Bertini, I.; Gonnelli, L.; Luchinat, C.; Mao, J.; Nesi, A., A New Structural Model of A beta(40) Fibrils. *J. Am. Chem. Soc.* **2011**, 133, (40), 16013-16022.
208. Torok, M.; Milton, S.; Kaye, R.; Wu, P.; McIntire, T.; Glabe, C. G.; Langen, R., Structural and dynamic features of Alzheimer's A beta peptide in amyloid fibrils studied by site-directed spin labeling. *J. Biol. Chem.* **2002**, 277, (43), 40810-40815.
209. Maji, S. K.; Amsden, J. J.; Rothschild, K. J.; Condrón, M. M.; Teplow, D. B., Conformational dynamics of amyloid beta-protein assembly probed using intrinsic fluorescence. *Biochemistry* **2005**, 44, (40), 13365-13376.
210. Yong, W.; Lomakin, A.; Kirkitadze, M. D.; Teplow, D. B.; Chen, S. H.; Benedek, G. B., Structure determination of micelle-like intermediates in amyloid beta-protein fibril assembly by using small angle neutron scattering. *Proc. Natl. Acad. Sci. U. S. A.* **2002**, 99, (1), 150-154.
211. Walsh, D. M.; Hartley, D. M.; Kusumoto, Y.; Fezoui, Y.; Condrón, M. M.; Lomakin, A.; Benedek, G. B.; Selkoe, D. J.; Teplow, D. B., Amyloid beta-protein fibrillogenesis - Structure and biological activity of protofibrillar intermediates. *J. Biol. Chem.* **1999**, 274, (36), 25945-25952.

212. Nelson, R.; Sawaya, M. R.; Balbirnie, M.; Madsen, A. O.; Riekel, C.; Grothe, R.; Eisenberg, D., Structure of the cross-beta spine of amyloid-like fibrils. *Nature* **2005**, 435, (7043), 773-778.
213. Sawaya, M. R.; Sambashivan, S.; Nelson, R.; Ivanova, M. I.; Sievers, S. A.; Apostol, M. I.; Thompson, M. J.; Balbirnie, M.; Wiltzius, J. J. W.; McFarlane, H. T.; Madsen, A. O.; Riekel, C.; Eisenberg, D., Atomic structures of amyloid cross-beta spines reveal varied steric zippers. *Nature* **2007**, 447, (7143), 453-457.
214. McDonald, M.; Box, H.; Bian, W.; Kendall, A.; Tycko, R.; Stubbs, G., Fiber Diffraction Data Indicate a Hollow Core for the Alzheimer's A beta 3-Fold Symmetric Fibril. *J. Mol. Biol.* **2012**, 423, (3), 454-461.
215. Nadal, R. C.; Rigby, S. E. J.; Viles, J. H., Amyloid beta-Cu²⁺ Complexes in both Monomeric and Fibrillar Forms Do Not Generate H₂O₂ Catalytically but Quench Hydroxyl Radicals. *Biochemistry* **2008**, 47, (44), 11653-11664.
216. Shearer, J.; Callan, P. E.; Tran, T.; Szalai, V. A., Cu K-edge X-ray absorption spectroscopy reveals differential copper coordination within amyloid-beta oligomers compared to amyloid-beta monomers. *Chem. Commun.* **2010**, 46, (48), 9137-9139.
217. Shearer, J.; Szalai, V. A., The Amyloid-beta Peptide of Alzheimer's Disease Binds Cu-I in a Linear Bis-His Coordination Environment: Insight into a Possible Neuroprotective Mechanism for the Amyloid-beta Peptide. *J. Am. Chem. Soc.* **2008**, 130, (52), 17826-17835.
218. Himes, R. A.; Park, G. Y.; Siluvai, G. S.; Blackburn, N. J.; Karlin, K. D., Structural Studies of Copper(I) Complexes of Amyloid-beta Peptide Fragments: Formation of Two-Coordinate Bis(histidine) Complexes. *Angew. Chem. Int. Ed.* **2008**, 47, (47), 9084-9087.
219. Furlan, S.; Hureau, C.; Faller, P.; La Penna, G., Modeling the Cu⁺ Binding in the 1-16 Region of the Amyloid-beta Peptide Involved in Alzheimer's Disease. *J. Phys. Chem. B* **2010**, 114, (46), 15119-15133.
220. Raffa, D. F.; Rickard, G. A.; Rauk, A., Ab initio modelling of the structure and redox behaviour of copper(I) bound to a His-His model peptide: relevance to the beta-amyloid peptide of Alzheimer's disease. *J. Biol. Inorg. Chem.* **2007**, 12, (2), 147-164.
221. Furlan, S.; Hureau, C.; Faller, P.; La Penna, G., Modeling Copper Binding to the Amyloid-beta Peptide at Different pH: Toward a Molecular Mechanism for Cu Reduction. *J. Phys. Chem. B* **2012**, 116, (39), 11899-11910.
222. Hureau, C.; Balland, V.; Coppel, Y.; Solari, P. L.; Fonda, E.; Faller, P., Importance of dynamical processes in the coordination chemistry and redox conversion of copper amyloid-beta complexes. *J. Biol. Inorg. Chem.* **2009**, 14, (7), 995-1000.
223. Feaga, H. A.; Maduka, R. C.; Foster, M. N.; Szalai, V. A., Affinity of Cu⁺ for the Copper-Binding Domain of the Amyloid-beta Peptide of Alzheimer's Disease. *Inorg. Chem.* **2011**, 50, (5), 1614-1618.

224. Nakamura, M.; Shishido, N.; Nunomura, A.; Smith, M. A.; Perry, G.; Hayashi, Y.; Nakayama, K.; Hayashi, T., Three histidine residues of amyloid-beta peptide control the redox activity of copper and iron. *Biochemistry* **2007**, 46, (44), 12737-12743.
225. Tycko, R., Molecular structure of amyloid fibrils: insights from solid-state NMR. *Q. Rev. Biophys.* **2006**, 39, (1), 1-55.
226. Bertini, I. L., C.; Parigi, G., Solution NMR of Paramagnetic Molecules. *Solution NMR of Paramagnetic Molecules, Elsevier* **2001**.
227. Wickramasinghe, N. P.; Kotecha, M.; Samoson, A.; Past, J.; Ishii, Y., Sensitivity enhancement in ^{13}C solid-state NMR of protein microcrystals by use of paramagnetic metal ions for optimizing H-1 T-1 relaxation. *J. Magn. Reson.* **2007**, 184, (2), 350-356.
228. Lu, Y.; Prudent, M.; Qiao, L.; Mendez, M. A.; Girault, H. H., Copper(I) and copper(II) binding to beta-amyloid 16 (A beta 16) studied by electrospray ionization mass spectrometry. *Metallomics* **2010**, 2, (7), 474-479.
229. Alies, B.; Badei, B.; Faller, P.; Hureau, C., Reevaluation of Copper(I) Affinity for Amyloid-ss Peptides by Competition with Ferrozine: An Unusual Copper(I) Indicator. *Chem. Eur. J* **2012**, 18, (4), 1161-1167.
230. Li, S.; Hong, M., Protonation, Tautomerization, and Rotameric Structure of Histidine: A Comprehensive Study by Magic-Angle-Spinning Solid-State NMR. *J. Am. Chem. Soc.* **2011**, 133, (5), 1534-1544.
231. Barraud, P.; Schubert, M.; Allain, F. H. T., A strong ^{13}C chemical shift signature provides the coordination mode of histidines in zinc-binding proteins. *J. Biomol. NMR* **2012**, 53, (2), 93-101.
232. Hu, F.; Schmidt-Rohr, K.; Hong, M., NMR Detection of pH-Dependent Histidine-Water Proton Exchange Reveals the Conduction Mechanism of a Transmembrane Proton Channel. *J. Am. Chem. Soc.* **2012**, 134, (8), 3703-3713.
233. Jimenez, B.; Mori, M.; Battistoni, A.; Sette, M.; Piccioli, M., NMR assignment of reduced form of copper, zinc superoxide dismutase from *Salmonella enterica*. *Biomol. NMR Assign.* **2007**, 1, (1), 65-67.
234. Mukrasch, M. D.; Lucke, C.; Lohr, F.; Maneg, O.; Ludwig, B.; Ruterjans, H., Letter to the Editor: Complete ^1H , ^{15}N and ^{13}C assignment of the soluble domain of the ba(3) oxidase subunit II of *Thermus thermophilus* in the reduced state. *J. Biomol. NMR* **2004**, 28, (3), 297-298.
235. Roberts, B. R.; Ryan, T. M.; Bush, A. I.; Masters, C. L.; Duce, J. A., The role of metallobiology and amyloid-ss peptides in Alzheimer's disease. *J. Neurochem.* **2012**, 120, 149-166.

236. Hatcher, L. Q.; Hong, L.; Bush, W. D.; Carducci, T.; Simon, J. D., Quantification of the binding constant of copper(II) to the amyloid-beta peptide. *J. Phys. Chem. B* **2008**, 112, (27), 8160-8164.
237. Gong, Y. S.; Chang, L.; Viola, K. L.; Lacor, P. N.; Lambert, M. P.; Finch, C. E.; Krafft, G. A.; Klein, W. L., Alzheimer's disease-affected brain: Presence of oligomeric A beta ligands (ADDLs) suggests a molecular basis for reversible memory loss. *Proc. Natl. Acad. Sci. U. S. A.* **2003**, 100, (18), 10417-10422.
238. Chimon, S.; Ishii, Y., Capturing intermediate structures of Alzheimer's b-amyloid, A β (1-40), by solid-state NMR spectroscopy. *J. Am. Chem. Soc.* **2005**, 127, 13472-13473.
239. Yu, L. T.; Edalji, R.; Harlan, J. E.; Ho;zman, T. F.; Pereda, L.; Labokovsky, B.; Hillen, H.; Barghorn, S.; Ebert, U.; Richardson, P. L.; Miesbauer, L.; Solomon, L.; Bartley, D.; Walter, K.; Johnson, R. W.; Hajduk, P. J.; Ojejniczak, E. T., Structural characterization of a soluble amyloid beta-peptide oligomer. *Biochemistry* **2009**, 48, 1870-1877.
240. Ahmed, M.; Davis, J.; Aucoin, D.; Sato, T.; Ahuja, S.; Aimoto, S.; Elliott, J. I.; Van Nostrand, W. E.; Smith, S. O., Structural conversion of neurotoxic amyloid-beta(1-42) oligomers to fibrils. *Nat. Struct. Mol. Biol.* **2010**, 17, (5), 561-567.
241. Chimon, S.; Shaibat, M. A.; Jones, C. R.; Calero, D. C.; Aizezi, B.; Ishii, Y., Evidence of fibril-like β -sheet structures in neurotoxic amyloid intermediate for Alzheimer's β -amyloid. *Nat. Struct. Mol. Biol.* **2007**, 14, (12), 1157-1164.
242. Stroud, J. C.; Liu, C.; Teng, P. K.; Eisenberg, D., Toxic fibrillar oligomers of amyloid-beta have cross-beta structure. *Proc. Natl. Acad. Sci. U. S. A.* **2012**, 109, (20), 7717-7722.
243. Laganowsky, A.; Liu, C.; Sawaya, M. R.; Whitelegge, J. P.; Park, J.; Zhao, M.; Pensalfini, A.; Soriaga, A. B.; Landau, M.; Teng, P. K.; Cascio, D.; Glabe, C.; Eisenberg, D., Atomic View of a Toxic Amyloid Small Oligomer. *Science* **2012**, 335, (6073), 1228-1231.
244. Juarez, J.; Taboada, P.; Mosquera, V., Existence of Different Structural Intermediates on the Fibrillation Pathway of Human Serum Albumin. *Biophys. J.* **2009**, 96, (6), 2353-2370.
245. Klein, W. L., A beta toxicity in Alzheimer's disease: globular oligomers (ADDLs) as new vaccine and drug targets. *Neurochem. Int.* **2002**, 41, (5), 345-352.
246. Tycko, R.; Ishii, Y., Constraints on supramolecular structure in amyloid fibrils from two-dimensional solid-state NMR spectroscopy with uniform isotopic labeling. *J. Am. Chem. Soc.* **2003**, 125, (22), 6606-6607.
247. Takegoshi, K.; Nakamura, S.; Terao, T., C-13-H-1 dipolar-driven ^{13}C - ^{13}C recoupling without ^{13}C RF irradiation in nuclear magnetic resonance of rotating solids. *J. Chem. Phys.* **2003**, 118, (5), 2325-2341.

248. Luhrs, T.; Ritter, C.; Adrian, M.; Riek-Loher, D.; Bohrmann, B.; Doeli, H.; Schubert, D.; Riek, R., 3D structure of Alzheimer's amyloid-beta(1-42) fibrils. *Proc. Natl. Acad. Sci. U. S. A.* **2005**, 102, (48), 17342-17347.
249. Yu, L.; Edalji, R.; Harlan, J. E.; Holzman, T. F.; Lopez, A. P.; Labkovsky, B.; Hillen, H.; Barghorn, S.; Ebert, U.; Richardson, P. L.; Miesbauer, L.; Solomon, L.; Bartley, D.; Walter, K.; Johnson, R. W.; Hajduk, P. J.; Olejniczak, E. T., Structural Characterization of a Soluble Amyloid beta-Peptide Oligomer. *Biochemistry* **2009**, 48, (9), 1870-1877.
250. Paravastu, A. K.; Qahwash, I.; Leapman, R. D.; Meredith, S. C.; Tycko, R., Seeded growth of beta-amyloid fibrils from Alzheimer's brain-derived fibrils produces a distinct fibril structure. *Proc. Natl. Acad. Sci. U. S. A.* **2009**, 106, (18), 7443-7448.
251. Sheng Cai, C. S., Zoltan Kovacs, A. Dean Sherry, Yuan Chen, Sensitivity Enhancement of Multidimensional NMR Experiments by Paramagnetic Relaxation Effects. *J. Am. Chem. Soc.* **2006**, 128, (41), 13474-13478.
252. Wickramasinghe, N. P.; Ishii, Y., Sensitivity enhancement, assignment, and distance measurement in ^{13}C solid-state NMR spectroscopy for paramagnetic systems under fast magic angle spinning. *J. Magn. Reson.* **2006**, 181, (2), 233-243.
253. Reif, B., Ultra-high resolution in MAS solid-state NMR of perdeuterated proteins: Implications for structure and dynamics. *J. Magn. Reson.* **2012**, 216, 1-12.
254. Zhou, D. H.; Shah, G.; Cormos, M.; Mullen, C.; Sandoz, D.; Rienstra, C. M., Proton-detected solid-state NMR Spectroscopy of fully protonated proteins at 40 kHz magic-angle spinning. *J. Am. Chem. Soc.* **2007**, 129, (38), 11791-11801.
255. Ernst, M.; Meier, M. A.; Tuhem, T.; Samoson, A.; Meier, B. H., Low-power high-resolution solid-state NMR of peptides and proteins. *J. Am. Chem. Soc.* **2004**, 126, (15), 4764-4765.
256. Nishiyama, Y.; Lu, X.; Trebosc, J.; Lafon, O.; Gan, Z.; Madhu, P. K.; Amoureux, J.-P., Practical choice of ^1H - ^1H decoupling schemes in through-bond ^1H - $\{\text{X}\}$ HMQC experiments at ultra-fast MAS. *J. Magn. Reson.* **2012**, 214, 151-158.
257. Nishiyama, Y.; Endo, Y.; Nemoto, T.; Utsumi, H.; Yamauchi, K.; Hioka, K.; Asakura, T., Very fast magic angle spinning ^1H - ^{14}N 2D solid-state NMR: Sub-micro-liter sample data collection in a few minutes. *J. Magn. Reson.* **2011**, 208, (1), 44-48.
258. Takahashi, H.; Kainosho, M.; Akutsu, H.; Fujiwara, T., ^1H -detected ^1H - ^1H correlation spectroscopy of a stereo-array isotope labeled amino acid under fast magic-angle spinning. *J. Magn. Reson.* **2010**, 203, (2), 253-256.
259. Zhou, D. H.; Shah, G.; Cormos, M.; Mullen, C.; Sandoz, D.; Rienstra, C. M., Proton-detected solid-state NMR spectroscopy of fully protonated proteins at 40 kHz magic angle spinning. *J. Am. Chem. Soc.* **2007**, 129, 11791-11801.

260. Varughese, K. I.; Srinivasan, R., Crystal and molecular-structure of L-Isoleucine hydrochloride monohydrate form-2. *Pramana* **1976**, 6, (4), 189-195.
261. Trommel, J., Bijvoet, J.M, Crystal Structure and Absolute Configuration of the Hydrochloride and Hydrobromide of D(-)-Isoleucine. *Acta Cryst.* **1954**, 7.
262. Igumenova, T. I.; McDermott, A. E.; Zilm, K. W.; Martin, R. W.; Paulson, E. K.; Wand, A. J., Assignments of carbon NMR resonances for microcrystalline ubiquitin. *J. Am. Chem. Soc.* **2004**, 126, (21), 6720-6727.
263. Sun, S.; Yan, S.; Guo, C.; Li, M.; Hoch, J. C.; Williams, J. C.; Polenova, T., A time-saving strategy for MAS NMR spectroscopy by combining nonuniform sampling and paramagnetic relaxation assisted condensed data collection. *J. Phys. Chem. B* **2012**, 116, (46), 13585-96.
264. Paramasivam, S.; Suiter, C. L.; Hou, G.; Sun, S.; Palmer, M.; Hoch, J. C.; Rovnyak, D.; Polenova, T., Enhanced Sensitivity by Nonuniform Sampling Enables Multidimensional MAS NMR Spectroscopy of Protein Assemblies. *J. Phys. Chem. B* **2012**, 116, (25), 7416-7427.
265. Huber, M.; With, O.; Schanda, P.; Verel, R.; Ernst, M.; Meier, B. H., A supplementary coil for ^2H decoupling with commercial HCN MAS probes. *J. Magn. Reson.* **2012**, 214, 76-80.

IX) APPENDICES

A) Permission/Licence for copyrighted images used in this thesis

1) Figure 1

From: "Ed Berger" <eberger@ahaf.org>
Subject: Permission to use a image in thesis
Date: Mon, October 22, 2012 7:39 am
To: "sparth5@uic.edu" <sparth5@uic.edu>

Dear Sudhakar,

Thank you for your email. You may indeed use the illustration.

Please use the following citation:

The medical illustration is provided courtesy of Alzheimer's Disease Research, a program of the American Health Assistance Foundation. (c) 2012
<http://www.ahaf.org/alzheimers>

Kind regards,

Ed Berger

-----Original Message-----

From: Parthasarathy, Sudhakar [<mailto:sparth5@uic.edu>]
Sent: Saturday, October 20, 2012 1:42 PM
To: info
Subject: Permission to use a image in thesis

Dear Sir/Madam

I'm a PhD student in Chemistry at University of Illinois, Chicago. I'm doing research on Alzheimer's disease peptides. I would like to request your permission to use the image in the following website in my the thesis.

<http://www.ahaf.org/alzheimers/about/understanding/plaques-and-tangles.html>

Thank you
Sudhakar

2) **Figure 2****NATURE PUBLISHING GROUP LICENSE
TERMS AND CONDITIONS**

Jan 11, 2013

This is a License Agreement between Sudhakar Parthasarathy ("You") and Nature Publishing Group ("Nature Publishing Group") provided by Copyright Clearance Center ("CCC"). The license consists of your order details, the terms and conditions provided by Nature Publishing Group, and the payment terms and conditions.

License Number	3014271448329
License date	Oct 22, 2012
Licensed content publisher	Nature Publishing Group
Licensed content publication	Nature Neuroscience
Licensed content title	The toxic A[beta] oligomer and Alzheimer's disease: an emperor in need of clothes
Licensed content author	Iryna Benilova, Eric Karran, Bart De Strooper
Licensed content date	Jan 29, 2012
Type of Use	reuse in a thesis/dissertation
Volume number	15
Issue number	3
Requestor type	academic/educational
Format	print and electronic
Portion	figures/tables/illustrations
Number of figures/tables/illustrations	1
High-res required	no
Figures	Figure 2
Author of this NPG article	no
Your reference number	None
Title of your thesis / dissertation	Solid-State Nuclear Magnetic Resonance of Copper-Amyloid β , amylospheroids and fast magic angle spinning
Expected completion date	May 2013
Estimated size (number of pages)	160
Total	0.0 USD

3) **Figure 5****NATURE PUBLISHING GROUP LICENSE
TERMS AND CONDITIONS**

Jan 11, 2013

This is a License Agreement between Sudhakar Parthasarathy ("You") and Nature Publishing Group ("Nature Publishing Group") provided by Copyright Clearance Center ("CCC"). The license consists of your order details, the terms and conditions provided by Nature Publishing Group, and the payment terms and conditions.

All payments must be made in full to CCC. For payment instructions, please see information listed at the bottom of this form.

License Number	3023331080287
License date	Nov 06, 2012
Licensed content publisher	Nature Publishing Group
Licensed content publication	Nature
Licensed content title	Optimal isotope labelling for NMR protein structure determinations
Licensed content author	Masatsune Kainosho, Takuya Torizawa, Yuki Iwashita, Tsutomu Terauchi, Akira Mei Ono et al.
Licensed content date	Mar 2, 2006
Volume number	440
Issue number	7080
Type of Use	reuse in a thesis/dissertation
Requestor type	academic/educational
Format	electronic
Portion	figures/tables/illustrations
Number of figures/tables/illustrations	1
High-res required	no
Figures	Figure 1
Author of this NPG article	no
Your reference number	
Title of your thesis / dissertation	Solid-State Nuclear Magnetic Resonance of Copper-Amyloid β , amylospheroids and fast magic angle spinning
Expected completion date	May 2013
Estimated size (number of pages)	160
Total	0.00 USD

4) Chapter III

RightsLink®

Home

Create Account

Help

ACS Publications
High quality High impact

Title: Molecular-Level Examination of Cu²⁺ Binding Structure for Amyloid Fibrils of 40-Residue Alzheimer's β by Solid-State NMR Spectroscopy

Author: Sudhakar Parthasarathy, Fei Long, Yifat Miller, Yiling Xiao, Dan McElheny, Kent Thurber, Buyong Ma, Ruth Nussinov, and Yoshitaka Ishii

Publication: Journal of the American Chemical Society

Publisher: American Chemical Society

Date: Mar 1, 2011

Copyright © 2011, American Chemical Society

User ID
Password
<input type="checkbox"/> Enable Auto Login
<input type="button" value="LOGIN"/>
Forgot Password/User ID?
If you're a copyright.com user, you can login to RightsLink using your copyright.com credentials. Already a RightsLink user or want to learn more?

PERMISSION/LICENSE IS GRANTED FOR YOUR ORDER AT NO CHARGE

This type of permission/license, instead of the standard Terms & Conditions, is sent to you because no fee is being charged for your order. Please note the following:

- Permission is granted for your request in both print and electronic formats, and translations.
- If figures and/or tables were requested, they may be adapted or used in part.
- Please print this page for your records and send a copy of it to your publisher/graduate school.
- Appropriate credit for the requested material should be given as follows: "Reprinted (adapted) with permission from (COMPLETE REFERENCE CITATION). Copyright (YEAR) American Chemical Society." Insert appropriate information in place of the capitalized words.
- One-time permission is granted only for the use specified in your request. No additional uses are granted (such as derivative works or other editions). For any other uses, please submit a new request.

BACK

CLOSE WINDOW

Copyright © 2012 [Copyright Clearance Center, Inc.](#) All Rights Reserved. [Privacy statement.](#)
Comments? We would like to hear from you. E-mail us at customercare@copyright.com

X) CURRICULUM VITAE

Education

June 2000: B.S Chemistry, University of Madras, India

June 2002: M.S Chemistry, University of Madras, India

January 2013: PhD Analytical Chemistry, University of Illinois at Chicago, USA

Professional Experience

Jan. 2003 – July 2006: Junior Scientist, Dr. Reddy's Laboratories Ltd., Hyderabad, India

Aug. 2006 – Aug. 2009: Teaching Assistant, University of Illinois at Chicago

Aug. 2009 – Jan. 2013: Research Assistant, University of Illinois at Chicago

Research Experience

- Structure elucidation of drugs
- Impurity identification in pharmaceutical products by LC-MS, LC-NMR
- Absolute stereochemistry determination by NMR
- Preparative HPLC
- Method development and validation of HPLC methods
- Interpretation of MALDI, electrospray, EI, CI mass spectral data
- Solid-state characterization of drugs by Powder X-Ray diffraction(PXRD), Differential Scanning Calorimetry (DSC) and Thermo gravimetry (TG)
- Structure determination by single crystal X-ray diffraction
- GLP, SOP and technical report writing
- Structural characterization of peptides and proteins by Solid-state NMR (SSNMR) using magic angle spinning (MAS) and cross-polarization (CP) 1D, 2D homonuclear dipolar recoupling experiments such as RFDR, DARR, heteronuclear double CP experiments and internuclear distance measurements from REDOR, CT-fpRFDR experiments
- Method development-Sensitivity enhancement in SSNMR by paramagnetic relaxation assisted condensed data collection, non-uniform sampling, Ultra-fast MAS, ¹H detection pulse sequences with low power heteronuclear decoupling schemes
- Have experience in handling first of its kind 1mm JEOL Ultra-fast MAS probes (>75kHz) and 1.8mm high speed MAS probe (40kHz) . Handled 2.5mm and 3.2mm MAS probes frequently for routine analysis. Have knowledge in fixing solids probes.
- Have experience in working on 800MHz, 900MHz Bruker NMR instruments (Solids and Solutions equipped with cryo probe).
- Handled PC-12 Rat pheochromocytoma cells and performed toxicity assay experiments on these cells
- Structural characterization of peptides and proteins by solid-state and solution NMR spectroscopy
- NMR pulse sequence development and probe servicing

- Protein purification and crystallization
- Solid phase peptide synthesis, isotope labeling
- Protein and peptide characterization by MALDI, electro spray methods
- Toxicity assay
- NMR and analytical instruments maintenance and trouble shooting

Instruments Handled

- Bruker NMR 400-900MHz
- Varian NMR 200,400,500MHz
- Agilent 1100 series LC-MS with triple quadrupole MS system
- AB SCIEX 4700 MALDI TOF/TOF
- Agilent GC-MS
- Waters, Agilent HPLC
- Perkin-Elmer and Shimadzu FT-IR spectrophotometer
- Shimadzu Differential Scanning Calorimeter (DSC)
- Rigaku single crystal X-ray diffractometer (SXR)
- Rigaku powder X-ray diffractometer (PXRD)
- ABI, PTI solid phase peptide synthesizer
- Jasco Circular Dichroism spectrometer
- Perkin-Elmer CHNS elemental analyzer
- Shimadzu, Varian, Perkin-Elmer UV-VIS spectrophotometer
- Hitachi Fluorescence spectrometer
- Jasco Polarimeter

Publications

Dr. Reddy's Laboratories Ltd, 2003-2006

- Solid state structural studies of saccharin salts with some heterocyclic bases
P. Sudhakar, S. Vijay Kumar, Peddy Vishweshwar, J. Moses Babu, K. Vyas; CrystEngComm, 2008,10, 996-1002
- Spectral Characterization of Itraconazole Impurities in the Drug Product
Nirmala Munigela, J.Moses Babu, Anjaneyulu Yerramilli, **Sudhakar Parthasarathy**, Vyas Krishnamurthy, K.N.Reddy; Trade science Inc, Analytical Chemistry, An Indian Journal, Vol. 7, Issue 2, 2008
- Identification and characterization of potential impurities of rabeprazole sodium
Ganta Madhusudan Reddy, B. Vijaya Bhaskar, P. Pratap Reddy, **P. Sudhakar**, J. Moses Babu K. Vyas, P. Ramachandra Reddy, K. Mukkanti; Journal of pharmaceutical and Biomedical analysis, Volume 43, 2007, 1262-1269

- Structural identification and characterization of potential impurities of pantoprazole sodium
Ganta Madhusudan Reddy, B. Vijaya Bhaskar, P. Pratap Reddy, S. Ashok, **P. Sudhakar**, J. Moses Babu K. Vyas, K. Mukkanti; Journal of pharmaceutical and Biomedical analysis, Volume 43, 2007, 1262-1269
- Carboxylic acid-pyridine supramolecular heterocatenar in a co-crystal
P. Sudhakar, R. Srivijaya, B.R. Sreekanth, P.K. Jayanthi, Peddy Vishweshwar, Moses J. Babu, K. Vyas, Javed Iqbal; Journal of molecular structure, 885, 2008, 45-49
- Synthesis and Crystal Structure of 2-(1-methyl-1H-3-indolyl) nicotinonitrile
Sudhakar Parthasarathy, Surajit Banerjee, Krishnamurthi Vyas, J.Moses Babu, Indu Dager and Manojit Pal; Analytical sciences: X-Ray structure analysis online, March 2006, Vol.22, x55.
- Identification and characterization of potential impurities of amlodipine maleate
P. Sudhakar, M. Nirmala, J. Moses Babu, K. Vyas, Ganta Madhusudan Reddy, B. Vijaya Bhaskar, P. Pratap Reddy, K. Mukkanti; Journal of pharmaceutical and Biomedical analysis, Volume 40, 2006, Issue 3, 605-613
- Structural studies of impurities of risperidone by hyphenated techniques
P. Sattanathan, J. Moses Babu, K. Vyas, R. B. Reddy, S.T. Rajan, **P. Sudhakar**; Journal of pharmaceutical and Biomedical analysis, Volume 40, 2006, Issue 3, 598-604.
- Identification and characterization of impurities in Racecadotril by LC-MS
K. Mallikarjun Reddy, J. Moses Babu, **P. Sudhakar**, M.S.P. Sharma, G. Sudershan Reddy, K. Vyas; Pharmazie, 61, 2006, 994-998
- Crystal Structure and Synthesis of 1-benzyl-4-(5,6-dimethoxy-1H-2-indenylmethyl) piperidine, a donepezil impurity
P. Sudhakar, Surajit Banerjee, K. Vyas, J. Moses Babu, E.R.R. Chandrashekar, P. Anil Kumar and Vijayavithal T. Mathad; Analytical sciences: X-Ray structure analysis online, July 2005, Vol.21, Part 6, x97

PhD, University of Illinois at Chicago, 2006-2013

- NMR-based characterization of structures, redox reactions, and reactive oxygen species (ROS) production mechanism in Cu-ion bound Alzheimer's β amyloid fibrils
- Manuscript in preparation
- ^1H Indirect Detection for ^{13}C Biomolecular Solid-state NMR: Enhanced Sensitivity and Resolution by a Combined Use of Ultra Fast Magic Angle Spinning, High Field and Stereo Array Isotope Labeling - Manuscript in preparation

- Molecular-Level Structural Insights into a Pathologically Relevant Amyloid Intermediate of Alzheimer's β by Solid-state NMR- Manuscript in preparation
- Sensitivity and Resolution Enhanced Solid-state NMR for Biomolecules and Paramagnetic Systems under Very Fast Magic Angle Spinning
Sudhakar Parthasarathy, Yusuke Nishiyama, Yoshitaka Ishii; Submitted to Accounts of Chemical Research
- Molecular-Level Examination of Cu^{2+} Binding Structure for Amyloid Fibrils of 40-Residue Alzheimer's β by Solid-State NMR Spectroscopy
Sudhakar Parthasarathy, Fei Long, Yifat Miller, Yiling Xiao, Dan McElheny, Kent Thurber, Buyong Ma, Ruth Nussinov, and Yoshitaka Ishii; Journal of American Chemical Society, 2011, 133 (10), 3390–3400, 2011
- Nanomole-scale protein solid-state NMR by breaking intrinsic ^1H T_1 boundaries
Nalinda P Wickramasinghe, **Sudhakar Parthasarathy**, Christopher R Jones, Chhavi Bhardwaj, Fei Long, Mrignayani Kotecha, Shahila Mehboob, Leslie W-M Fung, Jaan Past, Ago Samoson and Yoshitaka Ishii; Nature Methods, 6, 3, 215-218, 2009

Teaching Experience

- Taught general, physical and analytical chemistry courses
- Trained colleagues and under graduate students in the industry as well as in academics

Awards and Honors

- University rank holder in MS, 2002
- ENC student travel award, 2009
- ISOTEC student Sponsorship award for ENC, 2010
- ISOTEC student Sponsorship award for ENC, 2011
- ISOTEC student Sponsorship award for ENC, 2012